RESEARCH ARTICLES

Title: Anomaly Detection and Performance Analysis by Using Big Data Filtering Techniques For Healthcare on IoT Edges

Authors: Şükrü Mustafa KAYA, Atakan ERDEM, Ali GÜNEŞ

Anomaly Detection and Performance Analysis by Using Big Data Filtering Techniques For Healthcare on IoT Edges

Şükrü Mustafa KAYA*[1], Atakan ERDEM[2], Ali GÜNEŞ[1]

Abstract

The IoT is a sensors world that detects countless physical events in our environment and transforms them into data, and transfers this data to different environments or digital systems. The usage areas of Internet of things-based technologies are constantly increasing and technologies are being developed to support the IoT infrastructure. But, in order to effectively manage the large number of big-data generate in the detection layer, it should be pre-processed and done in accordance with big-data standards. For the effective management of big data, it is imperative to improving the standards of the data set, and filtering methods are being developed for a higher quality data set. For instance, using data cleaning methods is a preprocessing method that facilitates data mining operations. In this way, more manageable data is obtained by preventing the formation of interference and big data can be managed more effectively. In this study, we investigate the efficient operation of IoT and big data originating from the internet of things. Additionally, real-time anomalous data filtering is performed on IoT edges with a data set consisting of six different data produced in real-time. Furthermore, the speed and accuracy performances of classifiers are compared, and machine learning algorithms such as the random cut forest-*RCF*, logistic regression-*LR*, naive bayes-*NB*, and neural network-*NN* classifiers are used for comparison. According to the accuracy performance values, the RCF and LR classifiers are very close, but considering the speed values, it is seen that the LR classifier is more successful in IoT systems.

Keywords: Internet of things, big data, big data analytics, data preprocessing

1. INTRODUCTION

The increase in the number of people suffering from chronic diseases, psychological problems, injuries and infectious diseases around the world also increases the costs of benefiting from health services. It is becoming inevitable day by day that the health services provided in health institutions using IoT technologies can be provided outside of these environments. Although the long-term use of health services in the hospital environment causes an undeniable financial burden, the long-term treatments performed in the hospital cause many physical, mental and social problems for the patients. In order to reduce such problems, the Internet of Things technology allows medical

* Corresponding author: mk3385@hotmail.com
[1] Istanbul Aydin University, Faculty of Engineering, Department of Computer Engineering.
E-mail: aligunes@aydin.edu.tr
ORCID: https://orcid.org/0000-0003-2710-0063, https://orcid.org/0000-0001-6177-0313
[2] Jackson's Lab, University of Calgary, Calgary, Canada
atakan.erdem1@ucalgary.ca
ORCID: https://orcid.org/0000-0003-4514-6719

KAYA et al.

Anomaly Detection and Performance Analysis by Using Big Data Filtering Techniques For Healthcare on I...

measurements to be made without adversely affecting the daily life of the patient.

IoT technology has emerged that can be used to facilitate healthcare services, monitor the physical world, generate data, and integrate with cloud computing and database systems. Sensors that take on tasks in Internet of things technology can communicate and share information with each other over the network. Because it has such a feature, IoT technology is widely used in smart cities, smart health services, and many similar smart systems. But, it is not possible for IoT devices and sensors to pre-process data while generating data. [1,2]. IoT edges are the first place where generated data can be pre-processed before it goes to the cloud. It is significant to pre-process the data before it goes to the network environment because if pre-processing is not done, the achievement of the services serving on the network will decrease in sense of speed and accuracy [3,4]. Hence, speed and accuracy are two significant factors that should not be ignored. Because not much work has yet been done in healthcare that focuses on the speed and accuracy components, it is considered that the experimental outcomes obtained in this study will contribute significantly to the studies to be carried out in the field of health care services. Similar problems experienced in different IoT fields can be given as an example.

Yar H. et al. In their work, offer a cost-effective framework for smart home applications within the scope of internet of things and edge-computing. The framework is aimed at eliminating security problems by controlling home appliances remotely. The Raspberry Pi acts as a hub that connects sensors and other devices used in the home to each other on the network. Finally, the advantages of the proposed system are presented in the study [5]. Hamdan S. et al. in this paper extensively examines edge computing architectures for IoT. Also, the paper presents significant restrictions of existing edge computing architectures internet of things and recommends solutions to them. Additionally, this study details the internet of things implementations in the edge-computing space. Finally, the paper proposes four different scenarios for using edge computing architectures-IoT by IoT applications [6]. Peyman M. et al., in their study, examine the situation of IoT in smart transportation systems. They develop a methodology based on agile optimization algorithms to solve the dynamic ride sharing problem based on the concepts of edge and fog computing. In the study, a numerical example is presented considering a dynamic ride-sharing problem, demonstrating the potential of using edge/fog computing, open data, and agile algorithms [7].

The aim of this study is to produce solutions by examining the IoT and big data management together. For this purpose, real-time anomaly detection is performed on the IoT data stream. The detection of anomaly is done using the RCF, LR, NB, and NN algorithms. The accuracy scores, classification performances, and confusion matrices of the classifiers are presented in the relevant section.

2. RELATED WORKS

This research paper focuses on water quality control and ecosystem protection using IoT technology. An IoT system is proposed to monitor water quality for solving problems encountered. The output of the ANN technique was tested using statistical methods in the proposed system. Arduino UNO R3 board is used because it can process low-power sensor data, and ESP 8266 Wi-Fi laptop computer is used to transfer real-time data streams [8]. In this study, Heba A. et al. studies on the based on internet of things and big data, IoT systems producing big data are examined. The current IoT-based systems and applications that are likely to become widespread in the future are discussed. Also, problems encountered in IoT architectures and solutions are determined [9]. Gulia P. and Chahal A. discuss different big data tools and techniques that can be used for IoT frameworks in their work. They also propose a method that demonstrates how big data can be used to intelligently analyze IoT datasets. Different platforms related to Big-data Analytics are explained in detail and it is shed light on which one is more suitable for IoT [10]. Another study investigates cloud computing and IoT applications, focusing on trending technologies and identifying issues, benefits, and threats. In addition, the relationship between internet of things and big data technologies and how they affect our lifestyle, how big data and IoT devices

KAYA et al.

Anomaly Detection and Performance Analysis by Using Big Data Filtering Techniques For Healthcare on I...

work are discussed and explained with the example of smart agriculture. [11]. In this study, focusing on the security issues of cloud computing and big data, a new solution is proposed for cloud computing integrated with the IoT within a base scenario for big data. Furthermore, an architecture is presented to reduce security issues along with the difficulties of IoT and cloud computing integration [12]. In a different study, within the scope of smart city, it is focused on overcoming parking problems, which have become a big problem for a city, by making use of IoT and big data technologies. In the study, the ability of smart parking platforms to process and analyse big data in Jakarta is investigated and requirements, system architecture, detection methods and technologies based on Hadoop MR platform are discussed [13]. Kodidala V.S.S.J. et al. in their study, they focus on industrial IoT and propose a new architecture to meet the IoT-based service and infrastructure demands of industrial companies. Moreover, in the implementation of the proposed architecture, MapReduce is used to control data streams, Apache Hadoop and Apache Spark are used to test data input [14].

3. BIG IoT DATA

Big IoT Data is becoming a widely used concept that develops spontaneously in different fields and disciplines where IoT technology is used. Big data management methods are being improved to help the processing of large volumes of data collected from many different fields such as health, education, agriculture, environment and industry by using smart technologies. As a result of these developments, the speed of which is increasing day by day, big data development processes become important and big data management undertakes the task of data analysis within IoT systems. Rajan et al., in their study, conduct a comprehensive research on IoT technologies that produce Big Data. [15,16]. In a different study, Li X. and colleagues address the problems related to the security of IoT technologies and offer solutions [17].

3.1. Integration of Big Data Analysis and IoT

It is predicted that the number of internet users will be over six billion by 2025 and billions of data will be produced every second as a result of the widespread use of network technologies. IoT technologies enable data generated by sensors to circulate over the network [18,19]. The main source of big data is IoT systems that are actively used in different fields [20]. As a result of this situation, the need to develop internet of things and big data together arises. These two different platforms, which have become a necessity to integrate with each other, should minimize all the problems to be encountered and be able to effectively manage their IoT environment. Data storage tools used in cloud computing systems are widely used in IoT systems. But this is not the only use of cloud-based storage tools [21,22] However, data processing and analysis processes in IoT systems can be done not only in the cloud, but also near the detection layer, at the IoT edge or in fog processing areas. [23]. When the literature is examined, it is seen as a negative factor that IoT increases the data volume and diversity. However, this is a factor that will accelerate the developments in the field of big data, speed up analysis methods and application development. Moreover, the use of big data techniques in IoT applications also accelerates R&D activities related to IoT systems. As a result, the interoperability and integration of IoT and Big data allows rapid development in both fields.

3.2. Data Mining in the Big IoT Data

The purpose of big data applications and analysis methods is to make accurate predictions in order to make the most accurate decisions. Heterogeneous and large-volume data sets help big data analysis make the right decisions. But at the same time, more data and more uncertainty can reverse the situation if this situation becomes uncontrollable. [24].

Internet of thing data is not homogeneous because it is produced from very different sources. Accuracy and speed are the two most important factors and must be analyzed simultaneously. Commonly used data mining methods are not sufficient to analyze internet of thing data. For effective management, data from the detection layer must be filtered and classified. A huge volume of raw data is collected through the internet of things systems. Thus, new methods and techniques should be developed to extract

KAYA et al.

Anomaly Detection and Performance Analysis by Using Big Data Filtering Techniques For Healthcare on I...

meaningful information from raw data. For example, raw data streams are produced with sensors used to measure values such as temperature, pressure, motion, oxygen, sound, smell, and taste in the healthcare domain. It is predicted that the data produced by billions of sensors will create a huge data stream. Different data streams from different systems are used for many different purposes. Therefore, it should be known how the data is produced and the methods in which it is processed, also necessary security precautions should be taken. Because if meaningful conclusions cannot be drawn from the collected data, it may not contribute to the relevant parties. Therefore, data mining methods are among the main methods recommended to obtain meaningful information from the moment the data is detected [9,25].

3.3. Big Data Analysis in the IoT

How to obtain meaningful and beneficial knowledge from complicated systems perceived at distinct times and with different methods is an important problem [26]. In order to effectively manage the data flows in the internet of things, it should be processed using data mining methods suitable for the data flow. In addition, data mining methods applied to the internet of things layers can adapt to the changes that will occur in the nodes on the network. It is thought that ML algorithms are suitable to eliminate anomalies that will occur on the data flow and adapt to the changes on the network. Since ML methods are within the scope of artificial intelligence, it aims to transfer information to people from digital environments without the need for outside intervention. Hence, ML methods are suitable for data mining in IoT-based systems. Because ML methods have some features that can make data mining in IoT-based systems. For instance, ML algorithms can continue to learn new rules when a new node is added to an IoT-based system. Despite there are many methods that can make IoT-based systems smart, one of the most successful and widely used methods is data mining [25,27].

4. MATERIAL AND METHODOLOGY

The classical internet of things architecture consists of four main layers: the detection layer, the network layer, the service, and management layer, and the application layer. [28] Temperature, pressure, motion, color, odor and similar sensors used in the internet of things detection layer can sense all perceptible events in the world and learn about the actions of the world. However, such sensors and edge tools are not appropriate for serious performance tasks such as calculation and analysis. Although the cloud has almost unlimited processing capacity, it is physically far from edge devices. For this reason, only a cloud-based internet of things architecture cannot perform effectively, especially in IoT systems where real-time processes are intense. As the edge is a key component in internet of things architectures, it can integrate cloud and IoT systems for the best performance, making it easy to work with other layers [29].

Accuracy and speed measures are two crucial aspects for real-time IoT designs. For this reason, Kim et al. proposes a method of data filtering using classifiers for servers in the cloud. The developed data pre-processing method is placed in front of the server, where the data is pre-processed before it goes to the server, and firstly, raw data is collected from the objects with the help of the sensing layer. After the raw data were collected, the corrupted data were classified using Naive Bayes classifiers. After data pre-processing is performed, the data is transmitted to the server for analysis, and the data processing load is reduced. [30].

The focus of our study is to detect anomalies in the real-time data flow between the detection layer and the network layer.

4.1. Data Set

The data set of the study consists of 10,000 sensor data consisting of time, gender, age, weight, height, and temperature values. 7000 of the 10,000 data that make up the data set are used for training. Classifiers use 3000 data in the dataset for verification and prediction. Additionally, the scikit learn library is used for modeling and normalization.

KAYA et al.

Anomaly Detection and Performance Analysis by Using Big Data Filtering Techniques For Healthcare on I...

5. CASE STUDY

In our study, classification success and data processing rates of RCF, LR, NB and NN classifiers used for anomaly detection are compared and the results are presented. AWS services are mostly used to create the simulation platform. The simulation architecture where data flow between IoT layers, anomaly detection and performance tests are performed is presented in Figure 1.
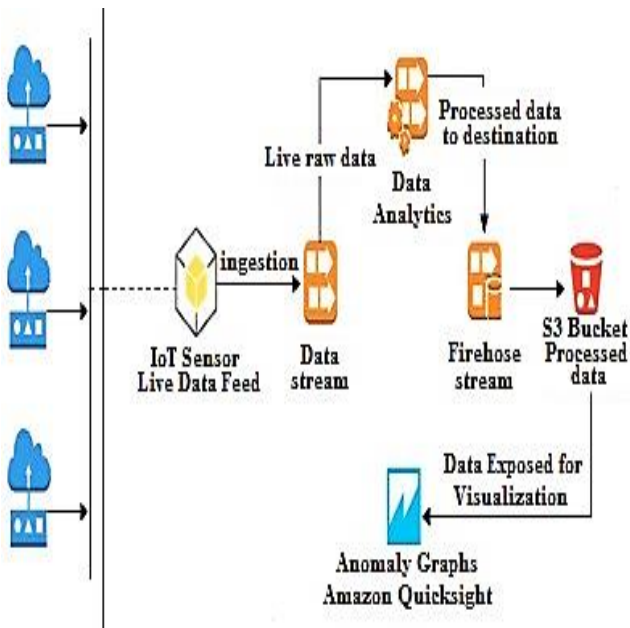
Figure 1 Architecture used for simulation

While an important part of Internet of things-based systems is about data collection, it is also analysis. Many different methods are used for data collection in IoT systems. Some of these can be listed as wired networks, low-power wide-area networks, cellular networks, wireless sensor networks, blueTooth, and Wi-Fi. In IoT-based systems, the server takes care of the data collected from the nodes. Likewise, this data is transmitted to servers in the cloud. Servers analyze the data collected in IoT-based systems to serve from the user interface and extract meaningful information. Therefore, data flows in IoT systems contain vital information. Data integrity becomes an important factor in all these data processing processes. Data integrity simplifies data analysis processes by reducing the workload of servers. Reducing the workload not only reduces energy consumption, but also allows many problems to be minimized. For all these reasons, there is a need for solutions that will ensure data integrity. The simulated

architecture to ensure data integrity is presented in figure 1. The architecture presented in the figure is placed in front of the server. Anomaly detection is performed by simultaneously pre-processing the data produced in the sensing layer. The data in the real-time data stream represents the kinesis data stream. After pre-processing on the data stream, meaningful data is stored in the target to be presented to users. As IoT devices, sensors are defined and simulated by obtaining data flow from the data produced by the sensors.

- Anomaly detection on the data stream is made in real time by utilizing the platforms provided by Amazon Web Service.
- The data is pre-processed to determine whether it is normal or anomaly.
- The software support required for the creation of the data set and data flow required to implement the simulation is provided by the Python programming language.

Figure 2 represents the data flow in the simulation completed on Amazon Web Service, and a five-layered process in section 5.1 is followed to complete this process.
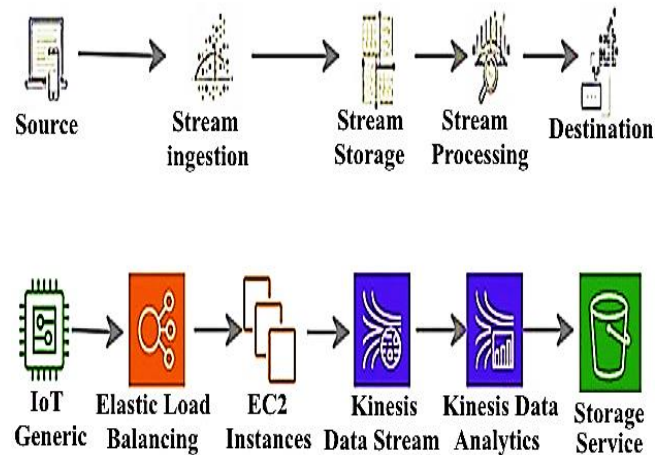
Figure 2 Data stream model

5.1. Platform Layers

Kinesis Data Stream: On the Amazon Web Service platform, is used to create a data flow by utilizing the data produced by the sensors and allows the necessary adjustments to be made according to the simulation model.

KAYA et al.

Anomaly Detection and Performance Analysis by Using Big Data Filtering Techniques For Healthcare on I...

Data Stream Load: According to the flowchart presented in Figure 3, the code developed with the help of python assumes the function of a sensor and generates data locally. In the data stream created with the data coming from the sensors, values in the range of 30-40 degrees Celsius indicate that the data are normal, while those greater than 100 degrees Celsius indicate anomaly data.
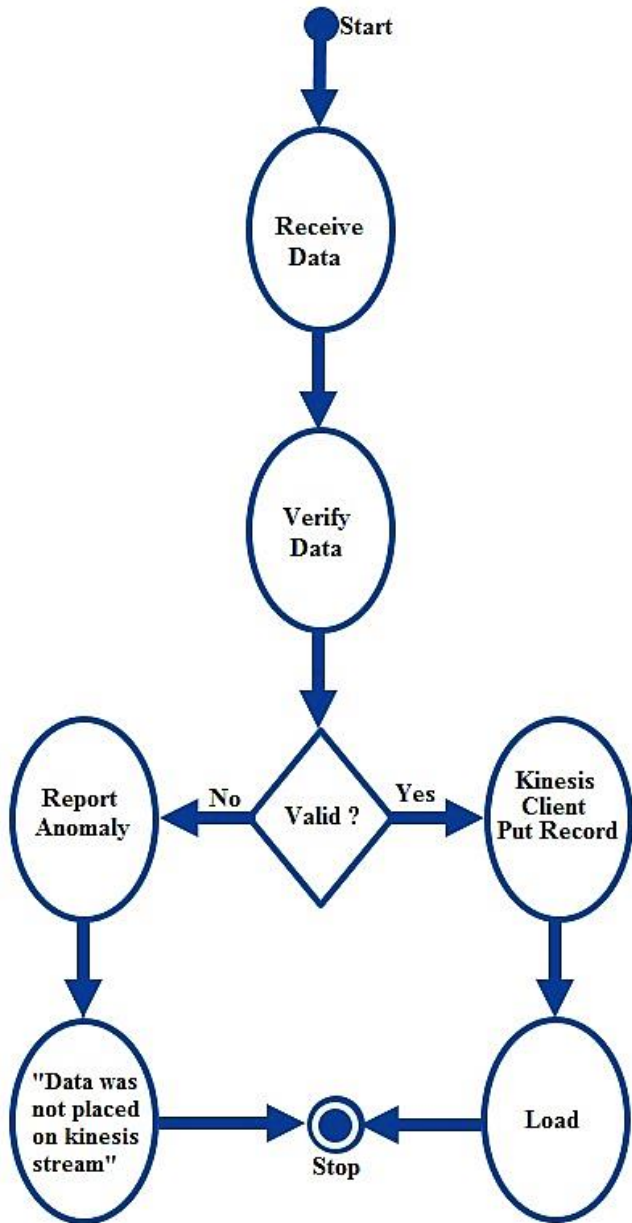
Figure 3 Data Source

Kinesis Data Analysis: is an AWS service used to analyze the data flow generated between the network and perception layers. Anomaly detection operations on the data stream of the used

classifiers are done by using Amazon Web Service.

Kinesis Firehose Stream: In the fourth layer, the target S3 bucket where the incoming data will be stored in the sensing layer is configured and a kinesis firehose stream is created. The firehose stream and the S3 bucket are associated and then the generated information is stored by the firehose data stream in CSV format.

Amazon Quick Sight: This service is used to visualize data stream and data processing processes in the created simulation model.

5.2. Experimental Results

In this section, classification performances of RCF, LR, NN, NB algorithms are tested on the data stream created with the data coming from the sensors, and classification performances, performance curves and complexity matrices are presented in the section. The formulas for the metrics presented in the classification reports are defined as follows [32].

There are different scales used to evaluate classification performance. These scales were formulated based on four different possibilities. If a correct prediction was made, this is defined as a "true positive" however, if the prediction is negative but the sample is positive, it is defined as a "false negative". If the prediction for a negative sample is negative, it is defined as a "true negative", but if the prediction is positive it is considered a "false positive". These four different situations are formulated in Table 1.

Table 1 Classification Measures

Name	Formula
Error and Accuracy	**(TP+FN) / N** **(TP + TN) / N=1−Error**
TP-Rate **FP-Rate**	**TP / P** **FN / N**
Precision **Recall**	**TP / P** **TP / P = TP / P Rate**
Sensitivity **Specificity**	**TP / P = TP / P Rate** **TN / N = 1− FP-Rate**

5.2.1. Classification Reports

The results we present in the classification reports are derived from 3000 data used in validation and

KAYA et al.

Anomaly Detection and Performance Analysis by Using Big Data Filtering Techniques For Healthcare on I...

prediction, representing 30% of the dataset. The reports present their effects on precision, recall, F1-score, and support metrics. How the metric values are obtained is explained in the following items:

- **Precision** is defined as the ratio of true positives to the sum of true positives and false positives in the class and it is formulated as follows:

Precision: *Accuracy of positive predictions=*

Precision = TP / (TP + FP)

- **Recall** refers to the ability of classifiers to find all of the correct examples. It is defined as the ratio of true positives to the sum of false negatives and true positives in all classes and it is formulated as follows:

FN: False Negatives

Recall = TP / (FN +TP)

- **F1 Score** is the harmonic mean of the Precision and Recall values and is a measure of how well the classifier is performing.

F1 Score = 2 * (Precision * Recall) / (Precision + Recall)

Table 2 Classification Report of RCF Algorithm

Classification Report of RCF Algorithm				
	Precision	**Recall**	**F1-Score**	**Support**
1	56/100	16/100	24/100	217
0	94/100	99/100	96/100	2783
Mic. Avge.	93/100	93/100	93/100	3000
Mac. Avge.	75/100	57/100	60/100	3000
Weighted Avge.	91/100	93/100	91/100	3000

In Table 2, where the classification report of the RCF classifier is presented, precision, recall, F1-score, and support metrics are given. The table shows the ratios of 3000 data used in validation and prediction on metrics.

Table 3 Classification Report of LR Algorithm

Classification Report of LR Algorithm				
	Precision	**Recall**	**F1-Score**	**Support**
1	56/100	17/100	26/100	217
0	94/100	99/100	96/100	2783
Mic. Avg.	93/100	93/100	93/100	3000
Mac.Avg.	75/100	58/100	61/100	3000
Weighted Avg.	91/100	93/100	91/100	3000

Table 3, which represents the classification report of the LR algorithm, shows the distribution of 3000 data used in verification and prediction over the metrics.

Table 4 Classification Report of NN Algorithm

Classification Report of NN Algorithm				
	Precision	**Recall**	**F1-Score**	**Support**
1	7/100	1.00	14/100	218
0	0	0	0	2782
Accuracy	---	---	7/100	3000
Mac. Avge.	4/100	50/100	7/100	3000
Weighted Avge.	1/100	7/100	1/100	3000

The report presented in Table 4 is the classification report of the NN classifier. The columns in the table contain values about precision, recall, F1-score, and support metrics.

Table 5 Classification Report of NB Algorithm

Classification Report of NB Algorithm				
	Precision	**Recall**	**F1-Score**	**Support**
1	64/100	3/100	6/100	1460
0	52/100	98/100	68/100	1540
Mic. Avge.	52/100	52/100	52/100	3000
Mac. Avge.	58/100	51/100	37/100	3000
Weighted Avge.	57/100	52/100	37/100	3000

Table 5 contains the classification report of the NB algorithm. When the report is examined, the metric values of the classification made with 3000 data used for verification and prediction are seen.

KAYA et al.

Anomaly Detection and Performance Analysis by Using Big Data Filtering Techniques For Healthcare on I...

Table 6 Accuracy Scores

	Accuracy Scores
RCF Algorithm	0,93
LR Algorithm	0,92
NB Algorithm	0,5193
NN Algorithm	0,0726

Accuracy scores according to the classification made by the algorithms are presented in Table 6. When the table is examined, it is seen that the RCF algorithm makes the most accurate classification, while the NN algorithm makes the worst classification.

Table 7 Comparison of data processing speed

Comparison of data processing speed		
	Execution time	CPU time
LR Algorithm	0,00044 sec.	0,000625 sec.
NB Algorithm	0,00167 sec.	0,00219 sec.
RCF Algorithm	0,148 sec.	0,15 sec.
NN Algorithm	0,0418 sec.	67 sec.

The data processing speeds of four different algorithms are presented in Table 7. When the algorithms are compared according to the table, it is seen that the LR classifier is the most successful in terms of data processing speed.

5.2.2. Performance Curve

ROC curves are presented in this section of the study. The ROC curve is constructed by plotting the true positive rate (TPR) and the false positive rate (FPR). The Y axis represents the true positive rate and the X axis represents the false positive rate. When TPR=1 and FPR=0 in a ROC curve, it means that the model is successful. Also, in this part of the study, Area Under the Curve (AUC) scores are presented. AUC scores show which algorithm makes more accurate predictions in the classification process.
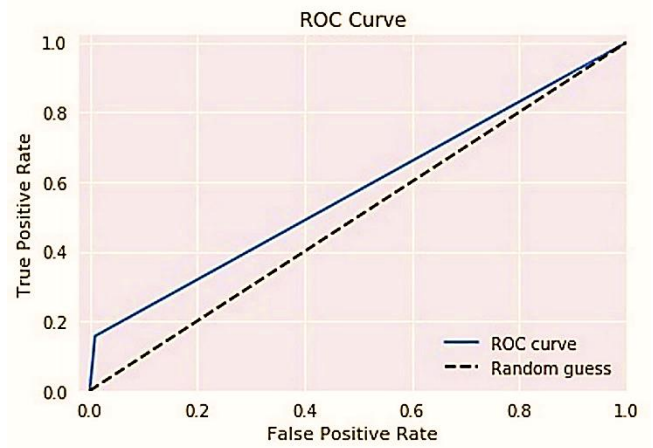
Figure 4 RCF Algorithm Roc Curve
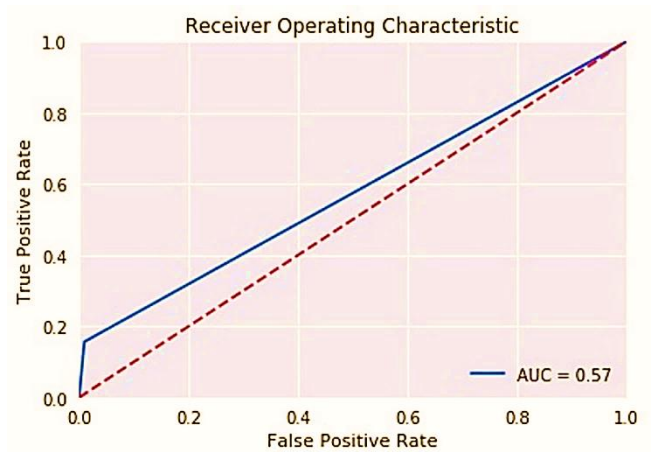
Figure 5 RCF Algorithm Auc Score
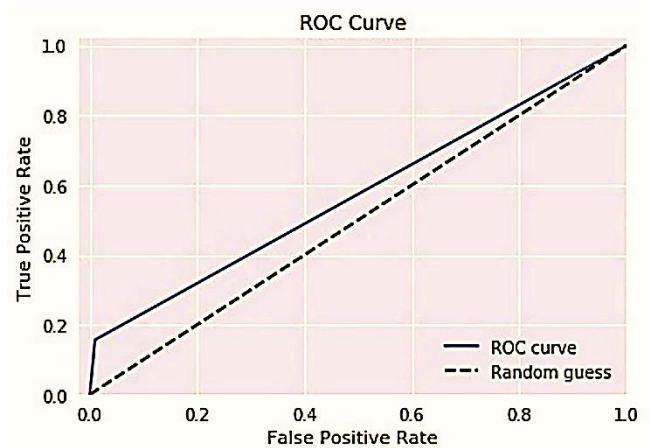
Figure 6 LR Algorithm Roc Curve

KAYA et al.

Anomaly Detection and Performance Analysis by Using Big Data Filtering Techniques For Healthcare on I...
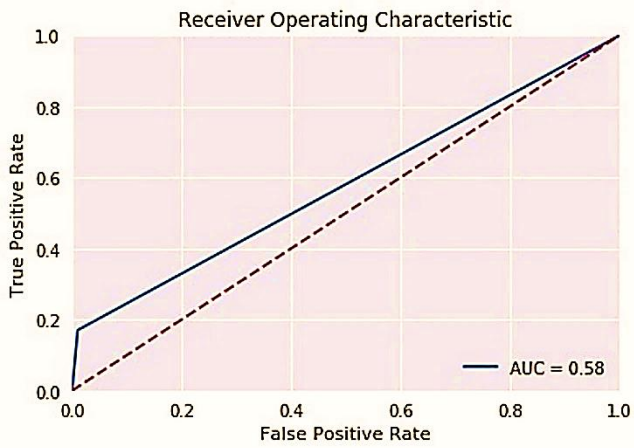
Figure 7 LR Algorithm Auc Score
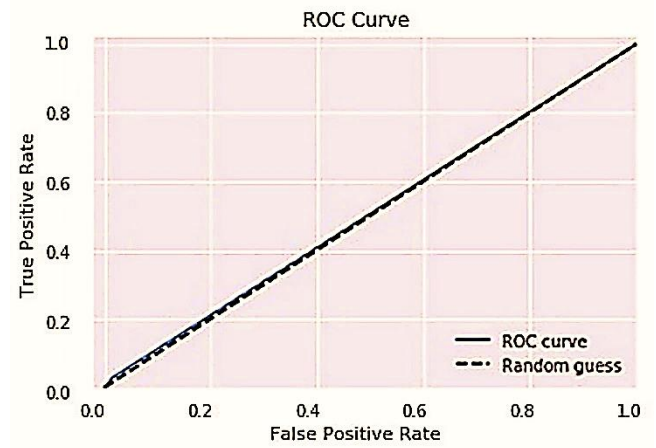
Figure 10 NB Algorithm Roc Curve
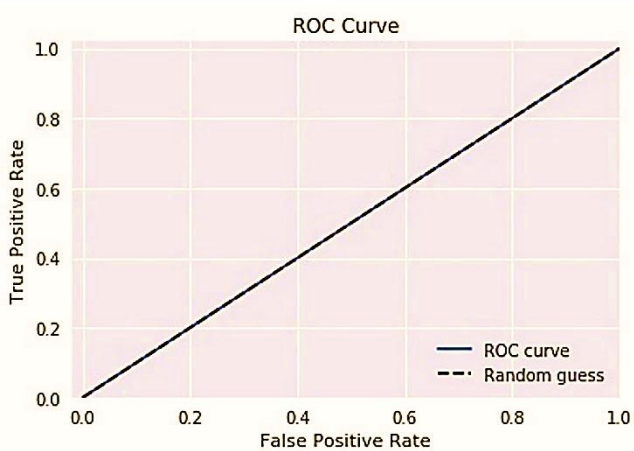
Figure 8 NN Algorithm Roc Curve
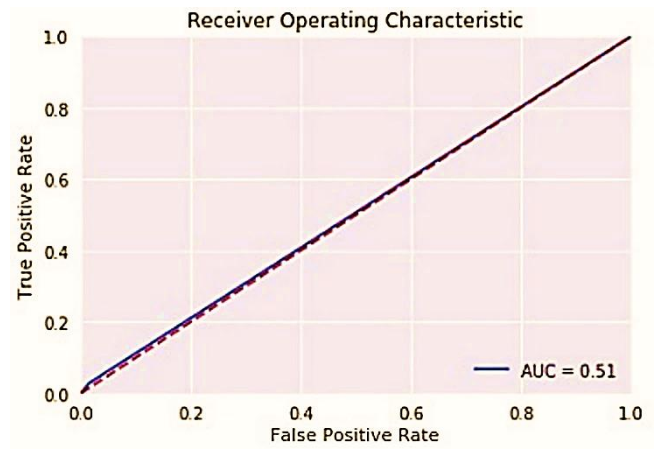
Figure 11 NB Algorithm Auc Score

5.2.3. Confusion Matrices
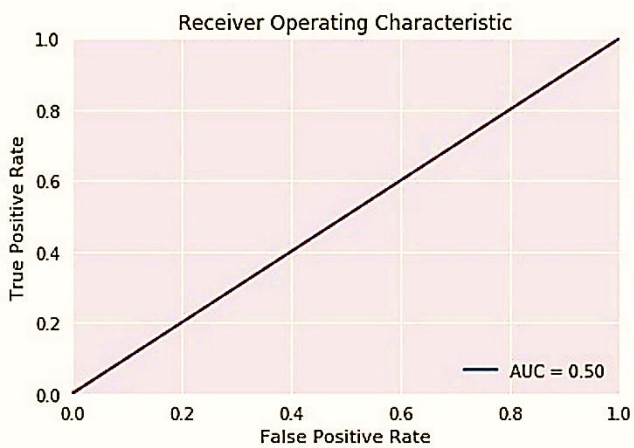
Figure 9 NN Algorithm Auc Score
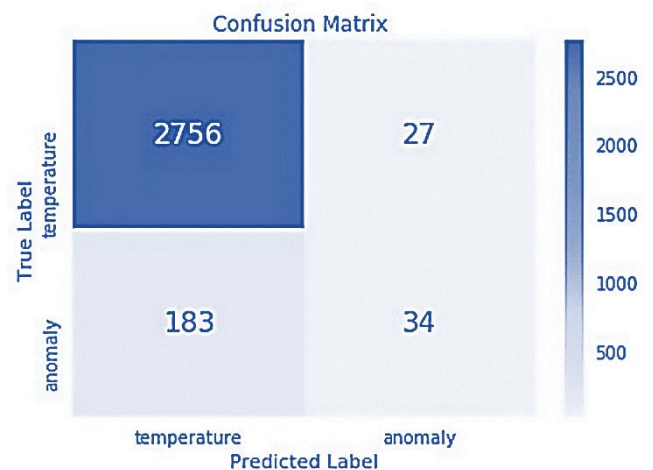
Figure 12 RCF Algorithm Confusion Matrix

As shown in Figure 13, the RCF algorithm concluded that 2756 of the data used for verification and prediction were true positive, while 183 data were false negatives. Also, the

KAYA et al.

Anomaly Detection and Performance Analysis by Using Big Data Filtering Techniques For Healthcare on I...

algorithm concluded that 27 of the remaining 61 data were false positives and 34 were true positives.

Figure 13 LR Algorithm Confusion Matrix

The confusion matrix of the LR classifier is given in Figure 13. According to the figure, 2754 data is true positive and 180 data is false negative. In addition, although there are 29 data anomalies by the algorithm, it is predicted as normal data, ie false positive. At the same time, 37 correctly predicted data are predicted as true negative.

Figure 14 NN Algorithm Confusion Matrix

Figure 14 shows the values related to the confusion matrix of the NN algorithm. When the figure is examined, it is seen that anyone data related to the part of the data set used in verification and prediction could not be detected as a true positive or false negative. Furthermore, even though the NN algorithm is an anomaly, it predicted that 2782 data are normal data, that is, false positives, and at

the same time the algorithm predicted 218 anomaly data as true negatives.

Figure 15 NB Algorithm Confusion Matrix

When figure 15 is examined, the confusion matrix of the NB algorithm is seen. In the testing process, 1516 of the 3000 data used in verification and prediction are predicted as true positives and 1418 as false negatives. In addition, of the remaining 66 data, 24 are predicted as false positives and 42 as true negatives.

6. DISCUSSION AND CONCLUSION

In this study, we focused on anomaly detection for IoT systems and compared ML classifiers. Anomaly detection and performance tests of machine learning algorithms are simulated using AWS cloud services. Classification reports, performance curves and confusion matrices are presented in the study. The purpose of the simulation is to detect the anomaly in the data stream from the temperature sensors and to deliver accurate data to the target. A data flow consisting of the data detected by the temperature sensors has been generated. The created data flow is classified in simultaneously with the RCF, LR, NB, and NN algorithms. The machine learning algorithms used allow incoming data to be classified in simultaneously before it reaches the target. This real-time data stream process means that the big data by data generated in the IoT detection layer will be separated from the anomaly. In addition, in the study, algorithms are analyzed based on data processing speeds and the results are discussed.

KAYA et al.

Anomaly Detection and Performance Analysis by Using Big Data Filtering Techniques For Healthcare on I...

When the experimental results section of the study is examined, the results of the algorithms, classification reports, performance curves and confusion matrices are seen. According to the results obtained, the RCF algorithm predicts 2756 data from the sensors as normal temperature values. These predictions are true predictions classified as true positives. In addition, although there are normal values, the algorithm predicts 183 data as anomalies and makes 183 false-positive predictions. Moreover, the RCF algorithm successfully detects 34 anomalies in 3000 data as true negatives. However, the accuracy values decrease due to the fact that it estimates 27 data as normal values even though there are anomalies, that is, it predicts as false negatives. When the test results are analyzed as measures of data processing time, the RCF algorithm is evaluated as the third best in terms of execution time and CPU time. However, when comparing all performance tests, RCF and LR algorithms are the closest to each other. When evaluated in terms of data processing speed, it is seen that the LR algorithm is in the first place. Even if the RCF algorithm is close to the LR algorithm according to its accuracy rates, its success in data processing speed is an indication that the LR classifier will be successful in IoT systems. In sense of data processing speed of the NB classifier, it achieved a better result than the accuracy scores, thus taking second place in terms of data processing speed, surpassing the RCF algorithm in data processing speed. In the final comparisons, it is seen that the NN classifier is the fourth and the most unsuccessful classifier in sense of accuracy scores and data processing time.

When our experimental results are examined, it is seen that anomaly detection can be made on IoT edges by using machine learning algorithms. However, it is vital to determine the appropriate algorithm in points of data processing speed and accuracy.

The Declaration of Conflict of Interest/ Common Interest

No conflict of interest and common interest has been declared by the authors.

Authors' Contribution

The authors contributed equally to the study.

The Declaration of Ethics Committee Approval

This study doesn't require ethics committee approval and any special permission

The Declaration of Research and Publication Ethics

In the writing process of this study, international scientific, ethical and citation rules were followed, and no falsification was made on the collected data. Sakarya University Journal of Science and its editorial board have no responsibility for all ethical violations. All responsibility belongs to the responsible author and this study has not been evaluated in any academic publication environment other than Sakarya University Journal of Science.

REFERENCES

[1]   T. Taneja, A. Jatain, S.B. Bajaj., "Predictive Analytics on IoT," International Conference on Computing, Communication and Automation., 2017.

[2]   M. Ahmed, S. Choudhury, "Big Data Analytics for Internet of Things," https://www.researchgate.net/publication/323163119, 2018.

[3]   D.P. Acharjya, A.P. Kauser, "A Survey on Big Data Analytics: Challenges, Open Research Issues and Tools," International Journal of Advanced Computer Science and

KAYA et al.

Anomaly Detection and Performance Analysis by Using Big Data Filtering Techniques For Healthcare on I...

Applications, vol. 7, no. 2, pp. 511-5187, 2016.

[4] P. Gupta, R. Gupra, "Data Mining Framework for IoT Applications," International Journal of Computer Applications (0975 – 8887), vol. 174, no. 2, pp. 4-7, 2017.

[5] H. Yar, A.S. Imran, Z.A. Khan, M. Sajjad, Z. Kastrati, "Towards Smart Home Automation Using IoT-Enabled Edge-Computing Paradigm," Sensors, vol. 21, no. 4, 4932, 2021.

[6] S. Hamdan, M. Ayyash, S. Almajali, "Edge-Computing Architectures for Internet of Things Applications: A Survey," Sensors, 20, 6441, 2020.

[7] M. Peyman, P.J. Copado, R.D. Tordecilla, L.C. Martins, F. Xhafa, A.A. Juan, "Edge Computing and IoT Analytics for Agile Optimization in Intelligent Transportation Systems," Energies, 14, 6309, 2021.

[8] A.H. Tasin, Ummasalma, Likhonbarua, Md. S. Hossain, S. Datta, A. Pathak, "IoT Based Low-Cost System For Monitoring Water Quality Of Karnaphuli River To Save The Ecosystem In Real-Time Environment," American Journal of Engineering Research (AJER), vol. 9, no. 2, pp-60-72, 2020.

[9] H. Aly, M. Elmogy, S. Barakat, "Big Data on Internet of Things: Applications, Architecture, Technologies, Techniques, and Future Directions," International Journal of Computer Science Engineering (IJCSE), ISSN: 2319-7323, vol. 4, pp. 300-313, 2015.

[10] P. Gulia, A. Chahal, Big Data Analytics For IoT, International Journal of Advanced Research in Engineering and Technology (IJARET), vol. 11, no. 6, pp. 593-603, 2020.

[11] N. Yadav, Er. P. Verma, Er. S. Srivastava, "Role of IoT in Big Data," International Journal for Research in Applied Science & Engineering Technology (IJRASET), vol. 8, no. XII, pp. 516-522, 2020.

[12] B. Nemane, R.D. Pahurkar, "Security Challenges in IOT, Big Data & Cloud Computing Integration," International Journal for Research in Applied Science & Engineering Technology (IJRASET), vol. 9, no. II, 2021.

[13] R.S.B. Cokro, E.Y. Wirawan, Y. Putra, A. Puspitarini, G. Wang, E.R. Kaburuan, "Designing Smart Parking System through the Use of IoT and Big Data," International Journal of Advanced Trends in Computer Science and Engineering, vol. 10, no. 5, 2021.

[14] V.S.S.J. Kodidala, S. Akkala, S.K. Mdupoju, V.S.S.T. Dasara, M. Juvvadi, N. Thangadurani, "Big Data analysis of demand side management for Industrial IoT applications," Materials Today: Proceedings, Elsevier, 2021.

[15] B.B.P. Sushree, B. Amiya, K.M. Brojo, "The Role of IoT and Big Data in Modern Technological Arena: A Comprehensive Study," Intelligent Systems Reference Library, vol. 154, pp. 13-25, 2019.

[16] R. Ranjan, D. Thakker, A. Haller, R. Buyya, "A note on the exploration of IoT generated big data using semantics," Future Generation Computer Systems., vol. 76, pp. 495-498, 2017.

[17] X. Li, H.N. Dai, Q. Wang, M. Imran, D. Li, M.A. Imran, "Securing Internet of Medical Things with Friendly-jamming schemes, Computer Communications," vol. 160, pp. 431–442, 2020.

[18] P.Y. Sai, P. Harika, "Illustration of IoT with Big Data Analytics," Global Journal of Computer Science and Technology, vol. XVII, no. III, Version I., 2017.

[19] Ş.M. Kaya, A. Erdem, A. Güneş, "A Smart Data Pre-Processing Approach to Effective Management of Big Health Data in IoT Edge," Smart Homecare Technology and TeleHealth, no. 8, pp. 9-21, 2021.

[20] E. Ahmed, I. Yaqoop, I.A.T. Hashem, I. Khan, A.I.A. Ahmed, M. Imran, A.V.

KAYA et al.

Anomaly Detection and Performance Analysis by Using Big Data Filtering Techniques For Healthcare on I...

Vasilakos, "The Role Of Big Data Analytics In Internet Of Things," Computer Networks, vol. 129, no. 2, pp. 459-471, 2017.

[21] J. Saldatos, "Building Blocks for IoT Analytics Internet-of-Things Analytics," Published, sold and distributed by River Publishers, Alsbjergvej 10, 9260 Gistrup, Denmark, 2017.

[22] M. Ge, H. Bangui, B. Buhnova, "Big Data for the Internet of Things: A Survey," Future Generation Computer Systems, vol. 87, pp. 601-614, 2018.

[23] E. Ahmed, M.H. Rehmani, "Mobile Edge Computing: Opportunities, Solutions, and Challenges," Future Generation Computer Systems, vol. 70, pp. 59-63, 2016.

[24] Ş.M. Kaya, A. Güneş, A. Erdem, "A Smart Data Pre-Processing Approach by Using ML Algorithms on IoT Edges: A Case Study." 2021 International Conference on Artificial Intelligence of Things (ICAIoT) (pp. 36-42). IEEE, 2021.

[25] P. Wlodarczak, M. Ally, J. Soar, "Data Mining in IoT," Association for Computing Machinery. ACM ISBN 978-1-4503-4951, 2017.

[26] Ş.M. Kaya,, "A smart data pre-processing approach for effective management of healthcare big data on IoT edges," Istanbul Aydın University, Graduate School of Natural and Applied Sciences, Department of Computer Engineering, PhD Thesis., 2021.

[27] F. Chen, P. Deng, J. Wan, D. Zhang, A.V. Vasilakos, X. Rong, "Data Mining for the Internet of Things: Literature Review and Challenges," International Journal of Distributed Sensor Networks, vol. 2015, Article ID 431047, 14 pages, 2015.

[28] S. Naveen, S.G. Hegde, "Study of IoT: Understanding IoT Architecture, Applications, Issues and Challenges," International Journal of Advanced Networking & Applications (IJANA), ISSN: 0975-0282., pp. 477-482, 2019.

[29] K. Sha, T.A. Yang, W. Wei, S. Davari, "A survey of edge computing-based designs for IoT security," Digital Communications and Networks, vol. 6, no.2, pp. 195-202, 2019.

[30] D.Y. Kim, Y.S. Jeong, S. Kim, "Data-Filtering System to Avoid Total Data Distortion in IoT Networking," Symmetry vol. 9, no, 16, 2017.

Title: Estimation of Some Population Parameters of Squalius cephalus (Linnaeus 1758) in Tabakhane Stream (Ordu-Turkey)

Authors: Serdar YEDIER

Estimation of Some Population Parameters of *Squalius cephalus* (Linnaeus 1758) in Tabakhane Stream (Ordu-Turkey)

Serdar YEDIER*[1]

Abstract

The purpose of this study is to estimate some population parameters such as length-length and length-weight relationships and condition factor of *Squalius cephalus* living in Tabakhane Stream (Ordu-Turkey). A total of 326 *S. cephalus* individuals were sampled from Tabakhane Stream, located in Ünye district in the Ordu Province, by using an electroshocker. It was determined that the mean total, fork and standard lengths of the fish samples were 7.58±0.143 cm, 7.06±0.133 cm, and 6.30±0.121 cm, respectively, and their average weight was 6.05±0.322 g. The length-weight relationship of the species was calculated as $W=0.0088TL^{3.0648}$ ($R^2=0.993$). As a result of our analyzes, it was determined that the *S. cephalus* population in Tabakhane Stream showed a positive allometric growth. In the present study, it was determined that the 95% confidence interval of the *b* value in the length-weight relationship equation was between 3.0566-3.0678 and there was a strong relationship between body weight and total length. Relationship equations between total, fork and standard lengths were calculated as $TL=1.0724FL+0.0086$ ($r^2=0.998$), $TL=1.1763SL+0.167$ ($r^2=0.997$), and $FL=1.0961SL+0.1529$ ($r^2=0.998$) and it was determined that there are strong relationships between standard, fork and total length measurements of *S. cephalus* living in Tabakhane Stream. It was determined that the condition factor values of *S. cephalus* ranged between 0.740 and 1.276. The average condition factor was 0.998±0.005. There is no previous study on the population of *S. cephalus* living in Tabakhane Stream. In this study, the condition factor, length-weight and length-length relationships of *S. cephalus* in this habitat were reported for the first time.

Keywords: *Squalius cephalus*, length-length relationship, length-weight relationship, Condition factor, Tabakhane Stream, Ordu

1. INTRODUCTION

Genus *Squalius* is a large fish group in the family Leuciscidae, represented by 50 species in the world [1]. *Squalius cephalus* (Linnaeus 1758) is a freshwater fish species and is widely distributed in European inland waters, Black Sea, Caspian Sea and Azov Sea Basins, and most of the inland waters in Caucasus Region and Anatolia [1, 2].

The conservation status of *S. cephalus* is *LC* in the IUCN Red List [3]. *S. cephalus* is an economically important fish species [4, 5] and many studies were carried out on different populations of this species both in Turkey and abroad such as determination of reproductive characteristics [6, 7], growth characteristics [8-11], morphological variation [12], genetics [13, 14], biological characteristics [15]. In nature,

* Corresponding author: serdar7er@gmail.com
[1] Ordu University, Faculty of Science and Arts, Molecular Biology and Genetics Department
ORCID: https://orcid.org/0000-0003-0017-3502

Serdar YEDIER

Estimation of Some Population Parameters of Squalius cephalus (Linnaeus 1758) in Tabakhane Stream (Or...

whether in terrestrial or aquatic habitats, living things inherit growth as an integral part of their life history, and this growth is also very important event for the life cycles of fish species [16, 17]. The growth dynamics, length-weight relationship (LWR), length-length relationship (LLR) and condition factor (K) of any fish species are important biological parameters to evaluate stock variation, determination of growth rate, spawning time and maturity appearance [18, 19].

Length-weight relationship (LWR) refers to the dynamics and growth patterns of fish populations in general. The slope *b* value calculated in this relationship is used to determine how the growth of fish is affected by changes in habitat, seasons and other factors [20]. Whether the slope *b* in this equation differ significantly from 3.0 value indicates the type of growth of the fish species in the respective habitat: for instance, negative allometric growth ($b<3$), isometric growth ($b=3$), or positive allometric growth ($b>3$) [21].

Length-length relationships (LLRs) of fish species are important in comparing growth studies of the species in different habitats and also different length measures of fishes are required for certain applications in fish biology and fisheries management [22, 23]. Also, standard length can be useful as a basic measure of length for scientific purposes, as total length is not always available (e.g. bitten or damaged). Furthermore, standard length is more commonly used in fisheries management, such as defining minimum legal lengths for commercial and recreational fishing. Therefore, reliable length-length relationships are required for data length conversions [24].

Likewise, condition factor (K) is an index that reflects the interactions between biotic and abiotic factors in the physiological state of fish in their respective habitats [17]. It shows the well-being of the population at various life cycle stages [25]. In other words, the K is an important tool for assessing environmental effects on fish and reflects the relative health of fish populations [26]. According to the calculated K value, the status of fish species in the relevant habitat can be evaluated and compared with their populations in other regions. For example, when the condition

factor value is $K=1$ and $K>1$, it can be understood that the fish is in a good growth state, and when $K<1$, the organism is in a weaker growth state compared to an average individual of the same length.

There are limited studies on the population of *S. cephalus*, which has a wide distribution in Turkish inland waters and has commercial value, in the Black Sea region. There is no study examining the population characteristics of this species in Tabakhane Stream in Ordu. For this reason, the main aim of this study is to determine the condition factor, length-weight and length-length relationships of *S. cephalus* which sampled from the Tabakhane Stream (Ordu-Turkey) in the Middle Black Sea Region.

2. MATERIALS AND METHODS

Tabakhane Stream is a lotic ecosystem located on the borders of Ünye district of Ordu Province in the central Black Sea region of Turkey (Figure 1). *Squalius cephalus* samples were collected from Tabakhane Stream (Ordu-Turkey) using the SAMUS 725 MP electroshocker (Figure 1).

Figure 1 Sampling area of *S. cephalus* in Tabakhane Stream (Ordu-Turkey).

Fish samples were measured for total length (TL), fork length (FL) and standard length (SL) (0.01 cm.) The weight of each fish (W) was recorded

Serdar YEDIER

Estimation of Some Population Parameters of *Squalius cephalus* (Linnaeus 1758) in Tabakhane Stream (Or...

(0.01 g). Gender of the fish samples was determined by microscopic and macroscopic examinations of the gonads.

All length-length relationships such as TL & SL, TL & FL, and FL & SL were calculated using linear regression model (y=ax+b) and the correlation coefficients of each relationship were determined. Length-weight relations of the fish samples were calculated using the equation W=aL^b, where L is the total length (cm), W is the weight of the fish (g), "*a*" and "*b*" are the parameters of the equation [27]. In this study, the 95% confidence interval (95%CI) of the b value was also calculated. In the current study, the parameters "*a*" and "*b*" were estimated from linear regression applied to the log-transformed variables such as logW=log*a* + *b*logL. Condition factor (*K*) of *S. cephalus* in this habitat was calculated using the equation $K=100(W/L^3)$ where L is the total length (cm), W is the weight of the fish (g) [28].

The t-test was used to test whether the slopes (*b*) were significantly different from 3 and based on these results the growth type of the species in this habitat was determined. In addition, whether there is a statistical difference between the length and weight measurements of female and male individuals was tested using the t-test. All statistical analyzes in the study were performed using the Minitab 17 software.

3. RESULTS AND DISCUSSION

A total of 326 *S. cephalus* individuals were caught in the field studies carried out in the Tabakhane Stream (Ordu-Turkey). As a result of field studies, it was determined that 111 samples (34.05%) were male, 71 samples (21.78%) were female and 144 samples (44.17%) were juveniles.

Average body weight and total length values of the fish samples were determined as 6.05±0.322 g and 7.58±0.143 cm, respectively. The descriptive statistics of the weight, total, fork and standard lengths data of the species of *S. cephalus* evaluated within the scope of the study are presented in Table 1.

Table 1 Descriptive statistics of *S. cephalus* from Tabakhane Stream (Ordu-Turkey).

Measurements		Mean	SE	SD	Min.	Max.
Weight (g)		6.05	0.322	5.814	0.53	32.40
Total Length (cm)		7.58	0.143	2.574	3.50	14.50
Fork Length (cm)	♀+♂	7.06	0.133	2.397	3.30	13.30
Standard Length (cm)		6.30	0.121	2.185	3.00	12.00

SE: Standard error, SD: Standard deviation, Min: Minimum, Max: Maximum.

The length and weight frequencies of *S. cephalus* from the Tabakhane Stream (Ordu-Turkey) were presented in Figure 2.
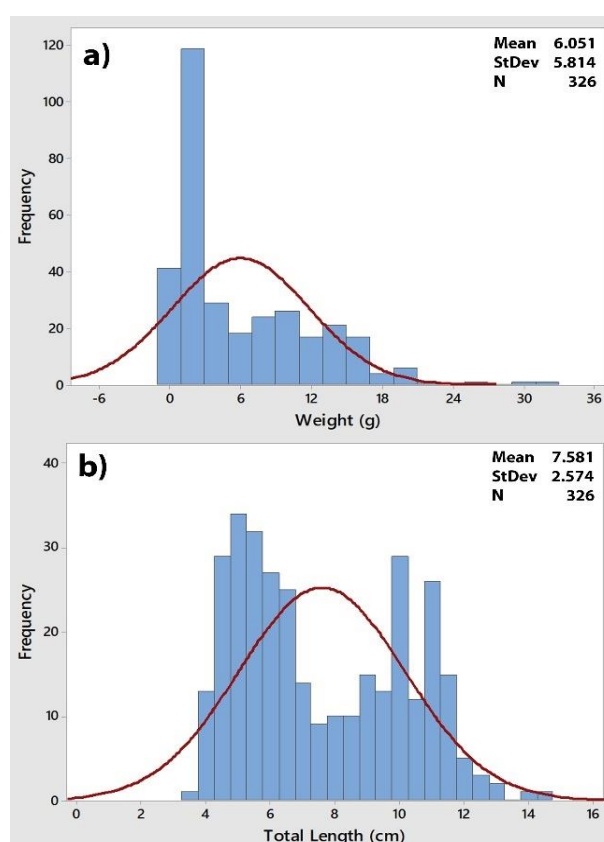
Figure 2 The weight-frequency and length-frequency distributions of *S. cephalus* in Tabakhane Stream (Ordu-Turkey).

As a result of the t test, it was determined that the total length and weight values were not statistically different between female and male *S. cephalus* individuals (P>0.05). Therefore, the calculations were carried out to represent the entire population, including all female+male individuals.

Serdar YEDIER

Estimation of Some Population Parameters of Squalius cephalus (Linnaeus 1758) in Tabakhane Stream (Or...

Growth parameters such as length-length, length-weight and condition factor are some of the most important data sources that provide information about the growth status of fish in the relevant habitat [29-31]. These parameters can also be used to compare populations of the same species in different habitats [32, 33].

When the literature is examined, it is seen that different total, fork and standard lengths are used in many growth studies [34-38]. These differences in some growth studies can cause confusion when making regional comparisons. At this point, the use of length-length relations of the relevant species can be beneficial in solving the problem. In addition, these relations allow the estimation of the length of a morphometrically damaged sample using the length-length relations.

Length-length relationships (LLRs) of *S. cephalus* from Tabakhane Stream were calculated by using the linear regression model. It was determined that the coefficients of determination (r^2) of the LLRs ranged from 0.997 to 0.998 and that there were strong relationships between the length values of the *S cephalus* from Tabakhane Stream (Figure 3).

Similar to present study, these strong relationships observed in total length, fork length, and standard length values were reported among *S. cephalus* living in the Abdal Stream (TL-FL, r^2=0.999, TL-SL, r^2=0.999, FL-SL, r^2=0.999), Akçay Stream (TL-FL, r^2=0.998, TL-SL, r^2=0.916, FL-SL, r^2=0.922), Terme Stream (TL-FL, r^2=0.981, TL-SL, r^2=0.984, FL-SL, r^2=0.985) and Yedikır Dam Lake (TL-FL, r^2=0.991, TL-SL, r^2=0.989, FL-SL, r^2=0.996) [39]. Similar results were also reported for *S cephalus* in the Karasu River (TL-FL, r^2=0.96, TL-SL, r^2=0.97, FL-SL, r^2=0.99) [40].
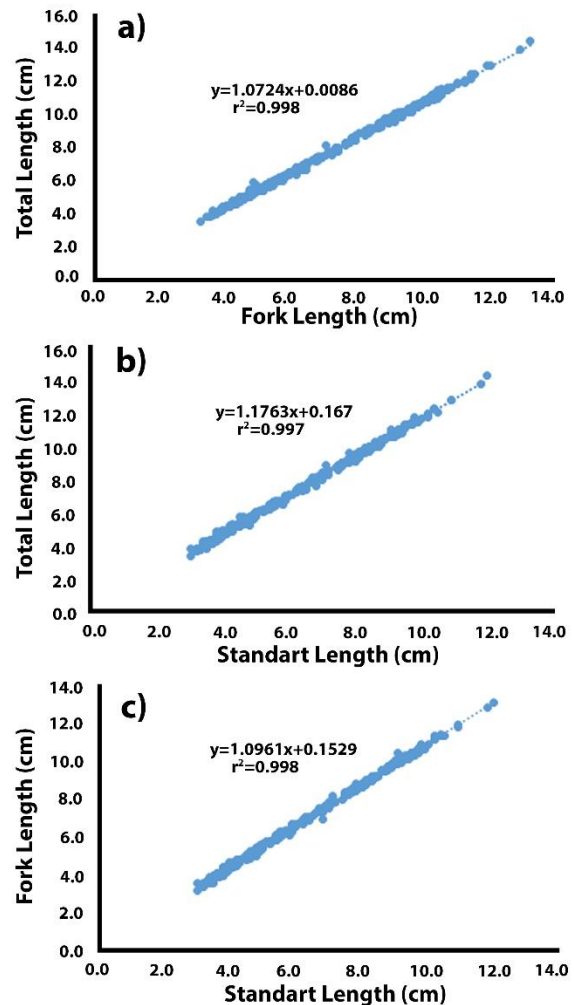
Figure 3 The length-length relationships for *S. cephalus* in Tabakhane Stream (Ordu-Turkey).

Length-weight relationship (LWR) was calculated as W=0.0088TL$^{3.0648}$ (R²=0.993) for *S cephalus* from Tabakhane Stream (Figure 4). It was determined that there is a strong relationship between the total length and weight values of *S cephalus* in this aquatic habitat (R²=0.993, Figure 4). In the present study, the *b* value in the total length-weight relationship equation was calculated as 3.0648 and the 95% confidence interval of the *b* value was calculated as 3.0566-3.0678. The *b* value calculated in present study was found to be within this confidence interval. Moreover, the *b* value of LWR was found to differ significantly from 3.0 in the *S cephalus* in this habitat. It was determined that the species showed a positive allometric growth in Tabakhane Stream.

Serdar YEDIER

Estimation of Some Population Parameters of Squalius cephalus (Linnaeus 1758) in Tabakhane Stream (Or...
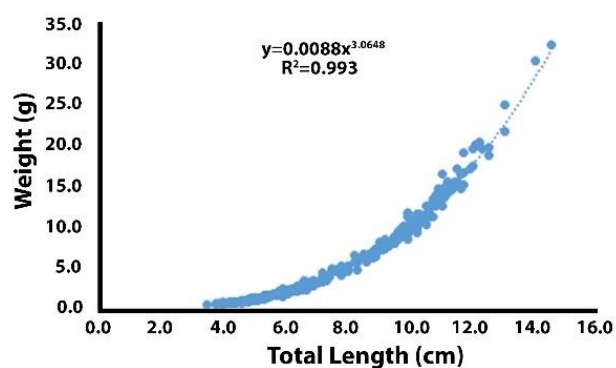
Figure 4 The length-weight relationship for *S. cephalus* in Tabakhane Stream (Ordu-Turkey).

Length-weight parameters are important data sources, especially in fisheries management and fish biology [41]. The *b* value is generally between 2.5 and 3.5 in many studies in which different marine and freshwater fish are studied [26, 27, 29]. The *b* values in fish can also vary according to gender, age, seasons, physiological conditions, growth rate and nutritional status of the fish [21, 27]. As the fish grows in the fish's life cycle, changes in weight are relatively larger than changes in length because of the cubic relationships between fish length and weight. When the literature was examined, many studies were found on the LWR and growth type of *S. cephalus* in different aquatic habitats (Table 2). As a result of a detailed literature review, although it was reported in many studies that *S cephalus* showed positive allometric growth [30, 39, 42, 43], similar to our study, in some studies it was reported that it showed isometric [9, 44, 45, 46] and even negative allometric growth [47, 48] (Table 2).

Table 2 Comparison of length-weight relationships of *S. cephalus* with previous studies.

Habitats	n	*b*	Growth Types	References
Karakaya Dam Lake (Turkey)	527	2.820	A(-)	[47]
Apa Dam Lake (Turkey)	474	2.43	A(-)	[48]
Işıklı Lake (Turkey)	528	3.04	I	[44]
Gelingülü Dam Lake (Turkey)	267	2.870	I	[9]
Hafik Lake (Turkey)	242	2.828	I	[45]
Tödürge Lake (Turkey)	466	3.088	I	[46]
Topçam Dam Lake (Turkey)	332	3.12	A(+)	[49]
Northern Aegean Eustuarine (Greece)	627	3.856	A(+)	[42]
Çamkoru Pond (Turkey)	374	3.012	A(+)	[11]
Almus Dam Lake (Turkey)	305	3.359	A(+)	[50]
Gamasiab River (Iran)	60	3.97	A(+)	[51]
Sakarya River (Turkey)	32	3.188	A(+)	[52]
Yeniağa Lake (Turkey)	729	3.109	A(+)	[53]
Uzunçayır Dam Lake (Turkey)	334	3.136	A(+)	[54]
Karasu Stream (Turkey)	254	3.24	A(+)	[40]
Yalıköy Stream (Turkey)	118	3.0444	A(+)	[30]
Akçay Stream (Turkey)	57	3.285	A(+)	
Abdal Stream (Turkey)	44	3.224	A(+)	[39]
Yedikır Dam Lake (Turkey)	62	3.210	A(+)	
Terme Stream (Turkey)	55	3.298	A(+)	
Karasu River (Turkey)	196	3.27	A(+)	[43]
Tabakhane Stream (Turkey)	326	3.0648	A(+)	Present Study

Condition factor (*K*) is one of the commonly used population parameters to understand the survival, reproduction, maturity and health of fish [20]. In addition, *K* can be used as a good indicator of the water quality or general health of fish populations living in a particular habitat or ecosystem [20, 26, 55]. In addition, the condition factor is an important biological parameter for the conservation and management of natural populations by providing information about the status of fish species [56, 57]. Maximum and minimum condition factors of *S. cephalus* distributed in Tabakhane Stream (Ünye-Ordu) were calculated as 1.276 and 0.740, respectively.

The mean condition factor was determined as 0.998 ± 0.005. The condition factor value above 1 indicates that the fish are in good condition in this habitat. In this study, the average condition factor was determined close to 1 value. In the literature, it was determined that the average condition factor of *S. cephalus* showed some differences between habitats. For instance, it was reported that the average condition factor of *S. cephalus* is 1.2915 in Çamligöze dam lake [58], 1.43 in Karakaya Dam Lake [43], 1.48 in Lake Yeniçağa [49], and 1.5759 in Lake Akşehir [59]. Differences in the *K* value of a fish species could be a reason for variations in sexual maturity, availability of food sources, age, and sex in the relevant habitat [20, 60].

4. CONCLUSION

The present study provides the first information about the condition factor, length-length, length-weight and relationships of *S. cephalus* from Tabakhane Stream (Ünye-Ordu). This study will help biologists to know the status of this fish and develop culture technology in natural waters and will be useful for the fishery biologists and conservation biologist, for successful development, management, production and ultimate conservation of the most preferred food fishes of the states. Since population parameters are important in fisheries management and fish biology, the determination of these parameters can provide important baseline data, especially by supporting future population monitoring and research studies. Genetic diversity and various factors such as temperature, eutrophication levels, diet and diseases may cause intraspecific differences in the growth parameters of fish species [10]; therefore, future studies in this field can be further improved by supporting these data.

Conflict of interest

There is no conflict of interest to be declared.

Funding

The Declaration of Ethics Committee Approval

This study does not require ethics committee approval or any special permission.

The Declaration of Research and Publication Ethics

The author of the paper declares that he complies with the scientific, ethical and quotation rules of SAUJS in all processes of the article and that he does not make any falsification on the data collected. In addition, he declares that Sakarya University Journal of Science and its editorial board have no responsibility for any ethical violations that may be encountered, and that this study has not been evaluated in any academic publication environment other than Sakarya University Journal of Science.

REFERENCES

[1] R. Froese, and D. Pauly, "FishBase. World Wide Web electronic publication,", [Data accessed: September 2021]. Available: https://www.fishbase.de/summary/*Squalius -cephalus*.html., 2021.

[2] R. Geldiay, and S. Balık, "Türkiye tatlısu balıkları," 5. Baskı, Ege Üniversitesi Basımevi, Bornova-İzmir, 644 p, 2007.

[3] J. Freyhof, "*Squalius cephalus*. The IUCN Red List of Threatened Species 2014 e.T61205A19009224," [Data accessed: September 2021].

[4] R. Mert, S. Bulut, and K. Solak, "Some biological properties of the *Squalius cephalus* (L., 1758) population inhabiting Apa Dam Lake in Konya (Turkey)," Afyon Kocatepe University Journal of Science, vol. 6, no. 2, pp. 1-12, 2006.

[5] H. T. Koç, Z. Erdogan, M. Tinkci, and T. Treer, "Age, growth and reproductive characteristics of chub, *Leuciscus cephalus* (L., 1758) in İkizcetepeler Dam Lake (Balıkesir)," Journal of Applied Ichthyology, vol. 23, no. 1, pp. 19-24, 2007.

[6] P. Poncin, C. H. Melard, and J. C. Philippart, "Controlled reproduction of chub, *Leuciscus cephalus* (L.) in captivity," In: De Pauw N, Jaspers E, Ackefors H, Wilkins N (Eds) Aquaculture-a Biotechnology in Progress, pp. 567-571, European Aquaculture Society, Bredene, Belgium, 1989.

[7] H. Şaşı, "The reproduction biology of chub (*Leuciscus cephalus* L. 1758) in Topçam Dam Lake (Aydın, Turkey)," Turkish Journal of Veterinary and Animal Sciences, vol. 28, no. 4, pp. 693-699, 2004.

[8] T. Treer, D. Habekovié, I. Anicié, R. Safner, and A. Kolak, "Standard growth curve for chub (*Leuciscus cephalus* L. 1758) in Croatia," Ribarstvo, vol. 55, no. 2, 47-52, 1997.

[9] Ş. G. Kırankaya, and F. G. Ekmekçi, "Variations in growth properties of chub (*Squalius cephalus*, L., 1758) living in Gelingüllü Dam Lake," Journal of Balıkesir University Institute of Science and Technology, vol. 9, no. 2, pp. 125-134, 2007.

[10] E. Stefanova, E. Uzunova, T. Hubenova, P. Vasileva, D. Terziyski, and I. Iliev, "Age and growth of the chub *Leuciscus cephalus* L., from the Maritz River (South Bulgaria)," Bulgarian Journal of Agricultural Science, vol. 14, no. 2, pp. 214-220, 2008.

[11] D. İnnal, "Population structures and some growth properties of three cyprinid species [*Squalius cephalus* (Linnaeus, 1758); *Tinca tinca* (Linnaeus, 1758) and *Alburnus escherichii* Steindachner, 1897] living in Camkoru Pond (Ankara-Turkey)," Kafkas Universitesi Veteriner Fakultesi Dergisi, vol. 16, no. Sup. b, pp. 297-304, 2010.

[12] D. Turan, L. Tomovic, and V. Peşi, "Morphological variation in a common Turkish cyprinid, *Squalius cephalus*, across Turkish water catchment areas," Journal of

Zoology in the Middle East, vol. 40, no. 1, pp. 63-70, 2007.

[13] C. Dehais, R. Eudeline, P. Berrebi, and C. Argillier, "Microgeographic genetic isolation in chub (Cyprinidae: *Squalius cephalus*) population of the Durance River: estimating fragmentation by dams," Ecology of Freshwater Fish, vol. 19, no. 2, pp. 267-278, 2010.

[14] A. Gouskov, "Impacts of river fragmentation on the genetic population structure of the chub (*Squalius cephalus*)," Doctor of Sciences of Eth Zurich, 131p, 2016.

[15] S. Bulut, R. Mert, M. Konuk, B. Algan, A. Alap, and K. Solak, "The variation of several biological characteristics of the chub, *Squalius cephalus* (L., 1758), in the Orenler Dam Lake, Northwest Anatolia, Turkey," Notulae Scientia Biologicae, vol. 4, no. 3, pp. 27-32, 2012.

[16] G. Petrakis, and K. I. Stergiou, "Length-weight relationships for 33 fish species in Greek waters," Fisheries Research, vol. 21, no. 3-4, pp. 465-469, 1995.

[17] M. Deuri, B.B. Nath, A. M. Ahmed, J. Sarma, B. Phukan, A. Ali, R. Gogoi, I. Ahmed, and D. Baruah, "Length-weight relationship, length-length relationship and condition factor of *Labeo bata* (Hamilton, 1822) from central Brahmaputra valley of Assam," Journal of Entomology and Zoology Studies, vol. 8, no. 4, pp. 2211-2215, 2020.

[18] C. Binohlan, and D. Pauly, "The length-weight table," In R. Froese and D. Pauly (Ed), Fish Base 1998: Concepts, design and data sources ICLARM, Manila, Philippines, 1998.

[19] G. Das, H. Chakravorty, and P. Deka, "Length-weight relationship and relative condition factor of *L. bata* (Hamilton, 1822) of Deepor Beel, a ramsar site of Assam,

Serdar YEDIER

Estimation of Some Population Parameters of Squalius cephalus (Linnaeus 1758) in Tabakhane Stream (Or...

India," International Journal of Applied Research, vol. 1, no. 11, pp. 947-950, 2015.

[20] E. D. Le Cren, "The length-weight relationship and seasonal cycle in gonad weight and condition in the perch (*Perca fluviatilis*)," Journal Animal Ecology, vol. 20, no. 2, pp. 201-219, 1951.

[21] W. A. Ricker, "Computation and interpretation of biological statistics of fish populations," Journal of the Fisheries Research Board of Canada, Ottawa, 1975.

[22] D. K. Moutopoulos, and K. I. Stregiou, "Length-weight and length-length relationships of fish species from the Aegean Sea (Greece)," Journal of Applied Ichthyology, vol. 18, no. 3, pp. 200-203, 2002.

[23] S. Yedier, D. Bostancı, and N. Polat, "Some population characteristics of *Oxynoemacheilus angorae* (Steindachner, 1897) from Perşembe Plateau Meandering Streams in Ordu-Turkey," Fisheries & Aquatic Life, vol. 29, no. 2, pp. 100-107, 2021.

[24] F. G. Biole, A. V. Volpedo, and G. A. Thompson, "Length-weight and length-length relationship for three marine fish species of commercial importance from southwestern Atlantic Ocean coast," Latin American Journal of Aquatic Research, vol. 48, no. 3, pp. 506-513, 2020.

[25] J. I. Mir, U. K. Sarkar, A. K. Dwivedi, O.P. Gusain, A. Pal, and J. K. Jena, "The pattern of inter basin variation in condition factor, relative condition factor, and form factor of an Indian major carp, *Labeo rohita* (Hamilton Buchanan, 1822) in the Ganges Basin, India," European Journal of Biological Sciences, vol. 4, no. 4, pp. 126-135, 2012.

[26] R. Froese, "Cube law, condition factor and weight-length relationships: history, meta-analysis and recommendations," Journal of

Applied Ichthyology, vol. 22, no. 4, pp. 241-253, 2006.

[27] T. B. Bagenal, and F. W. Tesch, "Age and growth," In T. Bagenal (Ed), Methods for assessment of fish production in fresh waters, 3rd ed: IBP Handbook No.3, Blackwell Science Publications, Oxford, 1978.

[28] D. Pauly, "Some simple methods for the assessment of tropical fish stocks," FAO Fisheries Technical paper, FAO, Rome, Italy, 1983.

[29] Ş. G. Kırankaya, F. G. Ekmekçi, Ş. Y. Özdilek, B. Yoğurtçuoğlu, and L. Gençoğlu, "Condition, length-weight and length-length relationships for five fish species from Hirfanlı Reservoir, Turkey," Journal of FisheriesSciences.com, vol. 8, no. 3, pp. 208-213, 2014.

[30] D. Bostancı, S. Yedier, S. Kontaş, G. Kurucu, and N. Polat, "Length-weight, length-length relationships and condition factors of some fish species in Yalıköy Stream (Ordu-Turkey)," Aquaculture Studies, vol. 17, no. 4, pp. 375-383, 2017.

[31] S. Yedier, S. Kontaş, and D. Bostancı, "Condition factor, length-length and length-weight relationships for *Pagellus acarne* inhabiting the Sea of Marmara," Journal of Anatolian Environmental and Animal Sciences, vol. 4, no. 2, pp. 82-88, 2019.

[32] E. K. Mbaru, E. N. Kimani, L. M. Otwoma, A. Kimeli, and T. K. Mkare, "Abundance, length-weight relationship and condition factor in selected reef fishes of Kenyan marine artisanal fishery," Advanced Journal of Food Science and Technology, vol. 3, no. 1, pp. 1-8, 2011.

[33] S. Yılmaz, O. Yazıcıoğlu, M. Erbaşaran, S. Esen, M. Zengin, and N. Polat, "Length-weight relationship and relative condition factor of white bream, *Blicca bjoerkna* (L., 1758), from Lake Lâdik, Turkey," Journal

Serdar YEDIER

Estimation of Some Population Parameters of Squalius cephalus (Linnaeus 1758) in Tabakhane Stream (Or...

of Black Sea/Mediterranean Environment, vol. 18, no. 3, pp. 380-387, 2012.

[34] M. Singh, and M. Serajuddin, "Length-weight, length- length relationship and condition factor of *Channa punctatus* collected from three different rivers of India," Journal of Entomology and Zoology Studies, vol. 5, no. 1, pp. 191-197, 2017.

[35] S. Saygın, M. Özpiçak, A. Aydın, E. Hançer, S. Yılmaz, and N. Polat, "Length-weight and length-length relationships of the European bitterling, *Rhodeus amarus* (Bloch, 1782) inhabiting inland waters of Samsun Province," Balıkesir Üniversitesi Fen Bilimleri Enstitüsü Dergisi, vol. 20, no. 2, pp. 201-210, 2018.

[36] S. Arslan, and D. Bostancı, "Length-weight and length-length relationships of Red Scorpionfish (*Scorpaena scrofa* L. 1758) from İzmir Bay (Aegean Sea)," Acta Aquatica Turcica, vol. 15, no. 4, pp. 433-439, 2019.

[37] S. Yedier, S. Kontaş, and D. Bostancı, "Length-length and length-weight relationships of Lessepsian *Saurida undosquamis* from the İskenderun Bay (Eastern Mediterranean, Turkey)," Journal of the Institute of Science and Technology, vol. 10, no. 1, pp. 616-623, 2020.

[38] D. Bostancı, and T. Coşkun, "A research on some biological properties of Mediterranean Sand Smelt (*Atherina hepsetus* L.) population in the Sea of Marmara," Acta Aquatica Turcica, vol. 16, no. 2, pp. 257-265, 2020.

[39] M. Özpiçak, S. Saygın, E. Hançer, A. Aydın, S. Yılmaz, and N. Polat, "Length-weight and length-length relationships of chub (*Squalius cephalus*, L., 1758) inhabiting a few inland waters of the Middle Black Sea Region," Ege Journal Fisheries and Aquatic Sciences, vol. 35, no. 2, pp. 175-179, 2018.

[40] E. İ. Özcan, O. Serdar, and R. Aydın, "Length-weight and length-length relationships of *Squalius cephalus* (L., 1758) in Karasu River (Erzincan-Erzurum)," Aquaculture Studies, vol. 17, no. 1, pp. 109-114, 2017.

[41] C. B. Garcia, J. O. Buarte, N. Sandoval, D. Von Schiller, and N. P. Mello, "Length-weight relationships of demersal fishes from the Gulf of Salamanca, Colombia," Naga, The ICLARM Quarterly, vol. 21, no. 3, pp. 30-32, 1989.

[42] E. T. Kautrakis, and A. C. Tsikliras, "Length-weight relationships of fishes from three northern Aegean estuarine systems (Greece)," Journal of Applied Ichthyology, vol. 19, no. 4, pp. 258-260, 2003.

[43] E. İ. Özcan, and O. Serdar, "Age and some growth parameters of *Squalius cephalus* (Linnaeus, 1758) inhabiting Karasu River (East Anatolia, Turkey)," Ege Journal of Fisheries and Aquatic Sciences, vol. 36, no. 1, pp. 25-30, 2019.

[44] S. Balık, M. H. Sarı, R. M. Ustaoğlu, and A. İlhan, "Age and growth characteristics of chub (*Leuciscus cephalus* L., 1758) population in Işıklı Lake, Çivril, Denizli, Turkey," Ege Journal of Fisheries and Aquatic Sciences, vol. 21, no. 3-4, pp. 257-262, 2004.

[45] B. Ünver, and S. Kekilli, "Growth properties of chub (*Squalius cephalus* L., 1758) in the Hafik Lake (Sivas)," Eğirdir Su Ürünleri Fakültesi Dergisi, vol. 6, no. 1, pp. 20-28, 2010.

[46] B. Ünver, and F. Erk'akan, "Population characteristics of *Squalius cephalus* in Lake Tödürge (Sivas)," Ege Journal of Fisheries and Aquatic Science, vol. 29, no.2, pp. 95-100, 2012.

[47] E. Kalkan, M. Yılmaz, and A. U. Erdemli, "Some biological properties of the *Leucisus cephalus* (L., 1758) population living in Karakaya Dam Lake in Malatya (Turkey),"

Serdar YEDIER

Estimation of Some Population Parameters of Squalius cephalus (Linnaeus 1758) in Tabakhane Stream (Or...

Turkish Journal of Veterinary and Animal Science, vol. 29, no. 1, pp. 49-58, 2005.

[48] R. Mert, S. Bulut, and K. Solak, "Apa Baraj Gölü'nde yaşayan *Squalius cephalus* (L., 1758)'un bazı biyolojik özellikleri," Afyon Kocatepe Üniversitesi Fen ve Mühendislik Bilimleri Dergisi, vol. 6, no. 2, pp. 1-12, 2015.

[49] H. Şaşı, and S. Balık, "Age, growth and sex ratio of chub (*Leuciscus cephalus* L., 1758) in Topçam Dam Lake," Ege Journal of Fisheries and Aquatic Science, vol. 20, no. 3-4, pp. 503-515, 2003.

[50] M. Karataş, and M. F. Can, "Growth, mortality and yield of chub (*Leuciscus cephalus* L., 1758) population in Almus Dam Lake, Turkey," Journal of Biological Sciences, vol. 5, no. 6, pp. 729-733, 2005.

[51] S. Sedaghat, W. D. P. Ahangari, M. H. Arabi, H. Rahmani, and S. Vatandoust, "Age and growth of chub, *Squalius cephalus* (Bonaparte, 1837), in Gamasiab River of the Hamadan Province, Iran," World Journal of Fish and Marine Sciences, vol. 4, no. 6, pp. 550-553, 2012.

[52] A. E. Kahraman, D. Göktürk, and E. Aydin, "Length-weight relationships of five fish species from the Sakarya River, Turkey," Annual Research & Review in Biology, vol. 4, no. 15, pp. 2476-2483, 2014.

[53] S. Kılıç, and Z. A. Becer, "Growth and reproduction of chub (*Squalius cephalus*) in Lake Yeniçağa, Bolu, Turkey," International Journal of Agriculture & Biology, vol. 18, no. 2, pp. 419-424, 2016.

[54] F. Demirol, F. Gündüz, N. Yıldız, M. Kurtoğlu, M. Z. Çoban, and F. Yüksel, "Some growth parameters of chub (*Squalius cephalus*) living in Uzunçayır Dam Lake (Tunceli-Turkey)," Journal of Limnology and Freshwater Fisheries Research, vol. 2, no. 2, pp. 67-76, 2016.

[55] M. Tsoumani, R. Liasko, P. Moutsaki, I. Kagalou, and I. Leonardos, "Length-weight relationships of an invasive cyprinid fish (*Carassius gibelio*) from 12 Greek lakes in relation to their trophic states," Journal of Applied Ichthyology, vol. 22, no. 4, pp. 281-284, 2006.

[56] U. K. Sarkar, P. K. Deepak, and R. S. Negi, "Length-weight relationship of clown knifefish *Chitala chitala* (Hamilton 1822) from the River Ganga basin, India," Journal of Applied Ichthyology, vol. 25, no. 2, pp. 232-233, 2009.

[57] Z. A. Muchlisin, M. Musman, and M. N. S. Azizah, "Length-weight relationships and condition factors of two threatened fishes, *Rasbora tawarensis* and *Poropuntius tawarensis*, endemic to Lake Laut Tawar, Aceh Province, Indian," Journal of Applied Ichthyology, vol. 26, no. 6, pp. 949-953, 2010.

[58] S. Dirican, S. and Çilek, "Condition factors of seven cyprinid fish species from Çamligöze dam lake on central Anatolia, Turkey," African Journal of Agricultural Research, vol. 7, no. 31, pp. 4460-4464, 2012.

[59] A. Altındağ, "Akşehir (Konya) Gölündeki tatlısu kefali (Leuciscus cephalus L. 1758)'nin biyolojisi," Ankara Üniversitesi, Fenbilimleri Enstitusu, Doktora tezi, 1995.

[60] C. L. P. Anibeze, "Length-weight relationship and relative condition of *Heterobranchus longifilis* (Valencienness) from ldodo River, Nigeria," Naga, The ICLARM Quarterly, vol. 23, no.2, pp. 34-35, 2000.

Title: Boost Converter Based 3-Phase AC-AC Active Tracking Voltage Regulator Controlled by a Robust Hybrid Control Method

Authors: Faruk YALÇIN, Felix HIMMELSTOSS

Boost Converter Based 3-Phase AC-AC Active Tracking Voltage Regulator Controlled by a Robust Hybrid Control Method

Faruk YALÇIN*[1], Felix HIMMELSTOSS[2]

Abstract

In this study, a switch-mode three-phase active tracking AC-AC voltage regulator based on the boost converter is proposed with a moderate number of active and passive elements used in the topology. A robust hybrid control, where a novel designed feedforward controller supports the closed-loop PID controller, is proposed for the control of the regulator apart from similar studies in the literature. Active tracking response of the reference output phase voltages is augmented by the proposed hybrid control method. Thus nearly close to sine-wave output phase voltages can be obtained, whether the input AC phase voltages are ideal pure sine or not. Also, the modular structure of the regulator topology enables independent control for each output phase. Thus, the supply of balanced/unbalanced wye-connected three-phase loads or independent single-phase loads with nearly close to ideal sine wave voltages can be achieved by the modularity of the regulator. Both experimental and simulation test studies are performed for the proposed regulator system. A laboratory set-up for the regulator is designed for 0-200 Vp input phase voltages (50 Hz), and 0-300 Vp output phase voltages, and 1.8 kW output power. The achieved results for both simulation and experimental tests verify the proposed switch-mode boost-type regulator's ability to provide output phase voltages nearly close to sine wave with total harmonic distortion (THD) values under 5%.

Keywords: AC-AC regulator, active tracking, boost converter, three-phase, THD

1. INTRODUCTION

Distortion of power quality in power systems is continuously increased due to the increasing energy demand and this causes a major problem for AC loads. A required alternating voltage has to supply AC loads within a determined magnitude band, where some of the AC loads accept only a small band. Voltage sags or voltage swells occur due to the various operating conditions, such as loading in the distribution network, that affect the power quality of the AC loads. Besides, some AC loads such as AC motors need to be supplied by adjustable voltages that differ from the grid voltage levels. Many studies and solutions are presented in the literature for AC voltage regulation.

FACTS (flexible ac transmission systems) devices are the main providers of voltage

* Corresponding author: farukyalcin@sakarya.edu.tr
[1] Sakarya University of Applied Sciences, Faculty of Technology, Department of Mechatronics Engineering,
ORCID: https://orcid.org/0000-0003-2672-216X
[2] University of Applied Sciences Technikum Wien, Austria
E-Mail: felix.himmelstoss@technikum-wien.at
ORCID: https://orcid.org/0000-0001-8482-2295

Faruk YALÇIN, Felix HIMMELSTOSS

Boost Converter Based 3-Phase AC-AC Active Tracking Voltage Regulator Controlled by a Robust Hybrid C...

regulation for voltage variations in distribution systems. For this aim, voltage sag supporters [1, 2], voltage sag/swell compensators [3, 4], DVRs (dynamic voltage restorers) [5, 6], and voltage conditioners [7, 8], are developed and applied successfully. The desired distribution network voltage is provided by these devices to the distribution buses where the AC loads are connected. Therefore, it is not possible to provide voltage regulation for the end-user AC loads independently by this method. However, these VSI (voltage source inverter) structured FACTS need a coupling transformer. VSIs may be designed as a DC-AC converter or an AC-DC-AC converter in these FACTS devices based regulators. Independent external DC storage systems such as capacitors or batteries are needed for the VSIs which are based on a DC-AC converter. Because of this, long duration accurate voltage sags/swells compensation cannot be obtained by using DC-AC converter-based VSIs. In addition, capacities of the external storage units limit the compensation capabilities. External storage systems are not needed in AC-DC-AC based converters as the AC-DC sub-units already exist. But the effect of additional increasing loss, caused by the AC-DC topology, is the main disadvantage of the AC-DC-AC converters.

In many applications only VSIs based on AC-DC-AC converters are chosen for voltage regulation for AC loads [9, 10]. By this way, the need for additional coupling transformers, as used in the FACTS-based regulators mentioned above, is eliminated. In addition, this method provides independent voltage regulation control of each AC load individually where the distribution voltage level is constant at the load buses. However, AC-DC stage before DC-AC stage of the AC-AC conversion structure brings additional loss. This is the mayor disadvantage of these VSIs.

AC-AC conversion emerges as the ideal solution in contrast to direct VSI applications and FACTS devices-based regulation systems, because FACTS-based or direct VSI-based techniques have large complexity and limited feature problems. In the literature, the researchers developed many kinds of AC-AC regulators. The simplest and the traditional solution for direct AC-AC regulation can be provided by AC-AC PWM choppers [11]. But high-level harmonics occur at the output of the regulator, as the input sine wave input form is disturbed because of chopping. So, additional filtering units such as passive filters or coupling transformers have to be used at the output in these AC choppers, in order to eliminate the voltage harmonics. Nowadays there are many studies on switch-mode buck [12, 13], boost [14-17], and buck-boost [18, 19] type AC-AC regulators that are used for direct AC regulation. The mentioned switch-mode AC-AC regulators can achieve output voltages close to sine wave. The harmonic levels of the output voltages are reduced efficiently. So the requirement of additional filtering units is prevented in these types of regulators. Lower complex topology structure of these regulators brings another advantage. Although the application for AC regulation of these switch-mode AC-AC regulators is achieved successfully in the literature, application cases of input AC voltages that are far from sine wave are ignored in these studies. Just only the case of applying pure sine-wave input AC voltage is considered in these similar existing studies in the literature. But in practice, distribution network voltages are disturbed because of nonlinear loads. So AC loads may be supplied with input voltages that are not ideal sine-wave and include voltages harmonics. Thus harmonic elimination in addition to AC voltage regulation is a necessity. This is essential, because the AC loads require supply voltages with low harmonics under 5% THD [20].

A three-phase boost-type active tracking AC-AC voltage regulator is presented in this study. An improved control method is also proposed for the active tracking of the desired output sine-wave phase voltages. The presented control method and the topology of the regulator are patented by the co-author of this study [21]. The presented topology of the regulator incorporates just three capacitors, three inductors, and twelve active switches. This is a moderate number of components. The boost-type structure of the presented regulator enables the achievement of a wide range of output voltage amplitudes for each phase higher than the input phase voltage

Faruk YALÇIN, Felix HIMMELSTOSS

Boost Converter Based 3-Phase AC-AC Active Tracking Voltage Regulator Controlled by a Robust Hybrid C...

amplitudes. Also the modular structure of the regulator topology enables independent control for each output phase operation. Thus supplying of balanced/unbalanced wye-connected three-phase loads or independent single-phase loads by nearly close to ideal sine wave voltages can be achieved by the modularity of the regulator. The proposed control method for the proposed regulator is a novel hybrid control method apart from the similar studies in the literature, it is composed of a closed-loop PID controller and a new feedforward controller. In this way, active tracking of the reference sine-wave output phase voltages is improved to achieve nearly close to sine-wave output phase voltages independent whether the input phase voltages are pure sine-waves or not. Both experimental and simulation test studies are performed for the proposed regulator system. The achieved results for both simulation and experimental tests verify the proposed switch-mode boost-type regulator's ability to provide output phase voltages nearly close to the sine wave with THD values under 5%.

2. THE THREE-PHASE BOOST AC-AC REGULATOR

The proposed boost converter based three-phase AC-AC regulator topology, as well as the regulator's operation procedure and the dynamic analysis, are all discussed in this section.

2.1. The Topology of the Regulator

The proposed boost converter based three-phase AC-AC regulator's main circuit is shown in Figure 1 [21].
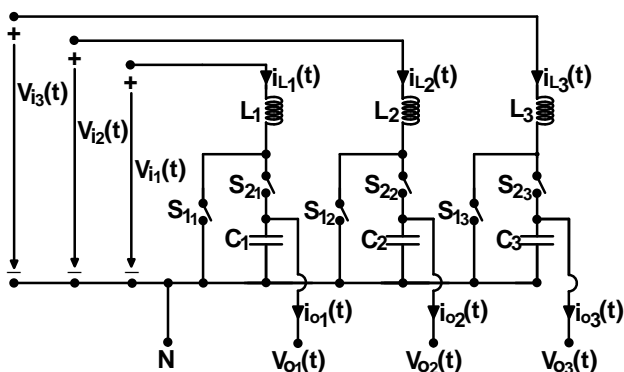
Figure 1 General topology of the proposed boost converter based three-phase AC-AC regulator

The proposed three-phase AC-AC regulator is structured by three boost converter-based sub-circuits, which are wye-connected at the common neutral point (N) as shown in Figure 1. In Figure 1, the "1,2,3" which are the second-order subscripts, mark the three-phase phase number. The mentioned phase number is generalized as "n" where n=1,2,3 in this paper. The neutral point N of the regulator sub-circuits and the three-phase load neutral are connected to provide a neutral return. Thus three-phase unbalanced or three independent single-phase modular regulator operations can also be provided by the proposed regulator structure.

In Figure 1, the input AC phase voltages, the output AC phase voltages, the inductors, and the capacitors are marked by V_{in}, V_{on}, L_n, and C_n, respectively. S_{1n} and S_{2n} represent the bidirectional active switches. IGBTs are used to obtain these bidirectional active switches. Thus the circuit of the proposed regulator, where S_{1n} and S_{2n} are structured by IGBTs, are depicted in Figure 2.
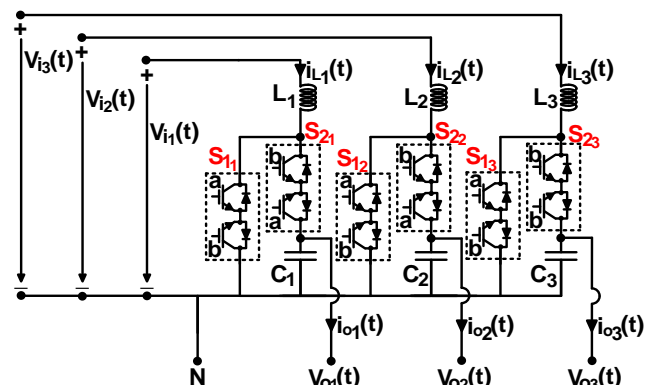
Figure 2 The proposed boost-type three-phase AC-AC regulator circuit with IGBTs

2.2. The Operation Procedure of the Regulator

The proposed three-phase AC-AC regulator's operation is based on the well-known conventional boost converter. The structures of each phase-sub-circuits are taken as identical in this study. The instant input phase voltages $V_{in}(t)$ are boosted as $V_{on}(t)$ phase voltages at the output, based on the PWM duty ratios (d_n) control of S_{1n}. As a result, the output phase voltages are AC voltages of the same polarity as the input phase voltages, but with larger amplitude values. The

Faruk YALÇIN, Felix HIMMELSTOSS

Boost Converter Based 3-Phase AC-AC Active Tracking Voltage Regulator Controlled by a Robust Hybrid C...

S_{2n} switches are the supplementary switches of the S_{1n} switches. S_{2n} are turned off, while S_{1n} are turned on. In this stage the inductors are supplied by V_{in}, and the output phase loads are supplied by the pre-energized capacitors. S_{2n} are turned on, while S_{1n} are turned off. In this stage the output phase loads and the capacitors are supplied by the pre-energized inductors.

As the input phase voltages V_{in} have alternating voltage wave forms, the polarities of V_{in} are forced to be changed in each half period. Thus, the states of the sub-active switches that are part of the bidirectional active switches S_{1n} and S_{2n} must be changed depending on the input phase voltages' half-periods. In Table 1, the control of S_{1n} and S_{2n} active switches are given in detail.

Table 1
Control signal of IGBTs used in Figure 2 as part of the bidirectional S_{1n} and S_{2n} active switches

| State | S_{1n} | | | | S_{2n} | | | |
| | Positive Half-Wave Stage | | Negative Half-Wave Stage | | Positive Half-Wave Stage | | Negative Half-Wave Stage | |
	S_{1an}	S_{1bn}	S_{1an}	S_{1bn}	S_{2an}	S_{2bn}	S_{2an}	S_{2bn}
ON	on	off	off	on	off	on	on	off
OFF	off	off	off	off	off	off	off	off

The switching pattern of the IGBTs can be seen in Figure 3.
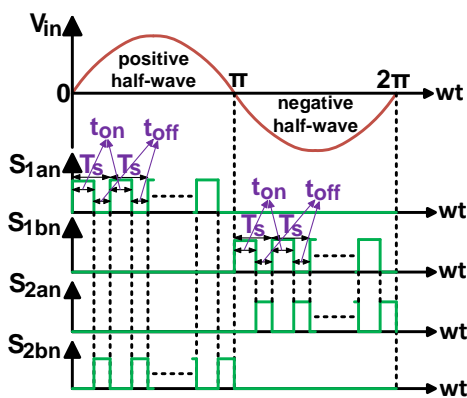
Figure 3 The switching pattern of the IGBTs

Figure 4 gives the proposed regulator topology's equivalent sub-circuits regarding Figure 2 and depending on the control of the active switches for one cycle of the input sine-wave voltage.
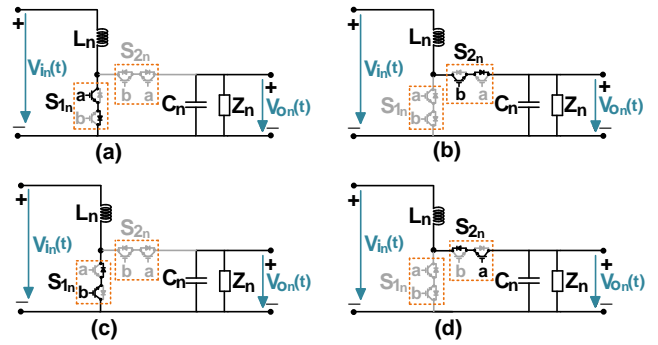
Figure 4 The equivalent sub-circuits of the proposed boost type regulator *(a) Positive half-wave output stage, on mode (S_{1n} is on, S_{2n} is off), (b) Positive half-wave output stage, off mode (S_{1n} is off, S_{2n} is on), (c) Negative half-wave output stage, on mode (S_{1n} is on, S_{2n} is off), (d) Negative half-wave output stage, off mode (S_{1n} is off, S_{2n} is on)*

So the proposed regulator's one cycle output phase voltage producing operation can be explained as a summary of Figure 3 and Figure 4 for the two main stages as below.

Stage 1 ($0 \leq wt < \pi$): The input AC phase voltages are in positive half-wave periods depending on the determined polarities in this stage. During PWM on-stages of S_{1n} (S_{2n} are off), S_{1an} are turned on, S_{1bn} are turned off and both S_{2an} and S_{2bn} are turned off. During PWM off-stages of S_{1n} (S_{2n} are on), both S_{1an} and S_{1bn} are turned off, S_{2an} are turned off, and S_{2bn} are turned on. From the input phase voltages, the desired positive half sine-waves output phase voltages are produced based on the continuous proper control of d_n, which are the PWM duty ratios of S_{1n}.

Stage 2 ($\pi \leq wt < 2\pi$): The input AC phase voltages are in the negative half-wave periods depending on the determined polarities in this stage. During PWM on-stages of S_{1n} (S_{2n} are off), S_{1bn} are turned on, S_{1an} are turned off and both S_{2an} and S_{2bn} are turned off. During PWM off-stages of S_{1n} (S_{2n} are on), both S_{1an} and S_{1bn} are turned off, S_{2bn} are turned off, and S_{2an} are turned on. From the input phase voltages, the desired negative half sine-waves output phase voltages are produced, based on the continuous proper control of d_n, which are the PWM duty ratios of S_{1n}.

Faruk YALÇIN, Felix HIMMELSTOSS

Boost Converter Based 3-Phase AC-AC Active Tracking Voltage Regulator Controlled by a Robust Hybrid C...

2.3. The Dynamic Analysis of the Regulator

This section presents the dynamic analysis of the proposed boost converter-based three-phase AC-AC regulator in detail. In order to provide an accurate analysis for real-time applications, the analysis takes real parasitic effects of the elements used in the topology into account.

Figure 5 gives the equivalent circuits of the proposed regulator for the positive half-wave input state. The selected IGBTs are considered identical in the equivalent circuit.

(a)

(b)
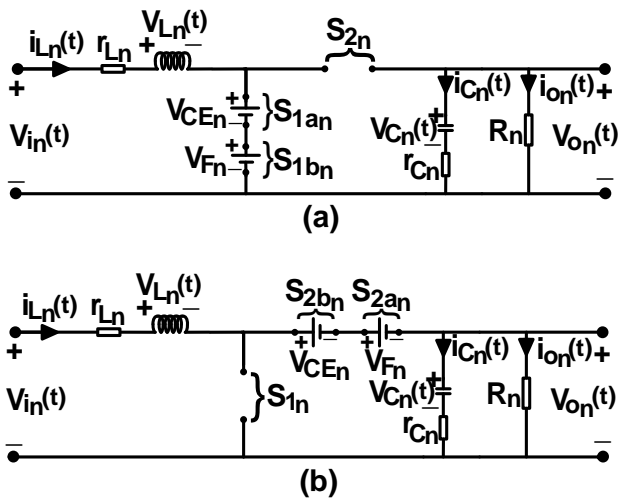
Figure 5 The positive half-wave stage equivalent circuit of the regulator *(a) on-mode − S₁ₙ is turned on and S₂ₙ is turned off, (b) off-mode − S₁ₙ is turned off and S₂ₙ is turned on*

In Figure 5 i_{on}, i_{Ln}, i_{Cn}, V_{Ln}, V_{Cn}, V_{Fn}, V_{CEn}, r_{Ln}, r_{Cn}, and R_n are the output currents, the inductor currents, the capacitor currents, the inductor voltages, the capacitor voltages, the forward biasing voltages of the IGBTs' anti-parallel diodes, the collector-emitter on-voltages of the IGBTs, the equivalent series resistances (ESRs) of the inductors, the ESRs of the capacitors, and the output phase load resistances, respectively.

The regulator's dynamic analysis can be derived from Figure 5 for the positive half-wave input state. The dynamic equations for the inductor currents and the output voltages are derived for two modes, on-mode and off-mode, as shown in Figure 5.

On-mode (S_{1n} are on and S_{2n} are off): For the on-mode, the state equations of the inductor currents and the output voltages can be achieved according to Figure 5a, respectively as below:

$$\frac{di_{L_n}(t)}{dt} = -\frac{1}{L_n} r_{L_n} i_{L_n}(t) + \frac{1}{L_n} V_{i_n}(t)$$
$$-\frac{1}{L_n}\left[V_{CE_n} + V_{F_n}\right] \quad (1)$$

$$\frac{dV_{o_n}(t)}{dt} = -\frac{1}{\left(R_n + r_{C_n}\right)C_n} V_{o_n}(t) \quad (2)$$

Off-mode (S_{1n} are off and S_{2n} are on): For the off-mode, the state equations of the inductor currents and the output voltages can be achieved according to Figure 5b, respectively as below:

$$\frac{di_{L_n}(t)}{dt} = -\frac{1}{L_n} r_{L_n} i_{L_n}(t) - \frac{1}{L_n} V_{o_n}(t)$$
$$+\frac{1}{L_n} V_{i_n}(t) - \frac{1}{L_n}\left[V_{CE_n} + V_{F_n}\right] \quad (3)$$

$$\frac{dV_{o_n}(t)}{dt} = \left(\frac{R_n}{R_n + r_{C_n}}\right)\left[\frac{1}{C_n} - \frac{r_{C_n} r_{L_n}}{L_n}\right] i_{L_n}(t)$$
$$-\left(\frac{R_n}{R_n + r_{C_n}}\right)\left(\frac{r_{C_n}}{L_n} + \frac{1}{R_n C_n}\right) V_{o_n}(t)$$
$$+\frac{r_{C_n} R_n}{\left(R_n + r_{C_n}\right)L_n} V_{i_n}(t)$$
$$-\frac{r_{C_n} R_n}{\left(R_n + r_{C_n}\right)L_n}\left[V_{CE_n} - V_{F_n}\right] \quad (4)$$

From (1) and (2), the equations of the state-space model for the on-mode can be derived as follows:

Faruk YALÇIN, Felix HIMMELSTOSS

Boost Converter Based 3-Phase AC-AC Active Tracking Voltage Regulator Controlled by a Robust Hybrid C...

$$\begin{bmatrix} \dot{i}_{L_n}(t) \\ \dot{V}_{o_n}(t) \end{bmatrix} = \begin{bmatrix} -\dfrac{r_{L_n}}{L_n} & 0 \\ 0 & -\dfrac{1}{\left(R_n + r_{C_n}\right)C_n} \end{bmatrix} \begin{bmatrix} i_{L_n}(t) \\ V_{o_n}(t) \end{bmatrix} + \begin{bmatrix} \dfrac{1}{L_n} & -\dfrac{1}{L_n} & -\dfrac{1}{L_n} \\ 0 & 0 & 0 \end{bmatrix} \begin{bmatrix} V_{i_n}(t) \\ V_{CE_n} \\ V_{F_n} \end{bmatrix} \tag{5}$$

From (3) and (4), the equations of the state-space model for the off-mode can be derived as follows:

$$\begin{bmatrix} \dot{i}_{L_n}(t) \\ \dot{V}_{o_n}(t) \end{bmatrix} = \begin{bmatrix} -\dfrac{r_{L_n}}{L_n} & -\dfrac{1}{L_n} \\ \dfrac{R_n}{R_n + r_{C_n}}\left[\dfrac{1}{C_n} - \dfrac{r_{C_n} r_{L_n}}{L_n}\right] & -\dfrac{R_n}{R_n + r_{C_n}}\left(\dfrac{r_{C_n}}{L_n} + \dfrac{1}{R_n C_n}\right) \end{bmatrix} \begin{bmatrix} i_{L_n}(t) \\ V_{o_n}(t) \end{bmatrix} + \begin{bmatrix} \dfrac{1}{L_n} & -\dfrac{1}{L_n} & -\dfrac{1}{L_n} \\ \left(\dfrac{R_n}{R_n + r_{C_n}} \dfrac{r_{C_n}}{L_n}\right) & -\left(\dfrac{R_n}{R_n + r_{C_n}} \dfrac{r_{C_n}}{L_n}\right) & -\left(\dfrac{R_n}{R_n + r_{C_n}} \dfrac{r_{C_n}}{L_n}\right) \end{bmatrix} \begin{bmatrix} V_{i_n}(t) \\ V_{CE_n} \\ V_{F_n} \end{bmatrix} \tag{6}$$

The above shown dynamic analysis is performed for the positive half-wave input case, as mentioned previously. A similar dynamic analysis for the negative half-wave input case provides the same state-space equations given in (5) and (6). Thus, this means that the state-space equations obtained in (5) and (6) are valid for all input cases.

So, through (5) and (6), the small signal transfer functions between the output phase voltages and the PWM duty ratios can be achieved as follows:

$$G_{boost_n}(s) = \frac{\hat{V}_{o_n}(s)}{\hat{d}_n(s)} = \frac{g_n s + \left(a_n g_n + c_n f_n\right)}{s^2 + \left(a_n + e_n\right)s + \left(a_n e_n - b_n c_n\right)} \tag{7}$$

The coefficients used in (7) are as follows:

$$a_n = \frac{r_{L_n}}{L_n} \tag{8}$$

$$b_n = -\frac{(1 - \bar{D}_n)}{L_n} \tag{9}$$

$$c_n = \frac{(1 - \bar{D}_n)R_n}{R_n + r_{C_n}}\left[\frac{1}{C_n} - \frac{r_{C_n} r_{L_n}}{L_n}\right] \tag{10}$$

$$e_n = \frac{(1 - \bar{D}_n)R_n}{R_n + r_{C_n}}\frac{r_{C_n}}{L_n} + \frac{1}{\left(R_n + r_{C_n}\right)C_n} \tag{11}$$

$$f_n = \frac{\bar{V}_{o_n}}{L_n} \tag{12}$$

$$g_n = -\frac{R_n}{R_n + r_{C_n}}\left[\frac{1}{C_n} - \frac{r_{C_n} r_{L_n}}{L_n}\right]\bar{i}_{L_n} + \frac{R_n}{R_n + r_{C_n}}\frac{r_{C_n}}{L_n}\left[\bar{V}_{o_n} - \bar{V}_{i_n} + V_{CE_n} + V_{F_n}\right] \tag{13}$$

In (9)-(13), $\bar{D}_n$, $\bar{i}_{L_n}$, $\bar{V}_{o_n}$, and $\bar{V}_{i_n}$ represent the values of PWM duty ratios, inductor currents, output phase voltages, and input phase voltages respectively at the operating point. $\bar{V}_{o_n}$ and $\bar{i}_{L_n}$ can be formulated as below:

$$\bar{V}_{o_n} = \frac{\bar{V}_{i_n}}{(1 - \bar{D}_n)}, \qquad \bar{i}_{L_n} = \frac{\bar{V}_{i_n}}{(1 - \bar{D}_n)^2 R_n} \tag{14}$$

3. THE PROPOSED HYBRID CONTROL METHOD FOR THE REGULATOR OPERATION

The proposed hybrid control method for the control of the proposed AC-AC regulator is presented in this section. Figure 6 demonstrates the general control diagram of the proposed regulator.

Faruk YALÇIN, Felix HIMMELSTOSS

Boost Converter Based 3-Phase AC-AC Active Tracking Voltage Regulator Controlled by a Robust Hybrid C...

THREE-PHASE BOOST AC VOLTAGE REGULATOR
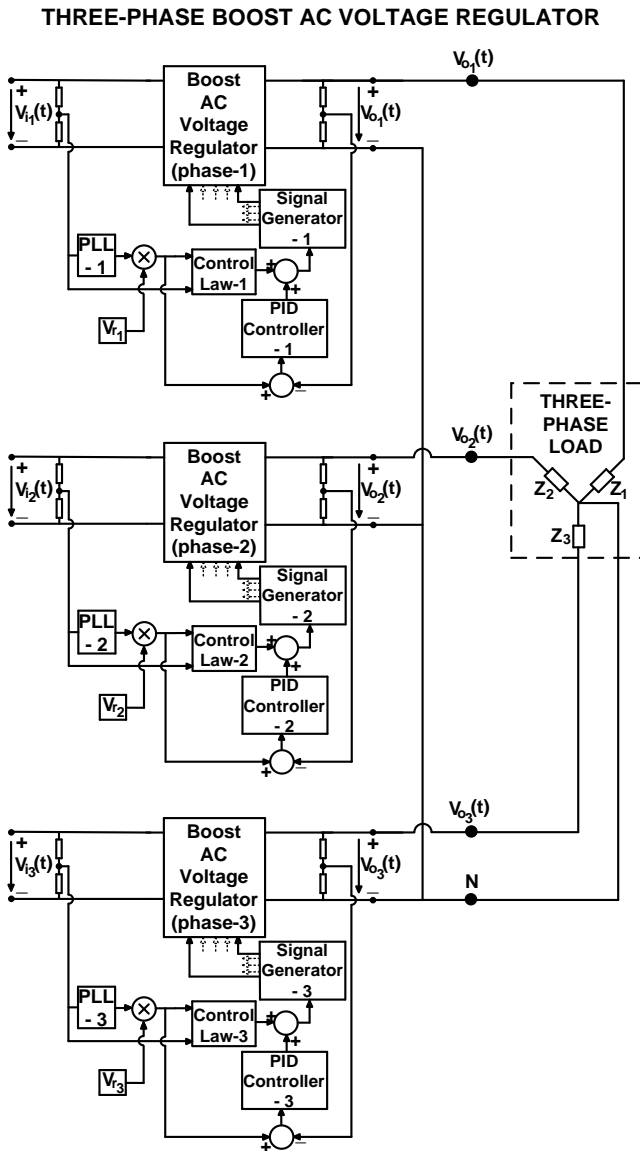
Figure 6 The general control diagram of the proposed regulator

The frequencies of the phase AC voltages of the input are determined by the PLLs, where the magnitudes of the reference output AC phase voltages are determined by V_{rn} as seen in Figure 6. So the requested sine-wave AC reference phase output voltages can be achieved as given below

$$\left. \begin{aligned} V_{ref_1}(wt) &= V_{r_1}\sin w_1 t \\ V_{ref_2}(wt) &= V_{r_2}\sin\left(w_2 t - 120^o\right) \\ V_{ref_3}(wt) &= V_{r_3}\sin\left(w_3 t + 120^o\right) \end{aligned} \right\} \quad (15)$$

The proposed hybrid controller is composed of two main units as depicted in Figure 6. One of these units is the traditional closed-loop PID controller. The main mission of the PID controller is to eliminate the error between the real output voltage and the reference output voltage, while it satisfies the response performance depending on the design criteria. The newly developed feedforward controller, which is referred to as "control law (CL)" in Figure 6, is the other unit of the hybrid controller. The developed CL is a controller based on the open-loop, which generates a PWM duty ratio depending on the equation below based on the topology parameters.

$$d_{CL_n}(wt) = \sqrt{\frac{2L_n\left|V_{r_n}\sin w_n t\right|^2\left(\left|V_{r_n}\sin w_n t\right| - \left|V_{i_n}(wt)\right| + V_{CE_n} + V_{F_n}\right)}{\left|V_{i_n}(wt)\right|\left|V_{r_n}\sin w_n t\right|\left(\left|V_{i_n}(wt)\right| - V_{CE_n} - V_{F_n}\right)T_{S_n}R_n}} \quad (16)$$

T_S determines the PWM switching period in (16). The CL's PWM duty ratio as generated in (16) is not capable of directly meeting the desired PWM duty ratio to obtain the reference output voltage. Instead it generates a duty ratio that is very close to the necessary one. It is clear from (16) that the duty ratio obtained by the CL can be produced in a fast manner as it has a static structure. Thus an improved response performance to obtain the requested duty ratio can be obtained, as the CL supports the PID controller. By this way, accurate and efficient active tracking of the reference output voltage can be provided by the proposed hybrid control method and thus close to sine-wave output voltage with low THD can be obtained with the hybrid control method. So the PID controller and the CL produce the requested PWM as given below:

$$d_n(wt) = d_{PID_n}(wt) + d_{CL_n}(wt) \quad (17)$$

Discrete time control is performed for the regulator operation control in the study. The block diagram of the regulator which is based on the proposed hybrid control method can be given in Figure 7.

Faruk YALÇIN, Felix HIMMELSTOSS

Boost Converter Based 3-Phase AC-AC Active Tracking Voltage Regulator Controlled by a Robust Hybrid C...
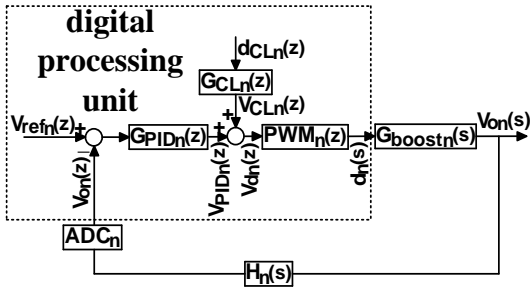
Figure 7 The discrete-time control block diagram based on the proposed hybrid control technique for the boost-type 3-phase regulator

By Figure 7, the fundamental relations between the transfer functions and the control signals of the discrete-time control block diagram are determined as given below.

$$G_{CL_n}(z) = \frac{1}{PWM_n(z)} \tag{18}$$

$$V_{d_n}(z) = V_{CL_n}(z) + V_{PID_n}(z) \tag{19}$$

$$d_n(z) = V_{d_n}(z).PWM_n(z) \tag{20}$$

The discrete PID controller's transfer function used in this study is given as

$$G_{PID_n}(z) = K_{P_n} + K_{I_n}\frac{z}{z-1} + K_{D_n}\frac{z-1}{z} \tag{21}$$

4. THE STUDY RESULTS

This section gives the design steps of the proposed regulator and also the test results of the simulation and of the experiments.

4.1. The Design Criteria of the Regulator Operation

A laboratory set-up is performed for the proposed regulator for a real-time experimental regulator operation. The set-up is designed for 0-200 Vp input phase voltages (50 Hz), and 0-300 Vp output phase voltages, and 1.8 kW output power. Table 4

IXGH20N60BU1 type n-channel high-speed IGBTs (V_{CES}=600 V, V_{CE}=1.7 V, V_F=1.6 V, I_C=40 A) are used in the set-up circuit. In Table 2, the determined values of the inductors, the capacitors and the switching frequencies for the phase sub-units of the regulator circuit are given.

Table 2
The selected values of the switching frequencies, capacitors and inductors

Switching Frequencies f_{sn} (kHz)	Capacitors		Inductors	
	C_n (μF)	r_{Cn} (mΩ)	L_n (μH)	r_{Ln} (mΩ)
50	10	190	50	150

Table 3 determines the operating point parameters of the discrete-time PID controllers for the phase sub-units.

Table 3
The considered operating point parameters of the regulator operation

$\bar{V}_{i_n}$ (V)	$\bar{D}_n$	$\bar{V}_{o_n}$ (V)	R_n (Ω)
50	0.5	100	40

The parameters of the PID controller used in (21) are found by the design and performance criteria as,

$$K_{P_n} = -0.0082, \ K_{I_n} = 0.0345, \ K_{D_n} = 0.014 \tag{22}$$

4.2. The Simulation Results

To validate the theoretical proposals of the study, simulation tests are applied with the proposed hybrid control approach on the proposed regulator.

In MATLAB Simulink, three different simulation test cases are applied to the regulator system, as shown in Table 4. In Figures 8-10, the simulation test results of the wave form are shown. In Table 5, the simulation numerical results of the output are also given. THD_{Vn} and THD_{In} in Table 5 denote the voltages THD and currents THD, respectively.

Faruk YALÇIN, Felix HIMMELSTOSS

Boost Converter Based 3-Phase AC-AC Active Tracking Voltage Regulator Controlled by a Robust Hybrid C...

Table 4
Test cases of the simulation studies

Test Case No	V_{in} (V)			Output Load Z_n			Desired output fundamental sine-wave voltage V_{on} (V)		
	V_{i1}	V_{i2}	V_{i3}	Z_1	Z_2	Z_3	V_{o1}	V_{o2}	V_{o3}
1	50V sine (f=50Hz)	80V sine (f=50Hz)	100V sine (f=50Hz)	Resistive R_1=25Ω	Resistive R_2=25Ω	Resistive R_3=25Ω	160	160	160
2	90V sine + HOH (f=50Hz)	75V sine (f=50Hz)	65V sine + LOH (f=50Hz)	Inductive R_1=5Ω, L_1=12mH	Inductive R_2=5Ω, L_2=12mH	Inductive R_3=5Ω, L_3=12mH	120	120	120
3	70V sine + LOH (f=50Hz)	40V sine + HOH (f=50Hz)	60V sine + fluct. (f=50Hz)	Resistive R_1=10Ω	Inductive R_2=8Ω, L_2=6,8mH	Capacitive R_3=5Ω, C_3=0.5mF	150	110	100
fluct.: fluctuations, HOH: high order harmonics, LOH: low order harmonics									

Figures 8-10 and Table 5 prove that the proposed three-phase AC-AC regulator based on the boost-converter can provide the desired AC sine-wave phase voltages close to a sine-wave with under 5% THD levels, though the input AC phase voltages have harmonics or the three-phase output is unbalanced. The results also show that the proposed three-phase AC-AC regulator based on the boost-converter can operate in modular mode for single-phase independent loading. The obtained results given in Figures 8-10 and Table 5 show that the proposed hybrid control method is capable of active tracking of the reference output phase voltages in an accurate and an efficient manner.
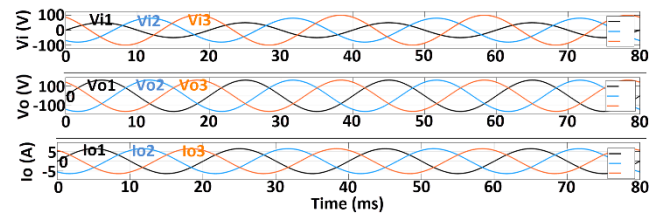
Figure 8 The simulation results for test case-1
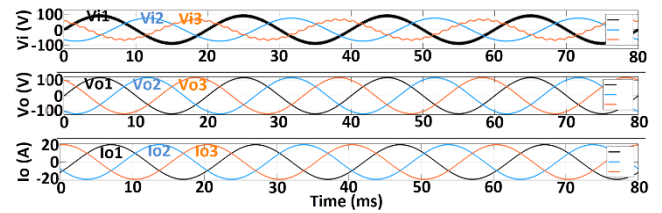
Figure 9 The simulation results for test case-2
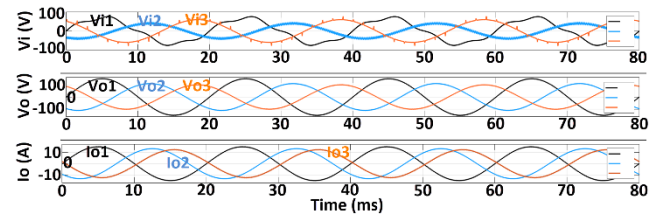
Figure 10 The simulation results for test case-3

Table 5
The numerical simulation results of the test cases

Test Case No	Obtained Fundamental V_{on} (V)			THD_{Vn} (%)			THD_{In} (%)		
	V_{o1}	V_{o2}	V_{o3}	THD_{V1}	THD_{V2}	THD_{V3}	THD_{I1}	THD_{I2}	THD_{I3}
1	160.1	160.1	160.1	1.72	1.72	1.72	1.72	1.72	1.72
2	119.8	119.8	119.8	1.93	1.93	1.93	1.76	1.76	1.76
3	150.3	109.9	100.4	1.89	2.13	2.07	1.89	2.02	2.23

Faruk YALÇIN, Felix HIMMELSTOSS

Boost Converter Based 3-Phase AC-AC Active Tracking Voltage Regulator Controlled by a Robust Hybrid C...

4.3. The Experimental Results

To validate the real-time practical application of the study, experimental tests are applied with the proposed hybrid control approach on the proposed regulator. In Figure 11, the experimental set-up of the regulator system which was built for this study is shown.
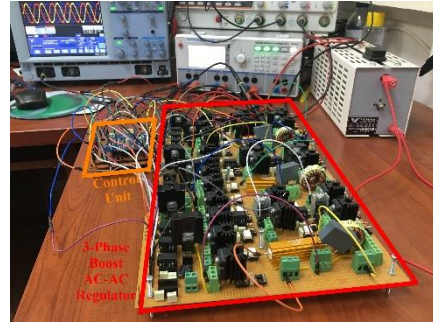
Figure 11 The designed experimental laboratory set-up of the regulator system

Table 6
Test cases of the experimental studies

Test Case No	V_{in} (V)			Output Load Z_n			Desired output fundamental sine-wave voltage V_{on} (V)		
	V_{i1}	V_{i2}	V_{i3}	Z_1	Z_2	Z_3	V_{o1}	V_{o2}	V_{o3}
1	100V sine (f=50Hz)	85V sine (f=50Hz)	55V sine (f=50Hz)	Resistive R_1=40Ω	Resistive R_2=40Ω	Resistive R_3=40Ω	150	150	150
2	25V sine (f=50Hz)	35V sine (f=50Hz)	45V sine (f=50Hz)	Inductive R_1=9Ω, L_1=5mH	Inductive R_2=9Ω, L_2=5mH	Inductive R_3=9Ω, L_3=5mH	75	75	75
3	40V sine (f=50Hz)	40V sine (f=50Hz)	40V sine (f=50Hz)	Resistive R_1=16Ω	Inductive R_2=7Ω, L_2=3.3mH	Capacitive R_3=20Ω, C_3=0.33mF	80	70	90

On the designed laboratory set-up, three different experimental test cases are applied to the regulator system, as shown in Table 6. In Figures 12-14 the experimental wave form test results are shown. In Table 7 the experimental numerical results of the output are also given.

Figures 12-14 and Table 7 prove that the proposed three-phase AC-AC regulator based on the boost-converter can provide the desired AC sine-wave phase voltages close to the sine-wave with under 5% THD levels although the three-phase output is unbalanced. The results also show that the proposed three-phase AC-AC regulator based on the boost-converter can operate in modular mode for single-phase independent loading. Hence, the obtained results given in Figures 8-10 and Table 5 show that the proposed hybrid control method is capable of active tracking of the reference output phase voltages in an accurate and an efficient manner experimentally.
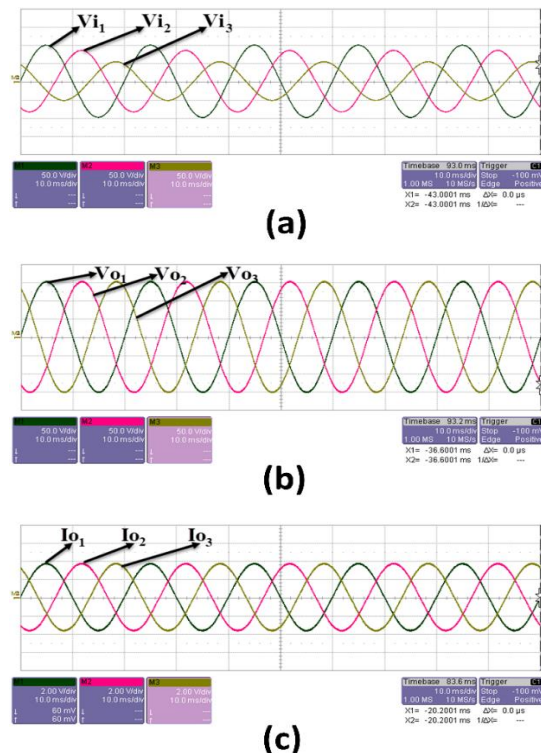
Figure 12 The experimental results for test case-1 (V/div=A/div for I_{On})

Faruk YALÇIN, Felix HIMMELSTOSS

Boost Converter Based 3-Phase AC-AC Active Tracking Voltage Regulator Controlled by a Robust Hybrid C...
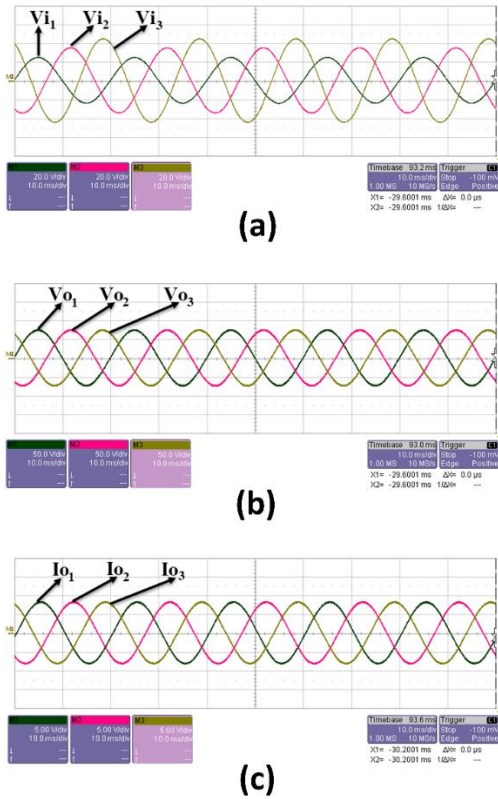
Figure 13 The experimental results for test case-2
(V/div=A/div for I_{On})
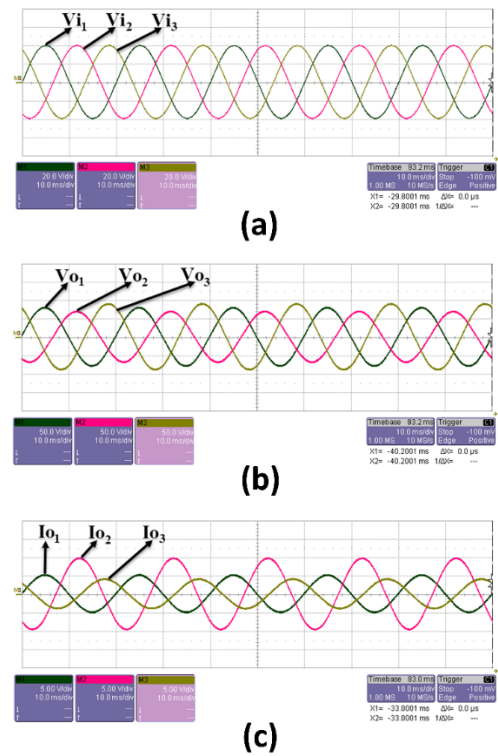
Figure 14 The experimental results for test case-3
(V/div=A/div for I_{On})

Table 7
The achieved numerical experimental results of the test cases

Test Case No	Obtained Fundamental V_{on} (V)			THD_{Vn} (%)			THD_{In} (%)		
	V_{o1}	V_{o2}	V_{o3}	THD_{V1}	THD_{V2}	THD_{V3}	THD_{I1}	THD_{I2}	THD_{I3}
1	150.1	150.3	150.2	1.91	1.94	1.92	1.86	1.89	1.84
2	74.8	74.8	74.9	2.12	2.23	2.09	1.99	2.07	1.94
3	80.4	70.2	89.9	1.86	2.07	1.99	1.81	1.90	2.18

Table 8
Comparative THD results for the proposed hybrid control and the standalone traditional PID control of the experimental test cases

Test Case No	THD (%) results of the proposed hybrid control method						THD (%) results of the traditional standalone PID control					
	THD_{Vn}			THD_{In}			THD_{Vn}			THD_{In}		
1	1.91	1.94	1.92	1.86	1.89	1.84	1.98	2.08	2.05	1.93	1.99	1.94
2	2.12	2.23	2.09	1.99	2.07	1.94	2.23	2.31	2.21	2.12	2.17	2.09
3	1.86	2.07	1.99	1.81	1.90	2.18	1.97	2.21	2.10	1.92	1.98	2.27

A comparative test study is done to show the proposed hybrid control technique's efficiency on the active tracking. The proposed hybrid control technique and the standalone PID control are applied separately to the proposed regulator for the comparative test case parameters as V_{i2}=50V sine, V_{o2}=110V, R_2=10Ω. In Figure 15 the

obtained output voltage waveforms of phase-2 for the mentioned two separate applications are demonstrated together. In Table 8 the comparative numerical output THD results of these applications are also presented.

Faruk YALÇIN, Felix HIMMELSTOSS

Boost Converter Based 3-Phase AC-AC Active Tracking Voltage Regulator Controlled by a Robust Hybrid C...
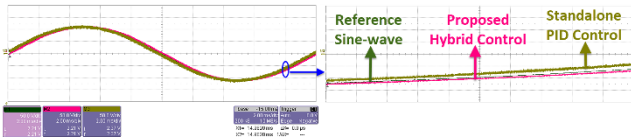
Figure 15 Comparative experimental wave forms for the output phase-2 voltage V_{o2} of the proposed hybrid control and of the standalone PID control for V_{i2}=50V sine, V_{o2}=110V, R_2=10Ω (50V/div, 2ms/div)

It is clear from Figure 15 that the proposed hybrid control technique provides better active tracking of the reference phase output sine-wave voltages than the traditional PID control. Thus, it is proved that the developed CL is capable of improving the active tracking by supporting the PID controller. The output THD results in Table 8 also prove this. It must be noted that in Table 8 the THD results are under 5%.

The proposed boost converter based three-phase regulator's efficiency is researched for different output power rates depending on the power rate determined in the design criteria. The obtained efficiency curve of the regulator is demonstrated in Figure 16. As seen from Figure 16, the proposed regulator efficiency is sufficient.
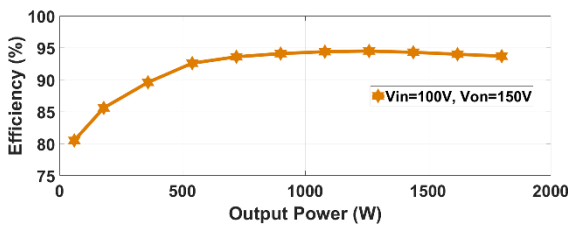
Figure 16 The regulator's efficiency curve for different output power rates

5. CONCLUSION

This study proposes a boost converter-based three-phase active tracking AC-AC voltage regulator operating in switch-mode. The proposed regulator topology includes a moderate number of active and passive elements. A new feedforward controller supports the closed-loop PID controller. This robust hybrid control method is proposed for the regulator operation control. By this hybrid control, the response of the active tracking for the reference output phase voltages is increased and provides close to sine-wave output

phase voltages, whether the input AC phase voltages are ideal pure sine or not. The modular regulator topology structure also enables independent control of each output phase operation that provides the supply of balanced/unbalanced wye-connected three-phase loads or independent single-phase loads with close to ideal sine-wave voltages. Both experimental and simulation test studies are done for the proposed three-phase AC regulator to demonstrate the accuracy and the efficiency of the proposals. The achieved results show that the proposed regulator with the proposed hybrid control method provides accurate and efficient operation for producing output phase voltages nearly close to sine-wave THD values under 5% for different regulator operation parameters.

The Declaration of Conflict of Interest/ Common Interest

No conflict of interest or common interest has been declared by the authors.

Authors' Contribution

The authors contributed equally to the study.

The Declaration of Ethics Committee Approval

The authors declare that this document does not require an ethics committee approval or any special permission.

Faruk YALÇIN, Felix HIMMELSTOSS

Boost Converter Based 3-Phase AC-AC Active Tracking Voltage Regulator Controlled by a Robust Hybrid C...

The Declaration of Research and Publication Ethics

The authors of the paper declare that they comply with the scientific, ethical and quotation rules of SAUJS in all processes of the paper and that they do not make any falsification on the data collected. In addition, they declare that Sakarya University Journal of Science and its editorial board have no responsibility for any ethical violations that may be encountered, and that this study has not been evaluated in any academic publication environment other than Sakarya University Journal of Science.

REFERENCES

A sample references list is given below;

[1] S. Subramanian and M. K. Mishra, "Interphase AC-AC topology for voltage sag supporter," IEEE Transactions on Power Electronics, vol. 25, no. 2, pp. 514–518, 2010.

[2] D. M. Lee, T. G. Habetler, R. G. Harley, T. L. Keister, and J. R. Rostron, "A voltage sag supporter utilizing a PWM-switched autotransformer," IEEE Transactions on Power Electronics, vol. 22, no. 2, pp. 626–635, 2007.

[3] K. Yamamoto, Y. Tsurusaki, S. Ehira, and M. Ikeda, "Suppression of compensation voltage pulsations for voltage sag/swell compensator utilizing single-phase matrix converter," 2015 18th International Conference on Electrical Machines and Systems, pp. 581–586, 2015.

[4] K. Yamamoto, S. Ehira, and M. Ikeda, "Synchronous frame control for voltage sag/swell compensator utilizing single-phase matrix converter," IEEJ Journal of Industry Applications, vol. 6, no. 6, pp. 353–361, 2017.

[5] L. R. Merchan-Villalba, J. M. Lozano-Garcia, J. G. Avina-Cervantes, H. J. Estrada-Garcia, A. Pizano-Martinez, and C. A. Carreno-Meneses, "Linearly decoupled control of a dynamic voltage restorer without energy storage," Mathematics, vol. 8, no. 10, article number: 1794, 2020.

[6] A. H. Soomro, A. S. Larik, M. A. Mahar, A. A. Sahito, and I. A. Sohu, "Simulation-based analysis of a dynamic voltage restorer under different voltage sags with the utilization of a PI controller," Engineering Technology & Applied Science Research, vol. 10, no. 4, pp. 5889–5895, 2020.

[7] K. Mikolajuk and A. Tobola, "Piecewise signals for the iterative control of the voltage conditioner," 2019 IEEE 20th International Conference on Computational Problems of Electrical Engineering, pp. 154–157, 2019.

[8] H. Hafezi, R. Faranda, and M. C. Falvo, "Single-phase dynamic voltage conditioner control under load variation," Proceedings of 2016 17th International Conference on Harmonics and Quality of Power, pp. 563–568, 2016.

[9] T. Shahsavarian, Y. Cao, E. Anagnostou, and R. Kalbfleisch, "Novel modulated equivalent model of point-to-point LCC-based high voltage AC/DC/AC system for geomagnetic storm-induced unbalanced harmonic studies," International Journal of Electrical Power & Energy Systems, vol. 122, article number: 106173, 2020.

[10] A. E. L. Da Costa, N. Rocha, C. B. Jacobina, and E. L. L. Fabricio, "Single-phase AC-DC-AC three-level three-leg converter with reduced switch count," IEEE Transactions on Power Electronics, vol. 35, no. 3, pp. 2295–2307, 2020.

[11] B. Triyono, M. Y. Fauzan, Soedibyo, and M. Ashari, "Filter design of PWM AC chopper on soft starting application 3 phase induction motors," 2016 1st International Seminar on Application for Technology of Information and Communication: Science and Technology for a Better Future, pp. 285–289, 2016.

Faruk YALÇIN, Felix HIMMELSTOSS

Boost Converter Based 3-Phase AC-AC Active Tracking Voltage Regulator Controlled by a Robust Hybrid C...

[12] U. A. Khan, A. A. Khan, H. Cha, H. G. Kim, J. Kim, and J. W. Baek, "Dual-buck AC-AC converter with inverting and non-inverting operations," IEEE Transactions on Power Electronics, vol. 33, no. 11, pp. 9432–9443, 2018.

[13] J. G. Wang and R. McMahon, "Highly reliable and efficient voltage optimizer based on direct PWM AC-AC buck converter," IEEE Transactions on Energy Conversion, vol. 35, no. 4, pp. 1897–1906, 2020.

[14] A. Kumar, R. Raman, D. Sarkar, P. K. Sadhu, and A. Banerjee, "Improvement in performance of induction heating system using direct AC-AC boost converter," 2018 2nd International Conference pn Power, Energy and Environment: Towards Smart Technology, 2018.

[15] H. Sarnago, O. Lucia, A. Mediano, and J. M. Burdio, "Direct AC-AC resonant boost converter for efficient domestic induction heating applications," IEEE Transactions on Power Electronics, vol. 29, no. 3, pp. 1128–1139, 2014.

[16] A. A. Khan, H. Cha, and H. F. Ahmed, "High efficiency buck and boost type AC-AC converters," 2015 17th European Conference on Power Electronics and Applications, 2015.

[17] A. Chakraborty, A. Chakrabarti, and P. K. Sadhu, "Analysis of a full-bridge direct AC-AC boost converter based domestic induction heater," Revue Roumaine Des Sciences Techniques - Serie Electrotechnique Et Energetique, vol. 64, no. 3, pp. 223–228, 2019.

[18] H. F. Ahmed, M. S. El Moursi, H. Y. Cha, K. Al Hosani, and B. Zahawi, "A reliable single-phase bipolar buck-boost direct PWM AC-AC converter with continuous input/output currents," IEEE Transactions on Industrial Electronics, vol. 67, no. 12, pp. 10253–10265, 2020.

[19] M. Zhou, Y. Sun, M. Su, X. Li, F. L. Liu, and Y. L. Liu, "A single-phase buck-boost AC-AC converter with three legs," Journal of Electrical Engineering & Technology, vol. 13, no. 2, pp. 838–848, 2018.

[20] F. Yalcin, "A novel buck converter based three-phase inverter with feedforward supported closed-loop control," Electric Power Components and Systems, vol. 48, no. 14-15, pp. 1445–1463, 2020.

[21] F. Himmelstoss, "Aktive Netzfilter," Austrian Patent, patent no: AT 505460 B1, filed 10 July 2007, applied 15 January 2012.

Title: Laboratory Experiments on Performance Evaluation of Geocomposite Drainage Materials

Authors: Ayşe ÖZDOĞAN DÖLÇEK

Laboratory Experiments on Performance Evaluation of Geocomposite Drainage Materials

Ayşe ÖZDOĞAN DÖLÇEK*[1]

Abstract

Method of geocomposite drainage systems (GCDs) is relatively new and has been used as an alternative drainage system for geotechnical applications. The advantages of this system are cost- and time efficiency, environmentally sustainable, and at the same time, having comparable or higher drainage capability compared to current practices. However, the geocomposite materials, which are the main products of the GCD systems, need to meet certain criteria that are required for the sufficient drainage systems. These criteria are mainly related to their hydraulic and mechanical parameters that control the drainage capacity and durability of the systems during/after the construction. In this study, laboratory testing and evaluation of five different commercially available geocomposite products are conducted to improve the understanding of their physical, hydraulic and mechanical properties. Physical properties are defined by measuring their thicknesses and apparent opening sizes. Hydraulic parameters; permittivity (volumetric flow rate of water in normal direction) under various hydraulic head was measured using a constant-head equipment. Additional transmissivity and flow rate are defined under various hydraulic gradient and normal compressive stresses using in-plane flow rate testing apparatus. A number of strength testing; compressive strength, grab tensile strength, elongations, trapezoidal and puncture strength are conducted to evaluate the mechanical behavior of the geocomposite products. Results show that the parameters defined for each product are in the same order of magnitude in corresponding testing program, yet some differences are observed when compared with the manufacturer values. The reason of differences and recommendations on the selection of standard testing methods are discussed. Use of a factor of safety (FS) was suggested in the design of geocomposite drainage system when selecting the geocomposite materials.

Keywords: Geocomposite drain materials, gecomposite drainage systems (GCDs), earth retaining structures, geotextile

1. INTRODUCTION

A main reason for failures of earth retaining walls is related to drainage [1-5]. Most retaining wall failures occur after heavy rainfalls due to surface infiltration or rise of groundwater level. Poor drainage system behind abutment and retaining walls will allow the water built-up behind the wall, thus increasing the hydrostatic pressures that will apply a tremendous amount of additional force on the walls. This reduces soil strength that can lead to catastrophic failure such as soil

* Corresponding author: aodolcek@balikesir.edu.tr
[1] Balıkesir University, Faculty of Engineering, Department of Geology Engineering
ORCID: https://orcid.org/0000-0001-9740-2273

collapse or erosion. These conditions therefore can result in damage of the abutment and retaining walls and can cause damage or settlement at locations adjacent to these walls, such as at the approach slabs and expansion and contraction joints. To prevent such damage, it is crucial to have a proper drainage system that permits water away from behind the abutment and retaining walls. A typical retaining wall structures with drainage components are shown in Fig.1.

A proper drainage system must perform the following two functions: 1) to relieve the hydrostatic pressure by allowing water to flow freely throughout the life of the structure, and 2) to prevent settlement by retaining the soil backfill and preventing the migration of soil particles [6]. For the proper drainage systems, geocomposite drainage material should meet the retention, permeability and clogging resistant criteria to perform these function properly [7]. Based on previous drainage application in the design of earth retaining structures, three different drainage method is currently utilized by USA transportation agencies (1) porous backfill around drainage pipe (Figure 2a), (2) porous backfill with filter fabric (geotextile) (Figure 2b), and (3) a geocomposite drainage system along the wall face (Figure 2c) [7].

The first method of porous backfill around drainage pipe requires high-quality graded porous materials that is predefined by the department of transportation agency. However, not all state agency has a sufficient quality control to meet the drainage criteria that prevent the drainage pipes from soil plugging during the construction. The method of porous backfill with geotextile provides better retention and clogging resistance to the drainage systems in the long run [2]. Due to their comparable performance and cost advantages, geotextile have been used successfully to replace the graded porous material [6].

Besides these three drainage systems, there is conventional methods being used commonly for retaining wall drainage system. Drainage system contains weep holes that is drilled through the wall, which relieve hydrostatic pressure by creating a controlled seepage path through the wall. Another method uses perforated pipe behind the wall placed through the length of wall to control drainage. Using a cohesionless granular soil as backfill material is also another method allowing water to penetrate the soil to reach the drain or weep pipes rather than trapping in the structure [2, 6].

In general, the conventional porous backfill drainage system has been well performing except for the fact that it typically requires a high-quality porous material, skilled workers, and considerable time for installation. Thus, alternative drainage systems that are more cost- and time effective, durable, and at the same time, have comparable or superior drainage capability compared to current practice should be evaluated. This study introduces the GCD system that has been used as an alternative drainage method for abutments and retaining walls. Different commercially available geocomposites, which is the main product used in the design of GCD systems are presented.
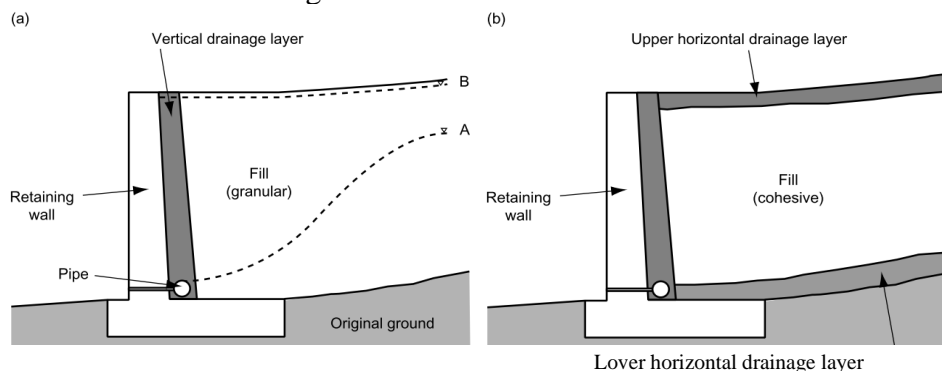
Figure 1 Schematically view of typical retaining wall structures: (a) a wall backfilled with granular resulting in vertical drainage, (b) a wall backfilled with fines resulting in horizontal drainage [2]
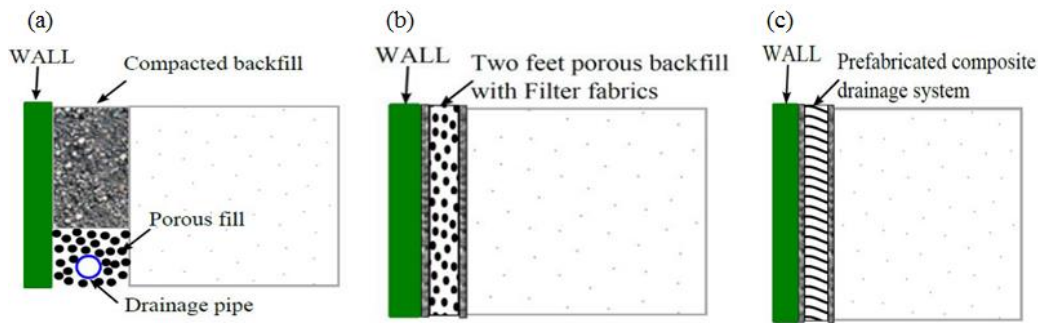
Figure 2 Different drainage methods: (a) porous backfill around drainage pipe, (b) porous backfill with geotextile, (c) geocomposite drainage system [5]

A number of laboratory experiments are conducted to define the drainage and strength properties required for selection of geocomposite materials and to improve the understanding of their functional use in drainage applications. Fig. 3a shows the product of geotextile used in this method. The method of geocomposite drainage (GCD) systems consist of a plastic drainage core bonded with geotextiles (Fig. 3b). Although the application of GCDs is relatively new, it has become increasingly accepted as an alternative drainage method for the structures due to its comparable performance, lower cost, consistent properties, and ease of placement.

1.1. Geocomposite Drainage Systems (GCDs)

GCD systems are defined as the state-of-art application that has been used as an alternative drainage systems in many states in the USA. A detailed assesment of the use of GCD systems behind vertical retaining structures was first published in 1995 by the Geosynthetic Research Institute (GRI) [10]. Similarly, usage of GCDs by various state Department of Transportaions (DOTs) are later uptaded by PenDOT. The report by OhioODOT showed the most current GCDs applications and their spesifications for the states where the GCDs are used [5].

Geocomposites are prefabricated product made by combining different geosynthetic materials including geotextile-geogrids, geotextile-geomembranes and geotextile with nonsynthetics materials (e.g. bentonite clay) which is called as geosynthetic clay liners. Other forms of

geocomposite materials are available in literature [11]. Geocomposites are composed of plastic drainage core that is bonded to a geotextile (Fig.3). They are capable of providing more than one function at the same time such as filtration, drainage, separation, barrier and protection. While geotextile filter is preventing soil migration into the drainage systems the drainage core is allowing water to flow. A schematic view of GCD system design and its functions are shown in Fig. 4. They are placed adjacent to foundations and behind retaining walls to mitigate any hydrostatic pressures beneath and behind these structures.

Drainage and strength properties of the geocomposite are the most important parameter for the successful drainage design. A previous study showed that 51% of retaining wall failures was from backfill soil (e.g. clay) used, and 33% of failures was due to insufficient drainage systems [12]. The case study presented the failue of retaining wall occured after heavy rain due to improper backfill soil and poor drainage systems used in the construction [13]. Fig.1 and 2 show the importance of backfill materials and drainage systems used when retaining wall is constructed [2]. To choose proper geocomposite materials for maximum drainage performance, physical, hydraulic and mechanical parameters should meet these requirements; (1) hydraulic requirements, (2) constructability requirements and (3) longevity (durability) requirements [5, 14, 15]. Therefore, a series of laboratory experiment on the hydraulic, mechanical and physical properties of the geocomposite are conducted to ensure that

the geocomposite drain meets those design criteria.

Aforementioned design criteria (retention, permeability, and clogging resistance) should be properly met and at the same time the strength and resilience to survive construction and survivability of the drainage system during life of the project must also met in the application of

geotextile and geocomposite drainage method [9]. Some states have developed specifications for the method of GCD systems design and construction, including those in California, Colorado, Indiana, Louisiana, Missouri, Nebraska, and New York [5].

Geotextile (a) woven, (b) non-woven, (c) knitted	
Geocomposite (a) sheet drain, (b) pipe combination drain	
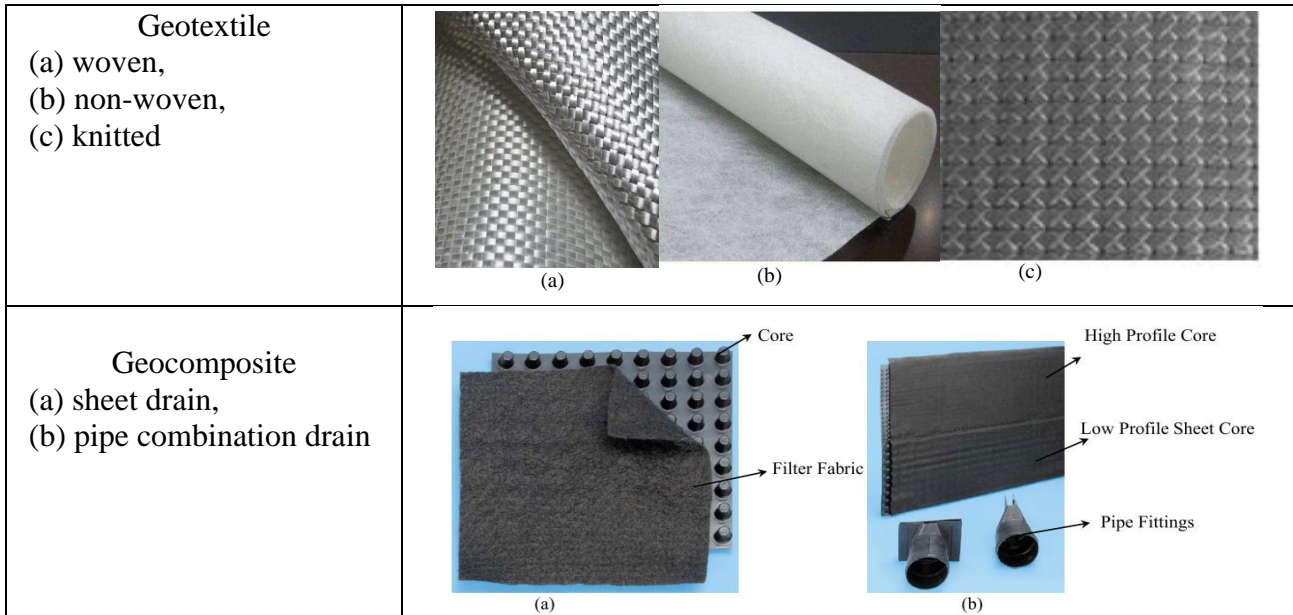
Figure 3 Types of geotextile: (a) woven, (b) nonwoven and (c) knitted and Geocomposite products: (a) sheet drain, (b) pipe drain
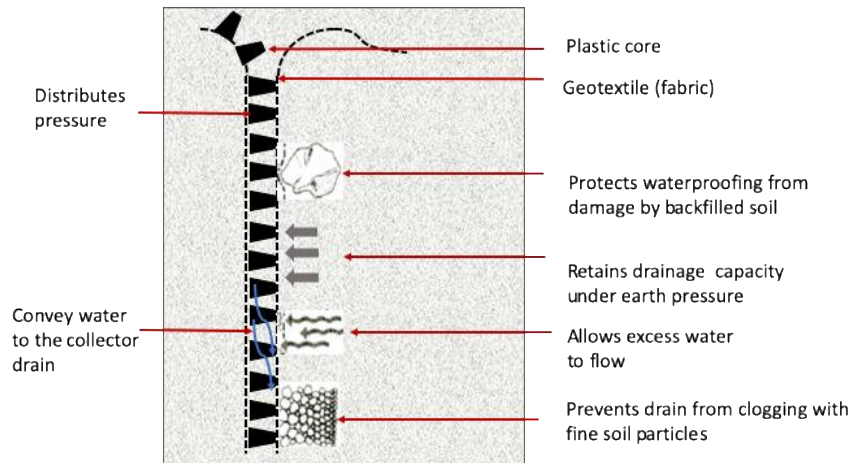
Figure 4 GCD system and its functions in the field (remodified from Maccaferri Geosynthetics [16])

2. MATERIALS AND METHODS

As discussed, the criteria for an efficient drainage system include permeability criteria for both the core and fabric as well as retention and clogging resistance criteria for the fabric. Additionally, the

system should have enough strength to survive during construction process and perform satisfactorily during its design life. Therefore, a series of laboratory experiment are conducted to

ensure that the geocomposite drain meets those design criteria. Details regarding to each testing procedures can be found in the study by [5].

2.1. Testing Materials

Five drainage geocomposite product were used for the laboratory experiments. All samples were shipped from different suppliers as composites with fabric bonded to the plastic core (Fig. 5). The basic physical features of the five products tested are listed for separate core and fabric in Table 1. The material properties listed in the manufacturer data sheets are for separate core and fabric. In order to compare the tested values with the ones

listed by the manufacturers, separate components were requested. However, only separate fabric materials for Products A, C and E were obtained. Since the bonded materials will actually be used in the field, direct testing with the bonded composites is more appropriate. This was particularly the case for the in-plane flow and compressive strength, where only bonded materials were used in this study. The laboratory tests were conducted at the University of Wisconsin-Madison (UW). The test results can be used for design and selection of proper geocomposite drainage systems, and they can also provide a measure for acceptance or rejection of commercial products.
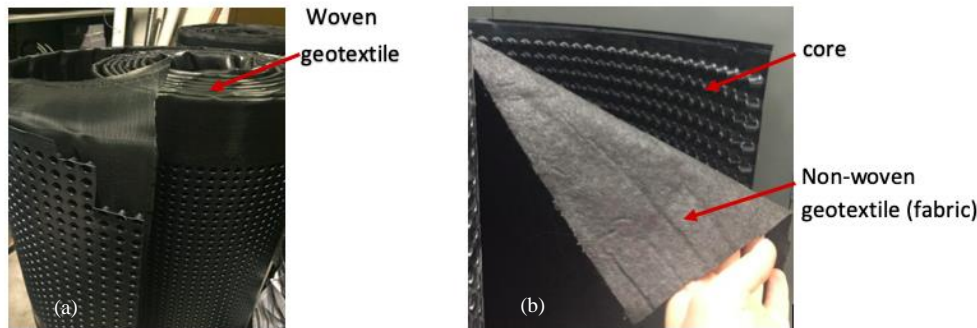
Figure 5 Types of geocomposites used in this study: (a) Woven, (b) non-woven (fabric)

Table 1
Tested products and corresponding material types for separate core and fabric

Products	Core Type	Fabric Type
A	Dimpled drainage core	Needle punched nonwoven
B	Dimpled drainage core	Woven Monofilament FW402
C	Dimpled polystyrene core	Needle punched nonwoven
D	Dimpled drainage core	Nonwoven filter fabric
E	Formed polystyrene core	Nonwoven filter fabric

2.2. Physical Properties of Geocomposite Drainage Materials

Two testing procedures was applied to define the physical properties of the geocomposites as follows:

Thickness measurement for the fabric and core: Nominal thickness of the geosynthetics was determined following ASTM D5199-12 [17] by measuring the distance between two parallel

surfaces of test specimens confined under specified normal stress (20 kPa or 2 kPa; Fig. 6). Thickness from manufacturer product sheet are defined for separate core and fabric, but thickness for both composite and separate products were measured in this study. Table 2 summarizes the results that the tested average composite thicknesses under two different levels of normal stress were very close to each other. For the separate core, three samples were received, and the tested thicknesses were slightly less than the values reported by the manufacturer.

Apparent opening size of fabric (AOS): AOS indicates the largest particle that would effectively pass through the geotextile (fabric) and determines the ability of geotextile to retain soil particles. Tests were conducted following ASTM D 4751-12 [18]. Five replicate circular specimens were cut to fit in a sieve (20 cm in diameter) along a diagonal line on the fabric rolls. Specimens were placed in a sieve frame and size-fractioned glass beads were placed on the geotextile surface. Using a mechanical sieve shaker, the specimen and frame were shaken laterally for 15 minutes such that the jarring motion induced the beads to pass through the specimen (Fig. 7). Table 3 summarizes the results.

Figure 6 Testing equipment for geocomposite thickness measuremen
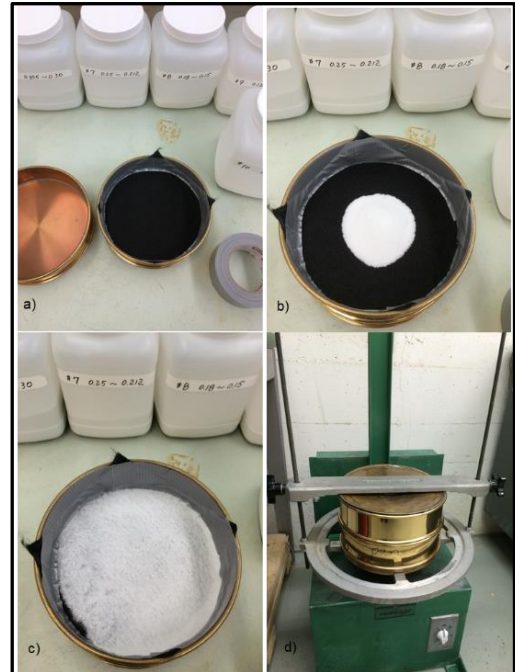
Figure 7 Apparatus for apparent opening size: (a) specimen placed in sieve, (b and c) specimen with glass beads, (d) mechanical sieve shaker

Table 2
Thickness of the composite and separate fabric and core, comparison with manufacturer value

Products	Fabric[1]	Core		Composite		Difference (tested vs. manufac.) %
	Tested (Avg) (mm)	Tested (Avg) (mm)	Manufacturer value (mm)	Tested (Avg.) mm		Core
				at 2 kPa	at 20 kPa	
A	1.21	10.5	11	11	11.2	-4.6
B	0.68	9.3	10.2	10	10	-8.8
C[2]	1.21	ND	10.2	10	10.4	ND
D[2]	ND	ND	10.2	11	11	ND
E	1.06	10	11	11	11	-9.1

[1] No fabric thickness was defined in the manufacturer data. [2] No separate core samples were obtained
ND=not determined

Table 3
Comparison of AOS to manufacturer value

Products	Tested Avg. mm (US Sieve)	Manufac. Value, mm (US Sieve)	Difference (tested vs. manufac.) %
A	0.32 (50)	0.212 (70)	51
B	ND	0.43 (40)	ND
C	0.33 (50)	0.212 (70)	56

| D | 0.42 (40) | 0.425 (40) | -1.2 |
| E | 0.36 (50) | 0.212 (70) | 70 |

ND= Not determined

2.3. Hydraulic Properties of Geocomposite drainage materials

Main function of the geocomposite products is drainage. In this testing program, permittivity and flow rate in normal direction to fabric of the geocomposite products, and transmissivity or in-plane flow rate of the geocomposite (fabric+core) are conducted to evaluate the hydraulic behavior of each products.

Permittivity and flow rate: The permittivity of separated fabric samples was measured using constant head test procedures following ASTM D4491-99a [19] (Fig. 8a). However, most products have both the permittivity and flow rate values listed on the manufacturer data sheet. Permittivity (Ψ) is the volumetric flow rate of water per unit cross-sectional area per unit head under laminar flow conditions, in the normal direction through a geotextile (fabric) as follows:

$$\Psi = \frac{Q}{A\Delta h} \tag{1}$$

Where ψ is permittivity (sec^{-1}), Q is flow rate of water passed through specimen (cm^3/s), Δh is the measured hydraulic head loss across the specimen (cm), and A is area of the specimen perpendicular to the direction of flow (cm^2). Four products (Products A, B, C and E) were tested for permittivity and flow rate. Four replicate specimens with 5.1 cm in diameter were taken diagonally from a 1-m long section of each full-width fabric roll (Fig. 8b). Hydraulic head was maintained in the range from 10 mm to 75 mm and five readings of flow rate were obtained at each hydraulic head. Head was increased by 5 mm after every five readings. These data were used to define the region of laminar flow for each specimen.

In-plane flow rate: This test was conducted to measure the flow rate per unit width within the manufactured plane of geosynthetics under varying normal compressive stresses and a constant head under the guidance of ASTM

D4716/D4716M-14 [20]. The flow rate per unit width was determined by measuring the quantity of water that passes through a test specimen in a specific time interval. Figure 9 shows the constant head (in-plane) flow rate testing device used for this test. Following equation was used to calculate the in-plane flow rate:

$$q = \frac{Q_t}{t\,W} \tag{2}$$

Where q is the flow rate per unit width, m^3/s-m [gpm/ft], Q_t is a measured quantity of water collected during collection time t [s], and W is width of specimen [0.304 m or 1 ft]. Hydraulic transmissivity, which is the volumetric flow rate per unit width of specimen per unit gradient in a direction parallel to the plane of the specimen was calculated from:

$$\theta = \frac{Q_t\,L}{WH} \tag{3}$$

Where θ is the hydraulic transmissivity [m^2/s] Q_t is a measured quantity of fluid discharged per unit time [m^3/s] L is the length of specimen subjected to the normal load [m], W is the width of the specimen [m], and H is the head difference. A number of specimens from each products were cut in size of 30.5 by 35.5 cm from the roll in two directions; parallel to machine direction (MD) and cross to machine direction (CD) as shown in Fig. 9.

Tested value defined herein in the lab or the value listed by the manufacturer is the ultimate transmissivity value. For field application, reduction factors should be applied to calculate the allowable transmissivity because the drainage capacity can decrease due to various reasons such as infiltration of the fabric into core space [21,5].

Geotextile intrusion occurs under the confining pressure resulting from weight of the soil backfill material. According to ASTM D4716 [20], for index testing, the contact surfaces in the construction should be prescribed by the material specification. In the absence of a specification, rigid sub and superstrates can be used to minimize

the variables impacting the test results. In this study only a rigid platen was used. Thus, effects of fabric intrusion on in-plane flow rate was evaluated. The specimen seating period under the applied load was selected as 0.25 h. Additionally, to see the time dependent structural instability of

the specimen seating period of 100 hour was used. Testing was performed at various hydraulic gradients of 0.1, 0.5 and 1.0 with normal compressive stresses of 35, 96 and 172 kPa. Test was conducted on fully saturated specimen with standard room temperature.
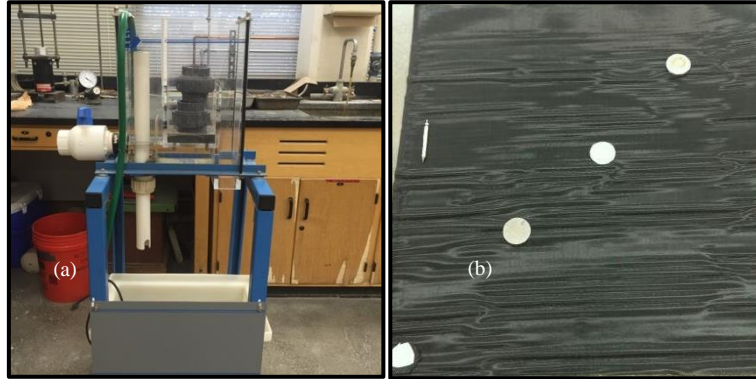
Figure 8 (a) Constant-head permittivity apparatus; (b) example locations of specimens sampled from fabric roll
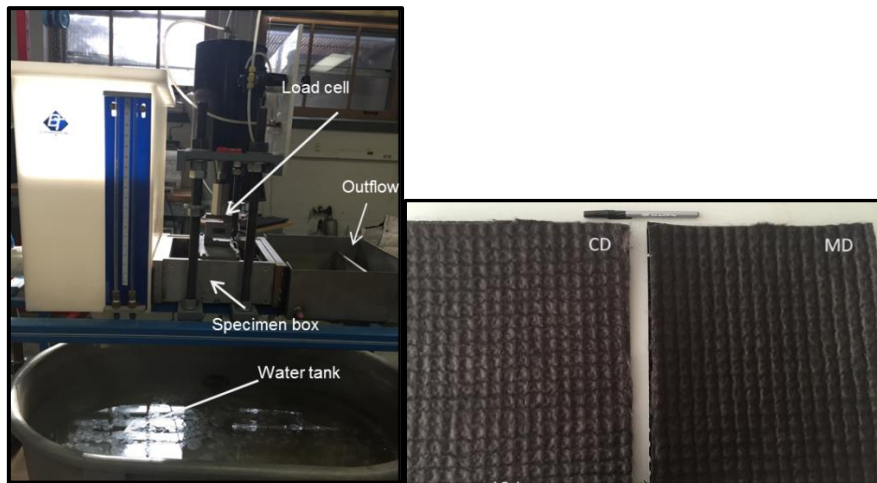
Figure 9 (a) Constant head (in-plane) flow rate testing device; (b) specimen cut into two directions and used for in-plane flow rate test

2.4. Mechanical Properties of Geocomposite Drainage Materials

Geocomposite drainage material should meet the strength criteria for an adequate lifelong drainage system design. To investigate the strength performance of the geocomposites used in this study, strength parameters for separate core and fabric are defined using the testing methods of compressive strength, grab tensile strength and elongation, trapezoidal tear strength, and puncture strength testing as follows.

Compressive strength of the core: This test method is used to determine the compressive properties of the geocomposite products under compressive loads according to ASTM D1621-10 [22]. Typical soil compression testing equipment by GeoTac was used (Fig. 10a). Compressive load and a displacement during test were accurately recorded using load measurement system, and a linear variable differential transformer (LVDT) displacement transducer, respectively. Five square specimens for each geosynthetic product (fabric + core) were prepared within a size of 10

by 10 cm (Fig. 10b). Load was applied with the rate of crosshead displacement of 0.25 mm/min.

Grab tensile strength and elongation of the fabric: Tests were performed according to ASTM Standard D4632/D4632M-15a [23] to quantify breaking load (grab strength) and elongation (grab elongation) of fabric samples separated from the composite fabric. A tension testing machine was used to perform the grab tensile/elongation tests (Fig. 11). Tests were conducted on dry samples at room temperature. The length of the specimen between the clamps at the start of test was set to 7.6 cm. Displacement rate was 30.5 cm/min.

Trapezoidal tear strength of the fabric: Tests were conducted according to ASTM D4533/D4533M-15 [24] to measure the force required to continue to propagate a tear in woven and non-woven geotextiles using the trapezoidal method. Apparatus and specimen preparation were the same as the grab tensile strength test described in the previous section. Tests were conducted on dry samples at room temperature. The length of the specimen between the clamps at the start of test was 2.5 cm and the machine was operated at a displacement rate of 30.5 cm/min.

Puncture strength of fabric: There are two different standards specified to define the puncture strength: ASTM D4833 [25] "Standard Test Method for Index Puncture Resistance of Geomembranes and Related Products" or ASTM D6241 [26] "Standard Test Method for Measuring the Damage Resistance of a Fiber-Reinforced Polymer-Matrix Composite to a Concentrated Quasi-Static Indentation Force." While ASTM D4833 [25] was used in this study, some of the manufacturers used ASTM D6241 [26].

Fabric samples were cut into a diameter of 10 cm and clamped without tension between circular plates of a ring clamp attachment secured in a compressive loading machine (Fig. 12).
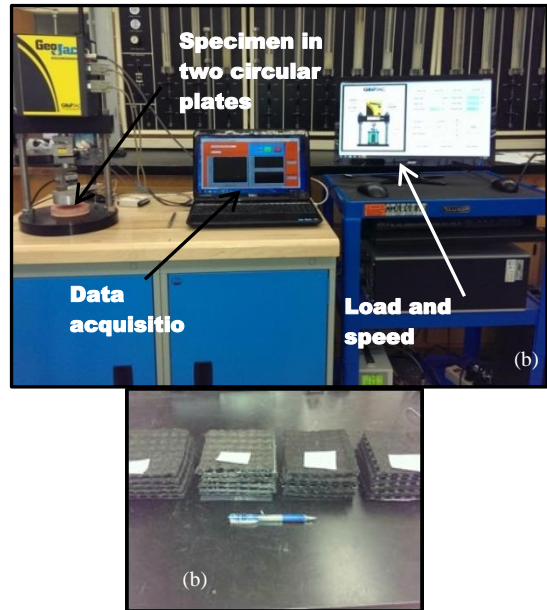
Figure 10 (a) Apparatus for measuring compressive strength of composite geosynthetics (bonded fabric and core); (b) five replicate specimens sampled with dimensions of 10 cm x 10 cm
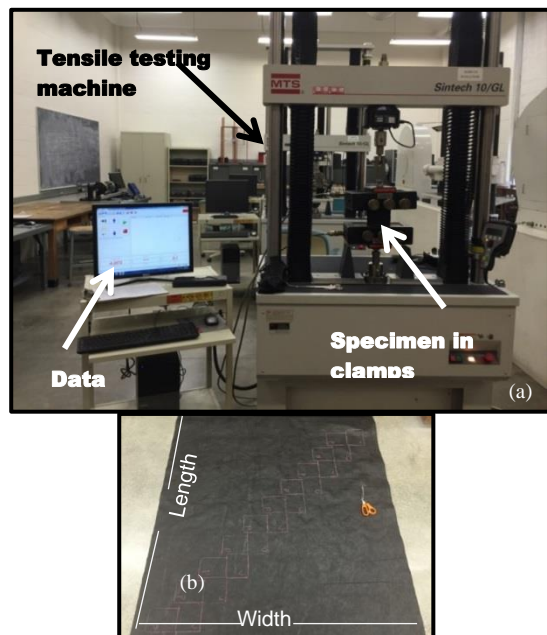
Figure 11 (a) Tensile testing machine used for grab strength and elongation tests; (b) specimens were obtained along a diagonal line across the entire width of the fabric roll and in the machine direction (MD) and cross machine direction (CD)

Force was applied with a solid steel rod and recorded with a load indicator until rupture of the specimen occurred. The maximum force was recorded as puncture strength of the specimen. Tested strength using ASTM D4833 [25] is also

called *pin puncture strength*. However, manufacturer values for puncture resistance values are defined using ASTM D6241 [26] is also called *CBR puncture strength*.

There is a correlation between the pin and CBR puncture strengths, considering different geotextile types and test conditions [27]. For nonwoven geotextile under common test conditions (using constant rates of compression of 300 mm/min and 50 mm/min for pin and CBR tests, respectively), the following equation can be used to estimate the CBR puncture strength for nonwoven geotextiles:

$$\text{Strength}_{\text{CBR,estimated}} = 5.27 \times \text{Strength}_{\text{pin,measured}}$$
(4)

The tested strength using ASTM D4833 [25] were converted to CBR puncture strength for nonwoven products (A, C, and D) used in this study.
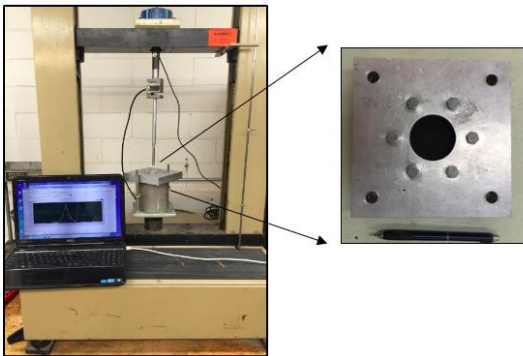
Figure 12 Testing equipment for puncture strength testing

3. RESULTS AND DISCUSSIONS

3.1. Results of Hydraulic Properties of Geocomposite Products

Results of permittivity: Permittivity and flow rate measured with the varying hydraulic head was plotted in Fig. 13. As expected permittivity decreases and flow rate increases with increased head values. Each measurement was confirmed based on the regime of laminar flow defined from the plot of volumetric flow rate versus head as described in ASTM D4491 [19]. Average permittivity value of five readings set at the head

of 50 mm was summarized in Table 4. All nonwoven textiles (Products A, C and D) showed lower permittivity than the manufacturer values. Product B has the highest permittivity and flow rate in both tested and manufacturer case. That can be attributed to the fabric type, which is the only sample being woven, and having a highest apparent opening size of 0.43 mm.

Results of in-plane flow rate: Results are presented in three different sections according to effects of fabric intrusion, normal stresses, and time period used for the specimen seating period (short term for 0.25 h and time depended for 100 h) on in-plane flow rate and transmissivity.

Effects of fabric intrusion: Results shows that the existence of the fabric in the specimen tends to reduce the in-plane flow rate significantly in Table 5. In this tested case, the reduction is about 42%. This is caused by the fact that the fabric on the core would go into the part of the clearance space of the core due to the load applied during the test. For the core alone, the tested value was comparable (slightly larger in this case) to the manufacturer value.

Effects of normal stress: The results of in-plane flow rate and transmissivity for the five products (tested on core only) under three levels of hydraulic gradients (i.e., 0.1, 0.5, and 1) and three levels of normal stresses (i.e., 35 kPa, 96 kPa and 172 kPa) are plotted in Fig.14 and 15. It is clear that flow rate nearly linearly increases and transmissivity decreases with increasing hydraulic gradient but not significant change seen with the tested stress levels, which shows that the stress levels used are not sufficient to deform the core. That is similar to previous study showing no structural and hydraulic change occurred up to the compressive stress of 200 kPa [28].

Effects of seating period (creep): For each product, both short-term and long-term in-plane flow rates were tested. The short-term test was conducted with a seating period of 0.25 hours (15 minutes), while the long-term test was conducted with a seating period of 100 hours. This test was conducted to determine if the product shows any performance degradation (creep) with time. Variation of flow rate (in-plane) and

transmissivity values in various gradient under different normal stresses for short term and long term are plotted in Fig.14 and Fig. 15, respectively. Table 6 summarizes the results that there were no significant differences between the flow rates for the seating periods of 0.25 hours and 100 hours for

Products A, B and E, which showed no deformation or creep under the test loading. Most of the tested products actually showed a higher flow rate for the longer seating period, a result that was not expected. In particular, the flow rates

for Products C and D were not well matched for the 0.25- hour and 100-hour seating periods. The flow rates increased by 42% and 9% for Products C and D, respectively, under a normal stress of 3,600 psf (172 kPa) and a hydraulic gradient of 1.0. These results can be attributed to the measurement uncertainty, as it is certain that all testing procedures were conducted under the same conditions, and no problems were encountered during the tests. However, results from longer seating period are more consistent and closer the manufacturer values than the short term period.
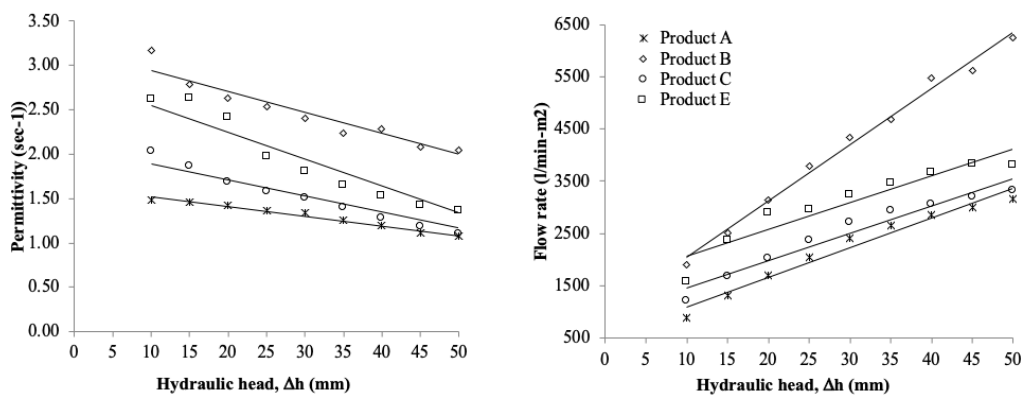
Figure 13 Permittivity and flow rate of geocomposites at various hydraulic gradient

Table 4
Comparison of permittivity and flow rate to the manufacturer value

Products	Tested		Manufac. Values		Difference (tested vs. manufac.)	
	Permittivity sec^{-1}	Flow rate l/min/m^2	Permittivity sec^{-1}	Flow rate l/min/m^2	Permittivity %	Flow Rate %
A	1.08	3233	1.5	4481	-28	-27.9
B	2.04	6124	2.1	5904	-2.86	3.7
C	1.08	3233	1.5	4481	-28	-27.9
D	ND	ND	NA	5700	ND	ND
E	1.4	4074	1.8	4483	-22.2	-9.12

ND= Not determined;NA= Not applicable

Table 5
Effect of fabric (geotextile) inclusion on the in-plane flow rate of Product A

Products	In-Plane Flow rate (l/min/m)			
	Tested (core+fabric)	Tested (core only)	Difference %	Manufac. Val. (core)
A	180	308	42	282

Table 6
Effects of seating period on in-plain flow rate

| Products | In-Plane Flow rate (l/min/m) | | | |
| | Tested (core+fabric) | | | Manufac. Val. (core) |
	Short Term 15 min	Long Term 100 hr	Difference %	
A	180.22	185.42	3	281.93
B	217.45	224.62	3	260.82
C	181.42	207.39	13	211.14
D	179.84	195.93	8	223.56
E	217.85	214.66	-1	260.82
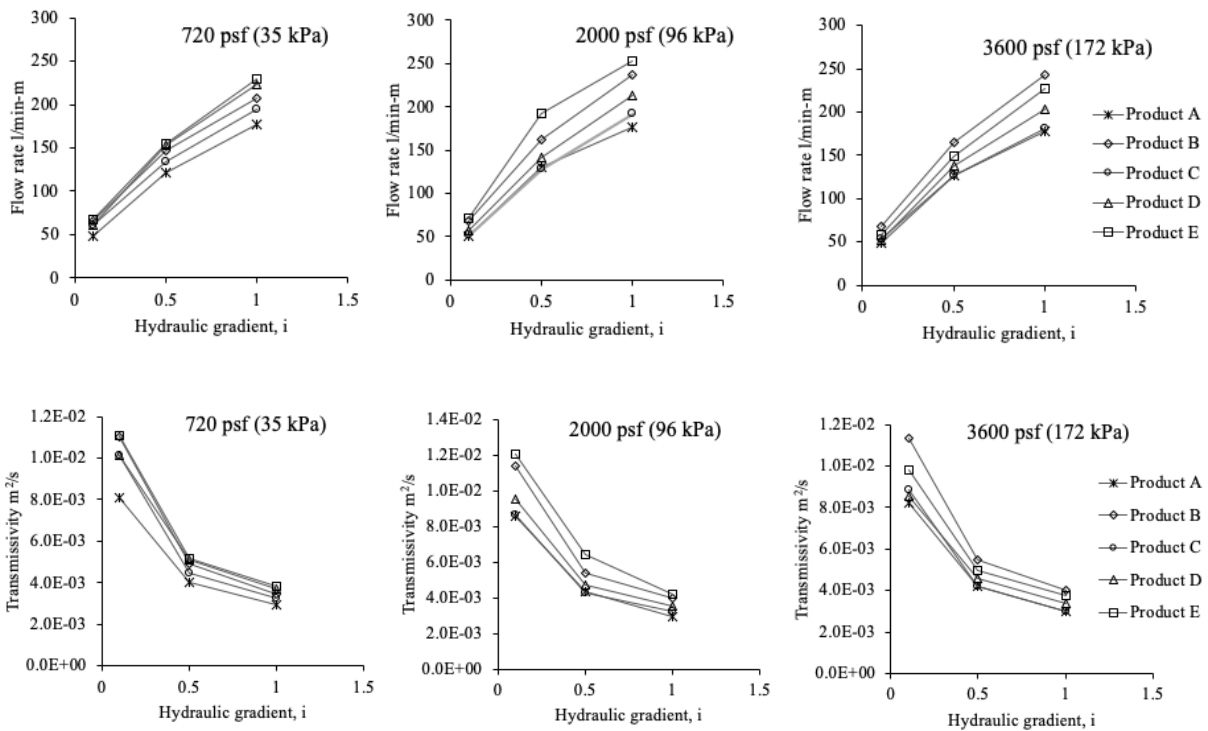
Figure 14 Short term in-plane flow rate (top) and transmissivity (bottom) at the hydraulic gradient of 0.1, 0.5 and 1 under three different normal stresses
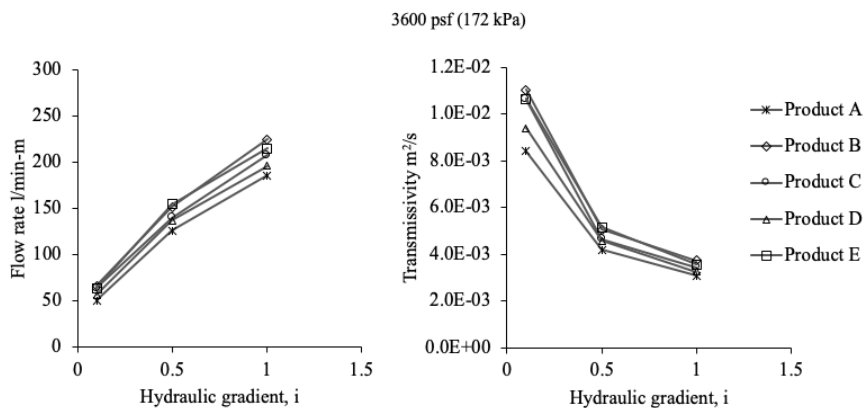
Figure 15 Long term in-plane flow rate and transmissivity for hydraulic gradients of 0.1, 0.5, 1 under a normal stress of 3600 psf (172 kPa)

3.2. Results of Strength Properties of the Geocomposite

All strength parameters defined in the laboratory are summarized in Table 7. The maximum average compressive strengths of five geosynthetics products (fabric + core) and the values from manufacturer (core only) are summarized in the first column in Table 10. The tested compressive strength values for the composite (fabric+core) deviate from the manufacturer values for the core alone. The differences vary from -25.5% to +12.6%. For four of the five tested products, the tested values were lower than the manufacturer values. Possible reasons could be: 1) the manufacturers typically report the strength of the core only; 2) the tests were performed using a single layer of the composite, which has a thickness less than 1 in (2.54 cm) minimum thickness requirement by ASTM D1621 [22]; and 3) a loading rate of 0.1 in (0.254 cm)/min was used, which was a relatively high loading rate for a sample that is thinner than 1 in. Note that the tested products in this study were about 0.4 in (1 cm) in thickness. ASTM D6364 [29] is designed specifically for geosynthetics, and it requires the specimen to be tested at a strain rate of 10% of the nominal thickness per minute or 1 mm/min (0.04 in/min), whichever is greater. Theoretically, ASTM D6364 [29] is more suitable for geocomposite drains. But to be consistent with the manufacturers' tests, ASTM D1621 [22] is followed in this study. It is recommended, however, that ASTM D6364 [29] should be adopted in future testing plan.

For grab tensile and elongation parameters, three products (Products A, C and E) were tested. Two of them (Products A and C) showed higher tested values in the weaker principle direction as compared to the manufacturer values. They also exhibited larger apparent elongation at the breaking load. For trapezoidal strength parameters, three products (Products A, C and E) were tested. The average value of 8 set of tested strength parameters are reported. Two of them (Products A and C) showed higher tested values as compared to the manufacturer values. The trapezoidal tear strength for Product E was not listed in the manufacturer data sheet, so no comparison was done. For puncture strength parameters, the CBR puncture strengths were estimated using the pin puncture strengths using Eq. 4 for nonwoven products (A, C and D). They show higher tested values compared to the manufacturer values. Product D is significantly higher (47%) than the manufacturer value. Product E showed a lower value in the test as compared to the value listed by the manufacturer.

4. CONCLUSIONS

Five geocomposite drain products from different vendors were acquired for index property testing in the laboratory. Physical, hydraulic and strength properties of these geocomposites were tested according to the corresponding ASTM standards. Regarding to the physical properties, thickness for the core and fabric and apparent opening size (AOS) of the products were defined. The tested average composite thicknesses under two different levels of normal stress were very close to each other. For the separate core, three samples were received, and the tested thicknesses were slightly lower than the manufacture values. The thickness of a core is an indirect indicator for the drainage capacity. For every tested product, the tested AOS was significantly larger than the listed value.

The hydraulic parameters were defined from the permittivity and the in-plane flow rate testing for the fabric and core were conducted. All nonwoven products showed lower tested permittivity than the listed values. Since the permittivity and flow rate of a geotextile product are correlated and the permittivity is a value normalized by the differential head across the fabric, it is also recommended to use permittivity, instead of the flow rate, in the specification. Regarding the in-plane flow of the core, it was observed that the presence of fabric tends to reduce the in-plane flow rate significantly. In this tested case, the reduction is about 42%. There were no significant differences between the flow rates for the seating periods of 0.25 hours and 100 hours under the normal stresses levels used in this study. In-plane flow increases nearly linearly with hydraulic gradient but does not change much with

the tested normal stress levels, which are not sufficient to significantly deform the core. Compared to the manufacturer-listed values, the tested in-plane flows fall short for all products when the fabric is bonded. When tested using the core only, the tested value exceeded the listed value. Testing the products as a composite (fabric+core) are more suitable as it performs in the field as fabric bounded geocomposites.

Regarding the compressive strength, the tested values for the composite deviated from the manufacturer values for the core alone. The differences varied from –25.5% to +12.6%. For four of the five tested products, the tested values were lower than the manufacturer values. It was later realized that this result may due to the testing method and conditions used. It is recommended that ASTM D6364 [29] "Standard Test Method for Determining Short- Term Compression Behavior of Geosynthetics" be used to test the compressive strength of PCDS, in place of ASTM D1621 [22].

Regarding the puncture strength properties of the fabric, only one product showed significantly higher values than the manufacturer values among the three products tested. It was found that different manufacturers test the puncture strength

of the fabric using different ASTM standards. ASTM D6241 [26] is actually more suitable than ASTM D4833 [25] for geotextile materials.

The differences observed between the tested and listed values in most cases could suggest use of a factor of safety (FS) in the design of geocomposite drainage system when selecting the geocomposite materials. Based on the differences, a proposed FS of 3 could be reasonable.

Table 7
The summary of results for the strength parameters and comparison with manufacturer values

Products	Compressive Strength kPa			Grab Tensile Strength N			Elongation %			Trapezoidal Tear Strength N			Puncture Strength N			
	Measured value	Manufac. Value	Difference (measured vs. manufac.)	Measured value	Manufac. Value	Difference (measured vs. manufac.)	Measured value	Manufac. Value	Difference (measured vs. manufac.)	Measured value	Manufac. Value	Difference (measured vs. manufac.)	Measured value	Estimated CBR	Manufac. Value	Difference (measured vs. manufac.)
A	664	892	-25.6%	752	712	5.6%	50.2	50	0.4%	300	267	12.4%	398.7	2101.3	1824.5	15.2%
B	838	862	-2.8%	ND	NR	ND	ND	NR	ND	ND	NR	ND	ND	ND	3003.8	ND
C	674	718	-6.1%	752	712	5.6%	50.2	50	0.4%	300	267	12.4%	398.7	2101.3	1824.5	15.2%
D	809	718	12.7%	ND	NR	ND	ND	NR	ND	ND	NR	ND	309.3	1629.9	1112.5	46.5%
E	839	862	-2.7%	511	712	-28.2%	43.6	70	-37.7%	267	NR	ND	378.7	1995.7	400.5	-5.4%

ND= Not determined; NR= Not recorded

The Declaration of Conflict of Interest/ Common Interest

No conflict of interest or common interest has been declared by the authors.

Authors' Contribution

The author solemly performed the experimental work and wrote the manuscript.

The Declaration of Ethics Committee Approval

This study does not require ethics committee permission or any special permission.

The Declaration of Research and Publication Ethics

The authors of the paper declare that they comply with the scientific, ethical and quotation rules of SAUJS in all processes of the article and that they do not make any falsification on the data collected. In addition, they declare that Sakarya University Journal of Science and its editorial board have no responsibility for any ethical violations that may be encountered, and that this study has not been evaluated in any academic publication environment other than Sakarya University Journal of Science.

REFERENCES

[1] A. Bobet, "Guidelines for Use and Types of Retaining Devices", Purdue, IN, Prepared in Cooperation with the Indiana Department of Transportation and the U.S. Department of Transportation Federal Highway Administration, FHWA/IN/JTRP-2001/28, 2001.

[2] G. West, "Review of drainage behind retaining walls," TRL Report 483, 2001.

[3] H. Moayedi, A. Asadi, and B.Huat, "Effect of Embedding Drainage System on Retaining Wall Structure Stability," Electronic Journal of Engineering Geotechnical Engineering., vol. 16, pp. 157-163, January 2011. [Online]. Available: https://citeseerx.ist.psu.edu/IEEE Xplore, http://www.ieee.org. [Accessed June 28, 2021].

[4] A. Boeckmann and J. E. Loehr, "Design of Maintainable Drains for Earth Retaining Structures," Department of Civil and Environmental Engineering University of Missouri-Columbia MO, Part of DTRT13-G-UTC37, 2017.

[5] R. Liang, A. Ozdogan-Dolcek, and W. Likos, "Performance Comparison of Abutment and Retaining Wall Drainage Systems," 2017.

[6] R.D. Holtz, B.R. Christopher, and R.R.Berg, "Geosynthetics Design and Constraction Guidelines," DTFH61-93-C-00120, 1998.

[7] B.R. Christopher and G.R. Fischer, "Geotextile Filtration Principlas, Practices and Problems," *Geotextile and Geomembrane*, vol.11,pp. 337-353, 1992.

[8] D.White, S. Sritharan, M. Suleiman, M. Mekkawy, and S. Chetlur, "Identıfıcatıon of the Best Practices for Design, Constructıon, And Repair of Bridge Approaches, Iowa State University, TR 481, 2005.

[9] U.S. Army Corp of Engineers, "Engineering Use of Geotextile," Departments of The Army And The Air

Force, ARMY TM 5-818-8, 1995.

[10] R.F. Wilson-Fahmy and R.M. Koerner, "Experimental Behaviour of Polymeric Geogrids in Pullout," *Journal of Geotechnical Engineering,* vol. 120, pp. 661, 1995.

[11] A. Patel, *Geotechnical Investigations and Improvement of Ground Conditions.* Woodhead Publishing Series in Civil and Structural Engineering, 2019.

[12] US Army Corps of Engineers, *Retaining and flood walls*. New York: American Society of Civil Engineers Press, 1994.

[13] S. V Abhishek and V. Tarachand, "Case Study of Failure of Retaining Wall At Dwarakanagar , Visakhapatnam," 2013, no. December, pp. 1–4.

[14] H. R. Cedergren, *Seepage, Drainage, and Flow Nets,* Third Edit. New York: John Wiley & Sons, 1989.

[15] B. Christopher and A. Zhao, "Design Manual for Roadway Geocomposite Underdrain Systems, Contech Construction Product Inc. Clough," 2001.

[16] Online Available : https://geosynt.files.wordpress.com/2013/04/maccaferri.pdf) [Accessed June 25, 2021].

[17] ASTM- DESIGNATION: D5199 - 12 "Determination of Nominal Thickness of Geosynthetics" Annual Book of ASTM Standards.

[18] ASTM- DESIGNATION: D4751 "Standard Test Method for Determining Apparent Opening Size of Geotextile. " Annual Book of ASTM Standards.

[19] ASTM-DESIGNATION: D4491. "Standard Test Methods for Water Permeability of Geotextiles by Permittivity." Annual Book of ASTM Standards.

[20] ASTM- DESIGNATION: D4716 "Standard Test Method for Determining In-Plane flow Rate of Geosynthetics" Annual Book of ASTM Standards.

[21] A. Bamforth, "Interpretation of In-Plane Flow Capacity of Geocomposite Drainage by Tests to ISO 12958 with Soft Foam and ASTM D4716 with Various Natural Backfill," 2012.

[22] ASTM- DESIGNATION: D1621" Standard Test Method for Compressive Properties of Rigid Cellular Plastics" Annual Book of ASTM Standards.

[23] ASTM-DESIGNATION: D4632. " Standard Test Method for Grab Breaking Load and Elongation of Geotextile" Annual Book of ASTM Standards.

[24] ASTM-DESIGNATION: D4533 "Standard Test Method for Trepozoidal Tearing Strength of Geotextile" Annual Book of ASTM Standards.

[25] ASTM-DESIGNATION: D4833/D4833M "Standard Test Method for Index Puncture Resistance of Geomembrane and Related Products" Annual Book of ASTM Standards.

[26] ASTM-DESIGNATION: D6241 "Standart Test Method for CBR Puncture Strength Test of Geotextile" Annual Book of ASTM Standards.

[27] S. Van Dyke, "Comparison of California bearing ratio and pin puncture strength testing used in the evaluation of geotextiles," 2014.

[28] N. Yarahmadi, I. Gratchev, and D.-S. Jeng, "The Effect of Structural Configuration on Hydraulic Capacity of Geonet Drains Used in Landfills," *Electron. J. Geotech. Eng.*, vol. 22.15, no. 2, pp. 31-40., 2017.

Title: An Investigation of the Effect of Asymmetry on the Free Vibration Behavior of Sandwich Structure

Authors: Ufuk DEMİRCİOĞLU, Ali Suat YILDIZ, Mutlu Tarık ÇAKIR

An Investigation of the Effect of Asymmetry on the Free Vibration Behavior of Sandwich Structure

Ufuk DEMİRCİOĞLU*[1], Ali Suat YILDIZ[1], Mutlu Tarık ÇAKIR[1]

Abstract

This study presents a free vibration analysis of asymmetric sandwich structures comparatively. Sandwich structures were manufactured by the hand-layup vacuum bagging method. Symmetric and asymmetric sandwich structures were analyzed experimentally to evaluate the effect of asymmetry on the free vibration characteristic of sandwich structures. Free vibration analysis was performed by using VIBXPERT II under clamped-free boundary conditions. The frequency response function (FRF) is obtained from the modal test. Modal parameters of sandwich structures were obtained from analysis by curve fitting to FRF using Matlab. The effects of asymmetry on the natural frequency of the sandwich structures are investigated and results are comparatively presented. The finite element method (FEM) was also implemented by using COMSOL Multiphysics® for verifying the selected system parameters and analyzing the experimental results. By the experimental study the accuracy of the model being having proven, it also has potential for the investigations of vibration behavior of the various applications including asymmetric sandwich structures.

Keywords: Sandwich structure, asymmetric sandwich structure, free vibration analysis, modal analysis

1. INTRODUCTION

Sandwich structures have been used in a variety of applications from sports equipment to sport car components so far. Due to the properties they possess, their usage and application area is increasing day by day especially, in the aviation, marine and, defense industry. Conventional materials are being replaced with sandwich structures in applications where a high strength to weight ratio is desired. Sandwich structure is a sub-group of composite materials consisting of a thick core material on which single or two thin face sheets materials are based. In this configuration, core material increases the stiffness of sandwich structures and face sheet materials carry tensile and compressive loads. As a result of this configuration, sandwich structures have better properties than their monolithic components. Some advantages of sandwich structures are resistant to heat and acoustic, resistance to impact loading, excellent fatigue life, resistance to corrosion and moisture, invisibility to radar waves, and better

* Corresponding author: udemircioglu@sivas.edu.tr
[1] Sivas University of Science and Technology, Faculty of Engineering and Natural Sciences, Mechanical Engineering Department
E-mail: suat@sivas.edu.tr, tcakir@sivas.edu.tr
ORCID: https://orcid.org/0000-0002-9707-8271, https://orcid.org/0000-0001-6914-5222, https://orcid.org/0000-0002-0107-594X

aerodynamic surfaces. These benefits can be further improved by using the advantages of having a variety of constituent materials. By combining the best properties of constituent materials, desired physical and mechanical properties can be obtained in a sandwich structure.

Despite fact that sandwich structures possess many advantages over conventional materials, these materials have also some drawbacks. For example, sandwich structures are not used as fabricated. Since other components like cables may have to go through them, as a result, different shaped cutouts are opened. Therefore, cutouts are inevitable, and the presents of cutouts significantly affect the dynamic behavior of the sandwich structure. Because of tool structure interactions, delamination occurs around the cutouts. Also, due to service conditions and production error, delamination may occur at a different location and in a different size. Furthermore, some components have curved shapes like leading edges of the wing consequently, there is a need for fabrication with curvatures. These aforementioned problems cause the reduction in stiffness and subsequently reduce the natural frequencies of the sandwich structures. However, the effect of these features on the vibration behavior of sandwich structures is still actively studied in theoretical and practical aspects.

Many researchers have studied the free vibration of the curved sandwich structure. A.V. Singh studied the free vibration of a curved sandwich structure by using the Rayleigh-Ritz method [1]. W. Wang and R.A. Shenoi investigated the free vibration of the initially stressed curved sandwich structure theoretically [2]. K.M. Ahmed studied the free vibration of curved sandwich beams by using the finite element method [3]. T. Sakiyama investigated the free vibration of sandwich structure with the elastic and viscoelastic core by applying the Greens function [4]. They reported the effect of curvature on the vibration behavior of sandwich structures.

The effects of the cutout on the vibration behavior of sandwich structures have been studied by several researchers extensively. N. Mishra et al. investigated the effect of the rectangular central cutout on the vibration behavior of sandwich structure by using the finite element method [5]. H. K. Bhardwaj investigated the influence of triangular cutout on the free vibration behavior of laminated composite plates by using ANSYS APDL code [6]. S. Ramakrishna et al. investigated the vibration of laminated composite with circular cutout at the center utilizing the finite element method [7]. S. Chikkol Venkateshappa et al. investigated the free vibration behavior of composite plates with different shaped cutouts by experiment and finite element method [8]. H. K. Bhardwaj et al. investigated the effects of skew cutouts on the vibration of a laminated composite plate by using the finite element method [9]. S. Mondal et al. investigated the influence of cutouts at a different position on the dynamic characteristic of sandwich composite plate experimentally and numerically [10]. J. Vimal et al. studied the effect of a circular hole on the vibration behavior of functionally graded composite plate by using the finite element method utilizing ANSYS [11]. J. Vimal et al. studied the free vibration of sandwich structure with different cutouts by using the finite element method [12]. They presented the influence of cutouts on the vibration behavior of composite plates.

T. Tuswan et al. investigated the influence of debonding on sandwich structure's vibration responses of the damaged stern ramp of the ferry by using the finite element method [13]. V. N. Burlayenko and T. Sadowski studied the effect of delamination at skin/core of sandwich structure on the dynamic characteristic of a sandwich structure by finite element method using ABAQUS software [14]. H. Y. Kim and W. Hwang investigated the effect of delamination on natural frequencies of honeycomb sandwich structures experimentally [15]. H. Schwarts-Givli et al. studied the influence of delamination on the free vibration behavior of sandwich beam numerically [16]. B. Saraswathy et al. investigated the effects of multiple-debond with various debond lengths on the dynamic behavior honeycomb sandwich structure using the split beam theory and fast Fourier transform [17]. V. N. Burlayenko and T. Sadowski investigated the

dynamic behavior of sandwich structure having debond of different size and location by finite element method using ABAQUS software [18]. I. Jayatilake et al. investigated the influence of single-multiple debond at core/skin interface on free vibration behavior sandwich panel by using finite element method [19]. They presented the influence of delamination on the vibration behavior of composite plates.

New needs give rise to the development of new technology and demands of new materials. Asymmetric sandwich structure is one of them that came after a need which is called stealth technology [20]. Stealth is a technique that makes objects nearly invisible to radar or other detection systems. Asymmetric means that face sheet materials (FSM) are different as shown in figure 1. As a result, the configuration of asymmetry enables the sandwich structure to be utilized in stealth applications [21, 22]. Since stealth technology is mostly used in aviation in the defense industry where dynamic loadings are severe it is vitally important to characterize the dynamic behavior of an asymmetric sandwich structure. However, there is less study about the free vibration analysis of asymmetric sandwich structures in the literature. Therefore, the objective of this study is to investigate the significant influence of asymmetry on the free vibration characteristic of sandwich structure experimentally.
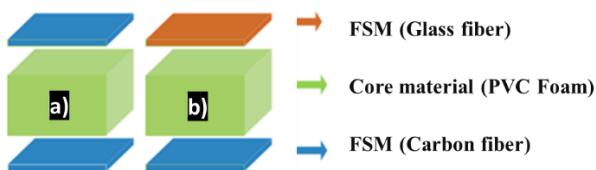
Figure 1 Configuration of sandwich structure a) Symmetric sandwich structure b) Asymmetric sandwich structure.

2. MATERIALS and METHODS

This study consists of fabrication and free vibration analysis of sandwich structures which is followed by experimental modal analysis and determining the influence of asymmetry on the free vibration behavior of a sandwich structure. The sandwich structures that were fabricated in

this study consist of 2x2 twill weave carbon fiber, 2x2 twill weave glass fiber fabrics, closed-cell rigid polyvinyl chloride (PCV) foam core, epoxy resin, and its hardener which were obtained from the market (Dost Kimya Inc.) were used. The properties of materials used in this study are given in Table 1. The sandwich structures were fabricated with the hand lay-up vacuum bagging method as shown in Figure 2. The matrix material was prepared considering the total weight of fabrics and foam core materials. And the weight ratio of the epoxy resin to its hardener was set to 100:40. The thickness of fabrics and foam is 0.26 mm and 10 mm respectively. The length and width of sandwich structures are 500 mm and 100 mm, respectively. As shown in Table 2 three different sandwich structures were prepared. Responses of sandwich structures were measured by using an impact hammer and accelerometer as shown in Figure 3. An accelerometer 3055D2 by Dytran (sensitivity 100 mV/g on the range 50 g) and dynapulse impact hammer were used in this study. The roving accelerometer procedure was selected for obtaining the FRF measurements. In this technique, the sandwich structure is divided into 40 nodes as shown in Figure 3. The external force was applied by the impact hammer at "Location 1" for each time while the measurements were taken from the rest of the location by VIBXPERT II. All signals were processed at 0.5 Hz resolution by using rectangular windowing at the frequency range of 0-700 Hz.

Table 1
Properties of all materials used in the study.

Property	Carbon Fiber Epoxy	Glass Fiber Epoxy	PVC Foam
Density (Kg/m³)	1440	2000	60
Young's Modulus E_x (Pa)	59.65x10⁹	2x10¹⁰	
Young's Modulus E_y (Pa)	59.65 x10⁹	2x10¹⁰	7 x10⁷
Young's Modulus E_z (Pa)	10.65 x10⁹	1x10¹⁰	
Poisson's Ratios v_{xy}	0.26	0.3	
Poisson's Ratios v_{yz}	0.26	0.4	0.3
Poisson's Ratios v_{zx}	0.26	0.3	

Modulus of Rigidity G_{xy} (Pa)	4×10^9	5×10^9	
Modulus of Rigidity G_{xz} (Pa)	4×10^9	3.84×10^9	2.69×10^7
Modulus of Rigidity G_{yz} (Pa)	3.3×10^9	5×10^9	
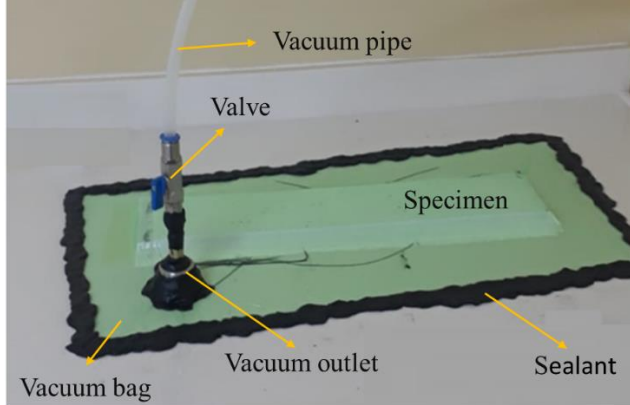
Figure 2 Production of sandwich structures by hand layup vacuum method.

Table 2
Configuration of sandwich samples

Sample-1 (CPC)	Sample-2 (GPG)	Sample-3 (GPC)
Carbon Fiber (2 layers)	Glass Fiber (2 layers)	Glass Fiber (2 layers)
PVC Foam	PVC Foam	PVC Foam
Carbon Fiber (2 layers)	Glass Fiber (2 layers)	Carbon Fiber (2 layers)
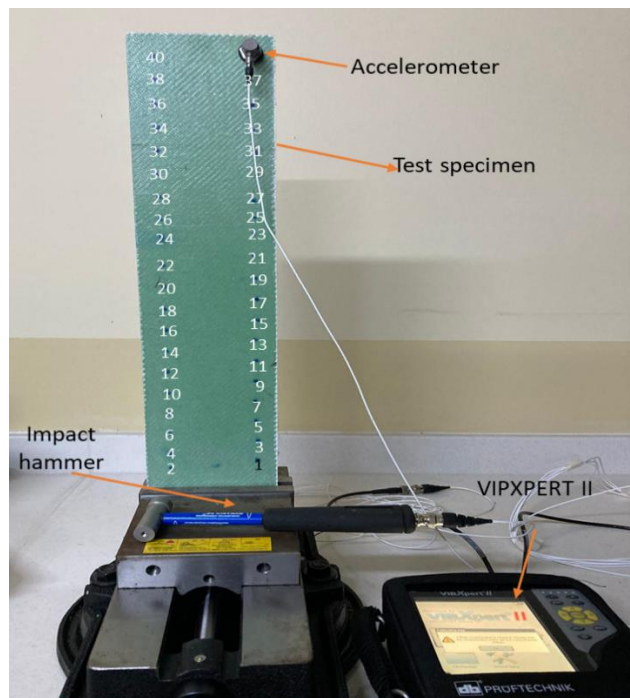
Figure 3 Roving accelerometer method.

Experimentally obtained results are used to calculate natural frequencies, damping ratios, and modal constants of manufactured sandwich structures. A curve fitting method was employed to extract modal parameters using rational fraction polynomials for multi-degree of freedoms system (MDOF) [23]. In this approach, curve-fitting is performed for experimentally obtained FRF values using rational fraction polynomials. The system can be expressed as follows, with the numerator and denominator degrees m and n, respectively.

$$\alpha(\omega) = \left. \frac{\sum_{k=0}^{m} a_k s^k}{\sum_{k=0}^{n} b_k s^k} \right|_{s=j\omega} \qquad (1)$$

Here a_k and b_k are unknowns which are determined by curve fitting method such that the error between the analytical expression and an FRF measurement is minimized over a chosen frequency range. α is the reception. S values are called the roots of the characteristic polynomial. In this approach, rational fraction coefficients are obtained by forming complex orthogonal polynomials given in the reference work of Richardson and Formenti [23]. Then, the damping and modal parameters depending on these values are obtained. The system receptor response is defined in terms of orthogonal polynomials as follows,

$$\alpha(\omega_i) = \left. \frac{\sum_{k=0}^{m} c_k \phi_{i,k}^{+}}{\sum_{k=0}^{n} d_k \theta_{i,k}^{+}} \right|_{s=j\omega} \qquad (i = 1, ..., L) \qquad (2)$$

Here the functions $\phi_{i,k}^{+}$ and $\theta_{i,k}^{+}$ are called the right half functions of the orthogonal functions of the numerator and denominator. Here c_k and d_k are unknowns which when determined is used to recover a_k and b_k. Orthogonal functions are given below in terms of rational fraction coefficients.

$$\phi_{i,0} = a_0$$
$$\phi_{i,1} = a_1 (j\omega_i)$$
$$\phi_{i,2} = a_2 (j\omega_i) + a_3 (j\omega_i)^2$$
$$\phi_{i,3} = a_4 (j\omega_i) + a_5 (j\omega_i)^3$$
(3)

The error in any frequency value can be defined as the difference between analytical and measured FRF values.

$$e_i = a_k (j\omega_i)^k - h_i \left[\sum_{k=0}^{n} b_k (j\omega_i)^k + (j\omega_i)^n \right] \quad (4)$$

Here, h_i is the FRF value measured at the relevant frequency. The square of error criterion is as follows.

$$J = \sum_{i=1}^{L} e_i^* e_i = \left\{ E^* \right\}^T \left\{ E^* \right\} \quad (5)$$

A system with multiple modes can be defined as follows.

$$\alpha(\omega) = \sum_{n=1}^{N} \frac{A_r}{\omega_n^2 - \omega^2 + 2j\omega\omega_n\zeta_n} \quad (6)$$

Equation 6 is obtained by using the peak picking method as follows[24]. Here ω_n are the natural frequencies of the MDOF system. And ζ_n is the viscous damping ratio of the MDOF system.

- Natural frequencies: Each resonant frequency is determined from the maximum points of the response function, $\alpha_{\text{ma ks}} = \left| \alpha_n (\omega_n) \right|_{maks}$

- Damping ratio: The lower and upper-frequency values of the band with the center frequency is determined as $\zeta_r = \left(\omega_b^2 - \omega_a^2 \right) / 4\omega_n^2$, ω_a and ω_b are amplitude ($\alpha_{\text{maks}} / \sqrt{2}$) of frequencies.

- Modal Constant: From a single degree of freedom system, $A_r = 2\alpha_{maks}\zeta_n\omega_n^2$

3. RESULTS and DISCUSSIONS

The study reveals the relationship between the asymmetry and cross-ponding natural frequency changes due to the change in rigidity. An experimental modal test was performed to study the effect of asymmetry on the free vibration behavior of sandwich structures under clamped-free boundary conditions. The natural frequencies, damping ratios, and modal constants of samples are extracted from the measured FRF and presented in table 3. Figures 4, 5, and 6 show the frequency responses of sample 1, sample 2, and sample 3 respectively that were obtained curve fitting method using MATLAB®. To validate experimental results, FEM is employed by using COMSOL Multiphysics® software, and results are presented in Table 2 comparatively.

Table 3
Modal parameters of MDOF curve fit.

MDOF Natural Frequencies (Hz)					
Sample 1		Sample 2		Sample 3	
Exp.	FEM	Exp.	FEM	Exp.	FEM
39.84	37.29	28.31	29.58	32.54	32.04
237.35	210.49	172.49	168.47	196.42	181.57
581.94	519.26	445.78	418.68	499.20	449.56
MDOF Damping Ratios					
Sample 1		Sample 2		Sample 3	
0.0026		0.0065		0.0016	
0.0083		0.0054		0.0094	
0.0156		0.0105		0.0096	
MDOF Modal Constant					
Sample 1		Sample 2		Sample 3	
430		260		570	
71150		32710		65630	
729820		6350		783980	

By replacing the MDOF system parameters given in Table 2, Equation 6 can be rewritten for Sample-1 as follows,

$$\alpha(\omega) = \frac{430}{4\pi^2 (39.84)^2 - \omega^2 + 4\pi j\omega(39.84)(0.0026)}$$
$$- \frac{71150}{4\pi^2 (237.35)^2 - \omega^2 + 4\pi j\omega(237.35)(0.0083)}$$
$$+ \frac{729820}{4\pi^2 (581.94)^2 - \omega^2 + 4\pi j\omega(581.94)(0.0156)}$$
(7)
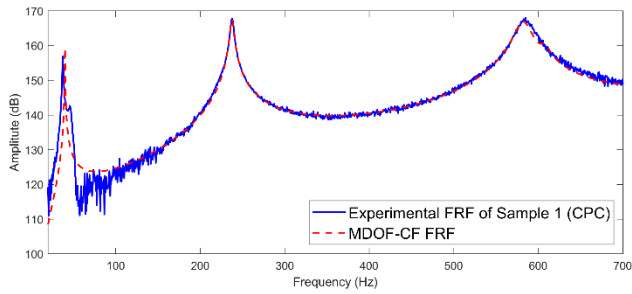
Figure 4 Curve fit-FRF response of Sample 1.
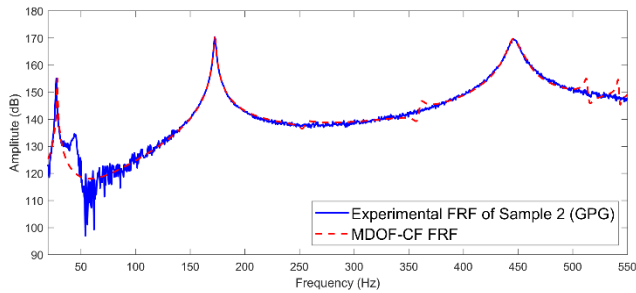
Figure 5 Curve fit-FRF response of Sample 2.
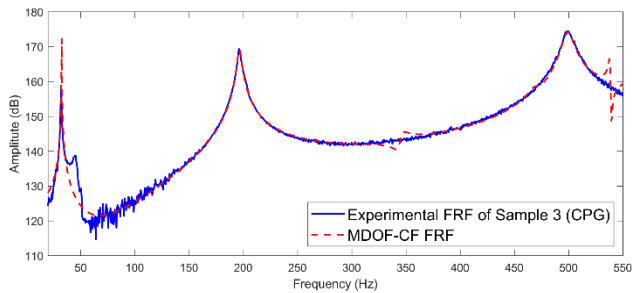
Figure 6 Curve fit-FRF response of Sample 3.
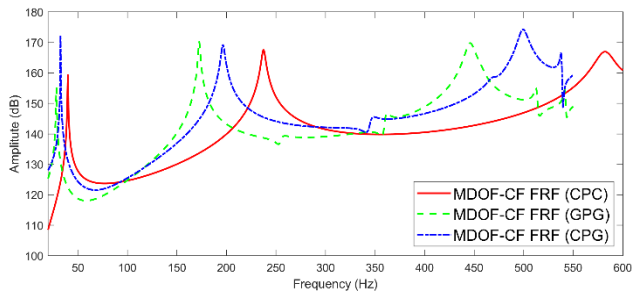
Figure 7 Curve fit results for all samples.

Figure 7 shows the comparison of the natural frequencies for different sandwich samples. The shift in natural frequencies of the asymmetric sandwich structure was observed for all modes concerning symmetric sandwich structures. It is obvious from Figure 7 that asymmetry affects the natural frequencies of sandwich structures. Sample one and sample two give the highest and the lowest frequencies for all modes, respectively.

Significant damping value was not observed. As can be seen from Table 2, each sample gives the best damping value at different modes. That is because in sandwich structure surface waves are restricted only to the face sheet [25]. It is clear from table 3 that the modal constant of the MDOF system is affected by the asymmetric configuration. The asymmetry causes an increase in the modal constant.

4. CONCLUSION

In this study, free vibration analysis of asymmetric sandwich structure was investigated by both experiment and FEM. The objective of the study is to evaluate the influence of asymmetry on the free vibration behavior of the sandwich structure. Three natural frequencies and damping ratios of symmetric and asymmetric sandwich structures were obtained by model vibration tests. The relationship between symmetry, asymmetry, and natural frequencies was observed and conclusions were made. From results, it was obtained that as configuration shifted from symmetric configuration to asymmetric configuration natural frequencies changed. This change gives the designer opportunity to get rid of resonance when occurred by manipulating the face sheet material. It was also obtained that a significant damping ratio was not observed. However, it was found out that asymmetry has a great effect on the modal constant of sandwich structures.

Authors' Contribution

The authors contributed equally to the study.

The Declaration of Ethics Committee Approval

This study does not require ethics committee permission or any special permission.

The Declaration of Research and Publication Ethics

"The authors of the paper declare that they comply with the scientific, ethical, and quotation rules of SAUJS in all processes of the paper and that they do not make any falsification on the data collected. In addition, they declare that Sakarya University Journal of Science and its editorial board have no responsibility for any ethical violations that may be encountered, and that this study has not been evaluated in any academic publication environment other than Sakarya University Journal of Science."

REFERENCES

[1] A. V. Singh, "Free vibration analysis of deep doubly curved sandwich panels," Comput. Struct., vol. 73, no. 1–5, pp. 385–394, 1999.

[2] W. Wang and R. A. Shenoi, "Local Free Vibration Analysis of Initially Stressed Curved Sandwich Beams," Sandw. Struct. 7 Adv. with Sandw. Struct. Mater., pp. 547–555, 2005.

[3] K. M. Ahmed, "Free vibration of curved sandwich beams by the method of finite elements," J. Sound Vib., vol. 18, pp. 61–74, 1971.

[4] T. Sakiyama, H. Matsuda, and C. Morita, "Free vibration analysis of sandwich arches with elastic or viscoelastic core and various kinds of axis-shape and boundary conditions," J. Sound Vib., vol. 203, no. 3, pp. 505–522, 1997.

[5] N. Mishra, B. Basa, and S. K. Sarangi, "Free vibration Analysis of Sandwich Plates with cutout," IOP Conf. Ser. Mater. Sci. Eng., vol. 149, no. 1, 2016.

[6] H. K. Bhardwaj, J. Vimal, and A. K. Sharma, "Study of free vibration analysis of laminated composite plates with triangular cutouts," Eng. Solid Mech., vol. 1, no. 1, pp. 43–50, 2015.

[7] S. Ramakrishna, K. M. Rao, and N. S. Rao, "Free vibration analysis of laminates with circular cutout by hybrid-stress finite element," Compos. Struct., vol. 21, no. 3, pp. 177–185, 1992.

[8] S. Chikkol Venkateshappa, P. Kumar, and T. Ekbote, "Free vibration studies on plates with central cut-out," CEAS Aeronaut. J., vol. 10, no. 2, pp. 623–632, 2019.

[9] H. K. Bhardwaj, J. Vimal, and A. K. Sharma, "Study of Free Vibration Analysis of Laminated Composite Plates with Skew Cut-outs based on FSD," J. Civ. Eng. Environ. Technol., vol. 1, no. 1, pp. 71–75, 2014.

[10] S. Mondal, A. K. Patra, S. Chakraborty, and N. Mitra, "Dynamic performance of sandwich composite plates with circular hole/cut-out: A mixed experimental-numerical study," Compos. Struct., vol. 131, no. April 2016, pp. 479–489, 2015.

[11] J. Vimal, R. K. Srivastava, A. D. Bhatt, and A. K. Sharma, "Free vibration analysis of functionally graded skew plates with circular cutouts," Int. J. Eng. Sci. Technol., vol. 6, no. 3, 2014.

[12] J. Vimal, R. K. Srivastava, A. D. Bhatt, and A. K. Sharma, "Free vibration analysis of moderately thick functionally graded plates with multiple circular and square cutouts using finite element method," J. Solid Mech., vol. 7, no. 1, pp. 83–95, 2015.

[13] T. Tuswan, A. Zubaydi, B. Piscesa, A. Ismail, and M. F. Ilham, "Free vibration analysis of interfacial debonded sandwich of ferry Ro-Ro's stern ramp door," Procedia Struct. Integr., vol. 27, pp. 22–29, 2020.

[14] V. N. Burlayenko and T. Sadowski, "Influence of skin/core debonding on free vibration behavior of foam and honeycomb cored sandwich plates," Int. J. Non. Linear. Mech., vol. 45, no. 10, pp. 959–968, 2010.

[15] H. Y. Kim and W. Hwang, "Effect of debonding on natural frequencies and frequency response functions of honeycomb sandwich beams," Compos. Struct., vol. 55, no. 1, pp. 51–62, 2002

[16] H. Schwarts-Givli, O. Rabinovitch, and Y. Frostig, "Free vibrations of delaminated unidirectional sandwich panels with a transversely flexible core-a modified Galerkin approach," J. Sound Vib., vol. 301, no. 1–2, pp. 253–277, 2007.

[17] B. Saraswathy, R. Ramesh Kumar, and L. Mangal, "Dynamic Analysis of Honeycomb Sandwich Beam with Multiple Debonds," ISRN Mech. Eng., vol. 2012, pp. 1–7, 2012.

[18] V. N. Burlayenko and T. Sadowski, "Dynamic behaviour of sandwich plates containing single/multiple debonding," Comput. Mater. Sci., vol. 50, no. 4, pp. 1263–1268, 2011.

[19] I. Jayatilake, W. Karunasena, and W. Lokuge, "Influence of Single and Multiple Skin-Core Debonding on Free Vibration Characteristics of Innovative GFRP Sandwich Panels," vol. 17, no. 5, pp. 1505–1510, 2015.

[20] M. A. M. Hunjra, M. A. Fakhar, K. Naveed, and T. Subhani, "Polyurethane foam-based radar absorbing sandwich structures to evade detection," J. Sandw. Struct. Mater., vol. 19, no. 6, pp. 647–658, 2017.

[21] A. A. Khurram, M. A. Raza, P. Zhou, and T. Subhani, "A study of the nanocomposite sandwich structures for broadband microwave absorption and flexural strength," J. Sandw. Struct. Mater., vol. 18, no. 6, pp. 739–753, 2016.

[22] A. A. Khurram, S. A. Rakha, N. Ali, M. T. Asim, Z. Guorui, and A. Munir, "Microwave Absorbing Properties of Lightweight Nanocomposite/Honeycomb Sandwich Structures," J. Nanotechnol.

Eng. Med., vol. 6, no. 1, pp. 1–6, 2015.

[23] M. H. Richardson and D. L. Formenti, "Parameter Estimation From Frequency Response Measurements Using Rational Fraction Polynomials.," Proc. Int. Modal Anal. Conf. Exhib., pp. 167–181, 1982.

[24] J. He and Z.-F. Fu, Modal Analysis, 1st ed. butterworth heinemann, 2001.

[25] R. P. Chennuri, "Dynamic Analysis of Sandwich Composites," Int. J. Appl. Eng. Res., vol. 10, no. 71, pp. 485-488, 2015.

Title: Hydrogen Generation from Methane on FeN3 and FeN4 Embedded Graphene Surface Using DFT Method with Grimme-D3 Dispersion Correction

Authors: Hilal KÜÇÜK

Hydrogen Generation from Methane on FeN3 and FeN4 Embedded Graphene Surface Using DFT Method with Grimme-D3 Dispersion Correction

Hilal KÜÇÜK*[1]

Abstract

In this article, the catalytic effect of Nx graphene embedded by Fe metal has been conducted for methane (CH_4) decomposition reaction using Density Functional Theory (DFT) calculations with Grimme-D3 dispersion correction. Recently, the catalytic activities of TMNx (x=3→4) graphene surfaces on chemical reactions have attracted a lot of attention. In particular, the activities of graphene surfaces can be increased by different numbers of doped nitrogen atoms on the graphene surface. For analyzing the adsorption mechanism, adsorption energy, Bader charge, charge density difference and the partial density of state have been calculated. CH_4 molecule is attached into FeN3 embedded graphene physically with higher adsorption energy (-0.41 eV) than that of FeN4 graphene. Their charge transfers from the molecule to the surface are quite small $0.0041e^-$ for FeN3 and $0.0003\ e^-$ for FeN4 graphene. The decomposition of methane has been calculated using the nudged elastic band method. There are the sequential four steps ($CH_x \rightarrow CH_{x-1} + H$, x=4,3,2,1). All reactions in these steps are endothermic. The activation energy of the first hydrogen production from methane ($CH_4 \rightarrow CH_3\ \ +H$) on FeN3 surface is 0.39 eV while the barrier energy is 0.20 eV. However, the same reaction on FeN4 graphene has a quite high activation energy same as its barrier energy (1.84 eV), and its initial state switches directly to the final state without the transition state. The activation energies of most steps on FeN3 embedded graphene are much lower than that of FeN4 graphene surface. Therefore, dehydration reactions can occur with lower energy on FeN3 surface. This study can assist to discover a promising catalyst for methane dissociation through their finding.

Keywords: FeN3 embedded graphene; FeN4 embedded graphene; methane, CH4 decomposition; single-atom catalysis.

1. INTRODUCTION

Attention has been drawn to 2D nitrogen-carbon surfaces embedded by transition metals to improve catalyst knowledge. Xinrui Cao and colleagues investigated the electric and magnetic behavior of TMN4 graphene surface (TM= Ti, V, Cr, Mn, Fe, Co, Ni, Cu) using DFT calculation [1]. According to their finding, lattice parameters of the surface can change their electronic and magnetic properties,

* Corresponding author: hilalkucuk@gazi.edu.tr
[1] Gazi University, Faculty of Science, Department of Physics,
ORCID: https://orcid.org/0000-0002-0777-1102

and also the concentration of the TMN4 graphene can change its electronic properties from metallic to half-metallic or semiconducting characteristics. Putting different transition metals into the center of the surface causes different magnetic moments in the range from 0 to 4 μ_B. Xin et recently determined spin states modulation of TMN4 graphene surface has been determined by Xin et all. Their investigations are that TMN4 graphene sheets are energetically stable and have tunable magnetic properties [2]. K. Fajrial and colleagues studied the pyrolyzed Fe–N–C catalyst doped with boron to investigate the adsorption and decomposition of O_2[3]. Many other valuable experimental and theoretical research has been extended to understand the oxygen reduction reaction using different approaches on TM-N-C catalyst for developing the fuel cell industry [4-10]. Gas adsorptions such as naphthenic acids [11], CO[12], CO_2[13], NO, NO_2, O_3[14], and conversion such as dinitrogen to ammonia [15] have been studied on TM-N-C catalysts as well.

Through greenhouse gas (CH_4, CO_2, CH_3N, O$_3$, water vapor), the temperature on Earth's surface is livable level. However, while the absence of greenhouse gas can cause its temperature would be lower than -15 °C, its extravagant increment makes the opposite effect; global warming [16]. Biogas, manure, rice farming, livestock farming, biomass burning, etc., pit gas, natural gas generate methane gas which increases this undesirable effect along with its rise [17, 18]. Additionally, if it exceeds its acceptable level, it might be responsible for Asphyxia and even death [19, 20]. To capture methane gas, many kinds of research have been made [21-24]. It is known that electronic and magnetic properties change after modification on graphene. Therefore, methane adsorption performances have been explored on graphene before and after modification by Gao's research group [25]. They tested graphene with single vacancy embedding Ni atom and double vacancy as well. According to their research, methane adsorption arises significantly after single vacancy defect and also including oxygen-containing functional groups. Another calculation of carbon

dioxide adsorption-assisted methane desorption on carbon surface showed that the addition of CO_2 to the environment makes methane is less stable on the surface compared with its single molecule adsorption [26].

Ammonia and methanol can be obtained from methane [27-30]. Additionally, hydrogen can be produced via methane decomposition without CO_x production for heating, electricity production, transportation, and industrial purposes and energy storage for portable devices. Hydrogen is a demanding energy source for clean energy. Although the usage of hydrogen energy in technology has been already started, its cost and performance should be improved using new catalysts [31-34]. To catalyze the reforming of methane, many studies have been performed such as methane decomposition on gold-nickel(111) surface [35], methane decomposition on 3d transition-metal clusters [36], and also many research about the reaction mechanism of CO_2 or H_2O activation for CH_4 reforming on various catalyst [37-42]. Ghanashyam Roy et al. worked on the dissociation of methane on Ni$_4$ cluster [43] and represented that the decomposition of CH_4 on the cluster is endothermic and not thermodynamically feasible at standard temperature and pressure. The other study of methane dissociation on Ni(111) with the presence of carbon showed that the increment of the activation barrier occurs along with the presence of carbon because the Ni-carbon surface repulses CH_x species[44]. Recently, the different aspect of dissociation mechanisms of methane on graphene sheets has been analyzed by Kun Li et al.[45] The finding was that almost all reaction energy barriers and reaction energies are higher on N-doped graphene compared with pristine graphene. The dissociation reactions from CH_4 to C_2H_2 can happen much easier on the vacancy graphene than that of N-doped graphene and pristine graphene.

The iron atom is the most preferable transition metal because the iron-based catalyst is well recognized and investigated. Fe-embedded metal Nx(x=3,4) graphene can reduce the catalyst cost for

this process. In this study, methane decomposition for hydrogen production has been discussed on FeN3 embedded graphene compared with FeN4 graphene surface. The reaction mechanism of CH_x (x = 1-4) and the activation/reaction energies for each pathway were calculated to find the most promising catalysts for methane decomposition.

2. COMPUTATIONAL DETAIL

In density functional theory (DFT), all analyses were calculated using Quantum Espresso software package [46, 47]. To get rid of the core electrons and an extremely large number of plane waves, (PAW) pseudopotential were chosen with non-linear core correction and scalar relativistic [48, 49]. For all systems, the kinetic energy cutoff for charge density and potential was 520 Ry, and the kinetic energy cutoff for wave functions was 65 Ry. Gaussian smearing is 0.01 Ry for brillouin-zone. The first model of FeN3 moieties in graphene (FeN3-G) was created by single vacancy and then embedded by Fe transition metal surrounded by 3 nitrogen atoms using 5x5x1 cells with periodic boundary conditions with 50 atoms in Figure 1a. The second model of FeN4 moieties in graphene (FeN4-G) was built using double vacancy and then embedded by Fe transition metal surrounded by 4 nitrogen atoms using the same cells with periodic boundary conditions with 49 atoms in Figure 1b.
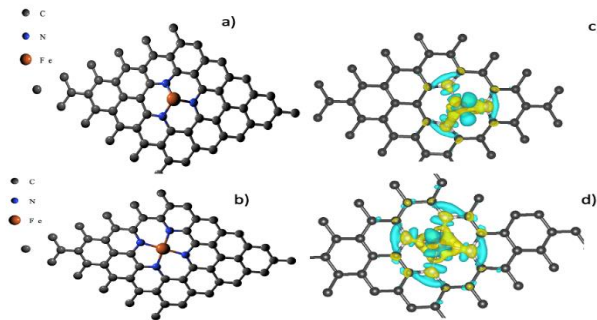
Figure 1 a) FeN3 graphene surface b) FeN4 graphene surface. C, Fe and N atoms represent gray, orange, and blue colors respectively. The charge density difference plot at iso-surfaces = ±0.005 $e/Å^3$ c) for FeN3-G and d) for FeN4-G. The meaning of yellow color is the loss of electron density, and turquoise color is the gain of electron density.

There was an implementation of the term Grimme-D3 for Van der Waals and relatively weaker interactions corrections and also the spin polarization effect [50]. The gaussian spreading is 0.01 Ry for brillouin-zone integration. The lattice parameters were selected as a=12.3 Å and c=20 Å to have the lowest energy with 4x4x1 Monkhorst-Pack k-point mesh. The bond distance (d), magnetic moments after optimization are in Table 1. There is a good agreement with previous work by Cao's group[51]. Figures 1c-d are drawn as the charge density difference. These two plots show that electrons accumulate on the N atoms around the metal atom on both surfaces as losing charges from the metal.

The formation energy as

$$E_f = E_{surface} + n.\mu_c - (E_{graphene} + m.\mu_N + E_M)(1)$$

where $E_{surface}$ and $E_{graphene}$ are respectively total energies of surface and pristine graphene.

Table 1 The bond distance (d), C_1 is on the right side of N atom on d_{N-C_1} and C_2 is on the left side. The second competitive results after slash on FeN4-G parameter belong to calculations taken by Cao's group[51]

Surface	d_{Fe-N} (Å)	d_{N-C_1} (Å)	d_{N-C_2} (Å)	Magnetic Mom. (μ_B)	E_{form}
FeN3-G	1.862	1.376	1.376	3.0	-2.70
FeN4-G	1.89/1.91	1.37/1.38	1.39/1.38	2.0/1.97	-3.75

The number of carbon atoms removed from the pristine graphene is symbolized by *n*, and the number of nitrogen atoms on the surface systems is *m*= 3 for FeN3 graphene and *m*=4 FeN4 graphene surface. μ_c and μ_N are the chemical potential of a single C atom and N respectively. E_{Fe} is the energy of the isolated Fe atom. The formation energies of these two surfaces are a negative value. This proves that both surfaces are stable.

The calculation of the adsorption energies (E_{ads}) of molecular structures on the surface as

$$E_{ads} = E_{\text{surface+molecule}} - E_{\text{surface}} - E_{\text{molecule}} \quad (2)$$

where $E_{\text{surface+molecule}}$ is the total energy of molecular structures on the surface. As E_{surface} is the total energy of the surface without molecule, E_{molecule} is the molecule energy in the gas phase. A release of energy during adsorption is demonstrated by the negative sign of adsorption energy. The transition state (TS) for structures is calculated by the nudged elastic band (NEB) method [52, 53]. The difference in energy between the final (E_{FS}) and the initial state (E_{IS}) gives the reaction barrier energy (E_R). The negative sign of reaction energy shows that reaction is exothermic while the endothermic process occurs in the positive value.

$$E_{act} = E_{TS} - E_{IS} \qquad (3)$$

$$E_R = E_{FS} - E_{IS} \qquad (4)$$

E_{act} is the activation and E_{TS} is the energy of TS. The electron transfer (Δq) is calculated by Bader charge analysis[54] as

$$\Delta q = q_{\text{surface+molecule}} - (q_{\text{surface}} + q_{\text{molecule}}) \qquad (5)$$

The Bader charge of adsorbed molecule and surface is $q_{\text{surface+molecule}}$. Surface charge is q_{surface} and molecule charge is q_{molecule}. The negative sign or positive sign of Δq shows donating charge or gaining charge from the molecule.

3. RESULT AND DISCUSSION:

3.1 Adsorption of CH_4 in FeN3 and FeN4 moieties in graphene

After the optimization of CH_4 on these surfaces, the most stable configurations are found as seen in Figure 3a for FeN3-G and Figure 4a for FeN4-G surfaces while CH_4 in the gas phase in Figure 2a. In Table 2, the bond lengths of $C - H_1$ and $C - H_2$ increase while the other hydrogen bond lengths are squeezed on FeN3-G surface. Also d_{Fe-N} is taller compared with its bare surface and d_{N-Cx} is getting smaller from 1.376Å to 1.372Å. The Bader charge exchange from molecule to FeN3-G is 0.0041 e^- as physical adsorption with the adsorption energy of -0.41 eV. Figure 3b illustrates the charge density difference plot. These all interactions can be viewed on the partial density of state (pDOS) Figure 3c as well. After methane adsorption(below plot of Figure3c) there is a big leap at the energy peak of H_1 and H_2 which are close to Fe atom and the energy peak of C between 7-8 eV interacting with Fe/3N atoms. However, they have very small effects in Figure 2b which is pDOS for methane in the gas phase. The sum of the energy peak of three nitrogen atoms where is near 0 on the bare surface (top plot) is getting lower after adding molecule.

Table 2 Some parameters for CH_4 on the graphene surfaces. d_{Fe-C} is the bond length between C atom on CH_4 and Fe on the surfaces. E_{ads} is the adsorption energy and d represents the length between two type atoms. d_{N-C_x} is the bond length between N and C atoms belonging to the surface as described above.

	E_{ads} (eV)	d_{Fe-N} (Å)	d_{N-C_1} (Å)	d_{N-C_2} (Å)	d_{Fe-C} (Å)	d_{C-H_1} (Å)	d_{C-H_2} (Å)	d_{C-H_3} (Å)	d_{C-H_4} (Å)	$\Delta q(CH_4)$ (e^-)
CH_4 in gas phase						1.096	1.096	1.096	1.096	
FeN3-G	-0.41	1.89	1.372	1.372	2.39	1.127	1.106	1.094	1.094	0.0041
FeN4-G	-0.17	1.89	1.39	1.37	3.25	1.096	1.097	1.096	1.096	0.0003

Figure 2 a) CH_4 on gas-phase b) Partial density of states (pDOS) of CH_4 in the gas phase. The energy of H_1, H_2, H_3, H_4 and C atoms are represented by violet, orange, cyan, gold and green colors.
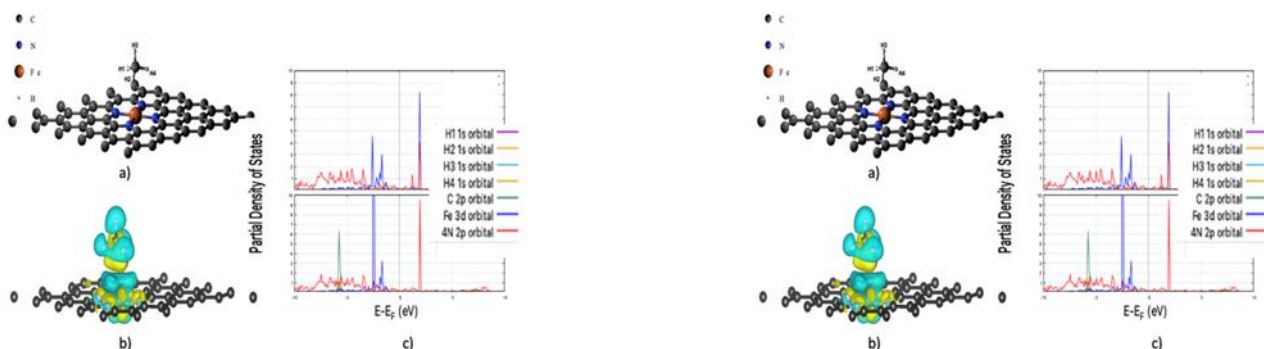
Figure 3 For the FeN3 graphene surface, a) CH_4 on the surface, b) The charge density difference plot at iso-surfaces $= \pm 0.001 \frac{e}{\text{Å}^3}$, c) Partial density of states (pDOS) of CH_4 on the FeN3 graphene surface. The energy of H_1, H_2, H_3, H_4, C, Fe and the sum of three N atoms energies around Fe are represented by violet, orange, cyan, gold, green, blue and red colors. On this figure, the top plot represents pDOS on the bare surface and, the below plot is pDOS of molecule and surface after adsorption.

Figure 4 For the FeN4 graphene surface, a) CH_4 on the surface, b) The charge density difference plot at iso-surfaces $= \pm 00.00012 \frac{e}{\text{Å}^3}$, c) Partial density of states (pDOS) of CH_4 on the FeN4 graphene surface. The energy of H_1, H_2, H_3, H_4, C, Fe and the sum of four N atoms energies around Fe are represented by violet, orange, cyan, gold, green, blue and red colors. On this figure, the top plot represents pDOS on the bare surface and, the below plot ispDOS of molecule and surface after adsorption.

After adsorption, the molecule on the FeN4 surface remains almost the same except its elongated bond length of $C-H_2$. On the surface, there is a small increment on d_{N-C_1} while decrescent on d_{N-C_2}. This weak change can cause the weak charge exchange by 0.0003 e^- from molecule to FeN4 surface and physisorption with the adsorption energy of -0.17 eV. The charge density difference in Figure 4b shows that there is not a big charge transfer between molecule and surface. It is seen that there is not chemical interaction between molecule and surface.

In the previous work[45], the methane adsorption in different sheets is similar to our result on FeN4-G. The interactions on different graphene sheets are physical with the adsorption energy of -0.13 eV on pristine graphene, the adsorption energy of -0.19 eV on N-doped graphene and the adsorption energy of -0.25 eV on vacancy graphene. However, methane is more stable on FeN3-G compared with the above surfaces.

Figure 4c is the partial density of state (pDOS) for FeN4-G. The small energy peak of H_2 is at near 6 eV and the peak of carbon atom increases

noticeably between 6-7 eV interacting with Fe/4N molecule after adsorption. The energy peak of Fe moves leftwards slightly with a big increment.

3.2 The decomposition of CH_4 on FeN3 graphene surface and FeN4 graphene surface

The decomposition steps with the initial, the transition and the final states are investigated as seen in Figure 5 for the FeN3 and Figure 6 for FeN4 surface. The various parameters are in Table 3 for CH_x (x= 1,2,3,4) species for the adsorption reaction and Table 4 for the CH_x species co-adsorption reaction. Our strategy of the H cleavage is that the removed H atom from the molecule is put onto Fe or N atom on the surface and then NEB calculation is made for one of these two positions which have the most stable geometry. The reaction pathways and the calculation of E_{act}/E_R by NEB method as explained in the computational method section is shown in Table 5. The reaction energy diagram of the sequential pathway is shown in Figure 7. As explained before in section 2, the reaction is the endothermic process if E_r is the positive value. According to the barrier energies in the steps, all reactions are endothermic as the result of previous work on Ni_4-cluster.

On FeN3 graphene surface, H_1 which has an elongated bond length from $1.096Å$ to $1.217\ \dot{A}$ in the adsorption geometry is broken off and settled on Fe atom with the distance of $1.54\ \dot{A}$ with the co-adsorption energy of -4.70 eV. The activation energies and the reaction energy barrier of the first hydrogen production from CH_4 are respectively 0.39eV and 0.20 eV on FeN3-G.

H_2 which has an elongated bond length with a small change by $0.001\ \dot{A}$ on FeN4-G surface is removed from the molecule with E_{act} = 1.84 eV and the barrier energy is the same as activation energy. In this reaction, the initial state directly transfers into the final state without the transition state as seen in Figure 6a. . The same case happens in the second pathway ($CH_3\ \rightarrow CH_2\ +H$) on FeN3-G with high barrier energy, 2.63 eV. In the second step of the

hydrogen cleavage on FeN4-G, the $C\text{-}H$ bond length increases from 1.086 Å to 1.098 Å. The distances between C and Fe atoms are 1.98 Å for FeN4-G after the adsorption and 1.73 Å after the co-adsorption. The broken H atom prefers to stay on the N atom with 1.034 Å of the distance. The reaction of $CH_3\ \rightarrow CH_2\ +H$ *occurs* with the activation energy of 2.91 eV and the barrier energy of 2.65 eV.

Table 3 The adsorption energy of CH_x and the bond length between atoms. The C-H bond length,$d_{\text{C-H}}$ will be broken for CH_x decomposition.

	Species	E_{ads}	$d_{\text{C-H}}$ (Å)		$d_{\text{Fe-C}}$ (Å)
			Gas Phase	Adsorbed	
FeN3-G	CH_3	-3.04	1.086	1.102	1.96
FeN4-G		-2.58		1.098	1.98
FeN3-G	CH_2	-4.67	1.122	1.111	1.74
FeN4-G		-4.11		1.103	1.72
FeN3-G	CH	-5.75	1.137	1.103	1.62
FeN4-G		-4.60		1.116	1.63

In the third decomposition step, the distance of CH_2 molecule to the surface on Figure 5c (IS) for FeN3-G and Figure 6c (IS) for FeN4-G are respectively 1.74 Å and 1.72 Å. The adsorption/co-adsorption energies are -4.67/-7.90 eV for FeN3-G and -4.11/-6.78 eV for FeN4-G surface. On both surfaces, the broken H atoms are attached to N atoms with the distance of ~1.03 Å. The activation energies of the pathway on FeN3-G and FeN4-G are respectively 0.57 eV and 2.82 eV while the barrier energies are 2.09 eV and 2.65 eV. The activation energy of previous work on Ni_4 cluster[43] is quite higher with 1.28 eV than that of FeN3-G.

In the last step as seen in Figure 5d for FeN3-G and Figure 6d for FeN4-G, the CH adsorption energies are -5.75 eV and -4.60 eV respectively. C-H bonds on both surfaces are squeezed in the initial state, and carbon atoms are ~1.62 Å away from Fe atom on both surfaces. In the final state, H atom broken from CH molecule holds on N atoms with the distance of ~1.032 Å for both surfaces. The high

activation energies/barrier energies are observed on both surfaces, are 1.664/1.663 eV for FeN3-G and 1.80/1.25 for FeN4-G.

Table 4 The co-adsorption energy of $CH_x + H$ and the bond length of *Fe/N-H* and *Fe-C*.

	Species	E_{ads}	$d_{Fe/N-H}$ (Å)	d_{Fe-C} (Å)
FeN3-G	$CH_3 + H$	-4.70	1.54	1.97
FeN4-G		-2.82	1.59	1.99
FeN3-G	$CH_2 + H$	-6.41	1.033	1.75
FeN4-G		-5.69	1.034	1.73
FeN3-G	$CH + H$	-7.90	1.029	1.64
FeN4-G		-6.78	1.03	1.65
FeN3-G	$C + H$	-8.01	1.032	1.54
FeN4-G		-7.26	1.031	1.55

Table 5 CH_4 decomposition pathways.

CH_4 Decomposition Pathways		FeN3 graphene E_{act}/E_r (eV)	FeN4 graphene E_{act}/E_r (eV)
TS1	$CH_4 \rightarrow CH_3 + H$	0.39/0.20	1.84/1.84
TS2	$CH_3 \rightarrow CH_2 + H$	2.63/2.63	2.91/2.65
TS3	$CH_2 \rightarrow CH + H$	0.57/2.09	2.82/2.65
TS4	$CH \rightarrow C + H$	1.664/1.663	1.80/1.25
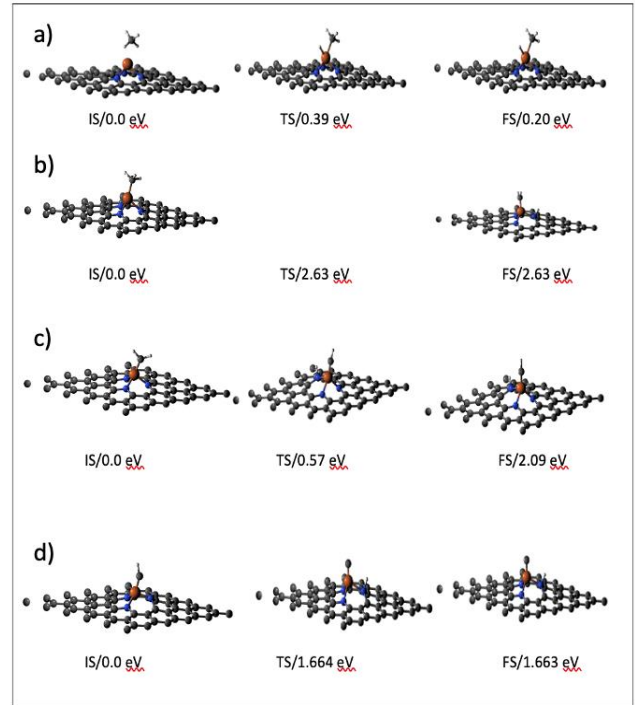
Figure 5 CH$_x$ (x=1→4) dehydrogenation generation pathway with the initial state (IS), the transition state (TS), the final state s(FS).
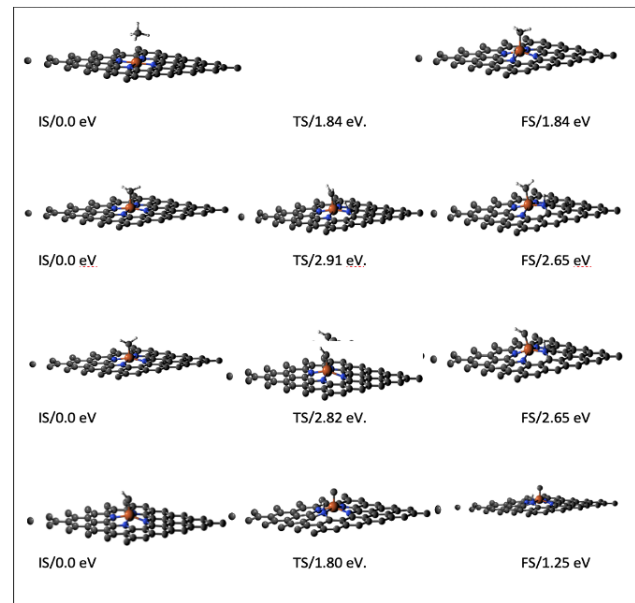
Figure 6 The CH$_x$ (x=1→4) dehydrogenation generation pathway with the initial state (IS), transition state (TS), the final state s(FS).
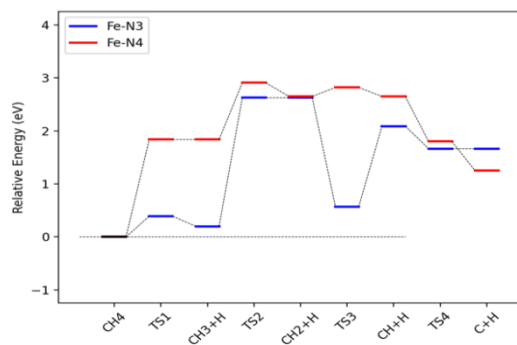
Figure 7 The reaction energy diagram of the sequential pathway. The reaction step is in Table-3 with related energy.

4. CONCLUSION

In this study, methane decomposition reaction mechanism on FeN3 embedded graphene and FeN4 embedded graphene were examined in detail using DFT density functional theory. On both surfaces, the physisorption interaction is observed for methane. In all steps, the most stable adsorption/co-adsorption geometries of CH_x (x=1→4) were observed on FeN3-G surface with more interaction. When removed H atom from the molecule, the adsorption energy increased gradually, and the molecule was much closer than that of previous CH_x configuration. While H atom settled on Fe atom on the first H cleavage, it stayed on N atom on the other steps because molecule was quite close to Fe metal and H could not stay on Fe atom because of this closeness. For the first dehydrogenation step, the energy barrier required to break the $C\text{-}H$ bond on both surfaces is quite low. This result shows that the surfaces on the $C\text{-}H$ bond have high activation. In the second dehydrogenation step, the reaction step $CH_3 \rightarrow CH_2 + H$ is the rate-determining step of the overall reaction. Therefore, the highest energy barrier occurs at this step. Since the activation energy of 0.57 eV obtained on FeN3 in the next reaction step has a very low value, many expensive transition metals in the literature can be compared. In the last reaction step, the $C\text{-}H$ bond is broken with an activation energy of 1.66 eV. The results obtained on the FeN3 graphene surface over the entire reaction pathway are quite low and can be replaced with other costly transition metals. With this feature, FeN3 graphene has the potential to be a candidate material for hydrogen production from methane due to its low cost and high catalytic activity.

The Declaration of Conflict of Interest/ Common Interest

No conflict of interest or common interest has been declared by the author.

The Declaration of Ethics Committee Approval

This work does not require ethics committee permission or any special permission.

The Declaration of Research and Publicatıon Ethics

The author of the paper declares that he complies with the scientific, ethical and quotation rules of SAUJS in all processes of the article and that she does not make any falsification on the data collected. In addition, she declares that Sakarya University Journal of Science and its editorial board have no responsibility for any ethical violations that may be encountered and that this study has not been evaluated in any academic publication environment other than Sakarya University Journal of Science.

REFERENCES

[1] M.T. Baei, A. Soltani, and S. Hashemian, "Adsorption properties of hydrazine on pristine and Si-doped Al12N12 nano-cage,"

Phosphorus, Sulfur, and Silicon and the Related Elements, vol. 191, no. 5, pp. 702-708, 2016.

[2] X. Xin, et al., "Spin states modulation of Four-Nitrogen coordinated Transition-Metal (TMN4) embedded graphene," Applied Surface Science, vol. 570, pp. 151126, 2021.

[3] A.K. Fajrial et al., "First principles study of oxygen molecule interaction with the graphitic active sites of a boron-doped pyrolyzed Fe–N–C catalyst," Physical Chemistry Chemical Physics, vol. 19, no. 34, pp. 23497-23504, 2017.

[4] C.W.B. Bezerra, et al., "A review of Fe–N/C and Co–N/C catalysts for the oxygen reduction reaction," Electrochimica Acta, vol. 53, no. 15, pp. 4937-4951, 2008.

[5] B. Merzougui, et al., "A Pt-free catalyst for oxygen reduction reaction based on Fe–N multiwalled carbon nanotube composites," Electrochimica Acta, vol. 107, pp. 126-132, 2013.

[6] G. Zhang, et al., "Is iron involved in the lack of stability of Fe/N/C electrocatalysts used to reduce oxygen at the cathode of PEM fuel cells?" Nano Energy, vol. 29, pp. 111-125, 2016.

[7] S. Stariha, et al., "PGM-free Fe-N-C catalysts for oxygen reduction reaction: Catalyst layer design," Journal of Power Sources, vol. 326, pp. 43-49, 2016.

[8] L. Yu, et al., "Oxygen reduction reaction mechanism on nitrogen-doped graphene: A density functional theory study," Journal of Catalysis, vol. 282 no. 1, pp. 183-190, 2011.

[9] G. Wu, and P. Zelenay, "Nanostructured Nonprecious Metal Catalysts for Oxygen Reduction Reaction," Accounts of Chemical Research, vol. 46, no. 8, pp. 1878-1889, 2013.

[10] Z. Lu, et al., "Novel catalytic activity for oxygen reduction reaction on MnN4 embedded graphene: A dispersion-corrected density functional theory study," Carbon, vol. 84, pp. 500-508, 2015.

[11] L. Ma and X. Chen, "Adsorption of naphthenic acids to the nitrogen-coordinated transition-metal embedded graphene: A DFT study," Russian Journal of Physical Chemistry B, vol. 10, no. 6, pp. 1027-1031, 2016.

[12] Q.-K. Li, et al., "Cooperative spin transition of monodispersed FeN3 sites within graphene induced by CO adsorption," Journal of the American Chemical Society, vol. 140, no. 45, pp. 15149-15152, 2018.

[13] H. Bae, et al., "High-throughput screening of metal-porphyrin-like graphenes for selective capture of carbon dioxide," Scientific reports, vol. 6, no. 1, pp. 1-10, 2016.

[14] C. Hu, et al., "Adsorption and sensing characteristics of air decomposed species onto pyridine-like PdN3-doped CNT: a first-principles study," Carbon Letters, vol. 32, pp. 109-117, 2022.

[15] X.-F. Li, et al., "Conversion of dinitrogen to ammonia by FeN3-embedded graphene," Journal of the American Chemical Society, vol. 138, no. 28, pp. 8706-8709, 2016.

[16] T.R. Karl, and K.E. Trenberth, "Modern Global Climate Change," Science, vol. 302, no. 5651, pp. 1719-1723, 2003.

[17] L. Milich, "The role of methane in global warming: where might mitigation strategies be focused?" Global Environmental Change, vol. 9, no. 3, pp. 179-201, 1999.

[18] A.R. Moss, J.-P. Jouany, and J. Newbold, "Methane production by ruminants: its contribution to global warming," in Annales

de zootechnie. EDP Sciences, vol. 49, no.3, pp. 231-253, 2000.

[19] R. Rossi, et al., "An unusual suicide: asphyxia by methane gas," The American journal of forensic medicine and pathology, vol. 34, no. 2, pp. 83-85, 2013.

[20] M. Gasparik, et al., "First international inter-laboratory comparison of high-pressure CH_4, CO_2 and C_2H_6 sorption isotherms on carbonaceous shales," International Journal of Coal Geology, vol. 132, pp. 131-146, 2014.

[21] K. Li, et al., "Adsorption of small hydrocarbons on pristine, N-doped and vacancy graphene by DFT study," Applied Surface Science, vol. 515, p. 146028, 2020.

[22] W. Zhou, et al., "Hydrogen and methane adsorption in metal− organic frameworks: a high-pressure volumetric study," The Journal of Physical Chemistry C, vol. 111, no. 44, pp. 16131-16137, 2007.

[23] W. Yuan, et al., "Experimental study and modelling of methane adsorption and diffusion in shale," Fuel, vol. 117, pp. 509-519, 2014.

[24] K. Fan, et al., "Three stages of methane adsorption capacity affected by moisture content," Fuel, vol. 231, pp. 352-360, 2018.

[25] X. Gao, et al., "Performance of intrinsic and modified graphene for the adsorption of H_2S and CH_4: a DFT study," Nanomaterials, vol. 10, no. 2, pp. 299, 2020.

[26] H. Xu, et al., "CO_2 adsorption-assisted CH_4 desorption on carbon models of coal surface: A DFT study," Applied Surface Science, vol. 375, pp. 196-206, 2016.

[27] A. Valera-Medina, et al., "Ammonia, Methane and Hydrogen for Gas Turbines," Energy Procedia, vol. 75, pp. 118-123, 2015.

[28] X. Bai, et al., "Microwave catalytic synthesis of ammonia from methane and nitrogen," Catalysis Science & Technology, vol. 8, no. 24, pp. 6302-6305, 2018.

[29] H.F. Abbas, and W.M.A. Wan Daud, "Hydrogen production by methane decomposition: A review," International Journal of Hydrogen Energy, vol. 35, no. 3, pp. 1160-1190, 2010.

[30] A. Akça, "Conversion of methane to methanol on C-doped boron nitride: A DFT study," Computational and Theoretical Chemistry, vol. 1202, pp. 113291, 2021.

[31] I. Staffell, et al., "The role of hydrogen and fuel cells in the global energy system," Energy & Environmental Science, vol. 12, no. 2, pp. 463-491, 2019.

[32] H. Council, "Hydrogen scaling up: A sustainable pathway for the global energy transition," 2017.

[33] E.S. Hanley, J.P. Deane, and B.P.Ó. Gallachóir, "The role of hydrogen in low carbon energy futures–A review of existing perspectives," Renewable and Sustainable Energy Reviews, vol. 82, pp. 3027-3045, 2018.

[34] S. Dunn, "Hydrogen futures: toward a sustainable energy system," International Journal of Hydrogen Energy, vol. 27, no. 3, pp. 235-264, 2002.

[35] H. Liu, et al., "A DFT theoretical study of CH_4 dissociation on gold-alloyed Ni (111) surface," Journal of natural gas chemistry, vol. 20, no. 6, pp. 611-617, 2011.

[36] K.F. Andriani, J. Mucelini, and J.L.F. Da Silva, "Methane dehydrogenation on 3d 13-atom transition-metal clusters: A density functional theory investigation combined with Spearman rank correlation analysis," Fuel, vol. 275, pp. 117790, 2020.

[37] S. Jiang, et al., "Insight into the reaction mechanism of CO_2 activation for CH_4 reforming over NiO-MgO: A combination of DRIFTS and DFT study," Applied Surface Science, vol. 416, pp. 59-68, 2017.

[38] Y. Guo, J. Feng, and W. Li, "Effect of the Ni size on CH_4/CO_2 reforming over Ni/MgO catalyst: A DFT study," Chinese Journal of Chemical Engineering, vol. 25, no. 10, pp. 1442-1448, 2017.

[39] Y.-P. Guo, W.-Y. Li, and J. Feng, "Reaction pathway of CH_4/CO_2 reforming over Ni8/MgO (100)," Surface Science, vol. 660, pp. 22-30, 2017.

[40] R. Ghanbari, R. Safaiee, and M. Golshan, "A dispersion-corrected DFT investigation of CH4 adsorption by silver-decorated monolayer graphene in the presence of ambient oxygen molecules," Applied Surface Science, vol. 457, pp. 303-314, 2018.

[41] MA. Lourenço, et al., "Interaction of CO_2 and CH_4 with functionalized periodic mesoporous phenylene–silica: Periodic DFT calculations and gas adsorption measurements," The Journal of Physical Chemistry C, vol. 120, no. 7, pp. 3863-3875, 2016.

[42] A. Akça and İ.Ö. Alp, "The Dissociation Reaction of Methane on Ti-And Co-Embedded Graphene: A Dft Study," Theory and Research in Science and Mathematics, pp. 45-64, Gece kitaplığı, ISBN. 978-625-7243-77-3, 2020

[43] G. Roy, and A.P. Chattopadhyay, "Dissociation of methane on Ni4 cluster-A DFT study," Computational and Theoretical Chemistry, vol. 1106, pp. 7-14, 2017.

[44] J. Li, E. Croiset and L. Ricardez–Sandoval, "Effect of carbon on the Ni catalyzed methane cracking reaction: A DFT study," Applied Surface Science, vol. 311, pp. 435-442, 2014.

[45] K. Li, et al., "Dissociation mechanisms of CH_4 on pristine, N-doped and vacancy graphene by DFT study," Diamond and Related Materials, vol. 114, p. 108323, 2021.

[46] P. Giannozzi, et al., "QUANTUM ESPRESSO: a modular and open-source software project for quantum simulations of materials," Journal of Physics: Condensed Matter, vol. 21, no. 39, p. 395502, 2009.

[47] P. Giannozzi, et al., "Advanced capabilities for materials modelling with Quantum ESPRESSO," Journal of Physics: Condensed Matter, vol. 29, no. 46, pp. 465901, 2017.

[48] W. Kohn and L.J. Sham, "Self-Consistent Equations Including Exchange and Correlation Effects," Physical Review, vol. 140, no. 4A, pp. 1133-1138, 1965.

[49] P.E. Blöchl, "Projector augmented-wave method," Physical Review B, vol. 50, no. 24, pp. 17953-17979, 1994.

[50] S. Grimme, J.Antony, S. Ehrlich and H. Krieg, "A consistent and accurate ab initio parametrization of density functional dispersion correction (DFT-D) for the 94 elements H-Pu," Journal of Chemical Physics, vol. 132, p. 154104, 2010.

[51] X. Cao, X.F. Li and W. Hu, "Tunable Electronic and Magnetic Properties of Graphene-Embedded Transition Metal-N4 Complexes: Insight From First-Principles Calculations," Chemistry–An Asian Journal, vol. 13, no. 21, pp. 3239-3245, 2018.

[52] G. Mills and H. Jónsson, "Quantum and thermal effects in H_2 dissociative adsorption: Evaluation of free energy barriers in multidimensional quantum systems," Physical Review Letters, vol. 72, no. 7, p. 1124, 1994.

[53] G. Mills, H. Jónsson and G.K. Schenter, "Reversible work transition state theory:

application to dissociative adsorption of hydrogen," Surface Science, vol. 324, no. 2-3, pp. 305-337, 1995.

[54] G. Henkelman, A. Arnaldsson, and H. Jónsson, "A fast and robust algorithm for Bader decomposition of charge density," Computational Materials Science, vol. 36, no. 3, pp. 354-360, 2006.

Title: Determination of Metabolic Rate from Physical Measurements of Heart Rate, Mean Skin Temperature and Carbon Dioxide Variation

Authors: Mehmet Furkan ÖZBEY, Aydın Ege ÇETER, Cihan TURHAN

Determination of Metabolic Rate from Physical Measurements of Heart Rate, Mean Skin Temperature and Carbon Dioxide Variation

Mehmet Furkan ÖZBEY*[1], Aydın Ege ÇETER[1], Cihan TURHAN[2]

Abstract

Thermal comfort depends on four environmental parameters such as air temperature, mean radiant temperature, air velocity and relative humidity and two personal parameters, including clothing insulation and metabolic rate. Environmental parameters can be measured via objective sensors. However, personal parameters can be merely estimated in most of the studies. Metabolic rate is one of the problematic personal parameters that affect the accuracy of thermal comfort models. International thermal comfort standards still use a conventional metabolic rate table which is tabulated according to different activity tasks. On the other hand, ISO 8996 underestimates metabolic rates, especially when the time of activity level is short and rest time is long. To this aim, this paper aims to determine metabolic rates from physical measurements of heart rate, mean skin temperature and carbon dioxide variation by means of nineteen sample activities. 21 male and 17 female subjects with different body mass indices, sex and age are used in the study. The occupants are subjected to different activity tasks while heart rate, skin temperature and carbon dioxide variation are measured via objective sensors. The results show that the metabolic rate can be estimated with a multivariable non-linear regression equation with high accuracy of 0.97.

Keywords: Metabolic rate, thermal comfort, heart rate, skin temperature, carbon-dioxide variation

1. INTRODUCTION

Thermal comfort is a major and significant phenomenon which affects the energy consumption of buildings while satisfying productivity and healthy indoor environments to the occupants [1]. A well-known thermal comfort model, Fanger's Predicted Mean Vote (PMV) and Percentage of Predicted Dissatisfied (PPD)

method, categorizes parameters that affect thermal comfort as environmental and personal [2]. Environmental parameters such as air temperature, relative humidity, air velocity, and mean radiant temperature are measured via objective sensors. Moreover, ISO 7726 [3] provides guidance on measuring environmental parameters to calculate thermal comfort. Besides, personal parameters such as clothing value and

---

* Corresponding author: m.furkanozbey@gmail.com

[1] Atılım University, Institute of Science, Mechanical Engineering

E-mail: aege.ceter@gmail.com

ORCID: https://orcid.org/0000-0002-5813-3514, https://orcid.org/0000-0002-1048-9642

[2] Atılım University, Faculty of Engineering, Department of Energy Systems Engineering

E-mail: cihan.turhan@atilim.edu.tr

ORCID: https://orcid.org/0000-0002-4248-431X

ÖZBEY et al.

Determination of Metabolic Rate from Physical Measurements of Heart Rate, Mean Skin Temperature and C...

metabolic rate generally are based on direct-look up tables which are given in International Standards such as ASHRAE 55 and ISO 7730 [4,5]. Clothing value is an influencing parameter

which reduces the heat exchange between the human body and thermal environment [6]. ISO 9920 [7] estimates the resistance of garments to dry heat loss and evaporative heat loss in steady-state conditions. However, a noteworthy finding of previous research clearly indicates that the metabolic rate is the most sensitive parameter on the PMV calculation errors among all influencing parameters of thermal comfort [8-10].

Metabolic rate (M) is defined as "the level of transformation of chemical energy into heat and mechanical work by metabolic activities within an organism" [4]. Generally, the metabolic rate expresses heat production rate in W/m^2 on a human body. It is worth to note that a 100 W heat is produced by an adult at rest time, and 1 met equals to 58 W/m^2 for a resting person. Further details on the heat balance on a human body and metabolic rate calculation can be found in [2,4,11]. Metabolic rate is the most influencing parameter on the accurate PMV calculation. For instance, Khan and Pao [12] stated that the metabolic rate is an expected parameter on the calculation of the PMV, for this reason, further studies are required for an adequate explication of thermal sensation. Moreover, Luo et al. [10] indicated that metabolic rate is the most problematic parameter on thermal comfort since yet researches and practices on the parameter are crudely evaluated. The authors concluded that more studies and experiments are needed for better understanding in built environmental and thermal comfort contexts. In addition, determining inadequate metabolic rates causes errors on the PMV value in real environments [13-15]. For instance, Humpreys and Nicol [14] found that the PMV value is underestimated above 1.4 met, which causes up to 1 unit error. The authors also stated the reason of this error as high sweating levels on high metabolic rates. Fanger and Toftum [16] represented the weaknesses of the adaptive thermal comfort model as not taking the metabolic rate into account on thermal sensation. On the other hand, Chamra et al. [9]

showed that the PMV model is only acceptable for 1 met values. At higher metabolic rate levels, uncertainty analysis is needed for a better understanding of the impact of metabolic rate levels on thermal comfort.

Conventional methods to determine the metabolic rate refer to tabulate methods such as in ASHRAE 55 [4] and ISO 7730 [5]. In metabolic rate tables, the sample activities represent typical metabolic rate values which are averaged across a group of people. However, metabolic rate always changes by time which causes significant errors on the PMV measurements. For instance, Havenith [6] indicated that the tabulate methods have an error of up to 20% on obtaining metabolic rate. Similarly, Broday et al. [17] compared metabolic rate tables with real-time measurements and concluded that there is a significant difference up to 20 W/m^2 between the measurements and tables.

Metabolic rate can be measured by direct or indirect calorimeters; however, the measurement method is quite inconvenient for real-time applications since the subjects should wear uncomfortable masks which measure oxygen intake and carbon dioxide outtake [18]. For this reason, the researchers aim to predict the metabolic rate from physical indicators of the parameter. It is worth to note that thermoregulatory responses of occupants to discomfort are used as indicators of thermal comfort. Similarly, for the metabolic rate, Heart Rate (HR) and Skin Temperature (ST) are used separately as an indicator of the parameter [11]. For instance, Choi et al. [19] stated that metabolic rate is meaningfully related with the HR, specifically in males with high body mass index occupants. Moreover, the HR is changed with different activities based on the response of thermoregulation. In addition to this study, Revel et al. [20] predicted metabolic rate with in-situ measurements by measuring the HR of occupants with low-cost sensors. The authors indicated that uncertainty in the estimation of metabolic rate changes the accuracy of PMV as ±0.05. Behind all these measurements, ISO 8996 [11] shows a protocol to predict metabolic rate from the HR. The standard limits the measurements with only neutral thermal environments. Similar to the HR,

ÖZBEY et al.

Determination of Metabolic Rate from Physical Measurements of Heart Rate, Mean Skin Temperature and C...

the ST can be used to predict the metabolic rate of the occupant since the sweating rate highly affects the thermal sensation of occupants. Indeed, the ST is one of the main parts of the thermoregulatory center with core temperature, and the sweat glands are significant thermoregulatory effectors [21]. Bligh [21] proved that sweat rate is affected by metabolic rate by receiving more impulses with the increase of metabolic rate. On the other hand, Le Blanc et al. [22] showed a significant correlation between the ST and thermal sensation. However, the subjects were exposed to experiments only with resting activity. Additionally, Shapiro et al. [23] predicted metabolic rate with sweat loss with respect to activity level. Zhang et al. [24] determined metabolic rate inversely from the proposed PMV method by taking the effects of physiological adaptation on metabolic rate into account. The authors determined a linear model of metabolic rate as a dependent parameter by using indoor air temperature (T_i) and air velocity (v_a) as independent parameters in the model. However, the authors also stated that the model is valid for a specific given activity task and should be repeated and re-developed for different activities. On the other hand, researchers showed that carbon dioxide production of the human body reflects the rate of body metabolism [25-28]. For instance, Na et al. [29] developed a deep learning system which predicts the M with the parameters of CO_2 concentration apart from the HR. However, the authors included only 8 activity tasks in the paper. Detailed studies on the relationship of metabolic rate with the physical parameters can be found in [30-32].

According to the authors' knowledge, there is no study in the literature which determines metabolic rate from real-time measurements of the heart rate, mean skin temperature and carbon dioxide variation. Since older adults generally show a lower metabolic rate than younger, subjects with different ages, sex and various body mass indices are also investigated in this study.

2. MATERIALS AND METHODS

The methods of the study consist of measurements and experiments on weekdays between 8.30 and 17.30 from 11th of August to 20th of October 2020 and data analysis. University Human Research Ethics Committee has given ethics approval to the activity to be carried out within the scope of this research study.

2.1. Measurements

The experiments were conducted in an air-tight climate chamber (Length: 4.7 m, Width: 3.25 m, Height: 2.8 m) under neutral thermal conditions (T_i=22°C and RH=50%) (Fig.1). Environmental parameters were controlled via a Heating, Ventilating and Air-Conditioning (HVAC) system, which was existed in the climate chamber. However, the climate chamber has a fixed air volume in order to store respiratory air. Even though the impact of environmental parameters on metabolic rate is very small in low variations of the parameters [28-33]. environmental parameters were measured and checked via objective sensors every 10 minutes in order to satisfy neutral thermal conditions. DHT22 [34] was used for the air temperature and relative humidity measurements, while an anemometer – TESTO 425 [35] – was placed in order to measure air velocity inside the chamber.
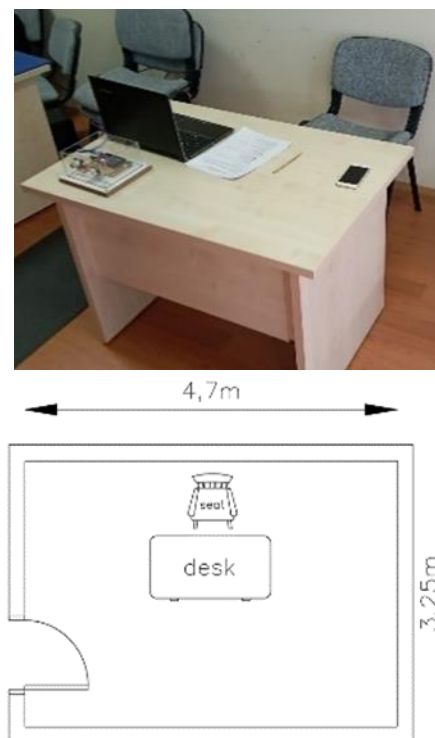
Figure 1 Climate-chamber used in the study.

ÖZBEY et al.

Determination of Metabolic Rate from Physical Measurements of Heart Rate, Mean Skin Temperature and C...

The door of the chamber was fully sealed and kept closed during experiments. The airtightness of the chamber was calculated as 0.1 1/h.

ISO 8996 [11] advice to use the measurement of carbon dioxide production to determine the metabolic rate with metabolic carts. However, metabolic carts are quite expensive and difficult to use for resting activities. For this reason, CO_2 production was assumed to be equal to the difference of CO_2 variation between pre-and post-activities, respectively (Eq.1).

$$\Delta CO_2 = CO_{2aa} - CO_{2ref} \qquad (1)$$

Where ΔCO_2 depicts the carbon dioxide variation in the air-tight climate chamber, CO_{2aa} is carbon dioxide concentration level after activity, while CO_{2ref} is the reference carbon dioxide concentration level of unoccupied climate chamber and is 400 ppm [36].

CO_2 concentration level was measured with the MG811 [37] sensor. Before the experiments, the uniformity of CO_2 distribution was tested and validated by measuring the CO_2 concentration level at different locations of the chamber. It is worth to note that CO_2 measurements were taken automatically by using microcontrollers in order to avoid researcher existence in the test chamber.

The sensors were placed at a 1.1 m level according to ASHRAE 55 [4]. Heart Rate was measured with a smart wristband – Xiaomi Mi Band 3 [38] – and skin temperatures were taken from 8 different points of the human body with an infrared thermometer – EXTECH 42530 [39] – simultaneously (Fig.2). The specifications of the measurement devices were given in Table 1.

Table 1 The Specifications of the measurement devices used in the study.

Device	Model	Specifications
Temperature and Relative Humidity Sensor	DHT22 [34]	RH Range: 0-100% Temperature Range: -40-80 °C RH Accuracy: +/- 3% (Max +/- 5%) Temperature Accuracy: < +/- 0.5°C
Infrared Thermometer	EXTECH Instruments 42530 [39]	Range: -50 °C to 538 °C Accuracy: ±2% Resolution: 0.1 °C
Anemometer	Testo 425 [35]	Range:0-20 m/s Accuracy: +/- (0.03 m/s +5% of Measured Value) Resolution: 0.1 m/s
Carbon Dioxide Sensor	MG811 [37]	Range: 350-10000 ppm Accuracy: ± 2% (depends on air temperature) Resolution: 1 ppm (depends on air temperature)
Wrist Band	Xiaomi Mi Band 3 [38]	Range: 0-150 bpm Accuracy: 2-4 bpm

The instruments, which were required for doing the activities, such as bed, office chair and desk and sports equipment were placed inside the chamber before the experiments. Experimental conditions inside the chamber are given in Table 2.

Table 2 Experimental conditions in the climate chamber.

	Unit	Average
Indoor Air Temperature	°C	22.1±0.3
Relative Humidity	%	50±2.1
Air Velocity	m/s	0.1±0.01
CO_2 Level	ppm	641±11

2.2. Experiments

Goldman [40] states that the minimum subject in thermal comfort studies should be at least 6 occupants. To this aim, for the experiments, 21 male and 17 female healthy volunteer subjects of different age (from 20 to 66 years) and body mass indices (from 20.23 to 43.44 kg/m^2) were recruited from Ankara/Turkey. The individual physical data of all subjects and demographic information of the subjects are given in Tables 3 and 4, respectively.

ÖZBEY et al.

Determination of Metabolic Rate from Physical Measurements of Heart Rate, Mean Skin Temperature and C...

Table 3 The physical data for all subjects used in the study.

Subject Number	Age (years)	Gender	Body Mass Index (kg/m²)
1	35	Male	22.99
2	26	Male	26.87
3	26	Female	23.66
4	23	Male	43.44
5	66	Male	25.95
6	26	Female	23.05
7	20	Male	21.65
8	20	Female	21.01
9	36	Male	33.18
10	38	Male	40.19
11	40	Male	26.38
12	24	Female	26.11
13	61	Male	31.28
14	54	Male	24.15
15	21	Male	28.89
16	21	Female	35.24
17	27	Male	21.98
18	65	Female	26.54
19	62	Female	24.87
20	31	Male	26.57
21	39	Male	24.45
22	40	Female	38.75
23	39	Male	31.54
24	35	Male	22.28
25	31	Male	39.65
26	24	Female	40.15
27	22	Female	34.25
28	23	Female	21.58
29	22	Female	29.61
30	26	Female	28.65
31	22	Male	30.05
32	21	Female	25.43
33	20	Male	20.96
34	29	Female	21.68
35	25	Male	20.23
36	36	Female	25.55
37	39	Male	29.81
38	41	Female	37.86

Table 4 The physical data for all subjects used in the study.

	Female	Male	Total
Subject Number	17	21	38
Age (years)	31.05 ±13.38	34.66±11.6	33.05±13.06
Body Mass Index (kg/m²)	28.47±6.19	28.21±6.40	28.32±6.31

All subjects were free of hypertension, asthma, coronary heart disease, or type 2 diabetes since

these diseases can cause disorders of respiration and metabolic rate [41]. Before the experiments, the subjects were informed of the aim and procedure of the study. Moreover, a commitment form, which explains that students are avoided from the factors such as vigorous physical activity before the experiments, caffeine, alcohol and smoking, which affect metabolic rate, heart rate and skin temperature, was designed to sign for all subjects. Additionally, the subjects were requested to wear the same garments (underwear, T-shirt, shorts, socks, and gym shoes) with a clothing value of 0.42 clo. The experiments were conducted in 19 different activity tasks, including sleeping, writing, dancing, and house cleaning. The activity tasks, which were included in the study, are depicted in Table 5. It is obvious that some activity tasks, i.e., handling 50 kg bags, were not suitable for female and/or older subjects. Therefore, these activities were only requested for younger (below 35 ages) male subjects. In the table, average values are taken for the activity tasks, which have a range of met values.

Table 5 The physical data for all subjects used in the study.

Test Activity	Activity Code	Met value in ASHRAE 55	W/m²
Resting			
Sleeping	R1	0.7	40
Reclining	R2	0.8	45
Walking			
0.9 m/s, 3.2 km/h	W5	2	115
1.2 m/s, 4.3 km/h	W6	2.6	150
1.8 m/s, 6.8 km/h	W7	3.8	220
Office Activities			
Reading, seated	O8	1	55
Writing, seated	O9	1	60
Typing, seated	O10	1.1	65
Filling, seated	O11	1.2	70
Filling, standing	O12	1.4	80
Walking about	O13	1.7	100

ÖZBEY et al.

Determination of Metabolic Rate from Physical Measurements of Heart Rate, Mean Skin Temperature and C...

Lifting, packing	O14	2.1	120
Miscellaneous Occupational Activities			
House Cleaning*	MOA15	2 to 4	115-200
Seated, heavy limp movement	MOA16	2.2	130
Handling 50 kg bags**	MOA17	4	235
Miscellaneous Leisure Activities			
Dancing, social	MLA18	2.4 to 4.4	140-255
Calisthenics, exercise	MLA19	3 to 4	175-235
***The subjects were requested to clean desk and floor in the climate chamber**			
***** This activity is requested just for young male subjects (below 35 ages)**			

Subjects were allowed to enter to the climate chamber in order and requested to do 19 different activity tasks, as shown in Table 5. Each subject was exposed to each activity for 30 minutes (Fig.3). Once the experiment was completed on a subject, a 10-minutes break was given not to lose neutral thermal conditions in the chamber for the next activity.

After the experiment days for an activity task for all subjects, another activity was conducted the day after. In the experiments, heart rate, mean skin temperatures and carbon dioxide concentration levels were taken after 10 minutes later from the beginning of the activity with 1-minutes interval. Simultaneously, environmental conditions including air temperature, relative humidity and air velocity were measured in order to ensure consistent neutral thermal conditions. The heart rate of subjects was taken from their wrist while skin temperatures were measured from 8 different points of the human body as advised in the ASHRAE 55 [4] (Fig.2).

Figure 2 Measurement points on the human body (Note: All measurements were taken from naked skin of the human body).

The eight-point weighted method was used to calculate mean skin temperature (MST) according to Eq.2 [42].

$$MST = 0.07T_{forehead} + 0.175T_{chest} + 0.175T_{back} + 0.07T_{upperarm} + 0.07T_{lowerarm} + 0.05T_{hand} + 0.19T_{thigh} + 0.2T_{calf} \qquad (2)$$

Figure 3 A sample subject while doing different activities during experiments a) seated, quiet (R3); b) typing, seated (O10); c) filling, seated (O11); d) standing, relaxed (R4); e) standing, filling (O12); f) sleeping (R1).

ÖZBEY et al.

Determination of Metabolic Rate from Physical Measurements of Heart Rate, Mean Skin Temperature and C...

Once all experiments with 19 different activity tasks for a subject were completed, a set of experiments were conducted for other subjects with the same experimental procedure. The collected data were then automatically uploaded on a computer through a data acquisition interface which was developed by the authors. The general methodology of the experiments is shown in Figure 4.
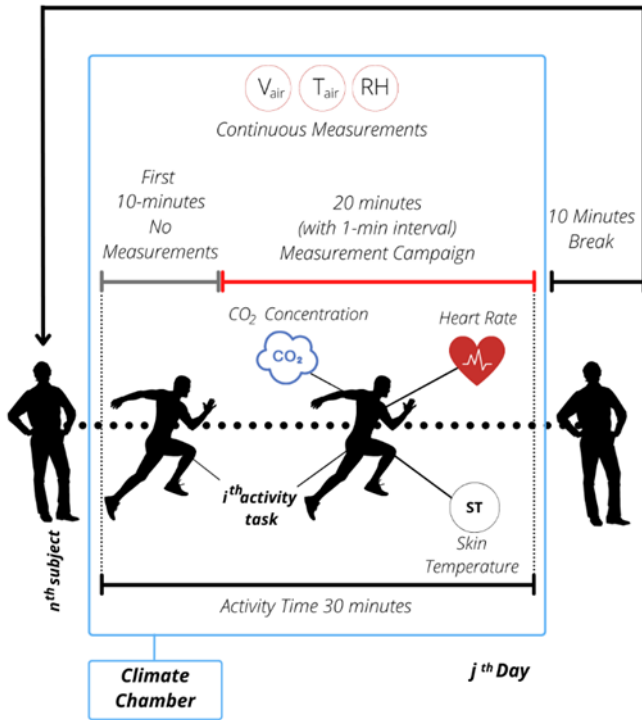
Figure 4 The methodology of the experiments.

2.3. Data Analysis

For data analysis, Multivariable Non-Linear Regression (MNLR) analysis method was used in MATLAB [43]. The MNLR is used to explain the relationship between one dependent variable and two or more independent parameters [44,45]. A general expression for a non-linear regression equation involving multiple parameters is shown in Eq.3.

$$M = a(HR)^e + b(MST)^f + c(\Delta CO_2)^g + d \quad (3)$$

The results of the equation, then, compared with the ASHRAE 55 [4] table and expressed in terms of statistical error, i.e., Normalized Root Mean Squared Error (NRMSE) according to Equation 4. The Determination of Multiple Coefficient (R^2) was used in order to validate the accuracy of the equation by using the following formula (Eq.5). One sample t-test was used in the study for comparison. The significance was tested and accepted at a .05 p-value.

$$R^2 = \frac{\sum_i (\hat{y}_i - \overline{y})^2}{\sum_i (y_i - \overline{y})^2} \quad (4)$$

$$NRMSE = \frac{\sqrt{\sum_{i=1}^{n} \frac{(\hat{y}_i - y_i)^2}{n}}}{y_{max} - y_{min}} \quad (5)$$

Where y_i represents the observed value for i^{th} data. Besides, $\hat{y}$, $\overline{y}$, y_{max} and y_{min} refer to the predicted value of data for observation i, the mean value of data set, maximum and minimum values of data, respectively. Additionally, it is worth to say that n represents the total amount of data.

Sensitivity analysis is used to investigate the most influencing parameter on the models. To this aim, the model was subjected to sensitivity analysis to determine the effect of each input variable on the metabolic rate. A detailed procedure on sensitivity analysis used in the study is found in [46].

3. RESULTS AND DISCUSSION

A total number of 16.781 data from 38 subjects were investigated in order to determine metabolic rate from the heart rate, mean skin temperature and carbon dioxide variation. 80% of the data was used for calibration of the equation, while the rest was used for validation. Table 6 represents the model statistics in detail.

ÖZBEY et al.

Determination of Metabolic Rate from Physical Measurements of Heart Rate, Mean Skin Temperature and C...
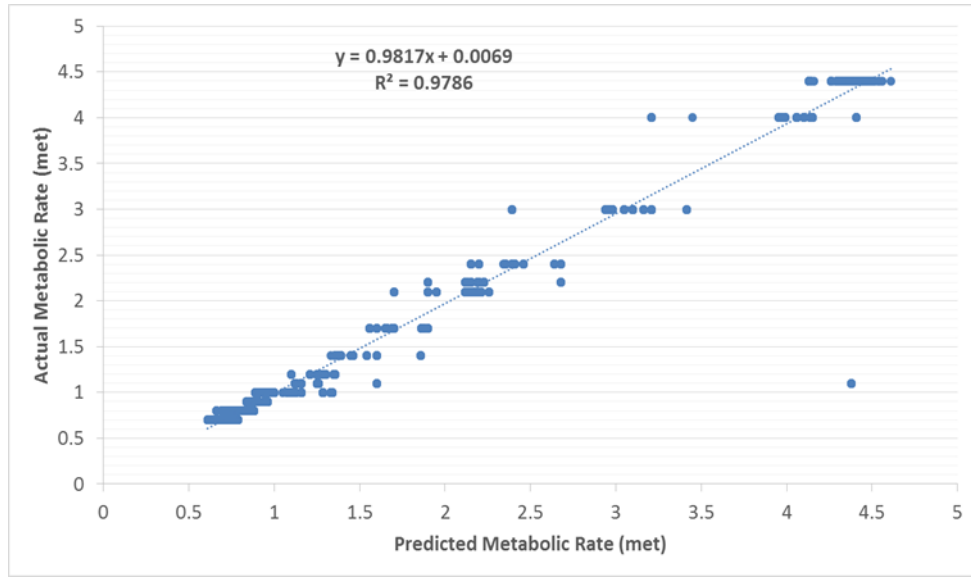
Figure 5 Comparison between predicted and actual metabolic rate.

Table 6 Model statistics for metabolic rate prediction.

	Unit	Model	t-value	p-value
Intercept (d)	-	0.19**	2.59	.009
HR	bpm	0.03**	2.68	.007
MST	°C	0.06**	2.58	.009
ΔCO₂	ppm	0.05*	2.17	.031
R²		0.97		

NOTES

1) e, f and g were found as 0.3, 0.2 and 1.1, respectively.

2) * significance at 5%, ** significance at 1%

Performing the values in Table 6, the Equation 3 is formed as;

$$M = 0.03(HR)^{0.3} + 0.06(MST)^{0.2} + 0.05(\Delta CO_2)^{1.1} + 0.19 \quad (6)$$

The estimating equation with three independent parameters determines the M with an accuracy of 97% and NRMSE of 3.9×10^{-5} "met" value. The model result indicated that there is a significant and positive relationship between HR and M at 1% significance. Similarly, MST is significant at 1% with a positive coefficient. However, ΔCO_2 is found to be significant at 5% with a positive coefficient. Figure 5 depicts the relationship between actual and predicted M values. It is worth to remind that actual values are "met" values in

the direct look up table, which is standardized in the thermal comfort standards. On the other hand, predicted values are obtained from the Equation 6. The figure indicates that there is a minor difference in small "met" values (i.e., resting activity tasks) while larger discrepancies are found in larger "met" values (i.e., miscellaneous leisure activities). The reason of this discrepancy may be the variety of the state of doing activities with large "met" values of subjects. For instance, one subject can dance in a fast way while another is slow. However, "dancing, social" has an average "met" value of 3.4 for both genders. This assumption reduced the accuracy of the model. In addition, body mass indices of male subjects are generally higher than female ones. With high activity tasks, high body mass index values limit subjects to do activities in proper ways.

Figure 6 represents the heart rate variation for several activity tasks for males. The thin lines depict the standard deviation of the values, while the black boxes show the average heart rate with respect to the corresponded activity task. The largest HR is found with "Dancing, social" (MLA18) activity tasks with 111 bpm, while the lowest HR is seen in sleeping (R1) with 70 bpm for males. Shifting activity from sleeping to reclining changes HR as 1 bpm for male subjects.

ÖZBEY et al.

Determination of Metabolic Rate from Physical Measurements of Heart Rate, Mean Skin Temperature and C...

Figure 7 indicates the HR variation with several activity tasks for females. Unlike the males, the

lowest HR is found while "sleeping (R1)" and "filling, seated (O11)" activity tasks.
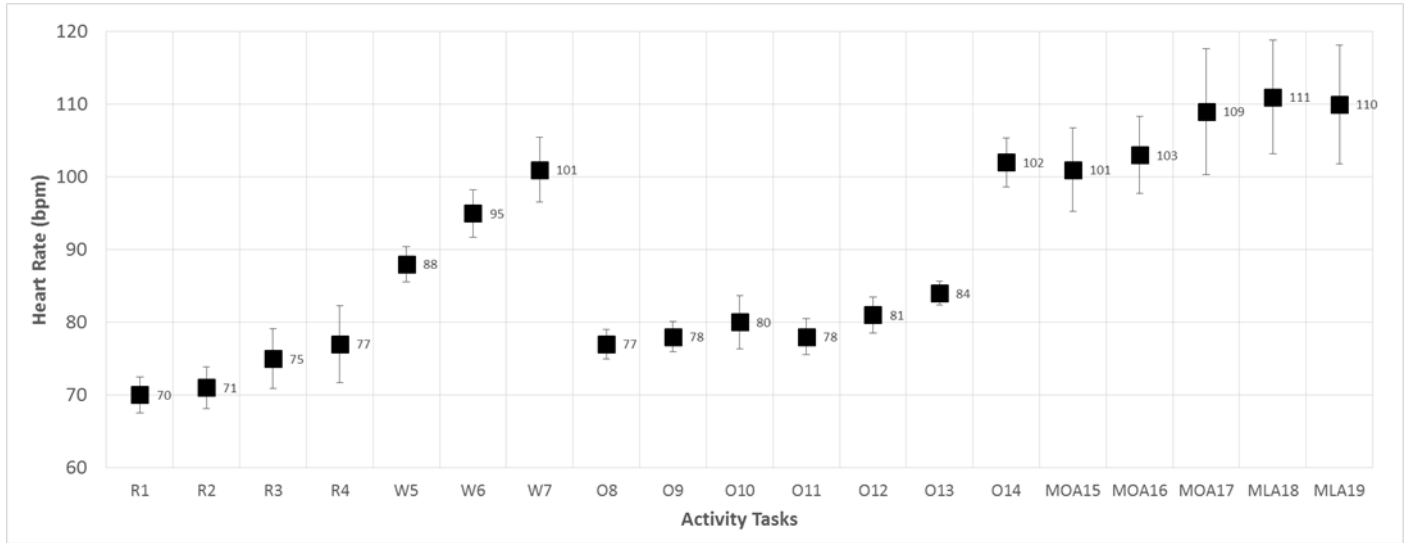
Figure 6 Heart rate variation with different activity tasks for males.
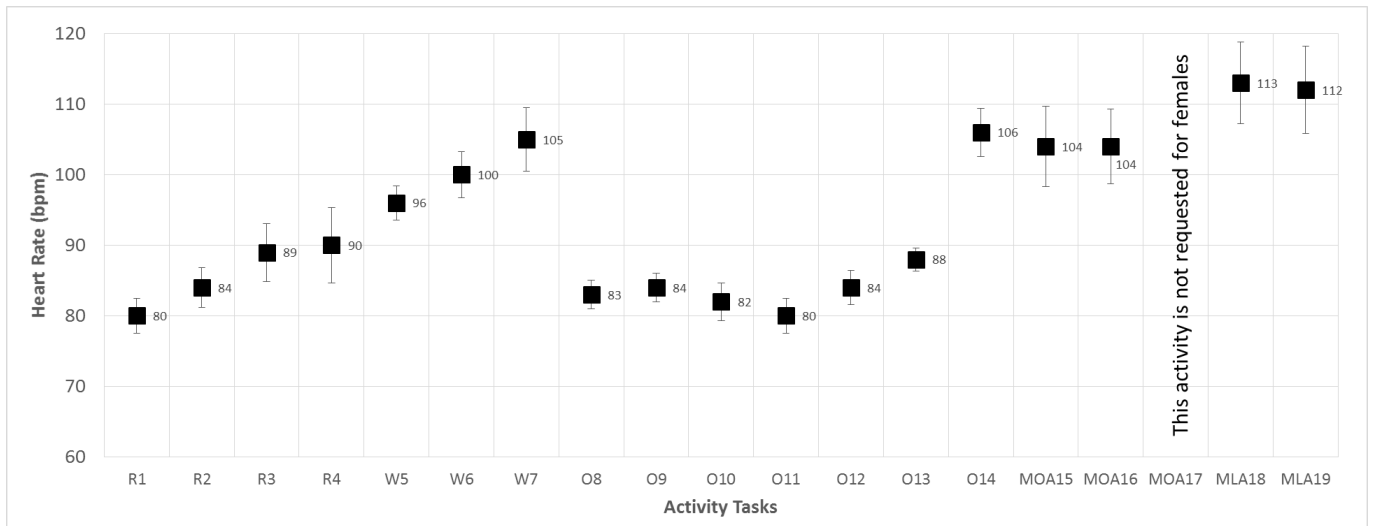
Figure 7 Heart rate variation with different activity tasks for females.

However, the largest HR is obtained while "dancing, social (MLA18)" activity similar to the males. It is worth to remind that "handling 50 kgs bags (MLA17)" is not requested for female subjects due to the activity can cause injury problems.

Figure 8 and 9 show MST variation with respect to different activity tasks. The largest MST values are obtained in MLA19 activity task as 38.2 and 38.4°C for male and female, respectively. The lowest MST values are in sleeping activity (R1) with 35.4 and 36.1°C for male and female,

respectively. The carbon dioxide variation shows a strong relationship with activity tasks (Figs.10 & 11). For instance, the change in carbon dioxide concentration during the high metabolic conditions was higher than the others. The lowest carbon dioxide variation is found in "reclining" activity (R^2) for each gender. One can think the least ΔCO_2 could be found in "sleeping" (R1) activity task. However, it is worth to remind that there are three main stages of sleeping such as light sleep, REM and deep sleep [47]. In the REM stage, the brain is very active, which means that CO_2 production is the same or even larger than

ÖZBEY et al.

Determination of Metabolic Rate from Physical Measurements of Heart Rate, Mean Skin Temperature and C...

other light activities. The subjects in the study could be in the REM stage while sleeping, which increases the carbon dioxide variation in the climate chamber. Another noteworthy result is that the ΔCO_2 value is always larger for male subjects than female subjects in every activity tasks. The reason is the larger CO_2 production of male subjects, as indicated in [33].
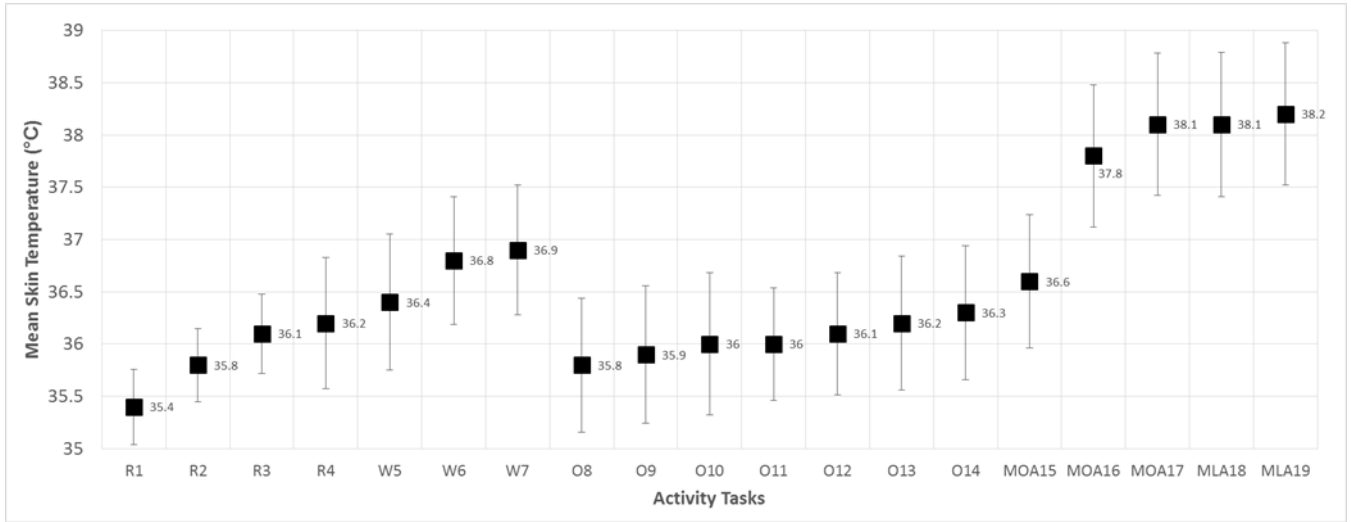
Figure 8 Mean skin temperature variation with respect to different activity tasks for males.
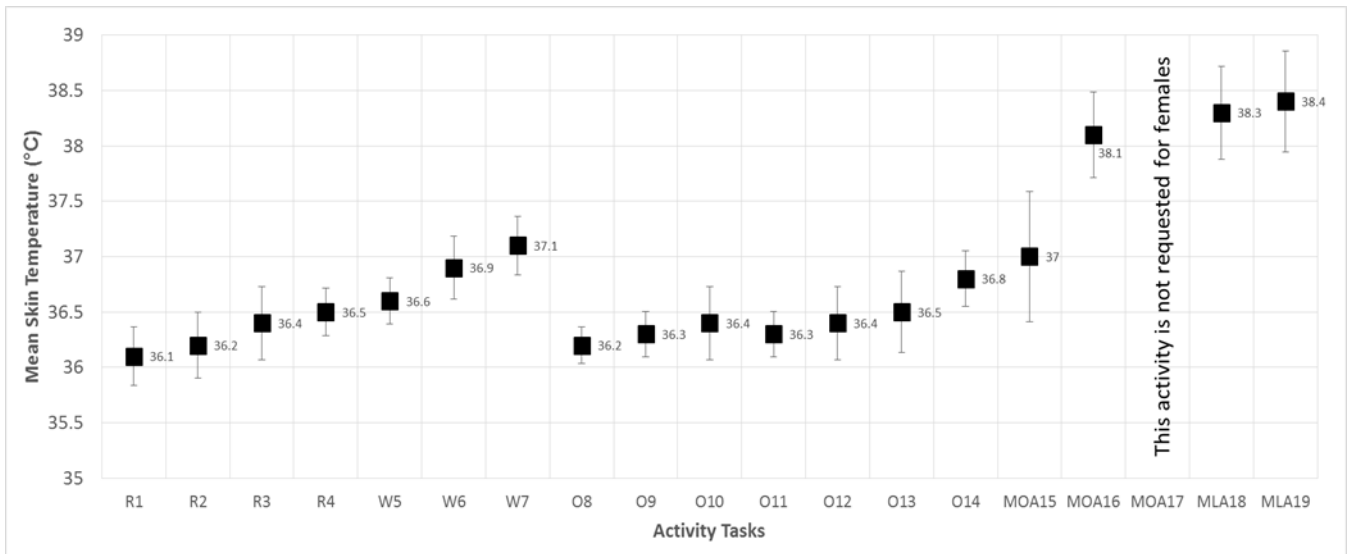
Figure 9 Mean skin temperature variation with respect to different activity tasks for females.
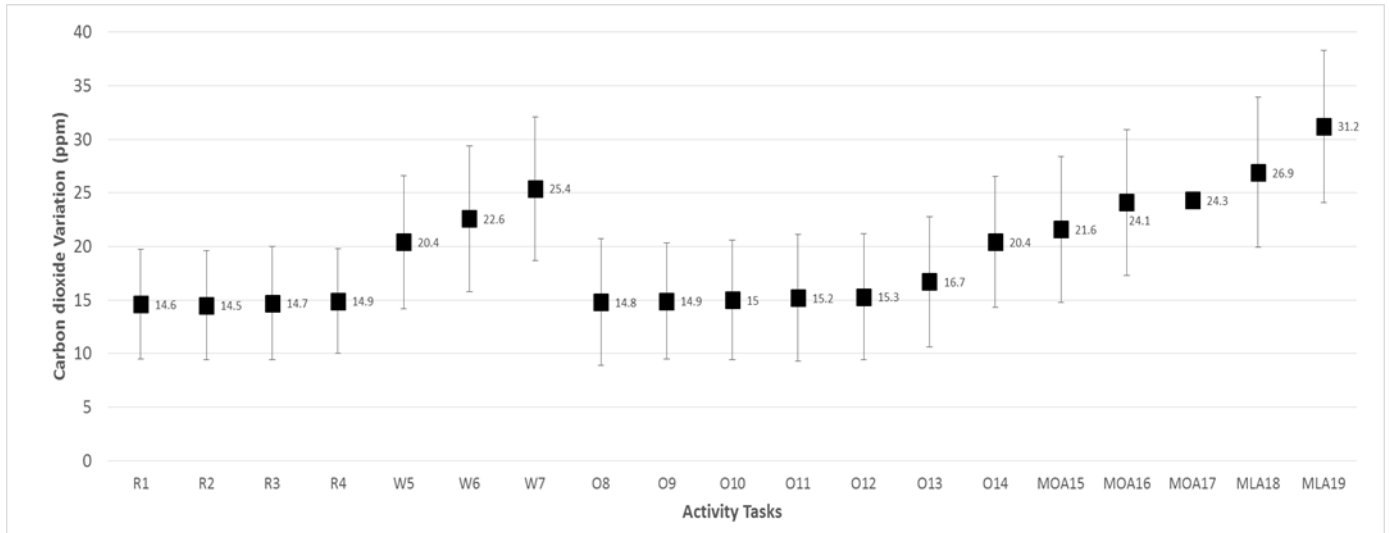
Figure 10 Carbon dioxide variation with respect to different activity tasks for males.
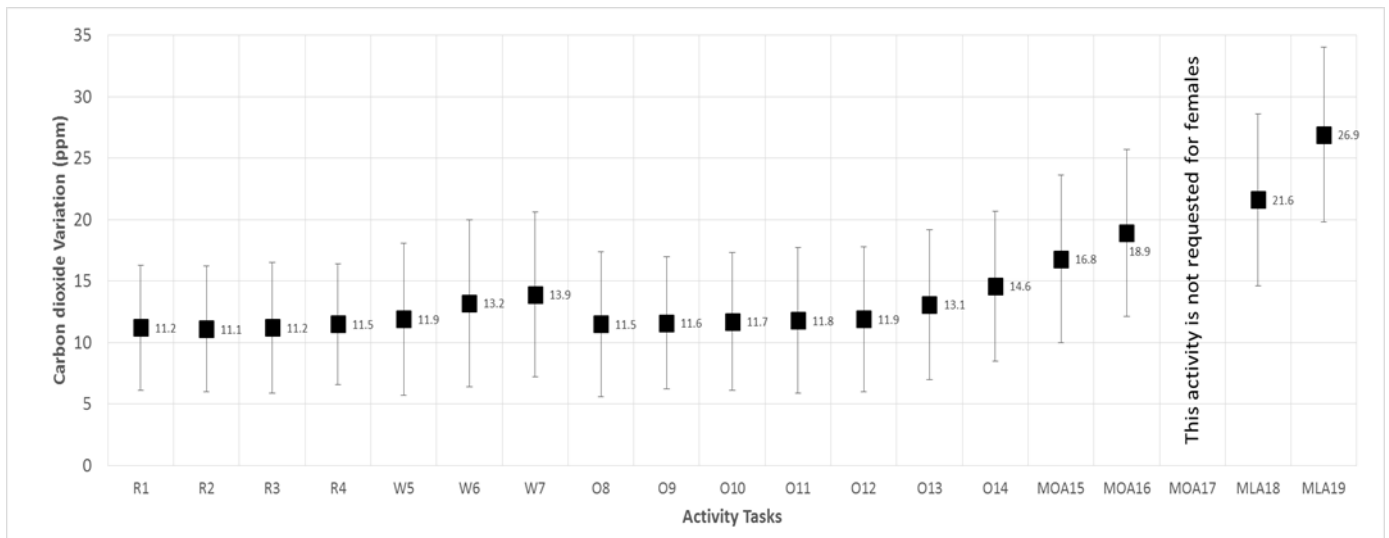
Figure 11 Carbon dioxide variation with respect to different activity tasks for females.

As an additional study, a sensitivity analysis was displayed for the study and the results were shown in Figure 12. Three parameters of the M formula were included in the analysis. The figure represents that HR is the most influencing parameter with 40% sensitivity while ΔCO_2 was found to be the least impact on determining the M. However, the results indicate that none of the parameters could be eliminated from the formula since the sensitivities of the parameters are above 20%.

Finally, the sensitivity analysis is re-obtained for age and gender variations, as shown in Figure13.

It is worth to note that the subjects below 35 ages are assumed as young in the analysis.

Notwithstanding the HR is found as the most influencing parameters for each gender and age group, the effect of HR increases with age in the M prediction. A noteworthy finding is that the MST affects the M in female subjects lower than male subjects. The reason could be the variations of blood flow in females. Slower blood flow than male subjects affect the importance of the MST in the M prediction as indicated in [48].

ÖZBEY et al.

Determination of Metabolic Rate from Physical Measurements of Heart Rate, Mean Skin Temperature and C...
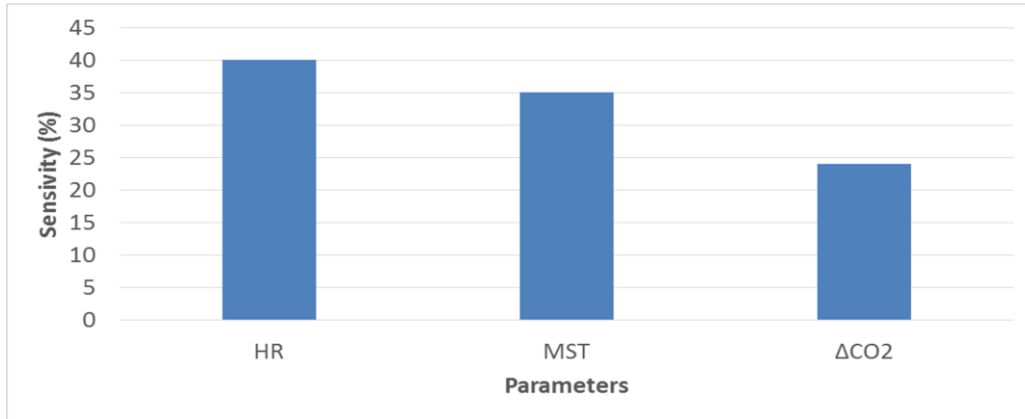
Figure 12 Results of sensitivity analysis for metabolic rate formula.
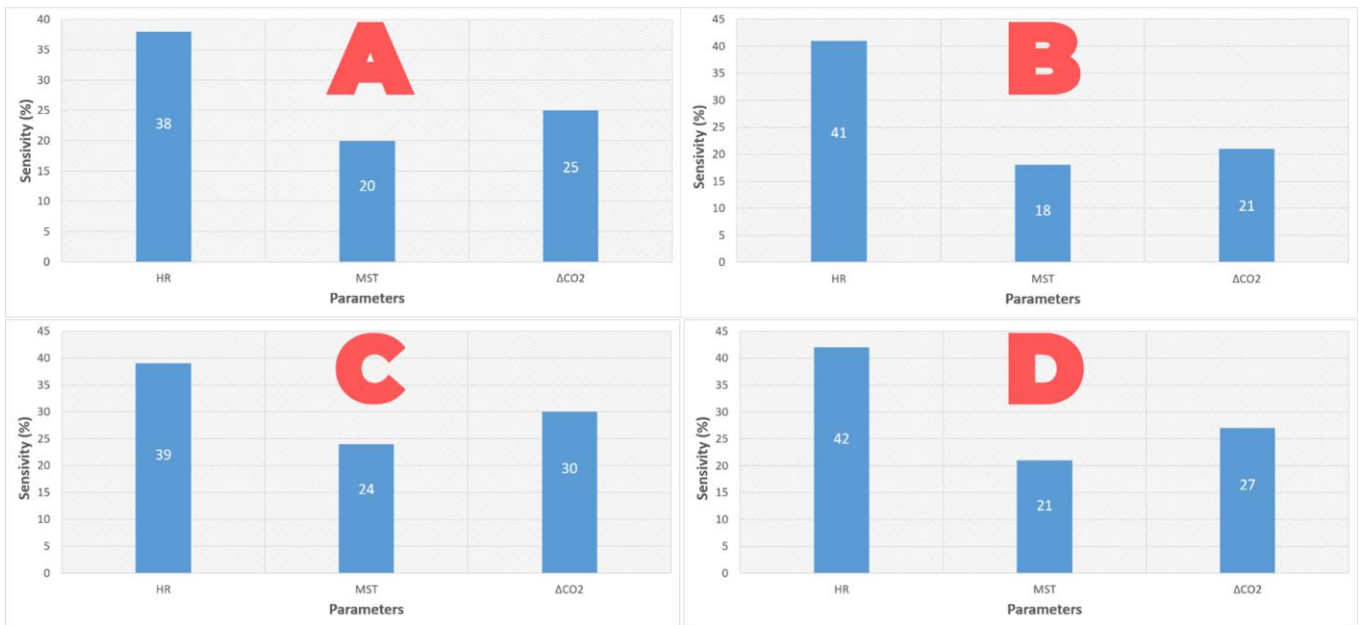
Figure 13 Sensitivity analysis for a) young female subjects b) adult female subjects c) young male subjects d) adult male subjects.

In addition, the importance of the MST decreases with increased ages for each gender. Similarly, the influence of the carbon dioxide variation decreases when the age increases for each gender. The reason could be the higher BMR of the young subjects than adults. Indeed, the BMR highly affects the exhalation and thus carbon dioxide production, as indicated in [49].

3.1. Limitations

Individual differences, such as personal factors like race, gender, age, weight, etc., can cause different metabolic rates as indicated in [50,51]. The experiments in this study were conducted with only Turkish subjects. The cultural differences and ethnical background may limit the use of equations and findings of the study for other populations. More accurate results would be obtained with subjects from different populations.

ÖZBEY et al.

Determination of Metabolic Rate from Physical Measurements of Heart Rate, Mean Skin Temperature and C...

On the other hand, metabolic rates are only predicted based on activities. However, the Basal Metabolic Rate (BMR), which represents the energy essential for life, for example, to maintain the body temperature and cardiac and respiratory functions of each subject, is different. By adding the BMR to the calculations (i.e., with Harris-Benedict formula [52] more accurate results would be obtained to predict the M. A report of the Food and Agriculture Organization of the United Nations advised that the M can be calculated by multiplying the BMR with a factor that characterizes the specific activity tasks [53].

Sweat rates could also affect the accuracy of metabolic rate determination, as indicated in [54]. However, this parameter varies with individuals and requires depth examination. The investigation of the effect of sweat rate on the M was out of the scope of this paper.

Dynamic changes of activity and environmental parameters should also be taken into consideration. Occupants are usually prone to do different activities during day, therefore, a combined approach is required to predict metabolic rates.

In the study, all subjects were requested to wear the same garments with a calculated 0.42 clo value. When the subjects have wider tolerance to adopt their garments to the real environments, i.e., living laboratories or residential buildings, the values in this study can lead to different results as indicated in [55].

In the present study, predicted M values derived from commonly used multivariable non-linear regression equation. Machine Learning techniques such as Artificial Neural Network [56,57] and Fuzzy Logic [58,59] models should also be derived for the prediction. These artificial intelligence models successfully predicted the thermal comfort of the occupants in past studies [1,56]. By applying similar strategies to the M prediction, the accuracy of the model would be increased.

Finally, in study of Luo et al. [60] it is indicated that the metabolic rate may change without activity changes. The authors concluded that the variation of ambient parameters affects the metabolic rate. Even though this study estimates the metabolic rate from ambient parameters and compares the results with "met" values in activity tables, further studies should focus on this issue for improving the accuracy of the models.

4. CONCLUSIONS

This paper aimed to predict metabolic rate from field-measurements of heart rate, mean skin temperature and carbon dioxide variation. A mathematical model was established according to experimental data. The results showed that metabolic rate could be predicted with high accuracy (R^2=0.97). HR and MST were found as significant in 1%, while carbon dioxide variation was significant at 5% in the M estimation. However, some discrepancies were found between the measured metabolic rate and existing international comfort standards. Larger differences were obtained with higher metabolic rates for each gender.

Future studies will include basal metabolic rate in metabolic rate estimations and develop better metabolic rate equations by taking other individual differences such as pregnancy situation and race of the subjects into account.

The outcome of this study can enlighten architects and engineers to calculate M in different functional architectures such as sports venues and educational buildings and, nevertheless, to design energy-efficient and fully comfortable environments for occupants.

The Declaration of Conflict of Interest/ Common Interest

No conflict of interest or common interest has been declared by the authors.

ÖZBEY et al.

Determination of Metabolic Rate from Physical Measurements of Heart Rate, Mean Skin Temperature and C...

Authors' Contribution

The authors contributed equally to the study.

The Declaration of Ethics Committee Approval

University Human Research Ethics Committee has given ethics approval to the activity to be carried out within the scope of this research study.

The authors declare that they have no known competing financial interests or personal relationships that could have appeared to influence the work reported in this paper.

The Declaration of Research and Publication Ethics

The authors of the paper declare that they comply with the scientific, ethical and quotation rules of SAUJS in all processes of the paper and that they do not make any falsification on the data collected. In addition, they declare that Sakarya University Journal of Science and its editorial board have no responsibility for any ethical violations that may be encountered, and that this study has not been evaluated in any academic publication environment other than Sakarya University Journal of Science.

REFERENCES

[1] Z. Deng, and Q. Chen, "Artificial neural network models using thermal sensations and occupants' behavior for predicting thermal comfort", Energy and Buildings, vol. 174, pp. 587-602, 2018.

[2] P. O. Fanger, "Thermal comfort. Analysis and applications in environmental engineering", Copenhagen, Denmark: Danish Technical Press, 1970.

[3] Ergonomics of the thermal environment-instruments for measuring physical quantities, 7726, International Standardization Organization, Geneva, Switzerland, 1998.

[4] Thermal Environment Conditions for Human Occupancy, 55, American Society of Heating, Refrigerating and Air-Conditioning Engineers, Atlanta, USA, 2020.

[5] Ergonomics of the thermal environment — Analytical determination and interpretation of thermal comfort using calculation of the PMV and PPD indices and local thermal comfort criteria, 7730, International Standardization Organization, Geneva, Switzerland, 2005.

[6] G. Havenith, I. Holmér, and K. Parsons. "Personal factors in thermal comfort assessment: clothing properties and metabolic heat production", Energy and Buildings, vol. 34(6), pp. 581-91, 2002.

[7] Ergonomics of the thermal environment - Estimation of thermal insulation and water vapour resistance of a clothing ensemble, 9920, International Standardization Organization, Geneva, Switzerland, 2007.

[8] J. Van Hoof "Forty years of Fanger's model of thermal comfort: comfort for all?", Indoor Air, vol. 18(3), pp. 182-201, 2008.

[9] L. M. Chamra, W. G. Steele, and K. Huynh, "The uncertainty associated with thermal comfort". ASHRAE Transactions, vol. 109, pp. 356-365, 2003.

[10] M. Luo, Z. Wang, K. Ke, B. Cao, Y. Zhai, and X. Zhou, "Human metabolic rate and thermal comfort in buildings: The problem and challenge". Building and Environment, vol. 131, pp. 44-52, 2018.

[11] Ergonomics of the thermal environment - Determination of metabolic rate, 8996, International Standardization Organization, Geneva, 2004.

[12] M. H. Khan, and W. Pao, "Thermal comfort analysis of PMV model prediction in air conditioned and naturally ventilated buildings". Energy Procedia, vol. 75, pp. 1373-1379, 2015.

ÖZBEY et al.

Determination of Metabolic Rate from Physical Measurements of Heart Rate, Mean Skin Temperature and C...

[13] F. R. Alfano, B. I. Palella, and G. Riccio, "The role of measurement accuracy on the thermal environment assessment by means of PMV index". Building and Environment, vol. 46(7), pp. 1361-1369, 2011.

[14] M. A. Humphreys, and J. F. Nicol, "The validity of ISO-PMV for predicting comfort votes in every-day thermal environments". Energy and Buildings, vol. 34(6), pp. 667-684, 2002.

[15] C. Yang, T. Yin, and M. Fu, "Study on the allowable fluctuation ranges of human metabolic rate and thermal environment parameters under the condition of thermal comfort". Building and Environment, vol. 103, pp. 155-164, 2016.

[16] P. O. Fanger and J. Toftum, "Extension of the PMV model to non-air-conditioned buildings in warm climates". Energy and Buildings, vol. 34(6), pp. 533-536, 2002.

[17] E. E. Broday, A. A. de Paula Xavier, and R. de Oliveira, "Comparative analysis of methods for determining the metabolic rate in order to provide a balance between man and the environment". International Journal of Industrial Ergonomics, vol.44(4), pp. 570-580, 2014.

[18] Y. Zhai, M. Li, S. Gao, L. Yang, H. Zhang, E. Arens, and Y. Gao, "Indirect calorimetry on the metabolic rate of sitting, standing and walking office activities". Building and Environment, vol. 145, pp. 77-84, 2018.

[19] J. H. Choi, V. Loftness, and D. W. Lee, "Investigation of the possibility of the use of heart rate as a human factor for thermal sensation models". Building and Environment, vol. 50, pp. 165-175, 2012.

[20] G. M. Revel, M. Arnesano, and F. Pietroni, "Integration of real-time metabolic rate measurement in a low-cost tool for the thermal comfort monitoring in AAL environments". Ambient assisted living, Springer International Publishing, Cham, pp. 101-110, 2015.

[21] J. Bligh, "Thermoregulation: what is regulated and how?" in New trends in thermal physiology, Y. Houdas, and J. D. Guieu, Eds., Paris, France, Masson, pp. 1-10, 1978.

[22] J. LeBlanc, B. Blais, B. Barabe, and J. Cote, "Effects of temperature and wind on facial temperature, heart rate, and sensation". Journal of Applied Physiology, vol. 40(2), pp. 127-131, 1976.

[23] Y. Shapiro, K. B. Pandolf, and R. F. Goldman, "Predicting sweat loss response to exercise, environment and clothing". European Journal of Applied Physiology and Occupational Physiology, vol. 48(1), pp. 83-96, 1982.

[24] S. Zhang, Y. Cheng, M. O. Oladokun, Y. Wu, and Z. Lin, "Improving predicted mean vote with inversely determined metabolic rate". Sustainable Cities and Society, vol. 53, 101870, 2020.

[25] D. Willner, and C. Weissman, "Carbon dioxide production, metabolism, and anesthesia", Capnography, J. Gravenstein, M. Jaffe, N. Gravenstein, and D. Paulus, Eds., Cambridge UK: Cambridge University Press, pp. 239-249, 2011.

[26] J. Takala, "Oxygen Consumption and Carbon Dioxide Production: Physiological Basis and Practical Application in Intensive Care", in Proceedings of the 11th Postgraduate Course in Critical Care Medicine, Trieste, Italy, pp. 155-162, 1996.

[27] J. Orr, "Evaluation of a Novel Resting Metabolic Rate Measurement System.", korr.com. https://korr.com/wp-content/uploads/ReeVue-Evaluation-of-a-Novel-Resting-Metabolic-Rate-Measurement-System_Orr_2002.pdf (Accessed Jul. 15, 2021).

[28] M. Luo, X. Zhou, Y. Zhu, and J. Sundell, "Revisiting an overlooked parameter in thermal comfort studies, the metabolic

ÖZBEY et al.

Determination of Metabolic Rate from Physical Measurements of Heart Rate, Mean Skin Temperature and C...

rate". Energy and Buildings, vol. 118, pp. 152-159, 2016.

[29] H. Na, H. Choi, and T. Kim, "Metabolic rate estimation method using image deep learning". Building Simulation, vol. 13(5), pp. 1077-1093, 2020.

[30] J. Timbal, M. Loncle, and C. Boutelier, "Mathematical model of man's tolerance to cold using morphological factors". Aviation, Space, and Environmental Medicine, vol. 47(9), pp. 958-964, 1976.

[31] E. H. Wissler "A mathematical model of the human thermal system". The Bulletin of Mathematical Biophysics, vol. 26(2), pp. 147-166, 1964.

[32] Y. Zotterman, "Special senses: thermal receptors". Annual Review of Physiology, vol. 15, pp. 357-372, 1953.

[33] W. Ji, M. Luo, B. Cao, Y. Zhu, Y. Geng, and B. Lin, "A new method to study human metabolic rate changes and thermal comfort in physical exercise by CO2 measurement in an air-tight chamber". Energy and Buildings, vol. 177, pp. 402-412, 2018.

[34] DF Robots, "DHT22, Temperature & Relative Humidity Sensor Datasheet", wiki.dfrobot.com. https://wiki.dfrobot.com/DHT22_Temperature_and_humidity_module_SKU_SEN0137 (Accessed Jul. 15, 2021).

[35] Testo, "Testo 425 Anemometer Datasheet", testo.com. https://www.testo.com/en-UK/testo-425/p/0560-4251 (Accessed Jul. 15, 2021).

[36] Global Monitoring Laboratory 2020. "Trends in Atmospheric Carbon Dioxide", esrl.noaa.gov. https://www.esrl.noaa.gov/gmd/ccgg/trends (Accessed Jul. 15, 2021).

[37] DF Robots, "MG811 Carbon-dioxide Sensor Datasheet", wiki.dfrobot.com. https://wiki.dfrobot.com/CO2_Sensor_SK

U_SEN0159#target_0 (Accessed Jul. 15, 2021).

[38] Xiaomi, Mi Band 3, "Wrist Band Datasheet". mi.com https://www.mi.com/uk/mi-band-3/specs (Accessed Jul. 15, 2021).

[39] Extech Instruments, "Extech 42530, Infrared Thermometer Datasheet", extech.com. http://www.extech.com/products/resources/42530_DS-en.pdf (Accessed Jul. 15, 2021).

[40] R. F. Goldman "Environmental ergonomics: Whence what wither". in 11th International Conference on Environmental Ergonomics, Ystad, Sweden, pp. 39-47, 2005.

[41] R. E. Hasson, C. A. Howe, B. L. Jones, and P. S. Freedson, "Accuracy of four resting metabolic rate prediction equations: effects of sex, body mass index, age, and race/ethnicity". Journal of Science and Medicine in Sport, vol.14(4), pp.344-351, 2011.

[42] D. Mitchell, and C. H. Wyndham, "Comparison of weighting formulas for calculating mean skin temperature". Journal of Applied Physiology, vol. 26(5), pp. 616-622, 1969.

[43] MathWorks. MATLAB, R2018b, 2018.

[44] C. Turhan, and G. G. Akkurt "Assessment of thermal comfort preferences in Mediterranean climate: A university office building case". Thermal Science, vol. 22(5), pp. 2177-2187, 2018.

[45] A. S. Nazih, E. Fawwaz, and M. A. Osama, "Medium-term electric load forecasting using multivariable linear and non-linear regression". Smart Grid and Renewable Energy, vol.2(2), pp.126-135, 2011.

[46] C. Turhan, T. Kazanasmaz, I. E. Uygun, K. E. Ekmen, and G. G. Akkurt, "Comparative

ÖZBEY et al.

Determination of Metabolic Rate from Physical Measurements of Heart Rate, Mean Skin Temperature and C...

study of a building energy performance software (KEP-IYTE-ESS) and ANN-based building heat load estimation". Energy and Buildings, vol. 85, pp. 115-125, 2014.

[47] B. Gothe, M. D. Altose, M. D. Goldman, and N.S. Cherniack. "Effect of quiet sleep on resting and CO2-stimulated breathing in humans". Journal of Applied Physiology, vol. 50(4), pp. 724-730, 1981.

[48] A. Bollinger, and M. Schlumpf, "Finger blood flow in healthy subjects of different age and sex and in patients with primary Raynaud's disease". Acta chirurgica Scandinavica. Supplementum, vol. 465, pp. 42-47, 1976.

[49] N. Meunier, J. H. Beattie, D. Ciarapica, J. M. O'Connor, M. Andriollo-Sanchez, A. Taras, C. Coudray, and A. Polito, "Basal metabolic rate and thyroid hormones of late-middle-aged and older human subjects: the ZENITH study". European Journal of Clinical Nutrition, vol. 59(2), pp. 53-57, 2005.

[50] B. Kingma, and V. M. Lichtenbelt, "Energy consumption in buildings and female thermal demand". Nature Climate Change, vol. 5(12), pp. 1054-1056, 2015.

[51] G. Havenith "Metabolic rate and clothing insulation data of children and adolescents during various school activities". Ergonomics, vol. 50(10), pp. 1689-1701, 2007.

[52] J. A. Harris, and F. G. Benedict, "A biometric study of human basal metabolism". National Academy of Sciences of the United States of America, vol. 4(12), pp. 370, 1918.

[53] United Nations University, & World Health Organization, "Human Energy Requirements: Report of a Joint FAO/WHO/UNU Expert Consultation: Rome, 17-24 October 2001 (Vol. 1)", Food & Agriculture Organization.

[54] S. Haddad, P. Osmond, S. King, and S. Heidari "Developing assumptions of metabolic rate estimation for primary school children in the calculation of the Fanger PMV model", in 8th Windsor Conference: Counting the Cost of Comfort in a Changing World, Windsor, UK, pp. 10-13, 2014.

[55] G. Brager, M. Fountain, C. Benton, E. A. Arens, and F. Bauman "A comparison of methods for assessing thermal sensation and acceptability in the field", in Proceedings, Thermal Comfort: Past, Present, and Future, Watford, UK, pp.17-39, 1993.

[56] C. Turhan, T. Kazanasmaz, and G. G. Akkurt, "Performance indices of soft computing models to predict the heat load of buildings in terms of architectural indicators". Journal of Thermal Engineering, vol. 3(4), pp. 1358-1374, 2017.

[57] Z. Karapınar Şentürk, "Artificial Neural Networks Based Decision Support System for the Detection of Diabetic Retinopathy", Sakarya University Journal of Science, vol. 24, no. 2, pp. 424-431, 2020.

[58] Von Grabe J. "Potential of artificial neural networks to predict thermal sensation votes". Applied energy, vol. 161, pp. 412-424, 2016.

[59] M. Erdoğan, "A New Fuzzy Approach for Analyzing the Smartness of Cities: Case Study for Turkey", Sakarya University Journal of Science, vol. 25, no. 2, pp. 308-325, 2021.

[60] M. Luo, W. Ji, B. Cao, Q. Ouyang, and Y. Zhu "Indoor climate and thermal physiological adaptation: Evidences from migrants with different cold indoor exposures". Building and Environment, 98, 30-38, 2016.

Title: Electricity Load Forecasting Using Deep Learning and Novel Hybrid Models

Authors: Muhammed SÜTÇÜ, Kübra Nur ŞAHİN, Yunus KOLOĞLU, Mevlüt Emirhan ÇELİKEL, İbrahim Tümay GÜLBAHAR

Electricity Load Forecasting Using Deep Learning and Novel Hybrid Models

Muhammed SÜTÇÜ*[1], Kübra Nur ŞAHİN[1], Yunus KOLOĞLU[1],
Mevlüt Emirhan ÇELİKEL[1], İbrahim Tümay GÜLBAHAR[1]

Abstract

Load forecasting is an essential task which is executed by electricity retail companies. By predicting the demand accurately, companies can prevent waste of resources and blackouts. Load forecasting directly affect the financial of the company and the stability of the Turkish Electricity Market. This study is conducted with an electricity retail company, and main focus of the study is to build accurate models for load. Datasets with novel features are preprocessed, then deep learning models are built in order to achieve high accuracy for these problems. Furthermore, a novel method for solving regression problems with classification approach (discretization) is developed for this study. In order to obtain more robust model, an ensemble model is developed and the success of individual models are evaluated in comparison to each other.

Keywords: Load forecasting, deep learning, regression by classification.

1. INTRODUCTION

Electricity is one of the most important energy sources all around the world. It has a big impact of development of economies and nations [1]. With developing technology and population, the need for electricity has been increased. The stability of electricity has vital importance in today's society. In order to achieve sustainable economic growth, continuous electricity production and supply are important. Because of the nature of electricity, it cannot be stored. It should be generated and consumed simultaneously [2].

In Turkey, electricity market operations are done on three different markets [3]. First one is "Day Ahead Market". In Day Ahead Market, electricity producer companies and suppliers notify EPIAS (Electricity Market Operations Co.) about the consumption and production hourly quantities for the following day. Purchasing price for electricity is announced after participants notify the system, and it is named "PTF" (Market Clearing Price) [3]. Second market in the electricity operations is called "Intra-day Market". In this market, participants have opportunity to make additional purchase and sell operations in case of unexpected events, such as sudden changes in temperature and failures in the system. Participants create bids of hour, amount and price for the electricity and transactions occur if the price of the offers for given hour in the system are matched. This market

* Corresponding author: muhammed.sutcu@agu.edu.tr
[1] Abdullah Gül University, Faculty of Engineering, Department of Industrial Engineering
E-mail: kubranur.sahin@agu.edu.tr, yunus.kologlu95@gmail.com, mevlutemirhan.celikel@agu.edu.tr, ibrahim.gulbahar@agu.edu.tr
ORCID: https://orcid.org/0000-0002-8523-9103, https://orcid.org/0000-0001-9786-6270, https://orcid.org/0000-0001-6198-569X, https://orcid.org/0000-0001-9264-4345, https://orcid.org/0000-0001-9192-0782

is useful to mitigate the losses caused by the forecasts that are done in the previous day. A new type of electricity price is formed in this market, and it is named "SMF" (System Marginal Price) [3]. SMF is based on the real consumption values, and it is announced at least four hours later than the consumption. The third market is called "Balancing Market" [3]. All plus and negative deviations in the forecasts of the participants are neutralized in this market, and they pay a penalty cost for their forecast errors according to the announced PTF and SMF.

Electricity distribution companies function as a bridge between producers and consumers of electricity. One of the most important concerns of electricity distribution companies is supplying the customer demands. In order to manage electricity demand and minimize financial loss, it is necessary to forecast the usage of electricity in a distribution network. Electricity producers also need to forecast their production in order to minimize their loss from their profit and contribute the stability of Turkish Electricity Market. Because, overproduction as a result of positively deviated forecasts causes the waste of resources and financial loss and underproduction as a result of negatively deviated forecasts may cause technical issues which can lead to power outage [4]. For electricity market participants, making accurate predictions reduces their financial loss besides making their planning activities easier. With this study which will be conducted with an electricity retail company, the operations of the company in the electricity markets will be improved and its financial loss will be reduced. In the company's current system, the forecasts are done intuitional way. Their forecast based on previous year data and current weather condition and the company do not any systematical way of forecasting. The forecasting strategy of the company based on personal experience. Using the personal experience-based forecasting method is not sustainable due to the increasing number of parameters that affect consumption of electricity and complexity of the forecasting. The pattern of electricity consumption depends on many different parameters such as seasons, hours, weekdays, holidays, temperature, humidity, rainfall, cloudage and etc. These parameters make electricity demand forecasting more complex. If the electricity demand of customers is underestimated, the electricity shortage may occur locally or countrywide. Moreover, if the demand overestimated, the surplus energy should be sold in the balancing energy market with at least %3 loss. Therefore, the company faces financial losses due to inaccurate forecasting the electricity consumption. In order to decrease these losses, the company needs more accurate and systematic forecasting method for electricity consumption.

In that study, hourly electricity consumption of a city is forecasted with machine learning approaches. The aims of the study are minimizing the hourly forecasting errors.

In terms of contributions, we developed a novel ensemble method to solve a multivariable and multi-dimensional estimation problem. The proposed method involves discretizing of a large regression problem into small problems and a deep neural network model with optimized hyper parameters. The discretization and deep neural network models are combined so that we obtained a more robust forecasting model. The ensemble model outperforms the two learning models it involves

2. LITERATURE REVIEW

Solar energy systems are the most abundant and preferred renewable energy in the world [5]. There are two ways to convert solar energy into electricity. Sun Thermal Power Plants (STPP) use the heat of beams to transfer direct normal solar irradiance to electricity, whereas Photovoltaic plants turn energy directly into electricity [6]. Worldwide photovoltaic production is steadily increasing, with the International Energy Agency (IEA) estimating that solar generation will meet 2% of global electricity demand by 2030 [7]. As these technologies were more integrated into large-scale power systems, it became necessary to estimate their production [8]. Although energy production from other traditional sources may be easily computed, it is difficult to predict exactly due to the considerable unpredictability in weather conditions. To achieve a successful integration

into the power systems, it is required to estimate output for the coming days and hours.

There are numerous instances of load forecasting models that scientists have applied. In load forecasting, Azedah (2008) used a fuzzy technique to determine the kind of ARMA models [9]. In an electricity forecasting problem, Wang (2008) coupled autoregressive models and moving averages with exogenous factors (such as weather conditions) [10]. To determine the load of power systems, Amjady (2007) used a hybrid model that combined the multilayer perceptron (MLP) neural network and the forecast-aided state estimator (FASE) [11]. Furthermore, several of these authors computed the load by dividing the days into 24-hour intervals or days in a week [12].

For predicting photovoltaic energy, machine learning methods are often utilized. The goal of supervised learning algorithms is to find a mapping between given inputs and outputs [13]. Unsupervised learning models, on the other hand, look for hidden structure between input values without using output variables [14]. In that way, it's equivalent to determining the input distribution. Aside from supervised and unsupervised approaches, it is also effective to combine several successful models to improve overall model performance, which is known as "ensemble learning" [15].

Vapnik developed Support Vector Machine (SVM) which is a supervised learning method for solving classification and regression applications. [16]. The goal of SVM is to determine the optimum hyperplane for accurately separating data into multiple groups. The data points with the shortest distance to the defined hyperplane are referred to as Support Vectors. Sharma, Sharma, Irwin and Shenoy (2011) used machine learning techniques and compared the forecast outcomes of National Weather Service (NWS) [17]. Weather data from January to December 2010 was utilized in their research. Temperature, dew point, wind speed, sky cover, chance of precipitation, and relative humidity are the weather metrics used in the data. Furthermore, days and hours are included in the data. Linear Regression and SVM with Radial Basis Function (RBF) kernel were employed as methods, and training data was taken

between January and August. Principal Component Analysis was used to remove redundant data, and as a consequence of the research, SVM with RBF kernel was found to be more successful with a smaller RMS error. Between January 2010 and October 2010, Shi et al. (2012) conducted a study in China to forecast solar production [18]. The study's data interval is fifteen minutes, and production values are normalized to improve accuracy throughout the preprocessing step. Data was divided into four groups based on weather conditions before being used to develop the model: sunny, foggy, rainy, and cloudy days. As indicated in the study, the RBF kernel was chosen for this purpose because it is the most commonly used kernel. The study found that cloudy days had a 12.42 percent mistake rate, foggy days had an 8.16 percent error rate, rainy days had a 9.12 percent error rate, and sunny days had a 4.85 percent error rate.

Random Forest (RF) is an ensemble approach for classification and regression applications. [19]. It effectively merges K decision trees and generates a result. Huertas Tato and Centeno Brito's (2019) research focuses on estimating the photovoltaic output of six solar panels in Faro (Portugal) [20]. Temperature, meteorological factors, and radiation are all aspects in the study. Three years of data were used, with minute intervals. The most critical hyper parameter in the RF method is the number of trees, which is set to 500 via brute force. Finally, it is mentioned that the type of solar plant module influences the effectiveness of the RF approach, and that the performance can be improved by using complicated trend analysis, more relevant data, and larger prediction intervals.

Nearest Neighborhood algorithms are supervised learning algorithms that make local approximations and discover the closest data in order to find an output. The output is computed by applying weights to the determined number of closest neighbors. Voyant, Paol, Muselli and Nivet (2013), did research to evaluate the performance of forecasting systems for estimating photovoltaic production over various time frames [21]. The study employs k-NN because it is necessary to use naive models to evaluate the relevance of complicated models. As a consequence of the

research, it was determined that k-NN is a suitable alternative for forecasting on a daily basis. According to the findings of the study, k-NN is not the best model for hourly forecasting.

Tibshirani (1996) proposed a new regression approach in which the sum of squares is minimized while the total of absolute values of coefficients is smaller than a constant [22]. It produces a sparse solution with a large number of zero coefficients. This regression employs the L1 norm in algebra and is also known as "LASSO" (Least Absolute Shrinkage Selector Operator). The model is applied to data on prostate cancer in three different scenarios. The first situation involves data in which a small number of attributes have a substantial impact. The second situation involves data in which a small to moderate number of attributes have a moderate influence, whereas the third scenario involves data in which a big number of attributes have a minor effect. In these circumstances, three approaches are compared: LASSO, Ridge Regression (L2 Regression), and Subset Selection. Subset Selection performs best in the first case, whereas the other two models perform badly. In the second case, LASSO is the most effective, and in the third, ridge regression and lasso are the most effective. It may be inferred that LASSO regression is a viable solution in problems similar to the second scenario.

Luo et al. (2018), provide three novel regression models to address data integrity issues that have been identified in previous models [23]. Under-forecasts are the most common cause of data integrity issues, as they might result in blackouts. The study's main goal was to address sudden anomalies in power load data rather than to solve aspects like trend, time variables, and temperature in the provided models. Two of the models were Iteratively Reweighted Least Squares (IRLS) models, in which anomalies were defined as observations with large residuals, and forecasting these anomalies contributed less to the objective function than precision on standard data points. The first IRLS technique assigns minimal weights to residuals with large values, whereas the second IRLS approach removes residuals above a threshold. The third model is an L1 regression model, which produced accurate findings even

when 30% of the data contained anomalies, with an accuracy of roughly 10%, because the L1 model was less susceptible to outliers.

For a case study of short-term electrical load forecasting in Turkey, Ishik et al. (2015) constructed a feed-forward neural network [24]. The authors of this study concentrated on forecasting short-term electricity consumption. Ishik et al. used the Levenberg-Marquardt algorithm to train a feed-forward neural network to estimate the next day load in Turkey's power market. Hour, day of week, month, year, temperature of cities, and power load are all included in their data file. The input variable has six units, while the study's output variable is hourly electricity load. The data samples from 2012 weekdays were randomly divided into three groups: 70% training, 15% validation, and 15% test. The authors divided the network among seasons in Turkey and used SVM to compare it to their own network. The findings of their research demonstrate that the neural network's overall accuracy is comparable to that of SVM, and that the neural network produces better results for winter and spring data, while Support Vector Machine forecasts perform better for summer and fall. The MAPE for each season ranges from 2.0 to 3.7.

In recent studies, researchers have used ensemble models which involves combination of neural network models and conventional models such as Auto Regressive Integration Moving Average and Support Vector Regression (SVR) [25], [26], [27], [28]. When the conventional models are compared with neural network models, the neural network models outperform in load forecasting [29]. Using combined hybrid model produces better results than individual models (SARIMA and LSTM) because of linear and nonlinear data estimation [30], [31].

With this study, discretization model that is not applied in load forecasting literature is used. Ensemble of a discretization model and deep neural network model created a robust load forecasting model with high accuracy rate. In addition to that novel features are used in the study.

3. ELECTRICITY LOAD FORECASTING

3.1. Methodology

3.1.1. Data Preprocessing

Data provided by an electricity retail company contains hourly electricity usage values from November 2016 to February 2019. In literature review it has seen that weather and climate parameters are essential to forecast electricity demand.

To be able to predict distributed electricity, parameters are decided. These parameters are;

- hours (binary), electricity usage changes by hours with people's behaviors,
- months (binary), because they add seasonality to data,
- days of the week (binary), usage of electricity differs from weekdays to weekends in general, in detail people behave different in each day,
- holy and official holidays (binary), directly affects the numbers of electricity usage,
- academic calendar (school days and holidays) (binary), with the big numbers of students not going to school, electricity usage will differ,
- weather (binary), have a big impact on human behavior and heating,
- temperature as Fahrenheit (float), cold weather may lead people to use electric heaters,
- electricity usage (float).

Weekends are not counted as official holidays or academic holidays since being specified over time adds them seasonality.

One-hot encoding is applied to hour, month, day, holiday, academic calendar and weather data since they are categorical. One-hot encoding is a method that used for turning categorical data to binary vectors. A binary vector consists of all zeros and a one in the index. This way, all categorical data has the same weight on the model.

Sliding windows method is used to add recurrence effect to model which are influenced by previous values and seasonality. Sliding window method is creating a new parameter and giving it the same value as previous value of real parameter, which window is created from. For example, if the first value for a parameter is 1, second value of window parameter is 1, first value being 0. The second value of the real parameter is equal to third value of window parameter. When sliding windows are applied, rows with no value in them occur at the first rows of data since there will be no previous value for them. These rows should be deleted to prevent errors when fitting a machine learning model to data. For weather parameter, 5 windows are used for previous hourly values and 3 windows are used for previous daily values. For each temperature parameters, 5 windows are used for previous hourly values. For electricity usage parameter, 4 daily windows, 5 daily windows, and 1 weekly window are used.

3.1.2. Model Development

For such forecasting problems, understanding the data then choosing the right models is crucial. There are lots of models to fit data in, yet in this study, the data follows a nonlinear pattern. As it is seen in figure 1, data has a pattern and it has seasonality. In order to forecast hourly consumption, models that can memorize patterns and nonlinearity are needed. It is thus decided to use deep neural networks to solve this problem.
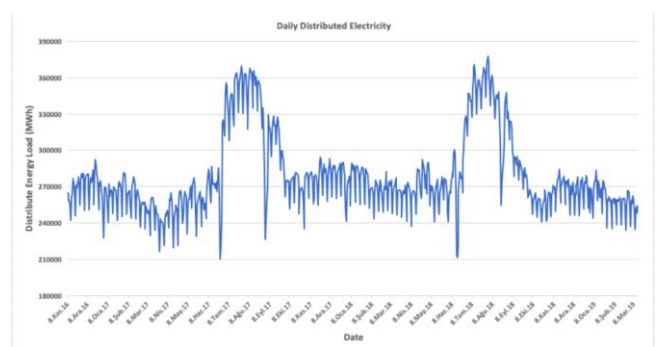
Figure 1 Daily distributed energy

3.1.3. Neural Networks

Load forecasting with traditional forecasting methods usually do not give accurate results. On

account of the fact that, it is a detailed, multidimensional and multivariate forecasting problem. However, machine learning techniques especially Neural Networks are extremely good at modelling nonlinearities and the seasonal patterns in data at many fields and in various kinds of forecasting tasks. Neural networks are models that simply simulate the human brain, built to find repetitive patterns in data. Also, Neural networks have theoretically provable capability to approximate any complex functions with arbitrary precision [32]. Deep Neural networks are capable of finding correlations between current and future events. Neural networks are able to do evaluations with limitless data on timely analysis and assessment. Machine learning techniques are proactive and specifically designed for "action and reaction" industries. Essentially, systems are able to give quick response upon the outputs of the machine learning models. In that project, deep neural networks are developed to capture nonlinearities and the seasonal patterns in energy demand.

Neural Networks are composed of several layers. Layer is the ultimate key stone in deep learning. Input with weight is generally stored in a layer which is like a container. It uses a set of functions to alter the weighted inputs and then transfers the values to the next layer. The first layer of a network is known as the input layer, while the last layer is known as the output layer. All levels in between are referred to as hidden layers.
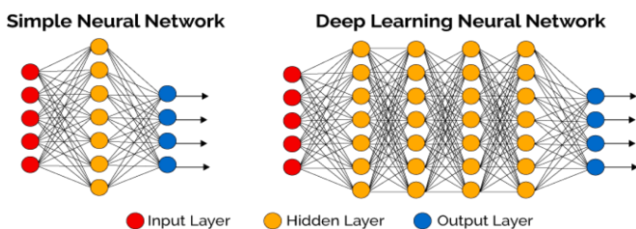
Figure 2 Neural network scheme [26]

Composition of many individual neurons form the Deep Neural Network. Inspiration comes from the architecture of a human brain for the Neural networks and as in human brain the basic building block is called a neuron. The term "artificial neuron" refers to a mathematical function. It accepts inputs, multiplies the weights, and adds them all up. The value is then given to a non-linear

function known as an activation function, which transforms it into a neuron's output.
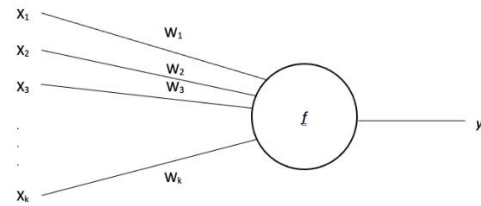
Figure 3 Neural network neuron

A signal's X value is present when it arrives at a node. This X value is passed to the activation function, which returns a value. When inputs are multiplied with weights in a neural network without activation functions, the outputs still fluctuate. However, in this case, the problem is that the model would be linear. Neural networks can handle complex models because they can implement nonlinear characteristics in the model through activation functions. Non-linearity is important because it is best suited for large and complex data sets. An exclusive activation function can be formed by anyone, yet there are some famous ones that can achieve the most out of the models. They are linear, ReLu, SeLu and ELu

The linear activation function is a simple function. It is a line function in which the activation is proportional to the input. Because it is a constant, in backpropagation, the change is constant. In this way, the changes are no longer dependent. Linear activation functions are usually not considered as preferably good.

The shortened version of rectified linear unit is known as ReLu. It captures interactions and nonlinearities very well.
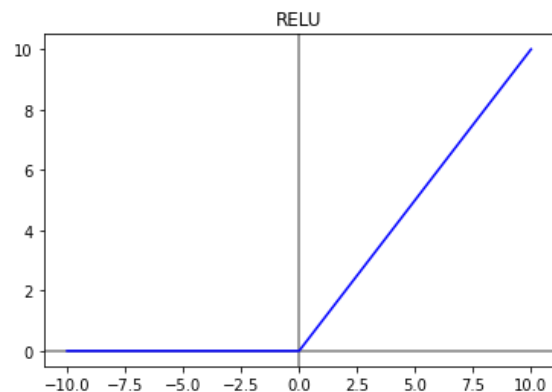
Figure 4 RELU activation function

Elu is exponential linear unit function. It is so similar to ReLu. Elu also avoids vanishing gradient. The difference of ReLu and Elu is that Elu has negative values. Negative values push mean activations closer to zero. Zero means makes learning faster and it works like a regularization method. They bring gradient closer to natural gradient and prevent overfitting.
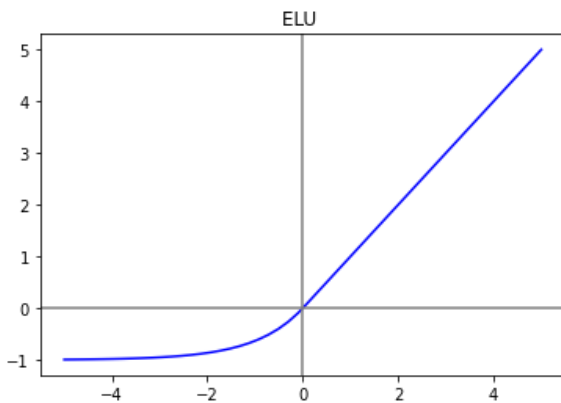
Figure 5 ELU activation function

The optimizer updates the model in response to the output of the loss function to shape and mold the neural network as accurately as possible.

Adam is an adaptive learning rate method which means, it computes individual learning rates for different parameters. Adam optimizer uses estimation of first and second moments of gradient to adapt the learning rate for each weight of the neural network. The method is computationally efficient. It has little memory requirements and is well suited for problems that are large in terms of data and parameters.

Adagrad uses frequency of features the update. It updates more frequent features. Adagrad is a stochastic gradient descent optimizer.

A loss function is an objective function that machine learning models attempt to maximize or minimize through its learning steps. The output of a loss function measures the accuracy of models.

Mean squared error (MSE) is that the sum of squared distances of data points to the regression curve. Squaring has two aims, one to extend the impact of distance and another is to get rid of negativity.

Mean absolute percent error (MAPE) is that the most used loss function in regression problems. It is used for measuring the prediction accuracy level of forecasting methods.

Epoch number implies how many times the weights will be updated. In neural networks, weights and inputs run through layers and nodes once. After the output layer, a loss function value is calculated, then weights are updated and run through again. These iterations are named epoch. Less epoch numbers may cause underfitting, more epoch numbers may cause overfitting. Thus, an optimal number is required.

3.1.4. Hyperparameter Optimization

A neural network consists of several hyperparameters. These are layer numbers, node numbers, epoch numbers, batch size numbers, activation function types and optimizer types. These parameters are highly affecting the algorithms and the results of a network. It is almost impossible to have an insight about the impact of selected parameters. In this project, models with 1 to 5 layers are applied. As number of neurons, 100, 200, 300, 500 and 1000 were applied to the models. 100, 200, 300, 400 epochs, 64, 128 and None batch sizes are applied. Relu, Elu and linear activation functions are used. As optimizer, Adam and Adagrad is used. MAPE is evaluated as loss function result. When calculated, 1800 different models will have to be evaluated. Since this process is time and energy consuming, there are hyperparameter optimization methods.

Grid search is one of the optimization methods. Grid search goes through all possible combinations with the given parameters. It builds the models and evaluates them sequentially, then returns the parameters that gives the best result. Grid search is not favorable for hyperparameter optimization because it is heavily time consuming and it requires strong devices for computation.

Random search is another method that takes given parameters randomly to build and evaluate models. Heuristically, after 30 iterations, random search is better than finding the best parameters. It consumes less time than grid search. In this

project, random search method is used to achieve best hyperparameters.

Since a strong computer is needed in order not to lose time in the random search, one of the servers of AGU (Abdullah Gül University) is used. In the server, five python codes for layers from 1 to 5 is run in five different terminals.

The parameters which give best accuracy in the random search were 5 layers, 100 nodes, 400 epochs, batch size of None, "Elu" activation function and "Adagrad" optimizer. Mean validation score was 2.9 with 0.5 standard deviation. Mean test score was 2.18 when 60 days are forecasted by the model.

A deep neural network includes randomness in different stages of the algorithm. First weights are created randomly and in every run they change, thus the result changes. Reproducibility is essential for a model because it helps keeping track of the changes in hyperparameter optimization, knowing that the result only changes due to parameters. Reproducibility is achieved by using the seed function in python as well as a weight initializer for first layer. Seed function produces a sequence for a random number generation method so that python uses that same sequence every time the code runs. It is the same for weight initializer. Weight initializing has its own random number generation method. Having the same weights in first layer produces same results in every run.

3.2. Results

Best parameters of the deep neural network which give the highest accuracy rate for the hourly electricity consumption in a city are found. Model is run to forecast 60 days interval from 14 January to 14 March. Predicted values and actual values are compared and the mean absolute percentage error is calculated to be 2.18. It means that the mean of all the errors is 2.18 and the accuracy of the model is 97.82%.
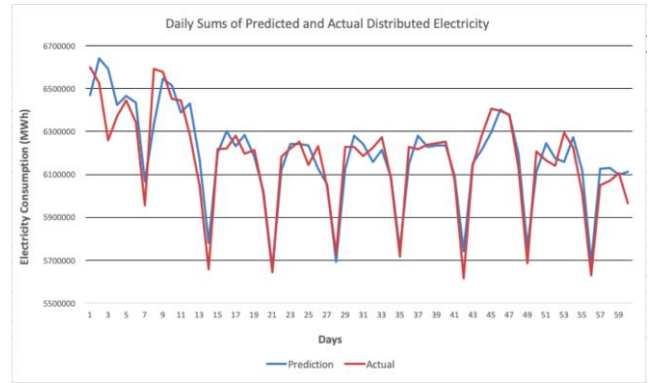
Figure 6 Predicted and Actual daily electricity distribution amounts

Figure 6 shows the daily predicted values and actual values. As it can be seen, even if at some days model fail to catch actual values, in general perspective, the model is able to detect the patterns and the trend.

If the results are inspected as hourly based, hourly errors and accuracies can be seen in the Table 1. Model is very strong on forecasting the first hours and the last hours of a day. As it goes to the mid hours, the accuracy is going down. Yet the worst accuracy is 96.12% at hour 16 which is still in acceptable range of the company so it can be still seen as a good result.

Table 1 Hourly accuracy values

Hour	Accuracy	MAPE	Hour	Accuracy	MAPE
0	98,65	1,35	12	97,84	2,16
1	98,48	1,52	13	97,74	2,26
2	98,24	1,76	14	97,31	2,69
3	98,43	1,57	15	96,49	3,51
4	98,15	1,85	16	96,12	3,88
5	97,94	2,06	17	96,43	3,57
6	97,8	2,2	18	96,86	3,14
7	97,87	2,13	19	98,03	1,97
8	97,97	2,03	20	98,49	1,51
9	97,94	2,06	21	98,2	1,8
10	97,76	2,24	22	98,35	1,65
11	97,39	2,61	23	98,71	1,29

If results are inspected as daily based, it is seen that Mondays have the least accuracy with 96.70% and the highest error rate with 3,30. In the rest of the

days, the error rates are between 1.70 to 2.31 which outperforms.

Table 2 Daily accuracy values

Days	Accuracy	MAPE
Monday	96,7	3,3
Tuesday	97,82	2,18
Wednesday	97,69	2,31
Thursday	98,3	1,7
Friday	98,25	1,75
Saturday	97,98	2,02
Sunday	97,98	2,02

In order to see the improvements in the results, the accuracy and error rates of the company should be examined. In the company's experience-based forecasting method, the error rate is 2,254 in 60 days interval from 14 January to 14 March. In the developed model in that project, the error rate is 2,18 %. While the accuracy of the company's forecasting method is 97,75 %, in the model it is 97,82 %. As it can be understood, the developed model in that project is better than the company's experience-based forecasting method.

When the results compared with respect to hours, the model gives less error rate than the company's forecasting method in 15 hours during a day (See Appendix 1).

When the results compared with respect to days of a week, the model gives less error rate than the company's forecasting method in 6 days during a week (See Table 3).

Table 3 Daily MAPE comparison with the forecast of the company

Days	MAPE (Company)	MAPE (Model)	Success
Monday	2,34	3,3	0
Tuesday	2,26	2,18	1
Wednesday	2,42	2,31	1
Thursday	2,05	1,7	1
Friday	2,27	1,75	1
Saturday	2,42	2,02	1
Sunday	2,42	2,02	1

3.3. A Novel Approach

Torgo and Gama (1996) focus on applying classification methods on regression problems in their study. Main aim is to discretize a larger problem into the smaller ones, and approach the solution in that way. In the examples that are used in literature, datasets are discretized in three approaches. These approaches are splitting the values in equal probable intervals, equal width intervals, and using K-NN algorithm to create clusters. After discretizing the values, usually median values of these discretized sets are taken as the outputs.

In the methodology proposed for this study, discretizing is done iteratively on the training set. In the first step, the whole dataset is split around the value of mean. The tuples which have the output greater than the mean are labelled as ""one" and the tuples which have output lower than the mean are labelled as "zero". This is done iteratively on the sets until a threshold point. This threshold point is determined based on the preferences of the decision maker and called "Lower Threshold". There is also "Upper Threshold", which is basically the two times bigger version of the lower threshold. According to the ratio proposed for this methodology, decision about splitting is determined.

After a splitting operation is done, ratio of the newly built dataset is checked. If the ratio is bigger than the upper threshold, according to the determined labels splitting is done again. If the ratio is between upper and lower threshold, a regression model is applied on the dataset. If the ratio is lower than the lower threshold, Gaussian white noise with a mean of 3 is added into the samples. Figure 7 below shows the process diagram of this iterative methodology.
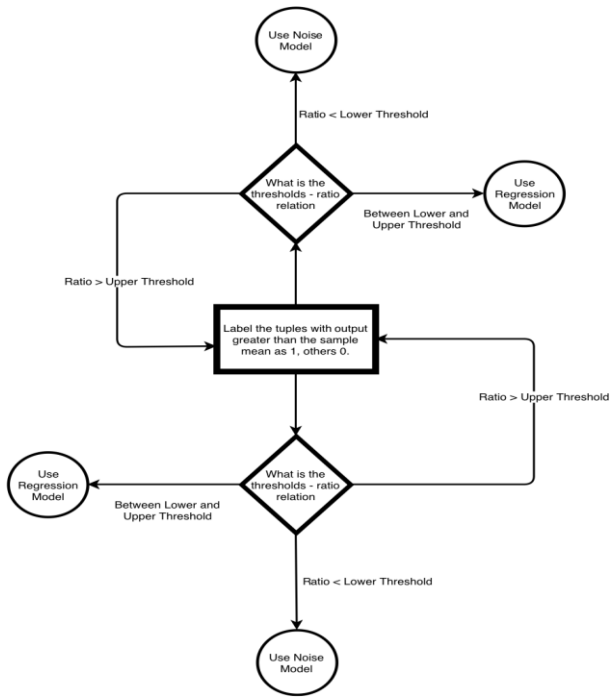
Figure 7 Subprocesses for the elimination in the novel approach

When this methodology is applied to the dataset of this study, 7 final subclasses are built. In order to learn the value of a new sample, there are 13 different ML models integrated. Classifications in this methodology are done via Random Forest, and regressions are done via MLP (Multi-Layer Perceptron). Appendix 2 shows the subclasses after the splitting operations. Figure 8 below is the process flow chart for new coming data according to dataset processed in this study. Currently, success of this methodology based on MAPE values is around 2.5 %. In the next steps, sub models will be optimized in order to obtain a better result.

3.4. Ensemble Model

In order to increase the forecasting performance deep neural network and discretization (novel) models are ensemble. The individual models are compared in terms of MAPE (See Table 5).

Table 5 Comparison of the models

Hour	Novel Method MAPE	ANN Method MAPE	Hour	Novel Method MAPE	ANN Method MAPE
0	1,47	1,35	12	3,22	2,16
1	1,69	1,52	13	3,85	2,26
2	1,35	1,76	14	2,2	2,69
3	1,85	1,57	15	2,9	3,51
4	2,25	1,85	16	3,2	3,88
5	1,92	2,06	17	3,45	3,57
6	2,7	2,2	18	3,07	3,14
7	2,5	2,13	19	2,42	1,97
8	2,3	2,03	20	1,49	1,51
9	2,32	2,06	21	2,15	1,8
10	2,45	2,24	22	2,76	1,65
11	3,72	2,61	23	1,52	1,29

With this ensemble model, we built more robust model. The accuracy results of the ensemble method are given in the Table 6.

Table 6 MAPE values of the ensemble model

Hour	Ensemble Model MAPE	Hour	Ensemble Model MAPE
0	1,35	12	2,16
1	1,52	13	2,26
2	1,35	14	2,2
3	1,57	15	2,9
4	1,85	16	3,2
5	1,92	17	3,45
6	2,2	18	3,07
7	2,13	19	1,97
8	2,03	20	1,49
9	2,06	21	1,8
10	2,24	22	1,65
11	2,61	23	1,29

The average accuracy of the ensemble model is 2,09 % so that the best model is obtained by the ensemble model.
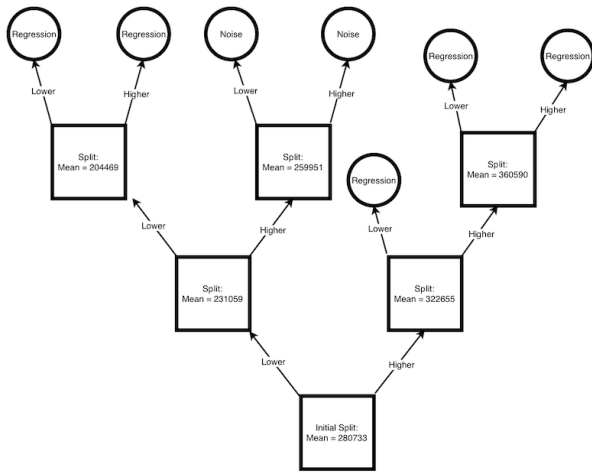
Figure 8 Prescription of the novel approach

4. CONCLUSION

Due to the competitive and dynamic nature of electricity industry, electricity load is highly critical for companies to be able to compete. Within the scope of this study, forecasting models are developed to predict hourly electricity load of a city.

In that study, Neural network are applied, trained and tested with the dataset. A novel method which include discretization of regression problem is developed. These two models are ensemble. Mean absolute percentage error is used as key performance indicators and models are assessed accordingly. The ensemble model develop for the load forecast predicts the consumption of electricity with a 97,91 % accuracy.

Funding

The Declaration of Conflict of Interest/ Common Interest

"No conflict of interest or common interest has been declared by the authors".

Authors' Contribution

Under this heading, "The authors contributed equally to the study" or "The first author contributed 60%, the second author 40%." expressions such as should be included.

The Declaration of Ethics Committee Approval

"This study does not require ethics committee permission or any special permission"

The Declaration of Research and Publication Ethics

"The authors of the paper declare that they comply with the scientific, ethical and quotation rules of SAUJS in all processes of the paper and that they do not make any falsification on the data collected. In addition, they declare that Sakarya University Journal of Science and its editorial board have no responsibility for any ethical violations that may be encountered, and that this study has not been evaluated in any academic publication environment other than Sakarya University Journal of Science."

APPENDICES

Appendix 1 Hourly MAPE Comparison with The Forecasts of the Company

Hour	MAPE (Company)	MAPE (Model)	Success	Hour	MAPE (Company)	MAPE (Model)	Success
0	1,80	1,35	1	12	2,26	2,16	1
1	1,46	1,52	0	13	2,46	2,26	1
2	1,49	1,76	0	14	2,67	2,69	0
3	1,70	1,57	1	15	2,76	3,51	0
4	1,85	1,85	1	16	3,03	3,88	0
5	1,79	2,06	0	17	3,20	3,57	0
6	1,90	2,20	0	18	3,50	3,14	1
7	2,18	2,13	1	19	2,36	1,97	1

8	2,77	2,03	1	20	1,87	1,51	1
9	2,90	2,06	1	21	2,02	1,80	1
10	2,77	2,24	1	22	2,07	1,65	1
11	2,43	2,61	0	23	1,69	1,29	1

Appendix 2 Subclasses for The Novel Method

	Min	Max	Mean	Median	Range	Data Points	Half Range Ratio	Decision
1	280741	440811	322655	312018	160070	8213	28,50848291	Classify
0	149404	280732	231059	228064	131328	6932	43,95063051	Classify
1_1	322667	440811	360590	351965	118144	2990	18,3074191	Classify
1_0	280741	322635	300950	300783	41894	5225	7,461325563	Regression
0_1	231060	280732	259951	262438	49672	3211	10,74872328	Classify
0_0	149404	231014	204469	205528	81610	3621	27,31185243	Classify
1_1_1	360682	440811	391171	387653	80129	1312	11,10798432	Regression
1_1_0	322667	360573	336698	334615	37906	1679	5,873857568	Regression
1_0_1	300963	322635	310938	310752	21672	2584	3,600442579	Noise
1_0_0	280741	300948	291161	291479	20207	2637	3,598868708	Noise
0_0_1	204471	231014	216079	215027	26543	1898	6,490651486	Regression
0_0_0	149404	204455	191688	193804	55051	1724	18,42353618	Classify
0_0_0_1	191732	204455	198526	198737	12723	984	3,3179459	Noise
0_0_0_0	149404	191678	182582	184709	42275	740	14,14774083	Regression

REFERENCES

[1] D. I. Stern, P. J. Burke & S. B. Bruns, "The Impact of Electricity on Economic Development: A Macroeconomic Perspective", EEG State-of-Knowledge Paper Series, 1.1, 2017.

[2] About the U.S. Electricity System and its Impact on the Environment, https://www.epa.gov/energy/about-us-electricity-system-and-its-impact-environment

[3] Energy Exchange İstanbul, Elektrik Piyasaları, https://seffaflik.epias.com.tr/transparency/

[4] CRO Forum, "Power Blackout Risks, Risk Management Options", Emerging Risk Initiative – Position Paper, 2011.

[5] P. Szuromi, B. Jasny, D. Clery, J. Austin, & B. Hanson, "Energy for the long haul,", 2007.

[6] V. Lara-Fanego, J.A. Ruiz-Arias, D. Pozo-Vázquez, F.J. Santos-Alamillos, & J. Tovar-Pescador, "Evaluation of the WRF model solar irradiance forecasts in Andalusia (southern Spain)," Solar Energy, 86(8), 2200-2217, 2012.

[7] IEA, "Global energy technology perspectives" International Energy Agency, OECD Publication Service, OECD, Paris, 2006a.

[8] B. Espinar, J.L. Aznarte, R. Girard, A.M. Moussa, & G. Kariniotakis, "Photovoltaic Forecasting: A state of the art," In 5th European PV-Hybrid and Mini-Grid Conference (pp. Pages-250). OTTI-Ostbayerisches Technologie-Transfer-Institut, 2010.

[9] A. Azadeh, M. Saberi, S.F. Ghaderi, A. Gitiforouz, & V. Ebrahimipour, "Improved estimation of electricity demand function by integration of fuzzy system and data mining approach," Energy Conversion and Management, 49(8), 2165-2177, 2008.

[10] B. Wang, N.L. Tai, H.Q. Zhai, J. Ye, J.D. Zhu, & L.B. Qi, "A new ARMAX model based on evolutionary algorithm and particle

swarm optimization for short-term load forecasting," Electric Power Systems Research, 78(10), 1679-1685, 2008.

[11] N. Amjady, "Short-term bus load forecasting of power systems by a new hybrid method," IEEE Transactions on Power Systems, 22(1), 333-341, 2007.

[12] M. Khadem, "Application of kohonen neural network classifier to short term load forecasting," In Panel Session on Application of Neural Networks to Short-term Load Forecasting, 1993 IEEE Winter Meeting, 1993.

[13] R.H. Inman, H.T. Pedro, & C.F. Coimbra, "Solar forecasting methods for renewable energy integration," Progress in energy and combustion science, 39(6), 535-576, 2013.

[14] H.B. Barlow, "Unsupervised learning," Neural computation, 1(3), 295-311, 1989.

[15] Y. Gala, Á. Fernández, J. Díaz, & J.R. Dorronsoro, "Hybrid machine learning forecasting of solar radiation values," Neurocomputing, 176, 48-59, 2016.

[16] V. Vapnik, "The nature of statistical learning theory," Springer science & business media, 2013.

[17] N. Sharma, P. Sharma, D. Irwin, & P. Shenoy, "Predicting solar generation from weather forecasts using machine learning," In 2011 IEEE international conference on smart grid communications (SmartGridComm) (pp. 528-533). IEEE, 2011.

[18] J. Shi, W.J. Lee, Y. Liu, Y. Yang, & P. Wang, "Forecasting power output of photovoltaic systems based on weather classification and support vector machines." IEEE Transactions on Industry Applications, 48(3), 1064-1069, 2012.

[19] L. Breiman, "Random forests," Machine learning, 45(1), 5-32, 2001.

[20] J. Huertas Tato, & M. Centeno Brito, "Using Smart Persistence and Random Forests to Predict Photovoltaic Energy Production," Energies, 12(1), 100, 2019.

[21] C. Voyant, C. Paoli, M. Muselli, & M.L. Nivet, "Multi-horizon solar radiation forecasting for Mediterranean locations using time series models," Renewable and Sustainable Energy Reviews, 28, 44-52, 2013.

[22] R. Tibshirani, "Regression shrinkage and selection via the lasso," Journal of the Royal Statistical Society: Series B (Methodological), 58(1), 267-288, 1996.

[23] J. Luo, T. Hong, & S.C. Fang, "Robust Regression Models for Load Forecasting," IEEE Transactions on Smart Grid, 2018.

[24] M.Y. Ishik, T. Göze, İ. Özcan, V.Ç. Güngör, & Z. Aydın, "Short term electricity load forecasting: A case study of electric utility market in Turkey," In 2015 3rd International Istanbul Smart Grid Congress and Fair (ICSG) (pp. 1-5). IEEE, 2015.

[25] W. Tan and B. Khoshnevis, "Integration of process planning and scheduling— a review," Journal of Intelligent Manufacturing, vol. 11, no. 1, pp. 51–63, 2000.

[26] S. Ai, A. Chakravorty, and C. Rong. "Household Energy Consumption Prediction using Evolutionary Ensemble Neural Network." Engineering Assets and Public Infrastructures in the Age of Digitalization. Springer, Cham, 2020. 923-931.

[27] K. Bot, A. Ruano, and M.G. Ruano. "Forecasting electricity consumption in residential buildings for home energy management systems." International Conference on Information Processing and Management of Uncertainty in Knowledge-Based Systems. Springer, Cham, 2020.

[28] S. Rahman, M.G. Rabiul Alam, and M. Mahbubur Rahman. "Deep Learning based

Ensemble Method for Household Energy Demand Forecasting of Smart Home." 2019 22nd International Conference on Computer and Information Technology (ICCIT). IEEE, 2019.

[29] T. Panapongpakorn, and D. Banjerdpongchai. "Short-Term Load Forecast for Energy Management System Using Neural Networks with Mutual Information Method of Input Selection." 2019 SICE International Symposium on Control Systems (SICE ISCS). IEEE, 2019.

[30] S. Chan, I. Oktavianti, and V. Puspita. "A deep learning cnn and ai-tuned svm for electricity consumption forecasting: Multivariate time series data." 2019 IEEE 10th Annual Information Technology, Electronics and Mobile Communication Conference (IEMCON). IEEE, 2019.

[31] M. Krishnan, Y.M. Jung, and S. Yun. "Prediction of Energy Demand in Smart Grid using Hybrid Approach." 2020 Fourth International Conference on Computing Methodologies and Communication (ICCMC). IEEE, 2020.

[32] H. S. Hippert, C. E. Pedreira, R. C. Souza, "Neural networks for short-term load forecasting: A review and evaluation", IEEE Transactions on power systems, 16 (1) 44–55, 2001.

Title: Micellar and Surface Properties of Cationic-Cationic Binary Surfactant Mixtures: Synergistic Interactions and Solubility Enhancement of Anthracene

Authors: Elif Berna OLUTAS

Micellar and Surface Properties of Cationic-Cationic Binary Surfactant Mixtures: Synergistic Interactions and Solubility Enhancement of Anthracene

Elif Berna OLUTAS*[1]

Abstract

The micellar and surface behaviors of decylammonium chloride (DACl) in presence of L-alanine hydrochloride decylester (L-ADE) and L-alanine hydrochloride dodecylester (L-ADDE) at various mole fractions were investigated by conductivity and surface tension measurements. From the conductivity measurements, the critical micelle concentration (CMC), the degree of counter-ion ionization (α) and standard Gibbs energy of micellization (ΔG°_{mic}) were investigated for both pure and binary mixtures. The molecular interaction parameter (β) and the micellar mole fraction (X^{m}_{DACl}) for mixed micelle formation by DACl/L-ADE (C_{10}-C_{10}) and DACl/L-ADDE (C_{10}-C_{12}) were calculated using the regular solution equation proposed by Rubingh. The ideal values of CMC (CMC_{ideal}) and the micellar mole fraction ($X^{m}_{DACl(ideal)}$) were also obtained for mixed micelle according to the pseudo phase theoretical models. The negative β values showed that there were synergistic interactions for all compositions of DACl/L-ADE and DACl/L-ADDE mixed systems. From the surface tension measurements, adsorption parameters such as the surface excess concentration (Γ_{max}), minimum surface tension at the CMC, efficiency in the surface tension reduction (pC_{20}), standard Gibbs energy of adsorption (ΔG°_{ads}), and minimum area per head group of a molecule (A_{min}) in pure, mixed and their ideal values were also determined. The results indicated that the synergism and attractive interactions in the studied binary mixtures depend on the chain length of the cationic L-alanine ester and their mole fractions in the mixed system. The solubilization capacity of pure DACl and its mixed system with L-ADE and L-ADDE towards anthracene were determined and discussed in terms of molar solubilization ratio (MSR). Based on the MSR values, the solubilization enhancement was found for anthracene in DACl/L-ADE and DACl/L-ADDE mixed systems.

Keywords: Surfactants, binary mixtures, micellization, synergistic interactions, solubilization.

1. INTRODUCTION

Surfactants, consist of both hydrophobic tail and hydrophilic head, are amphiphilic in nature and self-assemble in water to form aggregates called micelles. The micelles begin to form after a certain minimum concentration called the critical micelle concentration (CMC). Surfactants have important uses in detergent, food, medicine, cosmetics, and many other industries due to their

* Corresponding author: olutas_e@ibu.edu.tr
[1] Bolu Abant İzzet Baysal İzzet Baysal University, Faculty of Science and Science and Literature, Department of Chemistry
ORCID: https://orcid.org/0000-0002-0386-589X

Elif Berna OLUTAS

Micellar and Surface Properties of Cationic-Cationic Binary Surfactant Mixtures: Synergistic Interact...

unique properties [1,2], e.g., the formation of a micelle structure that can dissolve many substances that are not soluble in water.

The use of surfactants in different fields can be alone or as mixing systems consisting of different head groups (e.g., anionic, cationic, non-ionic and zwitterionic). In most case, the use of surfactant mixtures is preferred over single surfactant due to the better performance of the first one [3-6]. Mixing surfactants often leads to synergism that improves the properties and makes them suitable for their applications. Due to this synergism, surfactant mixtures show lower CMC values than those of pure surfactants. Many studies to understand the micelle formation, adsorption and solubilization phenomena of the surfactant mixtures have shown that physicochemical properties can be controlled by adjusting the compositions of these systems [7].

The hydrophilic head of cationic surfactants has a positive charge, so it adsorbs strongly onto most solid surfaces, that are usually negatively charged, and can give special properties to the substrate [1,8]. Therefore, they are widely used in many aspects, including anti-electrostatic, antibacterial, corrosion inhibitors for metals, dispersants for pigments, germicides for microorganisms, flotation agents for ores etc. [1,8]. The use of binary mixtures of cationic-cationic surfactants can also be improved the application properties. Therefore, the investigation of the micellar and surface properties of these kinds of mixed systems is important for new and effective formulations.

The solubilization is directly related to the micelle formation process and very important phenomenon in many areas such as detergency, oil recovery, dry cleaning, micellar catalysis, and pharmaceutical [1,9-12]. The solubility of organic substances, especially water-insoluble ones, increases by solubilization in the micelles formed by surfactants [9,10,13]. As well-known, polycyclic aromatic hydrocarbons (PAHs) contain fused aromatic rings with linear, cluster, or angular arrangements and contaminate the environment due to their stabilities, high toxicities, hard hydrophobicities, and low biodegradabilities. The low solubility of PAHs in

water limits the degradation of these pollutants. One of the promising techniques that increase the aqueous solubility of PAHs is micellar solubilization [4,9,11,14]. In literature, it has been noted that surfactant mixtures not only improve the micellar properties of the system but also increase the solubilization power as well. In studies conducted in this field, it has been observed that especially the solubility of PAHs in water is increased by using mixed surfactant systems [3,4,14-21].

The objective of this study is first to investigate micellization and adsorption properties of pure and binary surfactant mixtures containing the cationic surfactant DACl, and amino acid-based cationic surfactants (L-ADE and L-ADDE) with different hydrophobic tails. Secondly, to reveal the properties of the mixed micelle, the interaction parameters in the micelle phase and at the air/water interface are determined using theoretical models. Finally, the solubility of anthracene that is a kind of PAH in the presence of pure DACl, and its equimolar binary mixture of L-ADE and L-ADDE in water were investigated and compared.
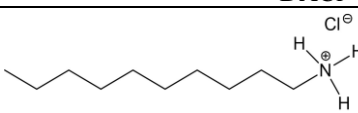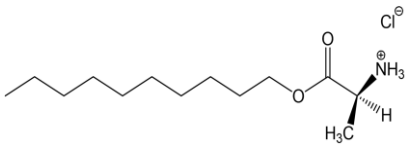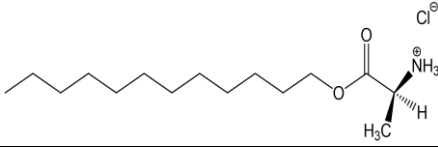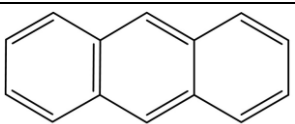
2. MATERIALS AND METHODS

2.1. Chemicals

L-alanine (purity, 99%), 1-decanol, 1-dodecanol (purity, 98%) decylamine (purity, 98%) and anthracene (purity, 98.5%) were obtained from Merck. They were used as received.

Decylammonium chloride (DACl) was obtained by neutralizing the decylamine with dilute hydrochloric acid in ethanol [22]. The esters of L-alanine, L-alanine hydrochloride decylester (L-ADE), and L-alanine hydrochloride dodecylester (L-ADDE), were synthesized using the corresponding alcohols and L-alanine, as described previously [23]. The structures and chemical formulas of DACl, L-ADE, L-ADDE and anthracene are listed in Table 1.

Elif Berna OLUTAS

Micellar and Surface Properties of Cationic-Cationic Binary Surfactant Mixtures: Synergistic Interact...

Table 1 The structures and chemical formulas of DACl, L-ADE, L-ADDE and anthracene, respectively.

DACl	
	$C_{10}H_{24}ClN$
L-ADE	
	$C_{13}H_{28}ClNO_2$
L-ADDE	
	$C_{15}H_{32}ClNO_2$
Anthracene	
	$C_{14}H_{10}$

2.2. Preparation of solutions

The stock solutions of surfactants were prepared in distilled water (Milli-Q water purification system) using an analytical balance (±0.00001 g). The concentration of stock solutions was chosen at a concentration well above the CMC values of single surfactants. The stock solutions were then homogenized with the aid of a magnetic stirrer. To prepare the mixed systems with different compositions, stock solutions of pure surfactants were mixed with a proper volume of each pure solution. For instance, for the binary system of DACl/L-ADE (or L-ADDE), 5.0 mL DACl and 5.0 mL L-ADE (or L-ADDE) stock solutions with the same concentrations were mixed to get desired mole fraction of 0.50/0.50. For all other binary mixtures of DACl/L-ADE (or L-ADDE) were prepared with the stock solutions of pure surfactants. The composition of the mixed systems was stated as a mole fraction of cationic surfactant α(DACl).

$$\alpha_{(DACl)} = \frac{n_{(DACl)}}{n_{(DACl)} + n_{(L\text{-}ADE\ or\ L\text{-}ADDE)}} \quad (1)$$

where n_{DACl} and n_{L-ADE} (or L-ADDE) are the moles of the cationic surfactants DACl and L-ADE (or L-ADDE) in the binary mixture, respectively. The temperature was kept at 25 °C for all measurements.

2.3. Conductivity measurements

A Cyberscan PC 510 digital conductivity meter (Oakton Instruments, cell constant 1.03cm⁻¹) was used to perform measurements. Firstly, the conductance of a known amount of distilled water in the conductivity cell was measured. Then, a certain volume of the stock solution consisting of pure or binary solutions was progressively added to the cell with a micropipette. The conductance was recorded after mixing well and equilibration of the temperature.

2.4. Surface tension measurements

Surface tension measurements were done by a du Noüy ring digital tensiometer (KSV Sigma 702). The accuracy of the tensiometer was within ± 0.01 mN.m⁻¹. The du Noüy ring was cleaned thoroughly and dried before use. The calibration of the tensiometer was done by measuring the surface tension of distilled water. Firstly, a known amount of water was placed into the vessel and the surface tension of the water was recorded. Then, a certain volume of the stock solution was progressively added to the vessel with a micropipette. After thorough mixing and temperature equilibration processes, the surface tension of the pure or mixed system was measured.

2.5. UV-Vis measurements

A UV–Vis double-beam spectrophotometer (Hitachi U-2900) was used for the determination of apparent solubility of anthracene in micellar solutions of DACl and its equimolar binary mixture of L-ADDE in water above their CMCs. Anthracene was added in an excess amount to surfactant solutions with different concentrations. Then, the surfactant solutions containing anthracene were mixed at 25 °C for 24 h. The solutions were centrifuged at 10000 rpm to remove undissolved anthracene. To eliminate the

Elif Berna OLUTAS

Micellar and Surface Properties of Cationic-Cationic Binary Surfactant Mixtures: Synergistic Interact...

effect of surfactants, the concentration of pure and binary mixture of surfactants was kept the same both in reference and experimental quartz cells having 1 cm of path length. Since anthracene has very low solubility in water (2.53×10^{-7} M), a known amount of anthracene was dissolved in methanol to construct a calibration curve [20,24]. Then, the concentration of anthracene in surfactant solutions was determined from the absorbance data using the standard curve. Therefore, each aliquot of the supernatant and its corresponding surfactant solution in reference cell was diluted with appropriate volume of methanol while measuring their absorbances as stated in the literature [21,24,25,26].

3. RESULTS AND DISCUSSION

3.1. Micellization properties

The conductivity measurements are frequently used method to determine the value of CMC. The conductivity of surfactants increases linearly with the concentration. This increase in conductivity is greater due to the counter ions and charged head groups of free surfactant monomers below the CMC, whereas above the CMC, it is low due to the lower ionic mobility of the micelle in proportion to free surfactant monomers [27]. Therefore, a break is observed at the intersection point of the two straight lines obtained from the conductivity (κ) versus total surfactant concentration (C) graph. This point is taken as the CMC. Representative plots of the κ versus C of single surfactant DACl, and its binary mixtures, DACl/L-ADE and DACl/L-ADDE, with mole fraction of 0.50 in aqueous solution are shown in Figure 1.
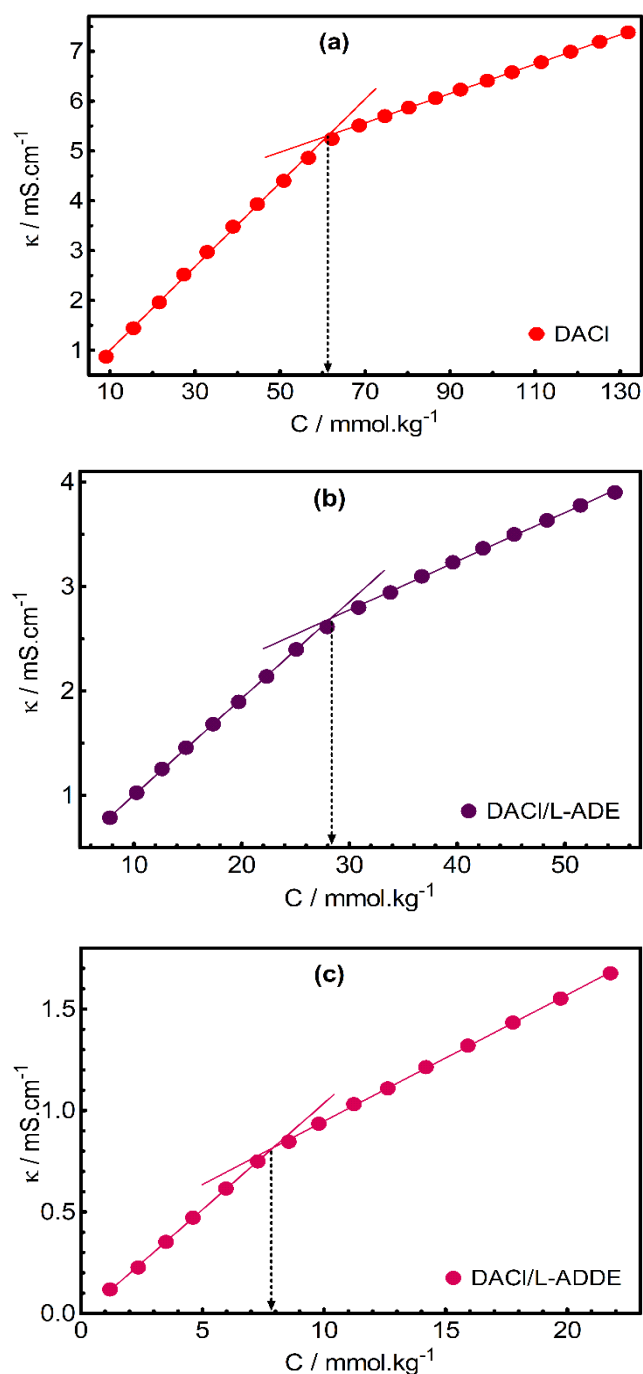
Figure 1 Plot of conductivity (κ) versus concentration (C) for (a) pure DACl, and binary mixtures of (b) DACl/L-ADE, and (c) DACl/L-ADDE with mole fraction of 0.50 in water at 25 °C. The CMC is indicated by the dashed arrow.

Similar behavior was also obtained for the single surfactants L-ADE and L-ADDE, and the binary mixtures of DACl/L-ADE (C_{10}-C_{10}) and DACl/L-ADDE (C_{10}-C_{12}) with different mole fractions. The parameter obtained from the ratio of the slopes of the curves above and below the CMC is the degree of counterion dissociation of the

Elif Berna OLUTAS

Micellar and Surface Properties of Cationic-Cationic Binary Surfactant Mixtures: Synergistic Interact...

micelle (α). The α values for both single and binary mixtures of the surfactants under study were also calculated. It was found that the α values of the mixed systems increased due to the addition of the second surfactant. In addition to that, the standard Gibbs energy of micellization for all systems was estimated using CMC and α values according to the pseudo-phase separation model [11,28]

$$\Delta G^\circ_{mic} = (2-\alpha)RT \, ln X_{CMC} \qquad (2)$$

where X_{CMC}, R and T are the CMC value in terms of mole fraction, the ideal gas constant, and the absolute temperature, respectively. The results have been tabulated in Table 2.

It was observed that the CMC value of DACl is in good agreement with the literature [29,30]. From Table 2, it was also seen that the CMC value of L-ADDE was significantly lower than that of L-ADE despite having the same hydrophilic group. As expected, this difference is due to two additional methylene groups that of L-ADDE has. In the literature, there is a general rule that the CMC of ionic surfactants is halved by adding a methylene group to a straight chain hydrophobic group [1]. The CMC values of mixed systems are generally between those of pure ones [4,31-34]. For our systems, it was found that the CMC values of binary surfactant mixtures were lower than the CMC of DACl and higher than L-ADE or L-ADDE, i.e., they were also between the pure surfactant CMC's, Table 2. Here, it was shown a schematic representation of the micelle consisting of an equimolar (0.50:0.50) binary mixture of DACl/L-ADE to give an idea for studied systems, Figure 2. In general, the studied systems are expected to have aggregates of two different sizes, mostly in the micellar region (below ~10 nm) as previously ones [35].

In addition, the values of ΔG°_{mic} were calculated using Eq. (2) for all systems. As seen from Table 2, ΔG°_{mic} values are all negative indicating the micelle formation is spontaneous process and favored for both pure and mixed surfactant systems.
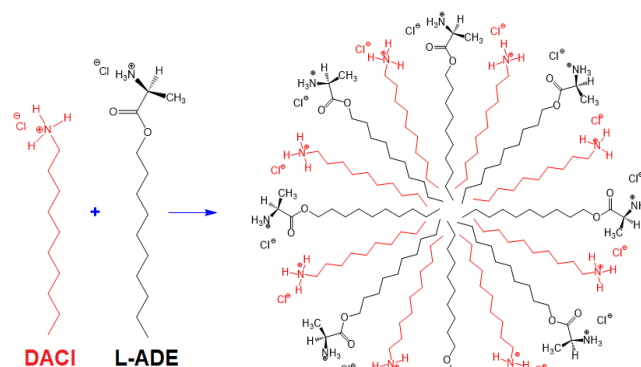
Figure 2 Representative structure of mixed micelle for DACl/L-ADE with 0.50:0.50 mole fraction.

To gain important information about the interactions between mixed surfactants, it is important to investigate the relationship between the CMCs and the composition of the surfactants. The pseudo-phase separation model was utilized to understand how the micellization behavior of DACl/L-ADE and DACl/L-ADDE mixtures deviate from the ideal mixing [36]. Firstly, the ideal CMC values (CMC$_{ideal}$) of the ideal binary surfactant mixture that has no net interactions between the monomers were obtained by using Clint's equation [2,6,17,27,31,34,37],

$$\frac{1}{CMC_{ideal}} = \frac{\alpha_{DACl}}{CMC_{DACl}} + \frac{(1-\alpha_{DACl})}{CMC_{L-ADE}} \qquad (3)$$

in which CMC$_{DACl}$ and CMC$_{L-ADE}$ represents the critical micelle concentrations of pure DACl and pure L-ADE (or L-ADDE). The α_{DACl} is the mole fraction of DACl in the binary mixture. The experimental and ideal CMC values (CMC$_{exp}$ and CMC$_{ideal}$) with a mole fraction of added DACl to L-ADE and L-ADDE are depicted in Figure 3. The experimentally determined CMC values (CMC$_{exp}$) for DACl/L-ADE and DACl/L-ADDE mixed systems were found to be lower than the CMC$_{ideal}$ values calculated from the individual DACl, L-ADE and L-ADDE surfactant molecules using Equation (3). As it is well known that any deviation of CMC$_{exp}$ from CMC$_{ideal}$ would indicate mutual interactions among surfactants. A positive deviation from ideality (CMC$_{ideal}$< CMC$_{exp}$) represents antagonism, whereas a negative deviation (CMC$_{ideal}$> CMC$_{exp}$) shows synergism in the system. It was clear that there were synergistic interactions characterized by a

Elif Berna OLUTAS

Micellar and Surface Properties of Cationic-Cationic Binary Surfactant Mixtures: Synergistic Interact...

reduction in CMC data for both binary mixtures, Table 2, and Figure 3.
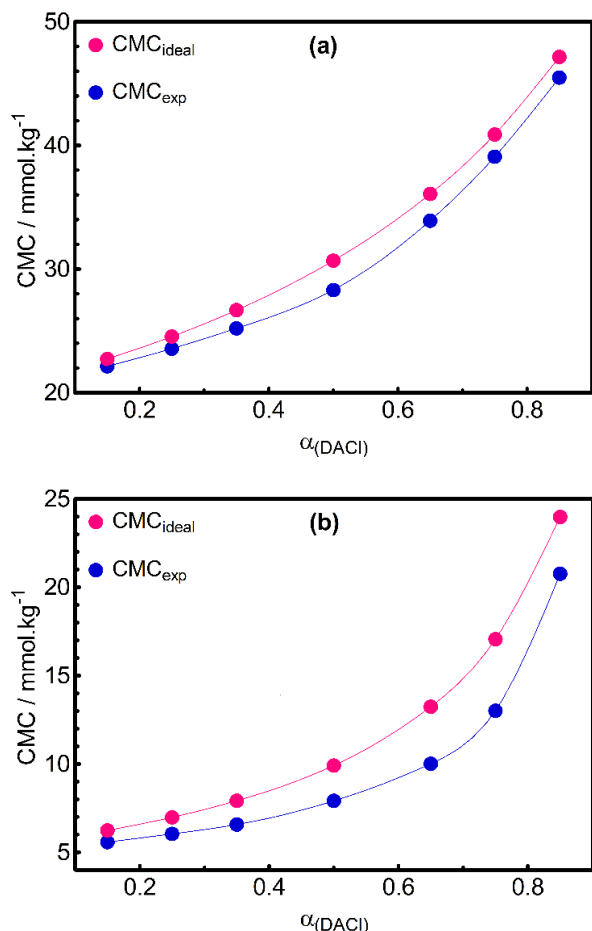
Figure 3 Plots of CMC values (experimental, CMC_{exp} and ideal, CMC_{ideal}) versus mole fraction of DACl, $\alpha_{(DACl)}$, for binary mixtures (a) DACl/L-ADE (C_{10}-C_{10}), and (b) DACl/L-ADDE (C_{10}-C_{12}), respectively. The solid lines are a guide for the eye.

Another important parameter that represents the nature and the strength of the interactions between the surfactant monomers in a mixed micelle is the interaction parameter (β^m), i.e., any deviation from the ideality indicating the existence of attractive (synergistic) or repulsive (antagonistic) interactions [3,4]. The negative magnitude of β^m shows synergism, whereas the positive one implies antagonism between the surfactant molecules in the mixed micelles [1,15,16,17]. The composition of mixed micelles, i.e., micellar mole fraction (X_{DACl}^m) and β^m are obtained from the CMC values and the equations of Rubingh's model [6,18,19,31,34,37,38],

$$\frac{X_{DACl}^{m2}\ln(\alpha_{DACl}CMC_{exp}/X_{DACl}^m CMC_{DACl})}{(1-X_{DACl}^m)^2\ln[(1-\alpha_{DACl})CMC_{exp}/(1-X_{DACl}^m)CMC_{L-ADE}]}=1 \qquad (4)$$

$$\beta^m=\frac{\ln(\alpha_{DACl}CMC_{exp}/X_{DACl}^m CMC_{DACl})}{(1-X_{DACl}^m)^2} \qquad (5)$$

Besides, the micellar mole fraction of DACl in the mixed micelles at an ideal state ($X_{DACl(ideal)}^m$) was determined using the following equation [6,31,34,39],

$$X_{DACl(ideal)}^m = \frac{\alpha_{DACl}CMC_{L-ADE}}{\alpha_{DACl}CMC_{L-ADE}+(1-\alpha_{DACl})CMC_{DACl}} \qquad (6)$$

The variations of X_{DACl}^m and $X_{DACl(ideal)}^m$ with $\alpha_{(DACl)}$ for DACl/L-ADE and DACl/L-ADDE mixed systems are given in Figure 4. For the studied binary surfactant mixtures, the values of X_{DACl}^m, $X_{DACl(ideal)}^m$ and β^m are also summarized in Table 2. As seen from Table 2, the values of α_{DACl} are greater than X_{DACl}^m and $X_{DACl(ideal)}^m$ for all cases. Therefore, it can be concluded that the contribution of DACl in mixed micelles (X_{DACl}^m) is less than the mixing ratios (α_{DACl}), indicating the priority of formation of mixed micelles are mainly governed by L-ADE or L-ADDE. This shows that the surfactant composition in mixed micelles is different from the composition in solution. The $X_{DACl(ideal)}^m$ values for all mixed systems, except $\alpha_{DACl} = 0.85$, are lower than X_{DACl}^m values indicating more DACl prefers to settle into mixed micelles when compared with the ideal state. The synergistic (attractive) interactions were observed among DACl and L-ADE (or L-ADDE) monomers in the mixed micelles indicating negative β^m at all mole fractions. As known, the higher the negative magnitude of β^m, the stronger is the synergism between the surfactants. The values β^m are larger for L-ADDE as compared to L-ADE. Even though L-ADE and L-ADDE have the same head group, this difference probably arises from the interactions between the dissimilar hydrophobic tails of DACl (C_{10}) and L-ADDE (C_{12}) that affect the CMC values.

Elif Berna OLUTAS

Micellar and Surface Properties of Cationic-Cationic Binary Surfactant Mixtures: Synergistic Interact...

Table 2 Physical parameters of the pure and binary (cationic-cationic) mixed systems as a function of the initial mole fraction of DACl ($\alpha_{(DACl)}$) from conductivity measurements at 25 °C.

(a) DACl/L-ADE (C_{10}-C_{10}) system

$\alpha_{(DACl)}$	CMC /mmol.kg^{-1}	CMC$_{ideal}$ /mmol.kg^{-1}	α	ΔG^o_{mic} /kJ.mol^{-1}	X^m_{DACl}	$X^m_{DACl(ideal)}$	β^m
1	61.28	61.28	0.35	−27.8	−	−	−
0.85	45.49	47.16	0.48	−26.8	0.6438	0.6542	−0.16
0.75	39.09	40.89	0.49	−27.2	0.5004	0.5004	−0.18
0.65	33.92	36.08	0.50	−27.5	0.3957	0.3828	−0.26
0.50	28.31	30.68	0.50	−28.1	0.2848	0.2503	−0.41
0.35	25.21	26.68	0.47	−29.1	0.1877	0.1524	−0.40
0.25	23.57	24.55	0.45	−29.8	0.1301	0.1002	−0.40
0.15	22.14	22.73	0.44	−30.3	0.0778	0.0556	−0.43
0	20.46 [a]	20.46 [a]	0.41 [a]	−31.2 [a]	−	−	−

(b) DACl/L-ADDE (C_{10}-C_{12}) system

$\alpha_{(DACl)}$	CMC /mmol.kg^{-1}	CMC$_{ideal}$ /mmol.kg^{-1}	α	ΔG^o_{mic} /kJ.mol^{-1}	X^m_{DACl}	$X^m_{DACl(ideal)}$	β^m
1	61.28	−	0.35	−27.8	−	−	−
0.85	20.76	23.98	0.70	−25.5	0.3700	0.3326	−0.63
0.75	13.01	17.06	0.66	−27.7	0.3099	0.2088	−1.40
0.65	10.01	13.24	0.64	−29.0	0.2663	0.1404	−1.71
0.50	7.91	9.91	0.59	−30.9	0.2063	0.0809	−1.84
0.35	6.57	7.92	0.54	−32.8	0.1626	0.0452	−2.09
0.25	6.04	6.98	0.50	−33.9	0.1287	0.0285	−2.18
0.15	5.58	6.24	0.46	−35.2	0.0988	0.0153	−2.44
0	5.39 [b]	−	0.37 [b]	−37.3 [b]	−	−	−

[a,b] Values are taken from [28] and [40], respectively.
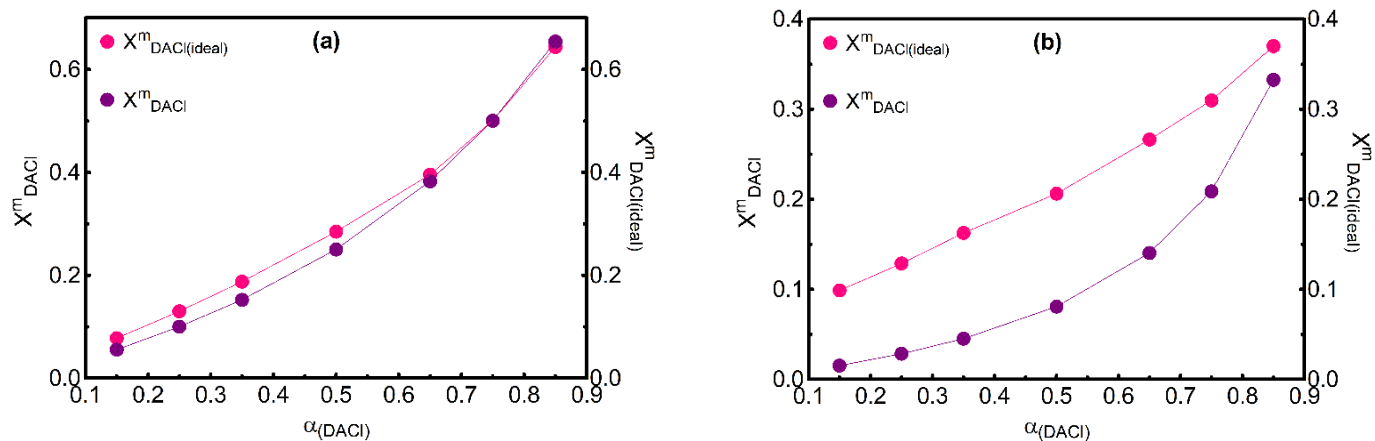
Figure 4 Variations of X^m_{DACl} and $X^m_{DACl(ideal)}$ versus mole fraction of DACl, $\alpha_{(DACl)}$, in systems (a) DACl/L-ADE (C_{10}-C_{10}), and (b) DACl/L-ADDE (C_{10}-C_{12}), respectively. The solid lines are a guide for the eye.

3.2. Surface properties

Adsorption properties of the studied systems were obtained by surface tension measurements. The values of surface tension (γ) were used to determine both CMC and γ_{CMC} values from the break-points of the curves of γ versus lnC, Figure 5. The surface tension values decrease with increasing concentration (C) of the surfactants, and in the range of above CMC, the variation is almost constant. As in the conductivity measurements, the CMC values of the binary mixtures were found to be between the CMC values of pure surfactants. In addition, the γ_{CMC} value of DACl/L-ADE system was between the γ_{CMC} values of pure surfactants, whereas the γ_{CMC}

Elif Berna OLUTAS

Micellar and Surface Properties of Cationic-Cationic Binary Surfactant Mixtures: Synergistic Interact...

values of DACl/L-ADDE system were slightly higher than the pure ones. All results were summarized in Table 3.

The maximum surface excess concentration (Γ_{max}) at the air/water interface, which is the number of moles of surfactant molecule adsorbed at the air/water interface per unit area, is evaluated from the surface tension plots using the Gibbs adsorption isotherm equation [5,40,41],

$$\Gamma_{max} = -\frac{1}{nRT}\left(\frac{\partial\gamma}{\partial lnC}\right)_{T,P} \qquad (7)$$

in which R and T are the ideal gas constant in J.mol^{-1}.K^{-1} and the temperature in Kelvin, respectively. Here, n denotes the number of ionic species in solution, which depends on the type and structure of the surfactant and the presence of extra solutes. It was found that Γ_{max} decreases with $\alpha_{(DACl)}$ for both mixed systems, Table 3.

The minimum surface area per head group of the surfactant molecule (A_{min}) occupied at the air/water interface was determined using the Γ_{max} values according to equation below [1,11,15,28,29,39,40]:

$$A_{min} = \frac{10^{16}}{N_A\Gamma_{max}} \qquad (8)$$

in which N_A is the is the Avogadro's number and the value of A_{min} in nm^2.

For ideal mixing, the values of A_{min}^{ideal} were calculated from the following expression [42,43]:

$$A_{min}^{ideal} = \alpha_{DACl}A_{min}^{DACl} + (1 - \alpha_{DACl})A_{min}^{L-ADE} \qquad (9)$$

where A_{min}^{DACl} and A_{min}^{L-ADE} are the minimum surface area per head group of DACl and L-ADE (or L-ADDE), respectively. It was seen that the experimentally obtained values deviate from those obtained for ideal mixing, i.e., the A_{min} values are smaller than the corresponding A_{min}^{ideal} ones, Table 3, and Figure 6. These results indicate synergistic interactions between the mixed surfactant systems, DACl/L-ADE and DACl/L-ADDE.

Figure 5 Surface tension versus lnC for (a) DACl/L-ADE (C$_{10}$-C$_{10}$), and (b) DACl/L-ADDE (C$_{10}$-C$_{12}$) mixed systems with mole fractions of $\alpha_{(DACl)}$=1, 0.75, 0.25 and 0 (pure L-ADE or L-ADDE), respectively. The solid lines are a guide for the eye. The intersection point is used for the determination of CMC and γ_{CMC} values.

Elif Berna OLUTAS

Micellar and Surface Properties of Cationic-Cationic Binary Surfactant Mixtures: Synergistic Interact...

Figure 6 Variations of $A_{min(exp)}$ and $A_{min(ideal)}$ versus mole fraction of DACl, $\alpha_{(DACl)}$, in systems (a) DACl/L-ADE (C_{10}-C_{10}), and (b) DACl/L-ADDE (C_{10}-C_{12}), respectively. The solid lines are a guide for the eye.

Table 3 Physical parameters of the pure and binary (cationic-cationic) mixed systems as a function of the initial mole fraction of DACl from surface tension measurements at 25 °C.

(a) DACl/L-ADE (C_{10}-C_{10}) system

$\alpha_{(DACl)}$	CMC /mmol.kg^{-1}	γ_{CMC} /mN.m^{-1}	Γ_{max} /x10^{-10}mol.cm^{-2}	A_{min} /Å^2	A_{min}^{ideal} /Å^2	pC_{20}	ΔG^o_{ads} /kJ.mol^{-1}
1	62.56	31.23	3.48	47.67	−	1.8	−39.5
0.75	35.28	33.86	3.21	51.81	53.16	2.1	−39.1
0.50	29.13	33.89	2.98	55.70	58.66	2.1	−40.9
0.25	20.38	34.88	2.86	58.14	64.16	2.3	−42.8
0	17.08	35.16	2.38	69.65	−	2.5	−46.4

(b) DACl/L-ADDE (C_{10}-C_{12}) system

$\alpha_{(DACl)}$	CMC /mmol.kg^{-1}	γ_{CMC} /mN.m^{-1}	Γ_{max} /x10^{-10}mol.cm^{-2}	A_{min} /Å^2	A_{min}^{ideal} / Å^2	pC_{20}	ΔG^o_{ads} /kJ.mol^{-1}
1	62.56	31.23	3.48	47.67	−	1.8	−39.5
0.75	8.40	33.02	3.16	52.47	53.36	3.6	−40.0
0.50	5.99	32.91	3.10	53.49	59.06	3.2	−43.2
0.25	4.72	32.41	3.08	53.98	64.75	3.0	−46.8
0	4.50 [a]	31.82 [a]	2.36 [a]	70.44 [a]	−	3.4 [a]	−54.6 [a]

[a] Values are taken from [40].

Elif Berna OLUTAS

Micellar and Surface Properties of Cationic-Cationic Binary Surfactant Mixtures: Synergistic Interact...

The efficiency of adsorption (pC_{20}) is the negative logarithm of the surfactant concentration required to produce a 20 mN.m^{-1} drop at the surface tension (C_{20}) for a given solvent and obtained by the given relation [1,8,28,40,44],

$$pC_{20} = -\log C_{20} \tag{10}$$

The greater the pC_{20} value of a surfactant, the more it tends to adsorb at the air-water interface, thus reducing the surface tension more efficiently. The pC_{20} values of mixed systems are greater than DACl, Table 3. This shows that the mixed systems are superior in their efficiency at reducing surface tension. Finally, the standard Gibbs energy of adsorption (ΔG°_{ads}) is calculated using the equation below [11,28,39,41],

$$\Delta G^{\circ}_{ads} = \Delta G^{\circ}_{mic} - \pi_{CMC}/\Gamma_{max} \tag{11}$$

in which π_{CMC} indicates the surface pressure at the CMC (the difference between the surface tension of the pure water and γ_{CMC} value) and is related to the effectiveness of a surfactant. The ΔG°_{ads} values, Table 3, were found to be all negative indicating the adsorption of pure and mixed systems at air/water interface is also spontaneous as in the case of the micellization process.

3.3. Solubilization properties

In addition to finding the micellization and surface properties of pure DACl and their binary mixtures with L-ADE and L-ADDE, it was also aimed to investigate the solubilization of anthracene using mixed systems. Investigating this phenomenon in the systems containing more than one surfactant would be of interest and importance from both practical and academic perspectives.

To find the molar solubility of anthracene in surfactant solutions, firstly, the absorbance of a series of anthracene solutions was measured, Figure 7(a). Then, a standard curve (R^2=0.9999) satisfying the Beer-Lambert law was obtained by plotting the absorbance versus the concentration, Figure 7 (b). The molar extinction coefficient (ε) of anthracene was determined as 7.28×10^3 M^{-1}cm^{-1} at the maximum absorption wavelength λ_{max}=355nm from the slope of the Figure 7 (b).

The value ε, which tallied well with the literature value, was then used to determine the total molar solubility of anthracene (S) for the studied systems using the Beer-Lambert law [20].
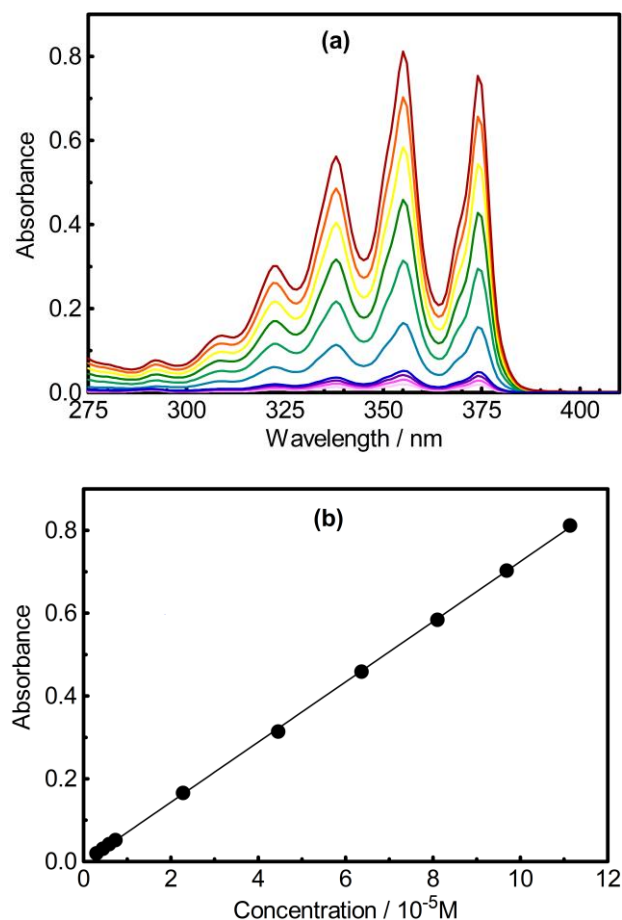
Figure 7 (a) Absorption spectra of anthracene in methanol at different concentrations. (b)Variations of maximum absorbance at 355 nm with anthracene concentration.

The solubilization capacity of a surfactant is expressed in terms of the molar solubilization ratio (MSR). The value of MSR can be calculated with the following expression [4,11,14-21]

$$MSR = \frac{(S_t - S_{CMC})}{(C_t - C_{CMC})} \tag{12}$$

in which S_t and S_{CMC} represent the total molar solubility of anthracene in the pure/mixed surfactant solutions at a particular total concentration (C_t) and CMC, respectively.

The change of anthracene solubility as a function of the concentration of pure DACl and its equimolar binary mixtures with L-ADE and L-

Elif Berna OLUTAS

Micellar and Surface Properties of Cationic-Cationic Binary Surfactant Mixtures: Synergistic Interact...

ADDE is shown in Figure 8. The values of MSR obtained from the slope of the plots for studied systems herein are given in Table 4. It was seen that the solubility of anthracene increased linearly with the concentration of single and mixed surfactants. This was related to solubilization of anthracene within single and mixed surfactant micelles. The solubilization capacity of mixed systems was found to be greater than that of the single one for anthracene in line with the literature [4,15,16,21,24,45]. This has been demonstrated the advantage of using a mixture rather than a single surfactant. Among the mixed systems, DACl/L-ADDE showed better solubilization capacity (higher MSR value) for anthracene than that of DACl/L-ADE, Table 4. This was related to the more hydrophobic environment of DACl/L-ADDE (C_{10}-C_{12}) mixed micelles where more solubilization occurred [24].
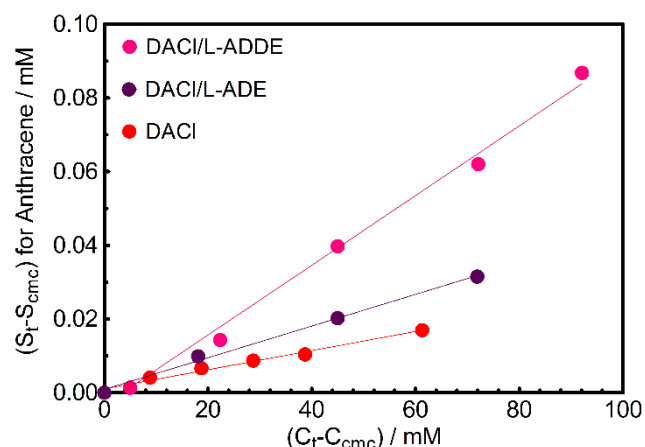
Figure 8 Variations of solubility of Anthracene with surfactant concentration in pure DACl and equimolar (0.50:0.50) binary mixtures with L-ADE and L-ADDE.

Table 4. Molar solubilization ratio (MSR) values pure and equimolar binary (cationic-cationic) mixed systems for anthracene at 25 °C.

	DACl	DACl/L-ADE	DACl/L-ADDE
MSR	0.00026	0.00043	0.00095

4. CONCLUSION

Mixed micelle formations in two systems consisting of cationic surfactants, DACl/L-ADE (C_{10}-C_{10}) and DACl/L-ADDE (C_{10}-C_{12}), were studied using conductivity and surface tension methods. It was found that synergism and attractive interactions between surfactants dominate micellization at all mole fractions of DACl. These synergistic interactions in surfactant mixtures are important in reducing the amount of surfactant required for certain applications, thus contributing to reduced cost and environmental impact. The effect of pure DACl and its equimolar binary mixture of L-ADE and L-ADDE on the solubilization of anthracene was studied. It was reported that the solubility of anthracene in water increases with the use of pure and mixed surfactants. This increase is more in mixed systems than in the single one. The results show that experiments can be extended to increase the solubility of other hydrophobic materials, such as dyes and drugs, and shed light on future studies.

The Declaration of Conflict of Interest/ Common Interest

No conflict of interest or common interest has been declared by the author.

The Declaration of Ethics Committee Approval

This study does not require ethics committee permission or any special permission.

The Declaration of Research and Publication Ethics

The authors of the paper declare that they comply with the scientific, ethical and quotation rules of SAUJS in all processes of the paper and that they do not make any falsification on the data collected. In addition, they declare that Sakarya University Journal of Science and its editorial board have no responsibility for any ethical violations that may be encountered, and that this study has not been evaluated in any academic publication environment other than Sakarya University Journal of Science.

Elif Berna OLUTAS

Micellar and Surface Properties of Cationic-Cationic Binary Surfactant Mixtures: Synergistic Interact...

REFERENCES

[1] M.J. Rosen, "Surfactants and Interfacial Phenomena," John Wiley & Sons Ltd., New Jersey, pp. 1–30, 400, 44, 83, 121, 2004.

[2] K. Holmberg, D. O. Shah, M. J. Schwuger, "Handbook of Applied Surface and Colloid Chemistry," John Wiley & Sons Ltd., England, pp.509–512, 55, 2002.

[3] T. Geng, C. Zhang, Y. Jiang, H. Ju, Y. Wang, "Synergistic effect of binary mixtures contained newly cationic surfactant: Interaction, aggregation behaviors and application properties," Journal of Molecular Liquids, vol. 232, pp. 36–44, 2017.

[4] S. Singh, K. Parikh, S. Kumar, V.K. Aswal, S. Kumar, "Spacer nature and composition as key factors for structural tailoring of anionic/cationic mixed gemini micelles: Interaction and solubilization studies," Journal of Molecular Liquids, vol. 279, pp. 108–119, 2019.

[5] A. Bera, K. Ojha, A. Mandal, "Synergistic Effect of Mixed Surfactant Systems on Foam Behavior and Surface Tension," Journal of Surfactants and Detergents, vol. 16, pp. 621–630, 2013.

[6] K. Singh, D. G. Marangoni, "Synergistic interactions in the mixed micelles of cationic gemini with zwitterionic surfactants: The pH and spacer effect," Journal of Colloid and Interface Science, vol. 315, pp. 620–626, 2007.

[7] D. Calvo, J. L. Ruiz, M. Valiente, "Phase equilibria of mixtures of surfactants and viscoelastic properties of the liquid crystal phases," Fluid Phase Equilibria, vol. 425, pp. 358–364, 2016.

[8] T. Cosgrove, "Colloid Science Principles, Methods and Applications," John Wiley &Sons Ltd, U.K., p. 65, 71, 2010.

[9] T. Morisue, Y. Moroi, O. Shibata, "Solubilization of Benzene, Naphthalene, Anthracene, and Pyrene in Dodecyl ammonium Trifluoroacetate Micelles," Journal of Physical Chemistry, vol. 98, pp. 12995–13000, 1994.

[10] P. A. Bhat, A. A. Dar, and G. M. Rather, "Solubilization Capabilities of Some Cationic, Anionic, and Nonionic Surfactants toward the Poorly Water-Soluble Antibiotic Drug Erythromycin," Journal of Chemical Engineering and Data, vol. 53, pp. 1271–1277, 2008.

[11] J. Lakra, D. Tikariha, T. Yadav, M. L. Satnami, K. K. Ghosh, "Study of Solubility Efficiency of Polycyclic Aromatic Hydrocarbons in Single Surfactant Systems," Journal of Surfactants and Detergents, vol. 16, pp. 957–966, 2013.

[12] S. Padasala, K. Kuperkarb, P. Bahadura, "Solubilisation study of water-insoluble dye in cationic single/dimeric surfactant micelles: effect of headgroup, non-polar tail, and spacer chain in aqueous and salt solution," Coloration Technology, vol. 132, pp. 217–221, 2016.

[13] Y. Moroi, K. Mitsunobu, T. Morisue, Y. Kadobayashi, M. Sakai, "Solubilization of Benzene, Naphthalene, Anthracene, and Pyrene in 1-Dodecanesulfonic Acid Micelle," Journal of Physical Chemistry, vol. 99, pp. 2372–2376, 1995.

[14] J. Wei, G. Huang, L. Zhu, S. Zhao, C. An a, Y. Fan, "Enhanced aqueous solubility of naphthalene and pyrene by binary and ternary Gemini cationic and conventional nonionic surfactants," Chemosphere, vol. 89, pp. 1347–1353, 2012.

[15] M. Panda, K.-Din, "Solubilization of polycyclic aromatic hydrocarbons by gemini–conventional mixed surfactant systems," Journal of Molecular Liquids, vol. 187, pp. 106–113, 2013.

Elif Berna OLUTAS

Micellar and Surface Properties of Cationic-Cationic Binary Surfactant Mixtures: Synergistic Interact...

[16] N. Fatma, M. Panda, W. H. Ansari, K.-Din "Solubility enhancement of anthracene and pyrene in the mixtures of acleavable cationic gemini surfactant with conventional surfactants of different polarities," Colloids and Surfaces A: Physicochemical and Engineering Aspects, vol. 467, pp. 9–17, 2015.

[17] Y. Liang, S. Zhang, H. Li, X. Mao, Y. Li, X. Xie, J. Ren, G. Li, R. Lian, "Solubilization of polycyclic aromatic hydrocarbons by novel ester-bonded Gemini prolinol-based surfactant and its binary mixtures with conventional surfactants," Journal of Dispersion Science and Technology, vol. 41, pp. 1–10, 2019.

[18] P. S. Sales, R. H. de Rossi, M. A. Fernández, "Different behaviours in the solubilization of polycyclic aromatic hydrocarbons in water induced by mixed surfactant solutions," Chemosphere, vol. 84, pp. 1700–1707, 2011.

[19] J. Weia, G. Huanga, H. Yua, C. An, "Efficiency of single and mixed Gemini/conventional micelles on solubilization of phenanthrene," Chemical Engineering Journal, vol. 168, pp. 201–207, 2011.

[20] K.-Dina, M. Shafia, P. A. Bhat, A. A. Dar, "Solubilization capabilities of mixtures of cationic Gemini surfactant with conventional cationic, nonionic and anionic surfactants towards polycyclic aromatic hydrocarbons," Journal of Hazardous Materials, vol. 167, pp. 575–581, 2009.

[21] L. Zhu, S. Feng, "Synergistic solubilization of polycyclic aromatic hydrocarbons by mixed anionic–nonionic surfactants," Chemosphere, vol. 53, pp. 459–467, 2003.

[22] M. Acimis, C. Ocak, S. Ozacar and K. Gocmen, "Effect of the thickness of the hydrophobic bilayer on the helical twisting power in micellar nematic liquid crystals," New Journal of Chemistry, vol. 26, pp. 427–432, 2002.

[23] M. Acimis, "A type II aqueous cholesteric lyomesophase," Canadian Journal of Chemistry, vol. 58, pp. 1533–1541, 1980.

[24] A. A. Dar, G. M. Rather, and A. R. Das, "Mixed Micelle Formation and Solubilization Behavior toward Polycyclic Aromatic Hydrocarbons of Binary and Ternary Cationic-Nonionic Surfactant Mixtures," J. Phys. Chem. B, vol. 111, pp. 3122–3132, 2007.

[25] T.-S. Choi, Y. Shimizu, H. Shirai, K. Hamada, "Solubilization of disperse dyes in cationic gemini surfactant micelles," Dyes and Pigments, vol. 45, pp. 145–152, 2000.

[26] J. Weia, G. Huanga, H. Yua, C. An, "Efficiency of single and mixed Gemini/conventional micelles on solubilization of phenanthrene," Chemical Engineering Journal, vol. 168, pp. 201–207, 2011.

[27] K. D. Danov, P. A. Kralchevsky, K. P. Ananthapadmanabhan, "Micelle–monomer equilibria in solutions of ionic surfactants and in ionic–nonionic mixtures:A generalized phase separation model," Advances in Colloid and Interface Science, vol. 206, pp. 17–45, 2014.

[28] E. B. Olutas, T. Taskesen, N. B. Kartal, "Double-Tailed Single-Head Amino Acid-Based Chiral Cationic Amphiphilic Molecules: Synthesis, Characterization, and Physicochemical Properties," Journal of Surfactants and Detergents, vol. 23, pp. 153–168, 2020.

[29] B. Janczuk, J. A. M. Sierra, M. L. Gonzalez-Martin, J.M. Bruque, W. Wojcik, "Properties of Decylammonium Chloride and Cesium Perfluorooctanoate at Interfaces and Standard Free Energy of Their Adsorption," Journal of Colloid and Interface Science, vol. 192, pp. 408–414, 1997.

Elif Berna OLUTAS

Micellar and Surface Properties of Cationic-Cationic Binary Surfactant Mixtures: Synergistic Interact...

[30] M. L. Gonzalez-Martin, B. Janczuk, J.A. Me´ndez-Sierra, J.M. Bruque, "Volumetric properties of the decylammonium chloride and cesium perfluorooctanoate from density measurements," Colloids and Surfaces A: Physicochemical and Engineering Aspects, vol. 148, pp. 213–221, 1999.

[31] N. Azum, A. Z. Naqvi, M. Akram, K.-Din, "Properties of Mixed Aqueous Micellar Solutions Formed by Cationic Alkanediyl-r,ω-bis(tetradecyldimethylammonium bromide) and Alkyltrimethylammonium Bromides: Fluorescence and Conductivity Studies," Journal of Chemical Engineering and Data, vol. 54, pp. 1518–1523, 2009.

[32] Z.-X. Chen, S.-P. Deng, X.-K. Li, "Micellization and synergistic interaction of binary surfactant mixtures based on sodium nonylphenol polyoxyethylene ether sulfate," Journal of Colloid and Interface Science, vol. 318, pp. 389–396, 2008.

[33] S. P. Moulik, Md. E. Haque, P. K. Jana, A. R. Das, "Micellar Properties of Cationic Surfactants in Pure and Mixed States," Journal of Physical Chemistry, vol. 100, pp. 701–708, 1996.

[34] K.-Din, M. A. Rub, A. Z. Naqvi, "Mixed Micelle Formation between Amphiphilic Drug Amitriptyline Hydrochloride and Surfactants (Conventional and Gemini) at 293.15-308.15 K," Journal of Physical Chemistry, vol. 114, pp. 6354–6364, 2010.

[35] E. B. Olutas "Interactions in mixed micellar systems comprising chiral cationic amino acid based and conventional anionic surfactants," Journal of Molecular Liquids vol. 275, pp. 126–135, 2019.

[36] P. M. Holland, D. N. Rubingh, "Nonideal multicomponent mixed micelle model," Journal of Physical Chemistry, vol. 84, pp. 1984–1990, 1983.

[37] S.K. Mehta, Bhawna, "Significant effect of polar head group of surfactants on the solubilization of Zein in mixed micellar (SDS–DDAB) media," Colloids and Surfaces B: Biointerfaces, vol. 81, pp. 74–80, 2010.

[38] R. Kakehashi, M. Shizuma, S. Yamamura, T. Takeda, "Mixed micelles containing sodium oleate: the effect of the chain length and the polar head group," Journal of Colloid and Interface Science, vol. 279, pp. 253–258, 2004.

[39] A. Ali, U. Farooq, S. Uzair, R. Patel, "Conductometric and tensiometric studies on the mixed micellar systems of surface-active ionic liquid and cationic surfactants in aqueous medium," Journal of Molecular Liquids, vol. 223, pp. 589–602, 2016.

[40] E. B. Olutas, M. Acimis, "Thermodynamic parameters of some partially fluorinated and hydrogenated amphiphilic enantiomers and their racemates in aqueous solution," Journal of Chemical Thermodynamics, vol. 47, pp. 144–153, 2012.

[41] C. M. C. Faustino, A. R Calado, L. B. Garcia−Rio, "Gemini Surfactants−Protein Interactions: Effect of pH, Temperature, and Surfactant Stereochemistry," Biomacromolecules, vol. 10, pp. 2508–2514, 2009.

[42] S. Javadian, H. Gharibi, Z. Bromand, B. Sohrabi, "Electrolyte effect on mixed micelle and interfacial properties of binary mixtures of cationic and nonionic surfactants," Journal of Colloid and Interface Science, vol. 318, pp. 449–456, 2008.

[43] N. A. Negma, M. R. Mishrif, D. E. Mohamed, "Vanillin based cationic surfactants mixed systems: Micellization and interfacial interaction behaviors in presence of nonionic conventional surfactant," Colloids and Surfaces A: Physicochemical and Engineering Aspects, vol. 480, pp. 122–129, 2015.

[44] N. Fatma, W. H. Ansari, M. Panda, K.-Din, "A Systematic Study of Mixed Surfactant

Elif Berna OLUTAS

Micellar and Surface Properties of Cationic-Cationic Binary Surfactant Mixtures: Synergistic Interact...

Solutions of a Cationic Ester-Bonded Dimeric Surfactant with Cationic, Anionic and Nonionic Monomeric Surfactants in Aqueous Media," Journal of Surfactants and Detergents, vol. 16, pp. 609–620, 2013.

[45] M. Yang, J. Ke, Q. Zhang, X. He "Effects of Mixed Surfactant on Enhancing High Concentration Anthracene and Pyrene Removal from Contaminated Soil," Water Air Soil Pollut., vol. 230: 121, pp. 1–12, 2019.

Title: Effect of Microchannel Dimensions in Electrochemical Impedance Spectroscopy Using Gold Microelectrode

Authors: Hamed GHORBANPOOR, Damion CORRİGAN, Fatma DOĞAN GUZEL

Effect of Microchannel Dimensions in Electrochemical Impedance Spectroscopy Using Gold Microelectrode

Hamed GHORBANPOOR[1], Damion CORRİGAN[2], Fatma DOĞAN GUZEL*[3]

Abstract

Microfluidic chip systems have been an area of interest for lab-on-a-chip and organ-on-a-chip studies in recent years. These chips have many advantages such as high efficiency, low sample consumption, fast analysis, durability and low cost. Today, electrochemical sensors are frequently applied in microfluidic chips because of their potential for label-free detection and low-cost production. A commonly employed electrochemical technique is electrochemical impedance spectroscopy (EIS), which captures changes in phase and amplitude as signal passes through the system under test. In the utilization of microelectrodes within microfluidic channels, noise becomes a problem in EIS measurements. In this study, EIS measurements were performed using microfluidic chips with various dimensions of width while the properties and dimensions of the microelectrodes were kept constant. It was found that the results of cyclic voltammetry (CV) cleaning and EIS experiments deteriorated when smaller than 1 mm wide-microchannels were integrated onto 100 µm wide microelectrodes. These finding sets the basics for on-chip electrochemistry experiments using microfluidic integrated microelectrodes and therefore is fundamentally important in future on-chip EIS measurements.

Keywords: Electrochemical sensing, microfluidic chip, lab-on-a-chip, organ-on-a-chip

1. INTRODUCTION

Electrochemical approaches using microelectrodes are useful for the development of rapid, label free and simple biological assays due to their enhanced electroanalytical capabilities, particularly for the sensitive measurement of the target analytes and the potential for the production of arrays for multi-analyte detection [1-5]. The combination of microfluidic approaches with electrochemical methods permits the development of a convenient and in-flow label-free lab-on-a-chip and organ-on-a-chip technologies for rapid detection methods [6, 7].

* Corresponding author: fdogan@ybu.edu.tr
[1] Eskişehir Osmangazi University, Faculty of Engineering and Architecture, Department of Biomedical Engineering
E-mail: hamedeghorbanpoor@gmail.com
ORCID: https://orcid.org/0000-0002-2665-8172
[2] University of Srrathclyde, Glasgow, Biomedical Engineering
E-mail: damion.corrigan@strath.ac.uk
ORCID: https://orcid.org/0000-0002-4647-7483
[3] Ankara Yıldırım Beyazıt University, Faculty of Engineering and Natural Sciences, Department of Biomedical Engineering
ORCID: https://orcid.org/0000-0002-0513-7431

GHORBANPOOR et al.

Effect of Microchannel Dimensions in Electrochemical Impedance Spectroscopy Using Gold Microelectrode...

One way to do so is to integrate microelectrodes with microfluidic channels.

Microelectrodes have one critical dimension on the scale of microns [8] and are produced in a number of geometries including discs, squares, bands and rings. They have the electroanalytical advantages of reduced iR drop, improved signal to noise, the rapid evolution of steady state diffusion profiles and a relative insensitivity to convection [9]. These properties make microelectrodes an excellent technology for healthcare applications where high sensitivity is required to measure low concentrations [10, 11]. The traditional method for producing microelectrodes is to encapsulate a metal wire in glass [12]. However, whilst effective for sensor production, analytical measurements are subject to significant error due to the variable electrode areas produced [13]. Microfabrication based on photolithographic processes has been demonstrated as a viable route to the production of consistent microelectrodes for analytical applications [12]. The ability to photo-lithographically pattern arrays of individually addressable microelectrodes allows the detection of multiple biomarkers on a single chip [14, 15].

In recent years, microfluidic systems have been developed for various sensor applications. This technology possesses many advantages such as system miniaturization, the ability to handle and process, reduced reagent volumes, vastly reduced instrumental footprint, facile parallelization through multiplexing, improved analytical performance, enhanced sensitivity, and the high analytical throughput [16]. The combination of microfluidic system with microelectrodes is not new however, to date, the performance of sensitive EIS measurements have not been outlined in detail.

In this study, we integrated a microelectrode sensor within a microfluidic chip in order to investigate effect of channels in EIS measurements. Four different microchannel with widths of 150, 300, 500 and 1000 μm were used in the design of the chips. The two-electrode system was applied to design of the microelectrodes. Reference/counter electrode and working electrode widths were 2 mm and 100 μm,

respectively. The experiments were performed by using CV cleaning and EIS analysis to evaluate the electrochemical response for particular microchannel sizes. We believe that the results obtained in this study provides fundamental knowledge for the study of EIS measurements on-chip and this would then help construct easier integrated devices and speed up the efforts towards research on the development of in-flow label-free electrochemical on-chip sensors.

2. MATERIALS AND METHODS

2.1. Microfluidic Channel Design and Production

Four different widths of microchannel dimensions were designed (150, 300, 500, and 1000 μm). The length and depth of microchannels were kept constant and were 10 mm and 50 μm, respectively. Designs were drawn and converted into pdf format with AutoCAD and CorelDRAW software programs, and then sent to Çözüm Tanıtım (Turkey) for acetate mask production. Molds were prepared by using classical lithography methods in a clean room with acetate masks. In the mold preparation, firstly, the surface of a 4 inch silicon wafer (Prime CZ-Si, Nanografi, Turkey) was first washed with isopropanol, acetone and distilled water, then dried with N2 gas. Next the wafer was heated at 100 °C for 5 minutes to remove moisture on the surface. SU8 2050 (Nippon Kayaku, MicroChem, Japan) photoresist was spin-coated onto the cleaned silicon wafer and then was exposed to UV. The soft bake step was completed firstly for 1 minute at 65 °C, then 7 minutes at 95 °C. In the developing step, the developer removed uncross-linked SU-8 photoresist and the design appeared on the wafer. The hard bake process was carried out by placing silicon wafer on the heater for 5 minutes at 150 °C, producing the Si template. Following that, microchannels were fabricated by using soft lithography method by casting Polydimethylsiloxane (PDMS-Sylgard 184, Dow Corning, USA), which is silicone elastomer:crosslinker ratio of 9:1 [17]. Inlet and outlet of microchannels were opened with a 1 mm biopsy punch (Selles Medical, UK).

GHORBANPOOR et al.

Effect of Microchannel Dimensions in Electrochemical Impedance Spectroscopy Using Gold Microelectrode...

2.2. Microelectrode design and production

Gold (Au) electrodes were fabricated on glass substrate via thermal evaporation. The microelectrode design consists of two electrodes, namely a 2 mm-wide counter (CE) / reference electrode (RE) and a 100 µm working electrode (WE), as shown in Figure 1. The length of the electrodes was 12 mm. Electrical connections were made via the contact pads attached to the electrodes and the dimensions of the electrodes were 10*10 mm. Alignment markers (with microchannel shape) were also designed around the microelectrode to ease the integration. Before deposition, electrode patterns were obtained using classical optical lithography method on glass by using the positive photoresist Az-9260, according to a protocol described elsewhere [18]. Firstly, the substrates were then rinsed with isopropyl alcohol, DI- water, and blow-dried with nitrogen gas. After cleaning, the substrates were coated with 2.5 µl positive photoresist AZ- 9620 using a single substrate spin processor. Before exposure, the photoresist coating was soft baked for 2 min 45 s at 110°C. The photoresist-coated substrates were placed under the pattern mask with scotch tape and exposed to an in-house developed UV light source for 70 s. After exposure, the photoresist on the substrates was developed in AZ 400K Developer for 2 min 30 s and rinsed with DI water.

To improve Au adhesion to glass, a 100 nm thickness chromium (Cr) layer was initially deposited on substrate; next, a 300 nm thick Au layer was coated to the Cr layer. Lift-off was performed using acetone to remove photoresists from substrate and hereby microelectrodes were produced.

2.3. Assembly of the Chip

Figure 1 demonstrates a schematic view of the microchannels and microelectrodes to be integrated. For the assembly, the electrodes and channels were first washed with acetone, then dried with nitrogen and finally surfaces were treated using a custom-made plasma device. Straight after the plasma treatment, the exposed surfaces were brought together for bonding and

left on a heater for 2 h at 80 °C. Precise bonding process of two platforms was performed with the help of the alignment marker. Electrically conducting adhesive cold soldering silver epoxy (M.G. Chemicals, Ontario, Canada) was applied on the electrode terminals in order to create electrical connections between clips and electrodes. The electrodes were then kept on a hotplate set to 60 ° C for 24 h to cure the epoxy.
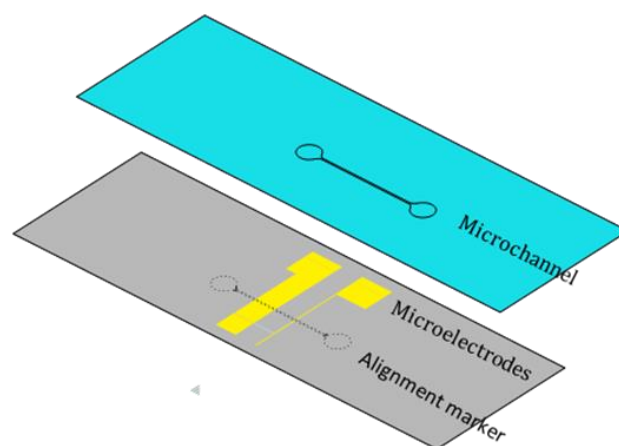
Figure 1 A schematic view of the microchannel and microelectrodes

2.4. Electrode Pretreatment and Electrochemical Measurement

0.1 M H2SO4 was injected into the microchannels for cleaning the surface of the microelectrodes by a micropipette. The inlet and outlet of chips were closed by using stopper after filling microchannel and applied CV (100 cycle) by a potentiostat device (PalmSens PS4, Houten, the Netherland). CV was implemented by sweeping the potential from −0.4 to 0.8 V at 100 mV / s scan rates. After CV cleaning, H2SO4 was removed by deionized water (DI) from the electrode surface, then soluble redox mediator (1 mM ferri/ferrocyanide (Fe(CN)6]3-/4-) was injected by micropipette into the microchannels to measure EIS between 100kHz and 0.1Hz frequencies. Randles equivalent circuit carried out in order to determine the charge transfer resistance (Rct) fitting.

3. RESULTS AND DISCUSSIONS

EIS is a label-free method which is frequently applied in molecular level measurements [6, 19].

GHORBANPOOR et al.

Effect of Microchannel Dimensions in Electrochemical Impedance Spectroscopy Using Gold Microelectrode...

Microelectrodes play a major role in the development of highly sensitive sensor platforms in EIS technology. Microelectrodes are considered to increase sensitivity in low concentrations and volumes when combined with micro systems. However, improvements in the analysis are still required due to the problem of noise when miniaturized. The presence of noise prevents collection of accurate CV and EIS measurements. Therefore, it will not be possible to take more complex measurements at molecular level. In this study, we evaluated the effect of microchannel size while keeping the size of the electrode constant. Figure 2 depicts CV cleaning graphics for 150, 300, and 1000 µm wide microchannels. In electrodes with micron-size, currents are in the pico- to nano-ampere range, therefore two electrode systems are often used [20]. In our study, a two electrode system containing WE and CE/RE were designed.

The lifetime has been set to 100 CV cycles. The noise became visible in the narrowest microchannel, 150 µm -wide channel (Figure 2a), while the widest microchannel 1000 µm (Figure 2c) did not demonstrate any noise in the CV graph and also displayed better oxidation and reduction peaks. In addition, the current amplitude was also seen affected. Figure 2a and Figure 2b show that current is less than 1 nA in noise containing chips. In the other words, 150 µm microchannel has the highest noise and shows the lowest current in the analysis. Therefore, it is clear that the cleaning process was better for wider channel dimensions of more than 300 µm width where the signal was not affected by noise.
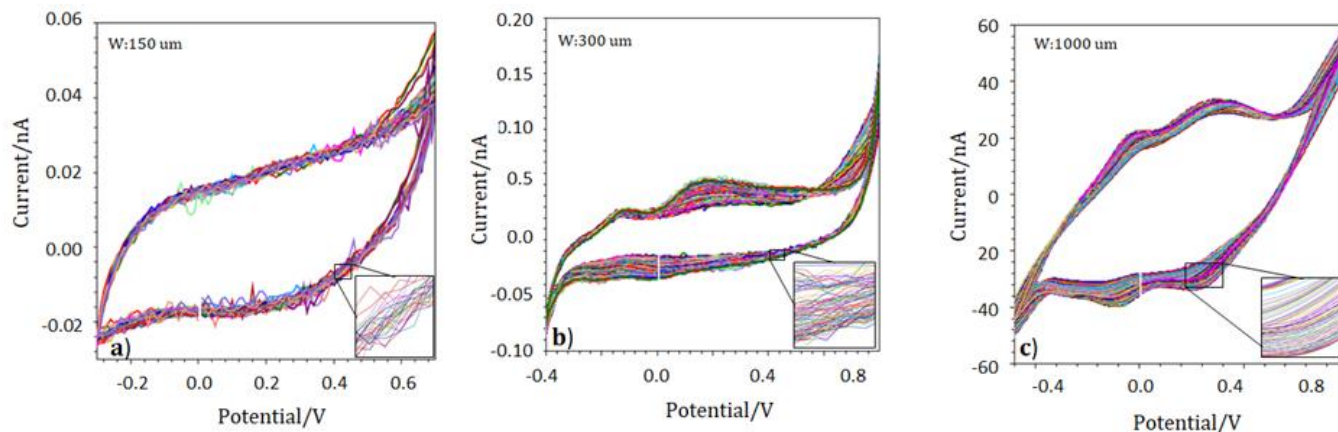
Figure 2 CV cleaning graphics for microchannels widths of a)150 µm ,b)300 µm, and c) 1000 µm.

Figure 3 demonstrates the EIS graphs after CV cleaning for 4 different types of microchannel integrated microelectrodes in the presence of 1 mM FF. The EIS response shows a semicircle transitioning into a 45° line, which is typical of a charge transfer reaction followed by diffusional behavior from the redox couple in solution [21]. Of particular importance to these experiments was the semicircular portion of the plot which was used to extract the Rct, which is indicative of electron transfer rates at the sensor surface [4]. Figure 3a shows that a highly complex graphic appears on the EIS plot for the narrowest microchannel 150 µm experiment. In the second

microchannel with 300 µm dimension, the noise decreases on the EIS plot as seen in Figure 3b. The 500 µm microchannel shows slightly better EIS plot (Figure 3d). It is clear that the EIS plots do not display a normal semicircle transitioning in narrow microchannels, as did not demonstrate normal CV graphs in the cleaning process. However the experiments with 1000 µm dimension depicts a semicircle transitioning approximately without noise in the EIS plot. Thus, we concluded that the wider channels of about 1 mm dimension in width produces more scientifically meaningful EIS respond.

GHORBANPOOR et al.

Effect of Microchannel Dimensions in Electrochemical Impedance Spectroscopy Using Gold Microelectrode...
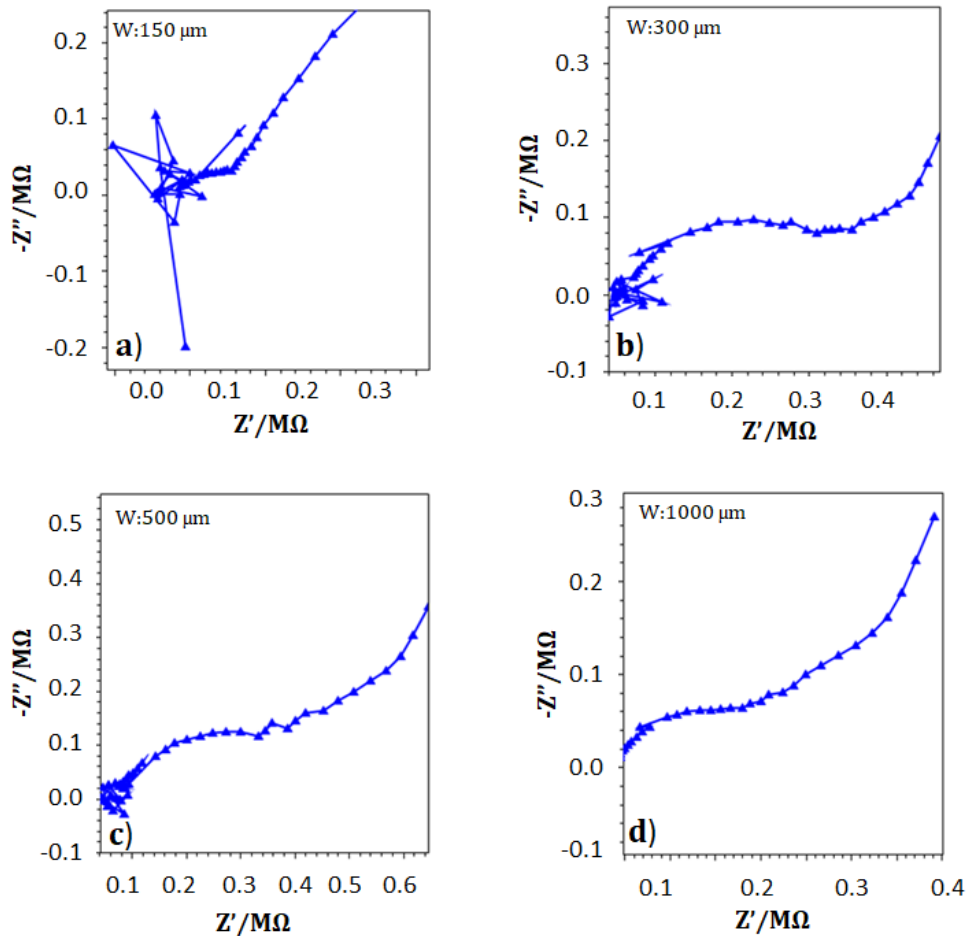
Figure 3 Graphs showing EIS results a) 150 μm, b)300 μm, c) 5000 μm, d 1000 μm

Horny et al. [22] applied a microchannel with 300 μm width and obtained EIS results without any noise. They used a working electrode with 30 μm wide working electrodes, while we applied a working electrode of 100 μm width. In this regard, it is clear that microelectrode sizes are inversely proportional to microchannels in obtained EIS results. Another important factor in EIS measurements is design and structure of microelectrodes. Ayliffe et al. [23] reported EIS results by using the microelectrodes and microchannels with width of the 0.5 and 10 μm, respectively. They designed a different design in study, where the working and other electrodes were placed against each other. It seems several parameters inter-play role in the production of an optimum signal.

In our study, we found that the size of the microchannels directly affects the EIS results. It is reasonable to think that the length and depth of the microchannel also affect the electrochemical output. This research suggests that miniaturization is not always the best option and a cross-over point also exists in the use of microfluidic integrated microelectrodes. We therefore presume that the combination of different design parameters for a particular study should be conducted for certain applications depending on the need.

4. CONCLUSIONS

In this study, we reported that fidelity of EIS measurements in microfluidic chips is dependent on microchannel dimensions. The best results were obtained when microchannels with 1000 μm widths were used. In narrower channels, noise was manifested in the EIS plot and CV cleaning.

GHORBANPOOR et al.

Effect of Microchannel Dimensions in Electrochemical Impedance Spectroscopy Using Gold Microelectrode...

As a result, when the working electrode width is 100 μm, microchannels width of 1000μm and above will be most suitable for performing EIS experiments with low noise. Further studies can be conducted for different electrochemical measurements and applications.

The Declaration of Conflict of Interest/ Common Interest

No conflict of interest or common interest has been declared by the authors.

Authors' Contribution

The authors contributed equally to the study.

The Declaration of Ethics Committee Approval

This study does not require ethics committee permission or any special permission.

The Declaration of Research and Publication Ethics

The authors of the paper declare that they comply with the scientific, ethical and quotation rules of SAUJS in all processes of the paper and that they do not make any falsification on the data collected. In addition, they declare that Sakarya University Journal of Science and its editorial board have no responsibility for any ethical violations that may be encountered, and that this study has not been evaluated in any academic publication environment other than Sakarya University Journal of Science.

REFERENCES

[1] S. O. Akbulut, H. Ghorbanpoor, B. Ö. İpteç, A. Butterworth, G. Avcıoğlu, L. D. Kozacı, G. Topateş, D. K. Corrigan, H. Avcı, and F. D. Güzel, "Impedance testing of porous Si3N4 scaffolds for skeletal implant applications," Applied Sciences, vol. 2, no. 5, pp. 1-6, 2020.

[2] E. O. Blair, S. Hannah, V. Vezza, H. Avcı, T. Kocagoz, P. A. Hoskisson, F. D. Güzel, and D. K. Corrigan, "Biologically modified microelectrode sensors provide enhanced sensitivity for detection of nucleic acid sequences from Mycobacterium tuberculosis," Sensors and Actuators Reports, vol. 2, no. 1, pp. 100008, 2020.

[3] A. Gencoglu, and A. R. Minerick, "Electrochemical detection techniques in micro-and nanofluidic devices," Microfluidics and nanofluidics, vol. 17, no. 5, pp. 781-807, 2014.

[4] F. D. Güzel, H. Ghorbanpoor, A. N. Dizaji, I. Akcakoca, Y. Ozturk, T. Kocagoz, D. K. Corrigan, H. Avci, "Label-free molecular detection of antibiotic susceptibility for Mycobacterium smegmatis using a low cost electrode format," 2020.

[5] Z. Taleat, A. Khoshroo, and M. Mazloum-Ardakani, "Screen-printed electrodes for biosensing: a review (2008–2013)," Microchimica Acta, vol. 181, no. 9-10, pp. 865-891, 2014.

[6] F. D. Güzel, B. Miles, "Development of in-flow label-free single molecule sensors using planar solid-state nanopore integrated microfluidic devices," Micro & Nano Letters, vol. 13, no. 9, pp. 1352-1357, 2018.

[7] S. Schneider, D. Gruner, A. Richter, and P. Loskill, "Membrane Integration into PDMS-free Microfluidic Platforms for

GHORBANPOOR et al.

Effect of Microchannel Dimensions in Electrochemical Impedance Spectroscopy Using Gold Microelectrode...

Organ-on-Chip and Analytical Chemistry Applications," Lab on a Chip, 2021.

[8] H. L. Woodvine, J. G. Terry, A. J. Walton, and A. R. Mount, "The development and characterisation of square microfabricated electrode systems," Analyst, vol. 135, no. 5, pp. 1058-1065, 2010.

[9] D. W. Arrigan, "Nanoelectrodes, nanoelectrode arrays and their applications," Analyst, vol. 129, no. 12, pp. 1157-1165, 2004.

[10] S. Gu, Y. Lu, Y. Ding, L. Li, H. Song, J. Wang, Q. Wu, and Bioelectronics, "A droplet-based microfluidic electrochemical sensor using platinum-black microelectrode and its application in high sensitive glucose sensing," Biosensors and Bioelectronics, vol. 55, pp. 106-112, 2014.

[11] G. Luka, A. Ahmadi, H. Najjaran, E. Alocilja, M. DeRosa, K. Wolthers, A. Malki, H. Aziz, A. Althani, and M. Hoorfar, "Microfluidics integrated biosensors: A leading technology towards lab-on-a-chip and sensing applications," Sensors, vol. 15, no. 12, pp. 30011-30031, 2015.

[12] X. J. Huang, A. M. O'Mahony, and R. G. Compton, "Microelectrode arrays for electrochemistry: approaches to fabrication," Small, vol. 5, no. 7, pp. 776-788, 2009.

[13] D. K. Corrigan, E. O. Blair, J. G. Terry, A. J. Walton, and A. R. Mount, "Enhanced electroanalysis in lithium potassium eutectic (LKE) using microfabricated square microelectrodes," Analytical chemistry, vol. 86, no. 22, pp. 11342-11348, 2014.

[14] G. Lee, J. Lee, J. Kim, H. S. Choi, J. Kim, S. Lee, and H. Lee, "Single microfluidic electrochemical sensor system for simultaneous multi-pulmonary hypertension biomarker analyses," Scientific reports, vol. 7, no. 1, pp. 1-8, 2017.

[15] Z. Lin, Y. Takahashi, Y. Kitagawa, T. Umemura, H. Shiku, and T. Matsue, "An addressable microelectrode array for electrochemical detection," Analytical chemistry, vol. 80, no. 17, pp. 6830-6833, 2008.

[16] P. Cui, and S. Wang, "Application of microfluidic chip technology in pharmaceutical analysis: A review," Journal of pharmaceutical analysis, vol. 9, no. 4, pp. 238-247, 2019.

[17] A. N. Dizaji, Y. Ozturk, H. Ghorbanpoor, A. Cetak, I. Akcakoca, T. Kocagoz, H. Avci, D. Corrigan, and F. D. Güzel, "Investigation of the effect of channel structure and flow rate on on-chip bacterial lysis," IEEE Transactions on NanoBioscience, vol. 20, no. 1, pp. 86-91, 2020.

[18] J. Kaur, H. Ghorbanpoor, Y. Öztürk, Ö. Kaygusuz, H. Avcı, C. Darcan, L. Trabzon, and F. D. Güzel, "On-chip label-free impedance-based detection of antibiotic permeation," IET Nanobiotechnology, vol. 15, no. 1, pp. 100-106, 2021.

[19] M. Vestergaard, K. Kerman, and E. Tamiya, "An overview of label-free electrochemical protein sensors," Sensors, vol. 7, no. 12, pp. 3442-3458, 2007.

[20] S. Kounaves, "Voltammetric techniques," Prentice Hall, Upper Saddle River, NJ, USA, 1997, pp. 709-726.

[21] A. N. Dizaji, Z. Ali, H. Ghorbanpoor, Y. Ozturk, I. Akcakoca, H. Avci, and F. D. Guzel, "Electrochemical-based ''antibiotsensor''for the whole-cell detection of the vancomycin-susceptible bacteria," Talanta, vol. 234, pp. 122695, 2021.

[22] M.-C. Horny, M. Lazerges, J.-M. Siaugue, A. Pallandre, D. Rose, F. Bedioui, C. Deslouis, A.-M. Haghiri-Gosnet, and J. Gamby, "Electrochemical DNA biosensors based on long-range electron transfer:

GHORBANPOOR et al.

Effect of Microchannel Dimensions in Electrochemical Impedance Spectroscopy Using Gold Microelectrode...

investigating the efficiency of a fluidic channel microelectrode compared to an ultramicroelectrode in a two-electrode setup," Lab on a Chip, vol. 16, no. 22, pp. 4373-4381, 2016.

[23] H. E. Ayliffe, A. B. Frazier, and R. D. Rabbitt, "Electric impedance spectroscopy using microchannels with integrated metal electrodes," Journal of Microelectromechanical systems, vol. 8, no. 1, pp. 50-57, 1999.

Title: Reinforcement Learning-Based Safe Path Planning for a 3R Planar Robot

Authors: Mustafa Can BİNGOL

Reinforcement Learning-Based Safe Path Planning for a 3R Planar Robot

Mustafa Can BİNGOL*[1]

Abstract

Path planning is an essential topic of robotics studies. Robotic researchers have suggested some methods such as particle swarm optimization, A*, and reinforcement learning (RL) to obtain a path. In the current study, it was aimed to generate RL-based safe path planning for a 3R planar robot. For this purpose, firstly, the environment was performed. Later, state, action, reward, and terminate functions were determined. Lastly, actor and critic artificial neural networks (ANN), which are basic components of deep deterministic policy gradients (DDPG), were formed in order to generate a safe path. Another aim of the current study was to obtain an optimum actor ANN. Different ANN structures that have 2, 4, and 8-layers and 512, 1024, 2048, and 4096-units were formed to get an optimum actor ANN. These formed ANN structures were trained during 5000 episodes and 200 steps and the best results were obtained by 4-layer, 1024, and 2048-units structures. Owing to this reason, 4 different ANN structures were performed utilizing 4-layer, 1024, and 2048-units. The proposed structures were trained. The NET-M2U-4L structure generated the best result among 4 different proposed structures. The NET-M2U-4L structure was tested by using 1000 different scenarios. As a result of the tests, the rate of generating a safe path was calculated as 93.80% and the rate of colliding to the obstacle was computed as 1.70%. As a consequence, a safe path was planned and an optimum actor ANN was obtained for a 3R planar robot.

Keywords: Artificial neural networks, Deep Deterministic Policy Gradients, path planning, reinforcement learning

1. INTRODUCTION

Path planning is a popular topic in field of robot. Therefore, many researchers have studied this topic and many methods have been developed to solve this task. To illustrate, an optimum path for mobile robots has been generated by using improvement adaptive ant colony algorithm [1]. In another study, a smooth path has been planned utilizing particle swarm optimization and high-degree Bezier curve [2]. In other study, path planning process has been realized faster by using bidirectional associate learning [3]. Path planning process for an industrial robot has been implemented by using genetic algorithm [4]. An improved A* algorithm has been compared to original A* algorithm and the developed algorithm has generated path which is short and high success rate [5]. Another path planning algorithm is reinforcement learning (RL). For example, a path for reconfigurable robot platform has been planned by using RL [6].

* Corresponding author: mustafacanbingol@gmail.com
[1] Fırat University, Faculty of Technology, Department of Mechatronics
ORCID: https://orcid.org/0000-0001-5448-8281

RL when compare to other learning methods such as supervised or unsupervised is more suitable to control robot motion because the method needn't a dataset. Many studies have been carried out utilizing RL in the literature [6]–[12]. For example, Matulis and Harvay have realized a digital twin of an articulated robot using P-proximal policy optimization (PPO) that is a RL method [8]. In another study, MIMO PID controller for mobile robots has been tuned using based on deep deterministic policy gradients (DDPG) method which is a RL method [12]. In other study, hybrid and end-to-end DDPG structures have been formed to control cable driven parallel robot. Two structures have controlled the robot but learn hybrid learned faster than end-to-end structure in the study [7]. The deep p-network and dueling deep p-network have been developed for reaching task of a n-DoF robot. Then, the structures have been realized filliping of a handkerchief and folding a t-shirt tasks [11]. In another study, energy-efficient and adaptive control structures for snake-like robot have been developed by using RL and inverse RL algorithms [10]. A robot has been navigated in mazes by utilizing RL [9].

In the current study, a safe path for 3R planar robot was planned by using DDPG. Also, to obtain an optimum actor artificial neural network (ANN), the proposed 12 different actor ANN structures were designed. The ANN structures, that generated the best results, were mixed and an optimum actor ANN structure was obtained.

2. MATERIALS AND METHODS

The developed system consists of two parts as environment and agent. The environment part contains the 3R planar robot kinematics, obstacle, and target positions. There are ANN that plan safe paths in the agent part. The detailed information about these parts and the communication between these parts were shown in Figure 1.

The main blocks and sub-blocks was shown in Figure 1. State (s), action (a), reward (r), and terminate (trm) variables were used the same as traditional RL algorithms to communicate parts with each other and train networks. The state contains 17 data which include six distances (d_i) between sensors and obstacle, six angles (γ_i) between sensors and obstacle, angles of three joints (θ_i), one distance (d) between the tool center point (TCP) and target, and one angle (γ) between TCP and target. The state variables were shown in Figure 2.

Sensors, target, and obstacle was illustrated orange, green, and red filled circles, respectively. d, γ, d_i, and γ_i were calculated by using Equations (1-4).

$$d = \sqrt{(x_{TCP} - x_{TRG})^2 + (y_{TCP} - y_{TRG})^2} \qquad (1)$$

$$\gamma = tan^{-1}((x_{TCP} - x_{TRG}), (y_{TCP} - y_{TRG})) \qquad (2)$$

$$d_i = \sqrt{(x_{SNS_i} - x_{OBS})^2 + (y_{SNS_i} - y_{OBS})^2} \qquad (3)$$

$$\gamma_i = tan^{-1}((x_{SNS_i} - x_{OBS}), (y_{SNS_i} - y_{OBS})) \qquad (4)$$
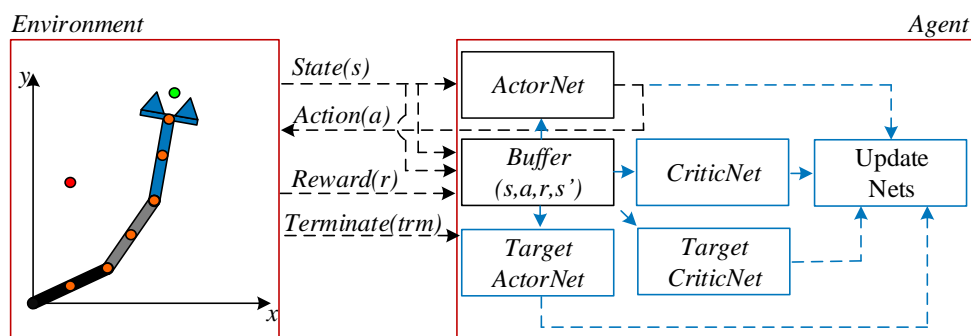
Figure 1 Block diagram of developed system

In Equations (1-4), (x_{TCP}, y_{TCP}), (x_{TRG}, y_{TRG}), and (x_{SNS_i}, y_{SNS_i}) were typified as position of TCP, target and sensor, respectively. After these calculations, s was obtained as [d, γ, d_1, $γ_1$, …, d_6, $γ_6$, $θ_1$, $θ_2$, $θ_3$]. Also, in the system, length of robot links was chosen 0.1 m. Position of target was randomly determined according to $x_{TRG} = 0.05 + 0.15Ω\cos(πΨ)$ and $y_{TRG} = 0.05 + 0.15Ω\sin(πΨ)$ equations. Here, Ω and Ψ were randomly generated numbers between 0 and 1. Position of obstacle was randomly determined according to $x_{OBS} = x_{TRG} + 0.05 + 0.05Ω\cos(πΨ)$ and $y_{OBS} = y_{TRG} + 0.05 + 0.05Ω\sin(πΨ)$ equations. Thus, when the TCP of the robot moves to the target, the possibility of collision that is between the robot and the obstacle increases with the obstacle equations. The TCP of the 3R robot could be calculated by using Table 1 and Equations (5-6).

Table 1 The 3-DoF Planar Robot DH Parameters

Link (i)	a_i	$α_i$	d_i	$θ_i$
1	0	0	l_1	$θ_1$
2	0	0	l_2	$θ_2$
3	0	0	l_3	$θ_3$

$$T_i^{i-1} = R_{Z_{i-1}}(θ_i)T_{Z_{i-1}}(d_i)T_{X_i}(a_i)R_{X_i}(α_i) \quad (5)$$

$$T_3^0 = T_1^0 T_2^1 T_3^2 \quad (6)$$

The kinematic model of the robot was formed by using the homogeneous transformation matrix (T_i^{i-1}). The R_{axis} and T_{axis} were typfied as revlution and translation relevant axis, respectively. Also, link lengths were represented as l in Table 1. The action provides control of the robot. In the current study, to control the robot, the action was designed three parameters as Δθ1, Δθ2, and Δθ3. The Δθ$_i$ parameter was symbolized angle change between two times. The range of Δθ$_i$ was chosen as ±3°. As a result, input of developed system a was designed as [Δθ1, Δθ2, Δθ3].

One of the important topics in RL is the reward function. The reward function directly affects learning performance. The designed reward function was given in Algorithm 1.

In Algorithm 1, thr was symbolized obstacle threshold distance, was chosen 0.025m, and could

be seen in Figure 2. Also, the collision refers to whether the robot and the obstacle collided.
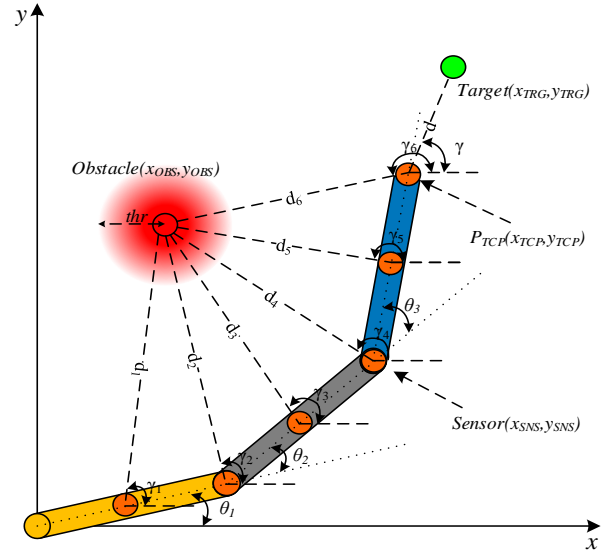
Figure 2 The 3R planar robot

Algorithm 1. Reward Function

function r(d, d_1, d_2, d_3, d_4, d_5, d_6, thr, collision)
$out = -10d$
for i: 1 to 6
    if d_i< thr
        $out = out + \log(d_i)$
if collision=1
    $out = -100$
if d<0.001
    $out = 100$
return out

Terminate function is that the desired operating has occurred or the system has broken down. For example, the state of a game over or arrived finish could be a terminate function for a car game. Terminate function was given in Equation (7) for the current study.

$$trm = \begin{cases} 1, & d < 1mm \text{ or collision} = 1 \\ 0, & other\ conditions \end{cases} \quad (7)$$

In Equation (7), d<0.001 condition was expressed that desired operating occurred and collision=1 condition was shown that the system was damaged. Hence, the system was terminated at these two conditions. The modeled system was simulated in Open AI Gym environment.

The developed 3R planar robot environment was controlled by utilizing DDPG Algorithm. The DDPG Algorithm was given in Algorithm 2. In

order to get detailed information about Algorithm 2, [13] could be examined.

Algorithm 2 DDPG Algorithm

Initialize CriticNet $Q(s, a|\theta^Q)$ and ActorNet $\mu(s|\theta^\mu)$ with θ^Q and θ^μ weight
Adjust TargetNets weights (Q' and μ') according to θ^Q and θ^μ
Initialize replay buffer (RB) memory
for episode: 1 to 5000
   Initialize noise (η)
   Reset environment and get s_t
   for step: 1 to 200
      $a_t = \mu(s_t|\theta^\mu) + \eta_t$
      $r_t, s_{t+1}, trm_t = Environment(a_t)$
      $(s_t, a_t, r_t, s_{t+1}) \to RB$
      if mod(step, update_coefficent)=0
         Get data up to batch size from RB
         $y_i = r_i + \gamma Q'(s_{t+1}, \mu'(s_{t+1}|\theta^{\mu'})|\theta^{Q'})$
         Update CriticNet using $L = \frac{1}{N} \sum_i (y_i - Q(s_i, a_i|\theta^Q))^2$
         Update ActorNet using $\nabla_{\theta^\mu} J \simeq \frac{1}{N} \sum_i \nabla_a Q(s_i, \mu(s_i)) \nabla_{\theta^\mu} \mu(s_i|\theta^\mu)$
         $\theta^{Q'} \leftarrow \tau\theta^Q + (1-\tau)\theta^{Q'}$
         $\theta^{\mu'} \leftarrow \tau\theta^\mu + (1-\tau)\theta^{\mu'}$

In Algorithm 2, update_coefficent, discount factor (γ), and network update coefficient (τ) were chosen as 1, 0.99, and 0.01, respectively. In this study, there was no static dataset since the online RL algorithm was applied. The replay buffer could be called a dataset, and the replay buffer consists of the current state, action, reward, and next-step state data. In the current study, 10^6 was selected as replay buffer size and batch size was chosen as 64. Also, there are 4 ANN structure (2 ActorNets and 2 CriticNets), in Algorithm 2. These ANN's were trained by using replay buffer. In the current study, it was aimed to obtain optimum actor ANN for safe path planning. The actor ANN was given in Algorithm 3.

Algorithm 3 ActorNet Algorithm

function ActorNet(U,L)
 $o = $ Dense Layer (Unit $= $ U, activation $= $ ReLU)(s)
for step: 1 to L-1
   $o = $ Dense Layer (Unit $= $ U, activation $= $ ReLU)(o)

 $out = $ Dense Layer (Unit $= 3$, activation $= $ tanh)(o)
return out

In Algorithm 3, dense layer [14] was preferred as layer type. U and L was shown that unit and layer count, respectively. In the current study, U was chosen 512, 1024, 2048, and 4096. L was determined as 2, 4, and 8. Thus, 12 different actor ANN was formed. The actor ANN models were named as NET-XXXXU-YL. Here, X and Y refers unit and layer count. After this step, the models were trained. As a result of the training, the best results were obtained from 4 layers 1024 and 2048-units networks. Because of this reason, 4 different actor ANN were performed as additionally. Unit count of layer in these 4 different actor ANN were 1024-2048-2048-1024 (NET-M1U-4L), 2048-1024-1024-2048 (NET-M2U-4L), 1024-2048-1024-2048 (NET-M3U-4L), and 2048-1024-2048-1024 (NET-M3U-4L).

3. RESULTS

The proposed 12 actor ANN structures were trained to plan safe path for the 3R planar robot. Each train process contains 5000 episodes and each episode consists of 200 steps. Also, Adam optimizer was utilized and learning rates were chosen as 10^{-4}. When training actor ANN structures, obtained average reward and score graphs were illustrated in Figure 3.

In Figure 3, average reward and score were calculated averaging last 100 episode rewards and scores, respectively. Score was calculated subtracting from number of target arrived by TCP to number of collision occurred. Results of NET-2048U-8L and NET-4096U-8L couldn't be shown because unstable results were obtained. When examined in Fig. 3-b, the best results were obtained by using 1024U,2048U-4L networks. Not only the reward but also the score of these networks were the best around the proposed networks. Descriptive analysis of the training rewards was given in Table 2.

(a) 2-Layers Structures

(b) 4-Layers Structures

(c) 8-Layers Structures
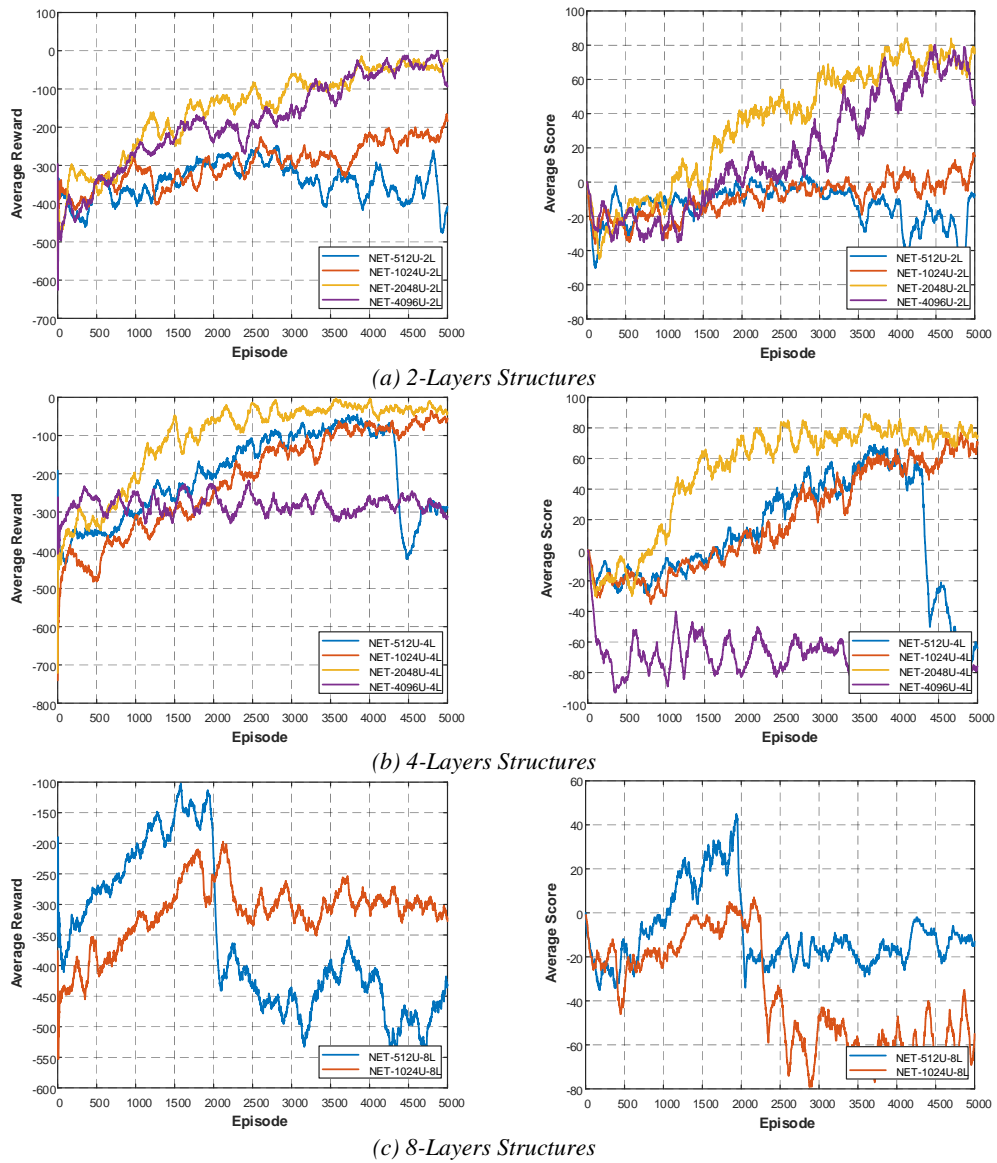
Figure 3 Training process graphs of ANN structures

Table 2 Descriptive analysis of the training rewards

Layer Count (n)	$\overline{X} \pm SD$	Min	Max
2 Layer (n: 20000)	-244.906 ±117.484	-625.914	0.488
4 Layer (n: 20000)	-203.830 ±121.018	-740.419	-2.500
8 Layer (n: 10000)	-336.793 ±96.777	-553.043	-102.201

Table 3 Group comparison of layer counts

Group (I)	Group (J)	p
2 Layer	4 Layer	<0.001
	8 Layer	<0.001
4 Layer	2 Layer	<0.001
	8 Layer	<0.001
8 Layer	2 Layer	<0.001
	4 Layer	<0.001

In Table 2, mean of average rewards ($\overline{X}$), standard deviation (SD), maximum, and minimum values were given according to layer counts. Also, these layer groups were compared with each other utilizing Tukey multiple comparison method. The result of comparison between groups was given in Table 3.

The three groups were found different from each other, as can be seen in Table 3. When Figure 3 and Table 2-3 were examined, 4-layer structure was most successful. The most successful results were obtained in 1024 and 2048 units among the 4-layer structures. In the line with this result, NET-M1U-4L, NET-M2U-4L, NET-M3U-4L, and NET-M4U-4L ANN structures, which were

mentioned in Section 2, were designed. The designed ANN structures were trained, as can be seen in Figure 4. After training process of

proposed ANN structures, the rewards results were analyzed and the analysis results were given in Table 4.
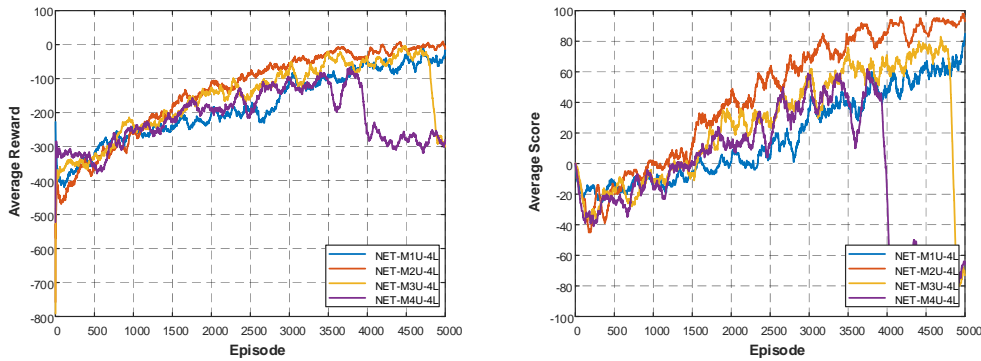
Figure 4 Training process graphs of proposed ANN structures

When Figure 4 and Table 4 were figured out, the best result was obtained from the NET-M2U-4L structure. Therefore, after the training process, the NET-M2U-4L structure was tested as in Figure 5.

The proposed structure successfully passed the single tests, as can be seen in Figure 5. Moreover, video result of these test and more was given in https://youtu.be/sB3wPZMt_pk. After single tests, the structure was tested for 1000 different scenarios. In the test scenarios, the rate of reaching target of the TCP was calculated as 93.80%. The rate of occurring collision was obtained as 1.70% in these scenarios. In other conditions, the median of the distance between TCP and target were calculated as 2.7mm (maximum:0.155m and minimum:0.001m). The current study was carried out according to targets and obstacles which are in located I and II regions

according to the Cartesian coordinate system. The proposed algorithm will be generated solutions according to the targets and obstacles that are in located other regions if the system can be trained for a long time.

Table 4 Descriptive analysis of the proposed ANN structures training rewards

NET (n)	$\bar{X} \pm SD$	Min	Max
NET-M1U-4L (n: 5000)	-180.993 ±100.771	-419.801	-8.658
NET-M2U-4L (n: 5000)	-134.144 ±129.831	-757.891	9.330
NET-M3U-4L (n: 5000)	-157.434 ±106.348	-791.622	-3.334
NET-M4U-4L (n: 5000)	-218.359 ±77.787	-522.497	-67.575

(Step:1)   *(Step:23)*   *(Step:45)*   *(Step:67)*   *(Step:88)*

(a) Test 1

(Step:1)   *(Step:15)*   *(Step:29)*   *(Step:43)*   *(Step:58)*

(b) Test 2

| (Step:1) | (Step:17) | (Step:33) | (Step:49) | (Step:65) |

(c) Test 3

| (Step:1) | (Step:11) | (Step:21) | (Step:31) | (Step:40) |

(d) Test 4
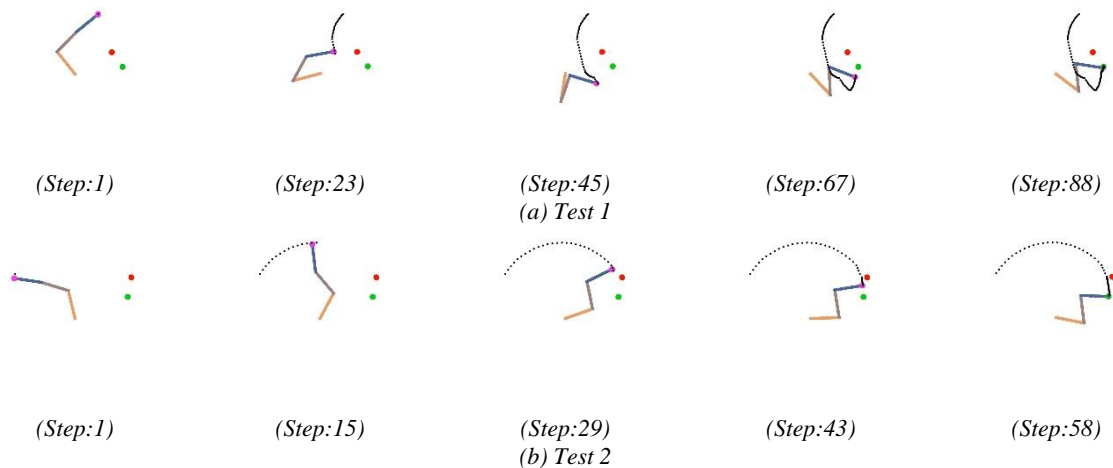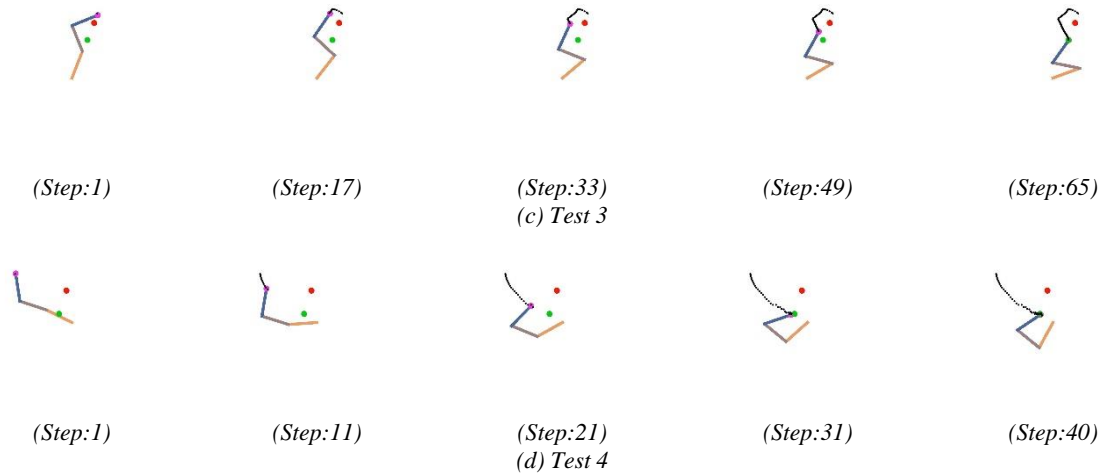
Figure 5 Test of NET-M2U-4L structure

4. CONCLUSIONS

Path planning is an important problem for robotic researchers. Some methods have been developed in order to solve the important problem and one of these developed methods is RL. In the current study, it was aimed that RL-based safe path planning for the 3R planar robot. In the line with this aim, firstly, the 3R planar robot environment was designed. When the environment was designed, state, action, reward, and terminate functions, which are basic components of RL, were determined. After, DDPG Algorithm that is a policy learning method was chosen to control the robot. DDPG Algorithm consists of actor and critic ANN structures. Another aim of the current study was that obtain optimum actor ANN. For this purpose, different ANN structures that have 2, 4, and 8-layers and 512, 1024, 2048, and 4096-units, were trained. After the training process, the best results were obtained from 4-layers ANN structures. Especially among 4-layers ANN structures, the best results were obtained in 1024 and 2048-units. Therefore, 4 different ANN structures, that have mixed unit count, were proposed. The best result was obtained by the proposed NET-M2U-4L structure among these structures. Later, the NET-M2U-4L structure was tested for 1000 different scenarios. In these scenarios, the rate of reaching the target of the TCP was calculated as 93.80%. Also, the rate of occurring collision was obtained as 1.70%. As a result, the RL-based safe path was significantly planned by the developed system and optimum actor ANN was obtained. In future works, the performance of system will be improved and the developed system will be implemented on more advanced robots such as industrial robots.

The Declaration of Conflict of Interest/ Common Interest

No conflict of interest or common interest has been declared by the authors.

Authors' Contribution

The study was performed by one author.

The Declaration of Ethics Committee Approval

The study doesn't need any ethics committee approval or any special permission.

The Declaration of Research and Publication Ethics

The authors of the paper declare that they comply with the scientific, ethical and quotation rules of SAUJS in all processes of the paper and that they do not make any falsification on the data

collected. In addition, they declare that Sakarya University Journal of Science and its editorial board have no responsibility for any ethical violations that may be encountered, and that this study has not been evaluated in any academic publication environment other than Sakarya University Journal of Science.

REFERENCES

[1] Y. Zheng, Q. Luo, H. Wang, C. Wang, and X. Chen, "Path planning of mobile robot based on adaptive ant colony algorithm," J. Intell. Fuzzy Syst., vol. 39, no. 4, pp. 5329–5338, 2020.

[2] B. Song, Z. Wang, and L. Zou, "An improved PSO algorithm for smooth path planning of mobile robots using continuous high-degree Bezier curve," Appl. Soft Comput., vol. 100, 2021.

[3] M. Zhao, H. Lu, S. Yang, Y. Guo, and F. Guo, "A fast robot path planning algorithm based on bidirectional associative learning," Comput. Ind. Eng., vol. 155, no. October 2020, p. 107173, 2021.

[4] L. Larsen and J. Kim, "Path planning of cooperating industrial robots using evolutionary algorithms," Robot. Comput. Integr. Manuf., vol. 67, no. August 2020, 2021.

[5] B. Fu et al., "An improved A* algorithm for the industrial robot path planning with high success rate and short length," Rob. Auton. Syst., vol. 106, pp. 26–37, 2018.

[6] A. Krishna Lakshmanan et al., "Complete coverage path planning using reinforcement learning for Tetromino based cleaning and maintenance robot," Autom. Constr., vol. 112, no. January, 2020.

[7] H. Xiong, T. Ma, L. Zhang, and X. Diao, "Comparison of end-to-end and hybrid deep reinforcement learning strategies for controlling cable-driven parallel robots," Neurocomputing, vol. 377, pp. 73–84, 2020.

[8] M. Matulis and C. Harvey, "A robot arm digital twin utilising reinforcement learning," Comput. Graph., vol. 95, pp. 106–114, 2021.

[9] J. Wang, S. Elfwing, and E. Uchibe, "Modular deep reinforcement learning from reward and punishment for robot navigation," Neural Networks, vol. 135, pp. 115–126, 2021.

[10] Z. Bing, C. Lemke, L. Cheng, K. Huang, and A. Knoll, "Energy-efficient and damage-recovery slithering gait design for a snake-like robot based on reinforcement learning and inverse reinforcement learning," Neural Networks, vol. 129, pp. 323–333, 2020.

[11] Y. Tsurumine, Y. Cui, E. Uchibe, and T. Matsubara, "Deep reinforcement learning with smooth policy update: Application to robotic cloth manipulation," Rob. Auton. Syst., vol. 112, pp. 72–83, 2019.

[12] I. Carlucho, M. De Paula, and G. G. Acosta, "An adaptive deep reinforcement learning approach for MIMO PID control of mobile robots," ISA Trans., vol. 102, pp. 280–294, 2020.

[13] T. P. Lillicrap et al., "Continuous control with deep reinforcement learning," in 4th International Conference on Learning Representations, ICLR 2016 - Conference Track Proceedings, 2016.

[14] "Dense Layer." [Online]. Available: https://www.tensorflow.org/api_docs/python/tf/keras/layers/Dense. [Accessed: 27-Mar-2021].

Title: Sustainable Remediation of Atrazine in Agricultural Fields by Reusing Contaminated Water for Irrigation

Authors: Zohre KURT

Sustainable Remediation of Atrazine in Agricultural Fields by Reusing Contaminated Water for Irrigation

Zohre KURT*[1]

Abstract

High yields of agricultural produce is reached traditionally by the application of fertilizers and/or pesticides. When agricultural soil is saturated with pesticides, any pesticide addition to the soil leaches and thus reaches the underlying groundwater. Preventing further contamination and remediation of this type of contamination remains to be a challenge. Although monitored natural attenuation has been shown as an ultimate solution for decontamination, additional applications have been introduced to rapidly achieve this goal. One solution that also contains economic benefits to the farmers is to pump and reuse. The study described here evaluates the possibility to use pump and reuse technique for atrazine. In this study, six field samples have been evaluated for their atrazine biodegradation capacity. By placing them in sterilized controls and inoculated active columns, field conditions are replicated to study the leaching and biodegradation at the topsoil of agricultural fields. The biodegradation capacities of inoculated active columns ranged between 34 and 75 mg/kg/day of atrazine. The results indicated that using the contaminated water for irrigation could eliminate the pesticide contamination from the soil and groundwater. Overall, this method provides a sustainable solution for pesticide use and remediation by minimizing the pesticide use in agricultural fields without affecting the yield of the planted crops.

Keywords: Biodegradation, pesticide, atrazine, sustainable treatment, pump and treat

1. INTRODUCTION

Pesticide application is inevitable when high yield of the crops is desired. Most of the recommended pesticide amounts overdose the soil and cause contamination that not only stays in the soil but also leaches to the underlying groundwater [1-3]. Since groundwater is a source for agricultural irrigation, contamination prevents its use or requires expensive treatment methodologies [4, 5]. One way to treat the contaminated groundwater is through microbial activities.

Biodegradation of pesticides in the soil has been studied extensively and when sufficient organisms, water, and electron acceptor were present it was shown that the soil is effectively decontaminated [6-9]. However, studies of biodegradation of pesticides in the groundwater have shown that microbial activity for the natural attenuation is slow and therefore the groundwater contamination can persist.

With the scarcity of clean water resources, new technologies and methodologies need to be

* Corresponding author: zkurt@metu.edu.tr
[1] Middle East Technical University, Faculty of Engineering, Environmental Engineering Department
ORCID: https://orcid.org/0000-0001-8862-5846

Zohre KURT

Sustainable Remediation of Atrazine in Agricultural Fields by Reusing Contaminated Water for Irrigati...

developed to save and clean the currently available resources. Pump and treat, biostimulation and bioaugmentation are methodologies that can be used to decontaminate the groundwater. Recently, a pump and reuse technique that uses contaminated groundwater for irrigation has been described where contaminated groundwater to remove nitrate from the groundwater was modeled and showed that decontamination of groundwater can be achieved while using the contaminant (nitrate) as a resource (in this case a fertilizer) [10]. The model showed that pump and treat could provide a sustainable treatment of the groundwater whereas reducing the fertilizer expenses for the farmers. However, the study did not include any experimental data showing that the model could actually work in field conditions and also could not provide any data for the microbial potential for bioremediation.

The present study proposes that pesticide contaminated water can also be used in agricultural lands to remediate the contamination in the field while reducing pesticide use. Atrazine extensively used in the field, were selected to test this hypothesis. Therefore, soil samples were collected and analyzed for their physical properties and columns representing the topsoil of the agricultural fields were operated in the lab to observe how the pump and treat technique would work in the field.

Atrazine is an a trizine herbicide found in many water bodies [11-13]. Its excessive use result in its appearance in the rivers and groundwater in many countries [14-17]. Although banned in the European Union, atrazine is still used extensively in maize weed controls in the USA [18], , the largest producer of corn in the world [19]. The excessive use of atrazine leads to groundwater contamination with concentrations reaching up to 90 μg/L [20]. Therefore, its bioremediation is an important act that needs to be evaluated. In this study not only its bioremediation but its reutilization has been evaluated.

One way to indicate the biodegradability is to study contaminated soils. Hence, soil samples were collected from different parts suspected with atrazine contamination for this study. Samples

analyzed in this study showed that microbial activity was ubiquitous for atrazine. Field columns were designed and operated to mimic the topsoil in the field to evaluate the biodegradation capacities. Operating the field sample columns also revealed that biodegradation capacities of 34 to 75 mg/kg/day for atrazine.

The study described here demonstrates that the novel idea of using contaminated water for irrigation instead of on-site treatment could provide a sustainable treatment option. The findings were further verified using HYDRUS-1D simulations. The overall results indicate that degradation in the topsoil is sufficient to prevent contamination of the groundwater underlying the agricultural field area whereas the adsorption and desorption in the soil provides pesticides concentration sufficient for the crops to grow with desired yield.

2. MATERIALS AND METHODS

2.1. Materials

Atrazine (> 99.5 %), acetonitrile (> 99.9 %), di-sodium phosphate (> 99.5 %) and mono-sodium phosphate (> 99.5 %) were bought from Sigma-Aldrich, USA. Clay was from Milipore Sigma, sand (fine laboratory grade) was from Fisher Scientific and silt (as silt loam) was from AGCLASROOMSTORE .

2.2. Analytical methods

Detection of atrazine was accomplished using high-pressure liquid chromatography (HPLC) for liquid and soil or sediment samples. Liquid samples were centrifuged for 1 min at 3000 rpm prior to analysis, whereas soil and sediment samples were extracted with 50:50 acetonitrile water mixture by vortexing for 3 minutes and letting it sit for 12 hours, then the supernatant was centrifuged for 1 min at 3000 rpm prior to HPLC analysis. Atrazine was analyzed with an isocratic method where Merck reverse phase C18 Chromolith column (100 mm, diameter 4.6 mm) was used with an Agilent 1260 HPLC with a flow rate of 0.5 ml/hr and injection volume of 40 μL. The atrazine was analyzed at 220 nm where the

Zohre KURT

Sustainable Remediation of Atrazine in Agricultural Fields by Reusing Contaminated Water for Irrigati...

minimum detection limits were 0.01 µg/L. The minimum detection limits were established based on the minimum concentration that could provide a measurable concentration through HPLC.

2.3. Field samples

The field soil samples were collected from agricultural soils known to be exposed to atrazine (date of application and concentrations not known) that were actively used for maize production in the Amasya, Balikesir and Denizli provinces of Turkey. The samples were analyzed for their atrazine concentrations, moisture content and porosity prior to microcosm or column preparation. Clay, silt, sand and the soil samples were dried in an oven preheated to 105°C for 12 hours before measuring porosity and amount of contaminants. The porosity was estimated by adding known amount of water to the oven dried sample and the moisture content was determined by weighing the sample before and after being placed in the oven. The samples were then classified according to their particle size based on their sand, silt and clay contents after drying [21]. Maximum adsorption capacities of the samples were determined by measuring atrazine concentrations after different quantities of soil was incubated with atrazine initially on their solubility levels. The methodology was developed with the soil quantity that did not have a final concentration of zero at the equilibrium. Briefly, 50 ml of distilled water containing 5 mg/L of atrazine was mixed with 1 g of dry soil, and the concentration of the mixture was measured before and 24 hours after adding the soil. Maximum desorption capacity of every soil sample was determined by filtering the soil after the adsorption tests, mixing 50 ml of distilled water with filtered soil samples, incubating the mixtures for 24 hours and measuring the released contaminant concentration to the distilled water via HPLC. All chemical and physio chemical analyses were performed in triplicates.

2.4. Microcosm

Microcosms were prepared in 50-ml bottles with 5 grams of dry soil and 20 ml of 20 mM phosphate buffer at pH 7.4 and were sealed with Teflon lids.

The microcosms were constructed sacrificially in duplicates, and they were incubated at room temperature between 21 and 25°C.

Atrazine was added to the bottles from stock solutions with concentrations of 12.5 mg atrazine/L, and microcosms were vortexed for 1 minute and placed in a shaker at 180 rpm. Controls were prepared with autoclaved soil that also contained the pesticides. The contaminant degradation was monitored by HPLC when a microcosm bottle as sacrificed and extracted for the analysis as described in the analytical methods.

2.5. Enrichments for column incubation

Enrichments were performed to validate the presence of degraders and to obtain a mixed culture for inoculating the columns that will determine the biodegradation potential of every soil. The results from the experiments in this study were used to estimate the amount of atrazine that could be reduced or reused for each agricultural soil type.

In order to prepare 0.1 diluted enrichments both for atrazine in Erlenmeyer flasks, the enrichments obtained after the final microcosm bottles were used. In every dilution, the contaminant concentrations were monitored until complete dissipation before additional 0.1 dilution was performed. The concentrations of the contaminants were measured by taking 1 ml samples from the Erlenmeyer flasks and extracting it with the sediment extraction procedure mentioned in the analytical methods. Final cultures used for the column studies were obtained after the overall 0.001 dilution of the original microcosm sample was reached.

2.6. Column Studies

Glass columns with 25 cm of height and 2.2 cm diameter were designed to mimic drip irrigation with flow rate of 60 ml/hr. similar to average solar dripper flow [22]. The pumped water was saturated with oxygen and contained either 10 mg atrazine/L, representing the concentration of the pesticide dissolved in water in the field. In order

Zohre KURT

Sustainable Remediation of Atrazine in Agricultural Fields by Reusing Contaminated Water for Irrigati...

to contain the filling material, the column contained stainless steel mesh on both ends with the size of 20 microns. Both ends of the column also contained sterile filters to prevent any external biological contamination (Figure 1). In order to determine the leaching and aerobic degradation capacity of atrazine in the topsoil in an agricultural field, the column was filled with sand and silt or soil samples from the field up to 15 cm of height. The sand, silt and clay content of the field soil are provided in Table 1. Clay was not used in the column because of its poor infiltration capacity.

The sterile columns were prepared with the column materials mentioned above and autoclaved 3 times for 2 hours each at 121°C under 15 psi. The active columns were prepared with the field samples and were inoculated by adding 10 ml of either atrazine enriched cultures described in the microcosm method above. The enrichments containing either atrazine degraders had optical densities between 0.2 and 0.4 at 600 nm. The contaminant concentrations were monitored via HPLC for influent and effluent of the columns.

2.7. Model Simulation

Model simulation was carried out using HYDRUS-1D package [23] for a soil column having a diameter of 1.1 cm with an active layer of 15 cm representing the topsoil. The entire modeled column was assumed to be 3 m deep representing a shallow vadose zone. The topsoil was assumed to be utilized for cultivation of corn, and the water uptake parameters of corn were taken from Hatipoğlu and Kurt (2019) and the water requirement of the corn was found using Criwar 3.0 based on the generic climate values of corn grown areas in Turkey [24]. The time frame for the corn growth was assumed to be from May to August. Based on the Criwar output data, the irrigation water requirement for the corn was considered as 290, 920, 2110 and 1815 m^3/ha for the months May, June, July and August, respectively. Similarly, the crop evapotranspiration and coefficient were estimated for time period from May to August as 58, 117,

223 and 190 mm, and 0.41, 0.70, 1.06 and 1.04, respectively.
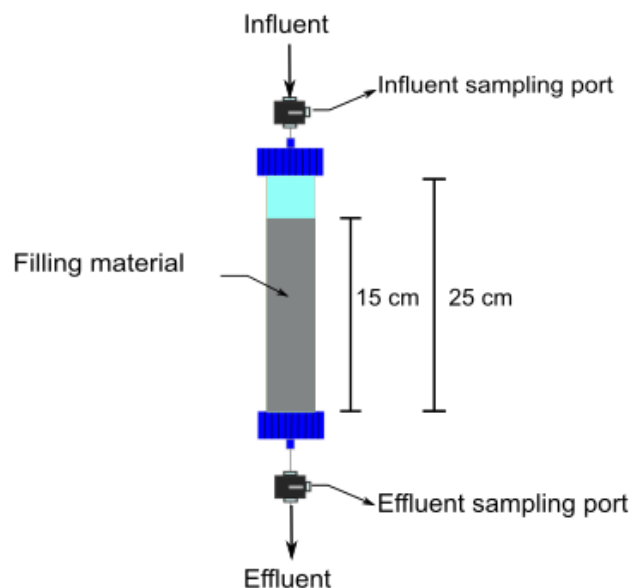
Figure 1 Schematic diagram of the column filled with sand, silt or field soil

Adsorption, desorption and biodegradation parameters were determined based on the field sample analyses conducted as part of this study. The pesticide concentration was kept at the solubility levels of the pesticides in water when introduced to the system, and the rest of the water was assumed to be contamination free. The two scenarios that were constructed to represent drip irrigation were conducted with flow rates of 60 ml/hr and 2 l/hr. representing the average solar drip systems and average conventional drip irrigation systems, respectively. Control scenarios were constructed without any biodegradation. The total amount of the atrazine application was assumed to be 2.5 pound/acre (0.1 mg / column modeled) representing the maximum allowed quantity [18]. The rest of the parameters were kept as default within HYDRUS 1-D.

3. RESULTS AND DISCUSSIONS

3.1. Estimating field sample characteristics

The soil samples collected for the study were characterized according to their silt, clay and sand

content after being autoclaved and dried (Table 1). The results showed that the majority of the soils were classified as loam based on the ternary diagram [25], indicating that the ratio of silt, clay and sand provides a good soil structure that is suitable for agricultural activities [26]. Measured soil properties are consistent with the sampling areas that are actively used for commercial agriculture. The measured sorption and desorption capacities for atrazine were similar to the previously obtained adsorption and desorption isotherms of atrazine with agricultural soil [27]. The desorption of atrazine was lower than its adsorption, because the atrazine was bonded with the soil particles as reported before [28]. The findings were consistent with chemical properties of atrazine with Log K_{ow} (5.8) value. Desorption of the contaminant showed that the leaching potential of atrazine was high, which is consistent with the high water solubility of atrazine (33 mg/L).

The soil samples were further analyzed for their porosity, moisture content and contamination levels (Table 2). The porosity levels of the soils were consistent with loamy soil [26]. Moisture content, on the other hand, could change easily with the irrigation habits or meteorological activity in the field, therefore cannot be compared to a reference value. Atrazine was detected in some samples. The results indicated that atrazine had been actively used in the field where samples were collected.

Table 1 Soil grain size distribution and sorption properties of sterile soil samples for atrazine collected from different fields. Analyses were performed in triplicates.

	Sand (%)	Clay (%)	Silt (%)	Maximum adsorption (mg /kg)	Maximum desorption (mg /kg)
Denizli-1	25 ± 2	17 ± 3	49 ± 7	22.7 ± 1.2	15.1 ± 0.2
Denizli-2	28 ± 3	23 ± 2	46 ± 9	19.1 ± 2.4	17.6 ± 1.2
Balikesir-1	31 ± 2	15 ± 4	51 ± 6	11.9 ± 1.1	9.3 ± 0.4
Balikesir-2	21 ± 1	28 ± 3	43 ± 8	25.9 ± 2.9	22.8 ± 0.4
Amasya-1	38 ± 4	16 ± 1	41 ± 10	20.1 ± 0.9	17.9 ± 1.8
Amasya-2	19 ± 1	24 ± 5	58 ± 12	9.2 ± 3.1	5.9 ± 0.3

3.2. Estimating biodegradation rates of field samples

Presence of active organisms that could degrade contaminants is strongly correlated with the detectable contaminant concentrations in the field [29]. Although not all samples contained atrazine as contaminant, microcosms were prepared for all samples (Figures 2) to investigate the possible biodegradation in the field. To develop a representative scenario, the concentrations were selected to be similar to the field concentrations that would be observed after 50 mg/kg of atrazine application [16, 30]. Not every soil sample contained atrazine (Table 2) but all the soil samples contained organisms that could biodegrade atrazine (Figure 2). The observation that all the soils were able to degrade atrazine was consistent with the previous findings that atrazine degraders are ubiquitous [31, 32]. High copy numbers of atrazine catabolic pathway genes are present in the genomes of the atrazine degraders that protects the bacteria from the loss of atrazine catabolic function [33]. In this study, not detecting atrazine but measuring biodegradation also suggested that atrazine degraders do not lose the ability to degrade atrazine even if they were starved.

Table 2 Contamination levels, porosity and moisture content of the soil samples collected. Analyses were performed in triplicates.

	Atrazine (mg/kg)	Porosity (% v/v)	Moisture content (% v/v)
Denzili-1	0.039 ± 0.0091	41 ± 5	17 ± 3
Denizli-2	0.0191 ± 0.0012	36 ± 4	26 ± 2
Balikesir-1	0.006 ± 0.0003	47 ± 2	21 ± 4
Balikesir-2	0.222 ± 0.0034	39 ± 5	18 ± 1
Amasya-1	ND*	33 ± 7	28 ± 3
Amasya-2	ND	48 ± 8	35 ± 2

*ND indicates that the pesticide of interest was not detected in the soil sample.

The biodegradation of atrazine was established by many different species of bacteria and it was found that governing biodegradation pathways are aerobic [34, 35]. The biodegradation in the field was found to follow first order kinetics [36]. Hence, the initial slopes of the concentrations in Figures 2 was used to estimate the biodegradation rates (Table 3). Controls (i.e., red lines) did not show any biodegradation, indicating that the

Zohre KURT

Sustainable Remediation of Atrazine in Agricultural Fields by Reusing Contaminated Water for Irrigati...

biodegradation was due to microbial activity rather than an abiotic process.

The biodegradability of atrazine in the field was previously reported and parameters as previous pesticide applications, additional contaminants, pH and time of sampling were reported to affect the biodegradation rates. The microbial atrazine degradation rates in different soil samples collected from the field ranged between 0.06-15 mg/kg/day [37-41]. The reported biodegradation rates in this study were within the range for atrazine.
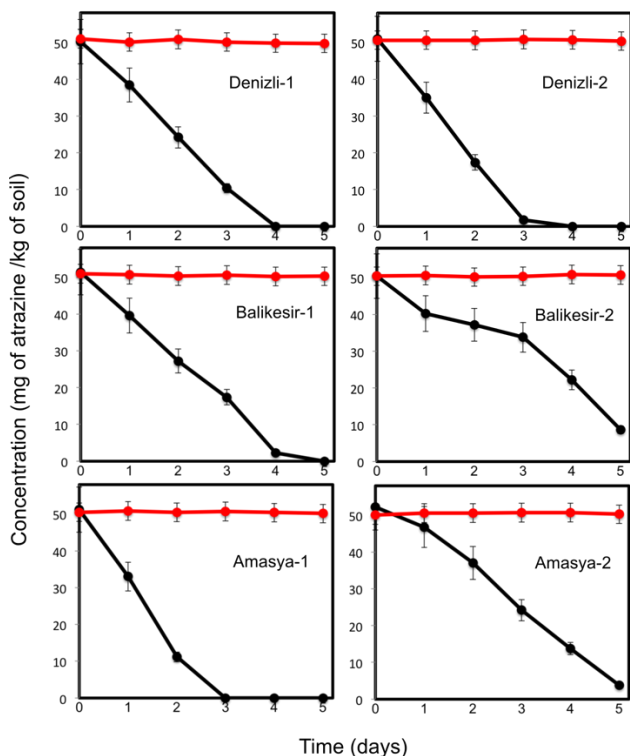
Figure 2 Atrazine concentrations (mg of atrazine/kg of soil) in the microcosms for every soil sample (black). Controls where samples were autoclaved, and atrazine is added (red). All the samples were prepared and measured in duplicates and error bars are the standard deviation between the measurements.

Enrichments were performed using the microcosm samples that showed biodegradation. The samples were diluted with 0.1 increments and monitored for the pesticide degradation until the dilution reached 0.0001. Every sample showing initial biodegradation was successfully enriched assuring that the biodegradation observed is not abiotic and that the degraders were present in the soil samples used for enrichments.

Table 3 Biodegradation rates of the soil samples for atrazine (mg/kg/day)

	Deniz li-1	Deniz li-2	Balikes ir-1	Balikes ir-2	Amasy a-1	Amasy a-2
Atrazi ne	12.4 ± 0.6	16.4 ± 0.4	12.0 ± 0.2	8.4 ± 1.8	19.1 ± 0.9	6.5 ± 1.1

The biodegradation rates were similar for all samples in terms of atrazine. Although the initial pesticide application to the field samples was not known, measurements of similar rates suggested that the microbial presences of atrazine degraders are similar in samples where biodegradation was observed. Similarly, those results indicated that differences in soil parameters, abiotic degradation, sampling time and leaching are the reasons of the variation of the initial concentrations measured (Table 2) as it was observed for other types of pesticides [41, 42].

3.3. Estimating biodegradation capacity in the topsoil

Columns were designed to mimic the topsoil in the field. Sterilized columns were operated abiotically until they reached steady state or until the influent and effluent concentrations were the same for both atrazine (Figure 3). All the columns reached steady state in less than 5 days. Operating the columns with higher flow rate than 60 ml/hr (100 ml/hr) was not physically possible. Only sterile columns were suitable to determine the adsorbed amounts of the contaminants to the soil because the biodegradation was eliminated. The adsorbed amount of pesticides that was calculated for the columns were between 4.8 and 14.1 mg/kg for atrazine. This quantity was calculated using the amount of influent passing through the column, multiplied by the concentration difference between influent and effluent data divided by the weight of the soil placed in the column (121-152 g). Comparison of the adsorbed amounts of pesticides in the column with the field sample analyses (Table 1) showed that only the field sample analysis provides a close estimate of the maximum adsorption of pesticides in the soil. The slightly lower adsorption in the column was due to the shorter contact time of the contaminant with the soil particles and the channeling effect that might have been observed in a column as also stated in the literature [43].

Zohre KURT

Sustainable Remediation of Atrazine in Agricultural Fields by Reusing Contaminated Water for Irrigati...
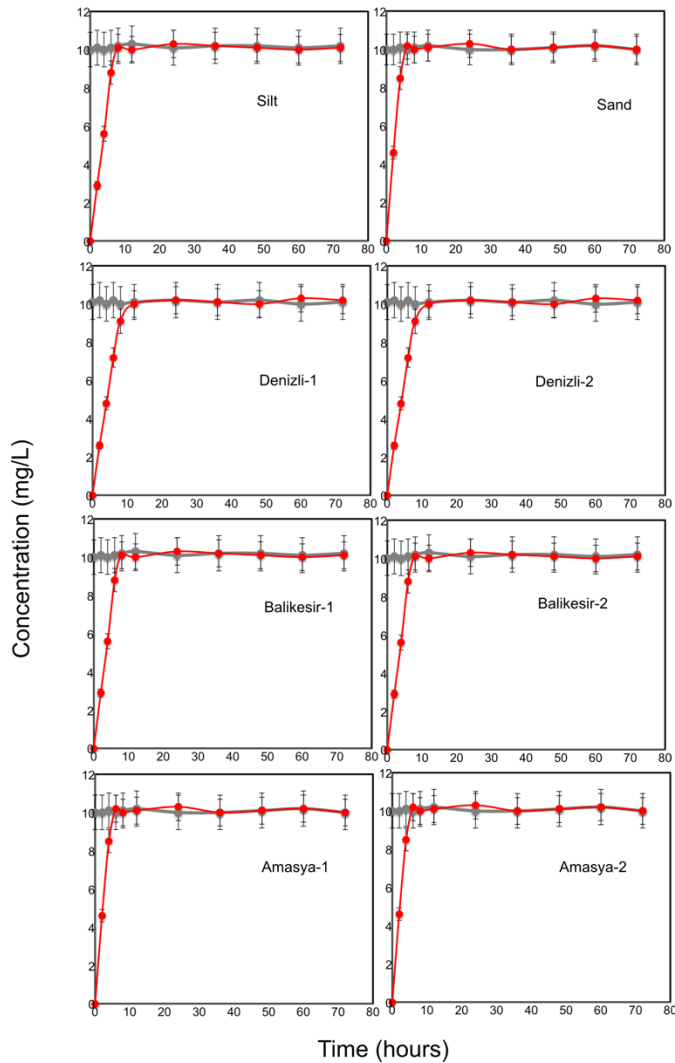
Figure 3 Influent (grey) and effluent (red) concentrations of atrazine (in mg/L) in abiotic columns filled with different types of soil. All the samples were prepared and measured in duplicates and error bars are the standard deviation between the measurements.

All the active columns showed biodegradation (Figure 4). The increase of the concentration of the influent was an expected result since there is a stationary phase until microbial community is established in the column and that results in uncomplete degradation. Seeing a stable output of the effluent indicated a steady state condition achieved in the column. The biodegradation capacities of the columns that were designed to represent topsoil was estimated by multiplying the flow rate of the feed with the difference between the influent and effluent concentrations in the column divided by the weight of the soil in the column. The biodegradation capacities for the

15 cm tall column ranged between 34 and 75 mg/kg/day for atrazine (Table 4). Similar biodegradation capacities were measured for every column because of the inoculation with the same mixture of microbial culture. To date, topsoil column studies were not performed for atrazine however, culture incubated studies were performed with various of isolates. The biodegradation rates in the studies where inoculated microcosms were analyzed, atrazine degradation ranged between 5-20 mg/kg/day [37-41, 44]. The column biodegradation rates of atrazine were higher than the reported microcosm biodegradation rates. The difference could be explained by a higher inoculation in the columns or sufficient oxygen presence during biodegradation because of a constant flow.

Biodegradability of atrazine in columns filled with soil samples were compared with the biodegradability in sand and silt filled columns to determine whether there was a relation between the sand and silt content of the soil, and biodegradation. No correlation was found between the biodegradation capacity of silt and sand columns and the silt and sand content in the soil columns. This finding indicated that the complexity of soil could not be simplified based on its sand or silt composition to estimate biodegradation capacity. The result was different than the previously published study stating that the biodegradability of a pesticide could be correlated with silt content of the soil [45]. The results of the current study showed that microbial activities should be measured for every sample of soil to be collected to estimate biodegradation capacity of atrazine.

Higher biodegradation rates obtained in the entire columns compared to the microcosms showed that topsoil readily degrades the pesticides within 15 cm of depth. When sufficient electron acceptor (oxygen), electron donor (pesticides) and microorganisms through inoculation is provided, the column was an ideal place for the organisms to biodegrade. Pesticides in the columns could not be completely degraded with the described optimal conditions, but their concentrations were decreased. Using pesticide-contaminated water for irrigation could decrease the concentration of

Zohre KURT

Sustainable Remediation of Atrazine in Agricultural Fields by Reusing Contaminated Water for Irrigati...

the pesticide and provide a sustainable remediation technique. Although it is a good practice to completely biodegrade the contaminants in the soil, it is not desirable by the users that all of the pesticides to be quickly biodegraded. This is because the effect of the pesticides would decrease when fast biodegradation occurs and other pesticide alternatives would be required to protect the crops in the field [46]. Therefore, a desirable outcome from this study was that a certain amount of chemicals remained in the columns and so it has been shown that the present methodology could be used not only to decrease the contamination but also to provide an alternative source of pesticides.
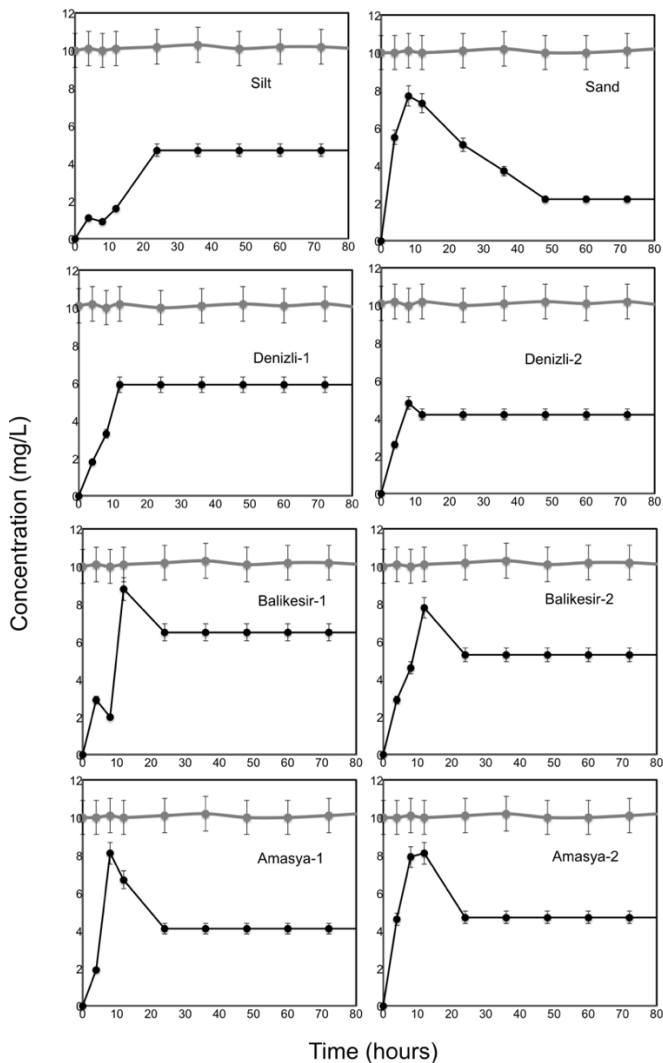
Figure 4 Influent (grey) and effluent (black) concentrations of atrazine (as in mg/L) in active columns filled with different types of soil. All the samples were prepared and measured in duplicates

and error bars are the standard deviation between the measurements.

Table 4 Biodegradation capacities of the columns for atrazine (mg/kg/day)

	Silt	Sand	Denizli-1	Denizli-2
Atrazine	50 ± 6	75 ± 11	40 ± 5	56 ± 7
	Balikesir-1	Balikesir-2	Amasya-1	Amasya-2
Atrazine	34 ± 3	45 ± 6	56 ± 9	51 ± 8

3.4. Estimating the sustainable treatment capacity

A HYDRUS-1D simulation [23] was run for both atrazine using the adsorption/desorption amounts, porosities and biodegradation rates of the characterized field samples (Table 1-3). It was assumed that those parameters did not change throughout the 15 cm of the topsoil and that the governing mechanism was only the adsorption and desorption for the uptake of the pesticides between 15 cm and 3 m. The application of the pesticide was assumed to be via drip irrigation throughout the entire irrigation period with the concentrations of 33 mg/L of atrazine in water during the entire irrigation or until the maximum amount of the pesticide was reached. The choice of the irrigation was consistent with the applications for corn fields [47]. The model provided the output flux for the atrazine at the end of the 3 m, deep soil columns. Atrazine leaches to the groundwater was not detected for the drip irrigation system with a water flow of 60 ml/hr. or 2 l/hr. The results were similar in models both with or without biodegradation. These simulations have verified that pump and reuse is also a valid groundwater treatment methodology.

Known groundwater contamination concentrations were applied to the model to calculate how much atrazine would be reused with this method. Based on the model outputs, groundwater contaminated with 90 μg/L of atrazine would recover 4.5 kg/ha/year of atrazine. Amount is higher than the maximum limits of the pesticides in the field by allowable the United States Department of Agriculture [48, 49], indicating that if contaminated water is used for irrigation, additional pesticides will not be required for the field.

Zohre KURT

Sustainable Remediation of Atrazine in Agricultural Fields by Reusing Contaminated Water for Irrigati...

4. CONCLUSIONS

The present work showed that pump and reuse is a new technique that can remediate contaminated groundwater within the topsoil as long as proper microorganisms are present. Although this study did not include the effect of capillary fringe in the soil column, where the most biodegradation activity is seen [50-53], it was observed that the atrazine could be biodegraded. The results have shown that pump and reuse method is an employable treatment technique for contaminated groundwater and can provide a sustainable remediation. Furthermore, the study showed that a portion of the pesticides in the contaminated groundwater is adsorbed to the topsoil while the rest is biodegraded. Adsorbed pesticide could be reused for crop growth as shown by HYDRUS-1D simulation. Reusing pesticides with this method showed that pump and reuse technique can reduce pesticide use in the long run as long as drip irrigation is applied.

Drip irrigation flow rates is an important parameter for contaminant adsorption due to the contact time of the contaminant with the soil. In this study, drip irrigation rates did not change the infiltration within the 3 m column, but this is a parameter that could be crucial for different chemicals and needs to be addressed in future work. Similarly, it is important to consider that the groundwater is not always contaminated with a single contaminant and it is essential to understand the effect of combined contaminants prior to the water being reused, which requires further investigation for every soil and groundwater.

Overall, this study provided an unconventional sustainable remediation technique to apply contaminated water as irrigation water while the contaminants can be reused during crop growth and excess contamination can be degraded as long as active organisms are present in the soil. It is crucial to evaluate the soil for its potential prior to crop growth to reduce the risk on the crop yield and quality. Therefore, further studies need to be conducted to determine the crop yield and quality once contaminated groundwater is used to assure the outcome.

The Declaration of Conflict of Interest/ Common Interest

No conflict of interest or common interest has been declared by the authors.

Authors' Contribution

The author wrote and conducted the study.

The Declaration of Ethics Committee Approval

This study does not require ethics committee permission or any special permission.

The Declaration of Research and Publication Ethics

The authors of the paper declare that they comply with the scientific, ethical and quotation rules of SAUJS in all processes of the paper and that they do not make any falsification on the data collected. In addition, they declare that Sakarya University Journal of Science and its editorial board have no responsibility for any ethical violations that may be encountered, and that this study has not been evaluated in any academic publication environment other than Sakarya University Journal of Science.

Zohre KURT

Sustainable Remediation of Atrazine in Agricultural Fields by Reusing Contaminated Water for Irrigati...

REFERENCES

[1] A. Abdullah, S. Brobst, I. Pervaiz, M. Umer, and A. Nisar, "Learning dynamics of pesticide abuse through data mining," in Proceedings of the second workshop on Australasian information security, Data Mining and Web Intelligence, and Software Internationalisation-Volume 32, 2004: Australian Computer Society, Inc., pp. 151-156.

[2] D. I. Gustafson, "Groundwater ubiquity score: a simple method for assessing pesticide leachability," Environmental Toxicology and Chemistry: An International Journal, vol. 8, no. 4, pp. 339-357, 1989.

[3] Y. Zhao and Y. Pei, "Risk evaluation of groundwater pollution by pesticides in China: a short review," Procedia Environmental Sciences, vol. 13, pp. 1739-1747, 2012.

[4] D. L. Hoag and A. G. Hornsby, "Coupling groundwater contamination with economic returns when applying farm pesticides," Journal of environmental quality, vol. 21, no. 4, pp. 579-586, 1992.

[5] C. Niti, S. Sunita, K. Kamlesh, and K. Rakesh, "Bioremediation: An emerging technology for remediation of pesticides," Research Journal of Chemistry and Environment, vol. 17, p. 4, 2013.

[6] C. Kao, C. Chai, J. Liu, T. Yeh, K. Chen, and S. Chen, "Evaluation of natural and enhanced PCP biodegradation at a former pesticide manufacturing plant," Water research, vol. 38, no. 3, pp. 663-672, 2004.

[7] D. K. Singh, "Biodegradation and bioremediation of pesticide in soil: concept, method and recent developments," Indian journal of microbiology, vol. 48, no. 1, pp. 35-40, 2008.

[8] W. A. Jury, D. D. Focht, and W. J. Farmer, "Evaluation of Pesticide Groundwater Pollution Potential from Standard Indices of Soil-Chemical Adsorption and Biodegradation 1," Journal of environmental quality, vol. 16, no. 4, pp. 422-428, 1987.

[9] X. Zhang, X. Zhu, R. Chen, S. Deng, R. Yu, and T. Long, "Assessment of Biodegradation in Natural Attenuation Process of Chlorinated Hydrocarbons Contaminated Site: An Anaerobic Microcosm Study," Soil and Sediment Contamination: An International Journal, vol. 29, no. 2, pp. 165-179, 2020.

[10] G. Hatipoglu and Z. Kurt, "Modeling irrigation with nitrate contaminated groundwater," Pamukkale Univ Muh Bilim Derg, vol. 1000, no. 1000, pp. 0-0, 2019, doi: 10.5505/pajes.2019.38963.

[11] U. Dorigo, X. Bourrain, A. Berard, and C. Leboulanger, "Seasonal changes in the sensitivity of river microalgae to atrazine and isoproturon along a contamination gradient," Science of the Total Environment, vol. 318, no. 1-3, pp. 101-114, 2004.

[12] D. Belluck, S. Benjamin, and T. Dawson, "Groundwater contamination by atrazine and its metabolites: risk assessment, policy, and legal implications," ACS Publications, 1991.

[13] A. Gawel, B. Seiwert, S. Sühnholz, M. Schmitt-Jansen, and K. Mackenzie, "In-situ treatment of herbicide-contaminated groundwater-Feasibility study for the cases atrazine and bromacil using two novel nanoremediation-type materials," Journal of Hazardous Materials, p. 122470, 2020.

[14] K. Jayachandran, T. Steinheimer, L. Somasundaram, T. B. Moorman, R. S. Kanwar, and J. R. Coats, "Occurrence of atrazine and degradates as contaminants of subsurface drainage and shallow

Zohre KURT

Sustainable Remediation of Atrazine in Agricultural Fields by Reusing Contaminated Water for Irrigati...

groundwater," Journal of environmental quality, vol. 23, no. 2, pp. 311-319, 1994.

[15] H. Pionke and D. Glotfelty, "Contamination of groundwater by atrazine and selected metabolites," Chemosphere, vol. 21, no. 6, pp. 813-822, 1990.

[16] R. Wauchope, "The pesticide content of surface water draining from agricultural fields—a review 1," Journal of environmental quality, vol. 7, no. 4, pp. 459-472, 1978.

[17] S. Beegum, J. Vanderborght, J. Šimůnek, M. Herbst, K. Sudheer, and I. M. Nambi, "Investigating Atrazine Concentrations in the Zwischenscholle Aquifer Using MODFLOW with the HYDRUS-1D Package and MT3DMS," Water, vol. 12, no. 4, p. 1019, 2020.

[18] Cornell University College of Agricultural and Life Sciences. "Atrazine Application Rates." Cornell University College of Agricultural and Life Sciences. https://fieldcrops.cals.cornell.edu/corn/weed-control-corn/atrazine-application-rates/ (accessed 13/11/19, 2019).

[19] J. Bethsass and A. Colangelo, "European Union bans atrazine, while the United States negotiates continued use," International journal of occupational and environmental health, vol. 12, no. 3, pp. 260-267, 2006.

[20] P. K. Kalita, R. S. Kanwar, J. L. Baker, and S. W. Melvin, "Groundwater residues of atrazine and alachlor under water-table management practices," Transactions of the ASAE, vol. 40, no. 3, pp. 605-614, 1997.

[21] S. K. Abd-Elmabod et al., "Modeling agricultural suitability along soil transects under current conditions and improved scenario of soil factors," in Soil mapping and process modeling for sustainable land use management: Elsevier, 2017, pp. 193-219.

[22] Solar dripper. "Drip irrigation efficiency and water saving." https://solar-dripper.com/en/drip-irrigation-efficiency/ (accessed 15/11/19, 2019).

[23] J. Šimůnek, M. T. Van Genuchten, and M. Šejna, "Recent developments and applications of the HYDRUS computer software packages," Vadose Zone Journal, vol. 15, no. 7, 2016.

[24] M. G. Bos, "Water requirements for irrigation and the environment," 2018.

[25] S. S. Staff, "Soil survey manual," 1993.

[26] R. D. Horrocks and J. F. Valentine, Harvested forages. Academic Press, 1999.

[27] L. Yue, C. Ge, D. Feng, H. Yu, H. Deng, and B. Fu, "Adsorption–desorption behavior of atrazine on agricultural soils in China," Journal of Environmental Sciences, vol. 57, pp. 180-189, 2017.

[28] S. A. Clay and W. C. Koskinen, "Characterization of alachlor and atrazine desorption from soils," Weed Science, pp. 74-80, 1990.

[29] J. C. Spain, J. B. Hughes, and H.-J. Knackmuss, Biodegradation of nitroaromatic compounds and explosives. CRC Press, 2000.

[30] S. Nasseri, M. Dehghani, S. Amin, K. Naddafi, and Z. Zamanian, "Fate of atrazine in the agricultural soil of corn fields in Fars province of Iran," Journal of Environmental Health Science & Engineering, vol. 6, no. 4, pp. 223-232, 2009.

[31] A. Hildebrandt, S. Lacorte, and D. Barceló, "Assessment of priority pesticides, degradation products, and pesticide adjuvants in groundwaters and top soils from agricultural areas of the Ebro river basin," Analytical and

Zohre KURT

Sustainable Remediation of Atrazine in Agricultural Fields by Reusing Contaminated Water for Irrigati...

bioanalytical chemistry, vol. 387, no. 4, pp. 1459-1468, 2007.

[32] S. Rousseaux, A. Hartmann, and G. Soulas, "Isolation and characterisation of new Gram-negative and Gram-positive atrazine degrading bacteria from different French soils," FEMS Microbiology Ecology, vol. 36, no. 2-3, pp. 211-222, 2001.

[33] N. Udiković-Kolić, C. Scott, and F. Martin-Laurent, "Evolution of atrazine-degrading capabilities in the environment," Applied microbiology and biotechnology, vol. 96, no. 5, pp. 1175-1189, 2012.

[34] L. E. Erickson, K. H. Lee, and D. D. Sumner, "Degradation of atrazine and related s-triazines," Critical Reviews in Environmental Science and Technology, vol. 19, no. 1, pp. 1-14, 1989.

[35] M. Radosevich, S. J. Traina, Y.-L. Hao, and O. H. Tuovinen, "Degradation and mineralization of atrazine by a soil bacterial isolate," Applied and Environmental Microbiology, vol. 61, no. 1, pp. 297-302, 1995.

[36] X. Fan and F. Song, "Bioremediation of atrazine: recent advances and promises," Journal of soils and sediments, vol. 14, no. 10, pp. 1727-1737, 2014.

[37] S. Sagarkar et al., "Monitoring bioremediation of atrazine in soil microcosms using molecular tools," Environmental pollution, vol. 172, pp. 108-115, 2013.

[38] L. Pussemier, S. Goux, V. Vanderheyden, P. Debongnie, I. Tresinie, and G. Foucart, "Rapid dissipation of atrazine in soils taken from various maize fields," Weed Research, vol. 37, no. 3, pp. 171-179, 1997.

[39] M. Dehghani, S. Nasseri, and H. Hashemi, "Study of the bioremediation of atrazine under variable carbon and nitrogen sources by mixed bacterial consortium isolated from corn field soil in Fars Province of Iran," Journal of environmental and public health, vol. 2013, 2013.

[40] H. Fang, J. Lian, H. Wang, L. Cai, and Y. Yu, "Exploring bacterial community structure and function associated with atrazine biodegradation in repeatedly treated soils," Journal of hazardous materials, vol. 286, pp. 457-465, 2015.

[41] I. Mirgain, G. Green, and H. Monteil, "Degradation of atrazine in laboratory microcosms: isolation and identification of the biodegrading bacteria," Environmental Toxicology and Chemistry: An International Journal, vol. 12, no. 9, pp. 1627-1634, 1993.

[42] M. Kah, S. Beulke, and C. D. Brown, "Factors influencing degradation of pesticides in soil," Journal of agricultural and food chemistry, vol. 55, no. 11, pp. 4487-4492, 2007.

[43] H. Patel, "Fixed-bed column adsorption study: a comprehensive review," Applied Water Science, vol. 9, no. 3, pp. 1-17, 2019.

[44] D. Lima et al., "Evaluating a bioremediation tool for atrazine contaminated soils in open soil microcosms: the effectiveness of bioaugmentation and biostimulation approaches," Chemosphere, vol. 74, no. 2, pp. 187-192, 2009.

[45] M. S. Rodríguez-Cruz, J. E. Jones, and G. D. Bending, "Field-scale study of the variability in pesticide biodegradation with soil depth and its relationship with soil characteristics," Soil Biology and Biochemistry, vol. 38, no. 9, pp. 2910-2918, 2006.

[46] C. A. Damalas and I. G. Eleftherohorinos, "Pesticide exposure, safety issues, and

Zohre KURT

Sustainable Remediation of Atrazine in Agricultural Fields by Reusing Contaminated Water for Irrigati...

risk assessment indicators," International journal of environmental research and public health, vol. 8, no. 5, pp. 1402-1419, 2011.

[47] F. R. Lamm and T. P. Trooien, "Subsurface drip irrigation for corn production: a review of 10 years of research in Kansas," Irrigation science, vol. 22, no. 3-4, pp. 195-200, 2003.

[48] F. Ackerman, "The economics of atrazine," International Journal of Occupational and Environmental Health, vol. 13, no. 4, pp. 437-445, 2007.

[49] J. Fernandez-Cornejo, R. F. Nehring, C. Osteen, S. Wechsler, A. Martin, and A. Vialou, "Pesticide use in US agriculture: 21 selected crops, 1960-2008," USDA-ERS Economic Information Bulletin, no. 124, 2014.

[50] Z. Kurt, E. E. Mack, and J. C. Spain, "Biodegradation of cis-dichloroethene and vinyl chloride in the capillary fringe," Environmental science & technology, vol. 48, no. 22, pp. 13350-13357, 2014.

[51] Z. Kurt, E. E. Mack, and J. C. Spain, "Natural attenuation of nonvolatile contaminants in the capillary fringe," Environmental science & technology, vol. 50, no. 18, pp. 10172-10178, 2016.

[52] Z. Kurt and J. C. Spain, "Biodegradation of chlorobenzene, 1, 2-dichlorobenzene, and 1, 4-dichlorobenzene in the vadose zone," Environmental science & technology, vol. 47, no. 13, pp. 6846-6854, 2013.

[53] J. Luo, Z. Kurt, D. Hou, and J. C. Spain, "Modeling aerobic biodegradation in the capillary fringe," Environmental science & technology, vol. 49, no. 3, pp. 1501-1510, 2015.

Title: An Investigation on Electric Dipole Transitions of Pt LXVII

Authors: Gülay GÜNDAY KONAN

An Investigation on Electric Dipole Transitions of Pt LXVII

Gülay GÜNDAY KONAN*[1]

Abstract

In the present work, we have reported the energy levels, wavelengths, weighted oscillator strengths, and transition probabilities for electric dipole (E1) transitions of magnesium like platinum (Pt LXVII, Z=78). Accurate knowledge of Mg-like ions are of great importance for astrophysics, plasma, and thermonuclear fusion research. The atomic data are calculated with the AUTOSTRUCTURE code, where relativistic corrections are introduced according to the Breit–Pauli distorted wave approach. In the calculations, quantum electrodynamics effects and correlation contributions have been considered. The present results are in good agreement with other available values. There are no experimental works for Pt LXVII in the literature. We predict new theoretical data for several levels will be helpful for future experimental works.

Keywords: Energy level, transition probability, oscillator strength, wavefunction

1. INTRODUCTION

In fusion research such as International Thermonuclear Experimental Reactor (ITER) project [1], there is a need for more accurate atomic data for energy levels, wavelengths, oscillator strengths, and radiative rates for a wide range of ions. So the interest in highly ionized heavy atoms is a subject of active research. Also, Mg-like ions play an important role in atomic physics, astrophysics, plasma, and thermonuclear fusion research [2-3]. In this framework, we have computed energy levels and radiative parameters for highly ionized Mg-like platinum (Pt LXVII, Z=78). A few works have been reported atomic data of Mg-like platinum.

Hu. et al. reported the transition parameters between the 3l levels for electric dipole transitions for Mg-like ions [4]. The energies of 3s3p, 3p^2, 3s3d, 3p3d, and 3d^2 levels in Mg-like Pt have been given by Santana [5,6]. Iorga and Stancalie have studied energy levels and transition parameters for Mg-like Pt using Flexible Atomic Code [7]. There is no experimental data in the literature.

In this paper, the AUTOSTRUCTURE atomic code is performed to calculate the energy levels and electric dipole wavelengths, oscillator strengths, transition probabilities for Mg-like Pt. The present study has been performed as a part of a continuing study on Mg-like ions [8-12].

2. METHOD OF CALCULATION

AUTOSTRUCTURE atomic code [13, 14] is a general program for the calculation of atomic and ionic energy levels, radiative and autoionization rates and photoionization cross sections using

---

* Corresponding author: ggunday@sakarya.edu.tr
[1] Sakarya University, Faculty of Science and Literature, Department of Physics
ORCID: https://orcid.org/0000-0003-1086-995X

nonrelativistic or semi-relativistic wavefunctions. The program uses Fortran 77/95 programming language and Unix or Windows operating systems. In AUTOSTRUCTURE atomic code, the configuration set is chosen optionally and added new configuration to improve accuracy (a configuration interaction expansion, CI expansion). The CI expansion is related to the choice of radial functions. Each (nl) radial function is calculated in Thomas-Fermi or Slater-Type-Orbital potential model. The Hamiltonian in any coupling model (LS, IC or ICR) is diagonalized to obtain eigenvalues and eigenvectors with which to construct the rates. This code makes use of non-relativistic or kappa-averaged relativistic wavefunctions and the full Breit interaction in the Pauli approximation. AUTOSTRUCTURE program steps are summarized in Figure 1.
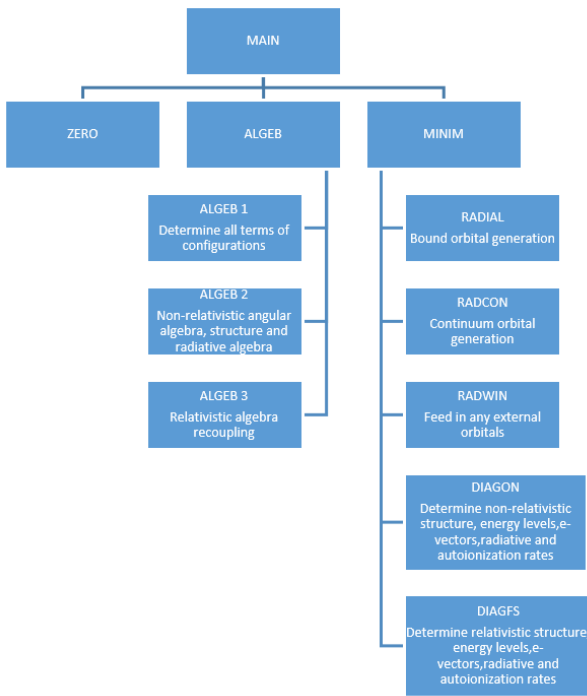
Figure 1 Program Steps of Autostructure [15]

The Hamiltonian can be written as

$$H_{BP} = H_{NR} + H_{RC} \qquad (1)$$

where H_{NR} is the usual nonrelativistic Hamiltonian

$$H_{NR} = \sum_{i=1}^{N} h(i) + \sum_{j>i=1}^{N} \frac{1}{r_{ij}} = \sum_{i=1}^{N} \left(-\frac{1}{2}\nabla_i^2 - \frac{Z}{r_i} \right) + \sum_{j>i=1}^{N} \frac{1}{r_{ij}} \qquad (2)$$

and H_{RC} contains the relativistic correction operators which include one-body relativistic operators (spin-orbit interaction, the non-fine-structure mass variation, and the one-body Darwin corrections) and two-body Breit operators (spin-other-orbit, the mutual spin–spin, the spin–spin contact, the two body Darwin and the orbit–orbit terms). Beside, quantum electrodynamics (QED) contributions (vacuum polarization and self-energy contributions) are treated as a perturbation.

For transitions, code computes Einstein coefficients and associated quantities for multipole transitions of low multipolarity (for electric dipole, E1, radiation). Generally, electric multipole transitions exist in LS coupling. As intermediate coupling wave functions contain admixtures of order α^2, radiative operators must also be expanded up to Breit contributions order.

In the long wavelength low intensity approximation the probability for spontaneous emission by E1 radiation,

$$A_{i'\to i} = 2.6774 \times 10^9 \, \frac{(E_i - E_{i'})^3}{g_i} \cdot S(i,i') \qquad (3)$$

where, g_i is statistical weighted of level, E_i and $E_{i'}$ are energies of levels and $S(i,i')$ is line strengths in form

$$S(i,i') = \left| < i' \| R^{[k]} \| i > \right|^2 \qquad (4)$$

where $R^{[k]}$ is a transition operator and describes each multipole, k is 1 for electric dipole radiation. In addition weighted absorption or emission oscillator strength (gf) value can be written in terms of line strengths

$$(gf)_{i,\,i'} = (gf)_{i',\,i} = \frac{|E_i - E_{i'}|}{3} \cdot S(i,i') \qquad (5)$$

The method has been described in detail in [13-16].

3. RESULT AND DISCUSSION

The AUTOSTRUCTURE calculations have been performed for the energy levels and electric dipole transitions in Mg-like platinum. Mg-like ions have an electronic structure with ten electrons in the closed shells and two valence electrons ($1s^2$ $2s^2$ $2p^6$ $3s^2$). Since they have been observed in solar plasmas [17,18] and laboratory plasmas [19], accurate data are needed for these ions. In this paper, we have calculated relativistic energies, for the levels of 3snl (n = 3–6, l = 0–4), 3pnl (n = 3–6, l = 0–4), 3dnl (n = 3–6, l = 0–4), $2p^53s^23p$, $2p^53s3p^2$, $2p^53p^3$, $2p^53s^23d$, $2p^53s^24s$, $2p^53s3p3d$, $2p^53p^23d$, $2p^53d^3$, $2p^53s3d^2$, $2p^53s3p4s$, $2p^53p3d^2$, $2p^53p3d4s$, $2p^43s^23p^2$, $2p^43s3p^3$ $2p^43s^23d^2$, $2p^43s^23p3d$, $2s2p^53s^23p3d$ configurations and the transition parameters such as wavelengths, weighted oscillator strengths and transition probabilities for electric dipole (E1) transitions between these levels. In the calculations QED (self-energy and vacuum polarization) and Breit interaction (magnetic interaction between the electrons and retardation effects of the electron-electron interaction) contributions have been taken into account. Beside various correlation effects (valence–valence (VV), core–valence (CV) and core–core (CC)), have been considered.

Table 1 displays the energies of 3l3l' (l,l'=0,1,2) levels relative to $3s^2$ $^1S_0$ ground-state level. To assess the accuracy and reliability of our present results, our AUTOSTRUCTURE energies have been compared with the other theoretical results of the relativistic Multi-Reference Møller–Plesset

(MR-MP) theory based on the relativistic Dirac–Coulomb–Breit Hamiltonian [6] and the multi-configurationDirac–Hartree–Fock (MCDHF) which the Breit interaction and leading quantum electrodynamics effects are included as perturbations [4] and fully relativistic model-potential Flexible Atomic Code [7]. There is no experimental data in the literature. We found the percentage difference to compare our results with these methods. The percent difference is calculated using the formula of $\left|\frac{E_{tw}-E_{ow}}{E_{ow}}\right| \times 100$. E_{tw} and E_{ow} show our results and other results, respectively. When we evaluate the percentage differences results, the differences (%) are less than 0.59 for MR-MP, less than 0.53 for FAC, and less than 0.58 for MCDHF. Additionally, the energy levels have been compared with other works drawing a graph. Figure 2 shows the comparison for energy levels. Linear correlation coefficient R^2 is 1. The agreement between the presented data is strong evidence for the reliability of the AUTOSTRUCTURE calculations.
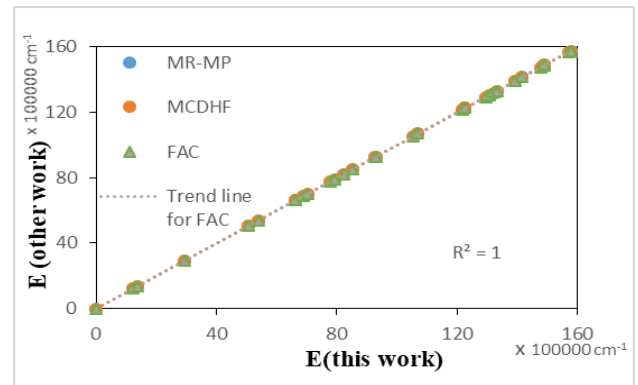
Figure 2 The comparison for energy levels between present AUTOSTRUCTURE results and other MR-MP [6] and MCDHF [4] and FAC [7] results

Table 1 Energy levels (cm^{-1}) and differences (%) in energies for Pt LXVII

Index	Levels		Energy Levels				Diff.%		
			This work	Other Works					
			A.S.	MR-MP[a]	MCDHF[b]	FAC[c]	MR-MP[a]	MCDHF[b]	FAC[c]
1	$3s^2$	$^1S_0$	0	0	0	0	0.00	0.00	
2	3s3p	$^3P_0$	1225050	1227195	1224802.1	1226702.5	0.17	0.02	0.13
3	3s3p	$^3P_1$	1369147	1363754	1361799.7	1364076.39	0.40	0.54	0.37
4	$3p^2$	$^3P_0$	2927825	2921397	2918146.63	2925339.9	0.22	0.33	0.08
5	3s3p	$^3P_2$	5057707	5050746	5054646.66	5054114.98	0.14	0.06	0.07
6	3s3p	$^1P_1$	5379831	5369075	5373970.93	5374991.19	0.20	0.11	0.09

7	$3p^2$	$^1D_2$	6616898	6603313	6604114.46	6606939.52	0.21	0.19	0.15
8	$3p^2$	$^3P_1$	6632746	6622421	6624625.98	6628428.54	0.16	0.12	0.07
9	3s3d	$^3D_1$	6902987	6896371	6895334.73	6900009.79	0.10	0.11	0.04
10	3s3d	$^3D_2$	7027544	7015382	7016204.56	7021734.91	0.17	0.16	0.08
11	3s3d	$^3D_3$	7795847	7754192	7753843.2	7756145.08	0.54	0.54	0.51
12	3s3d	$^1D_2$	7946414	7899749	7900846.29	7904214.68	0.59	0.58	0.53
13	3p3d	$^3F_2$	8225287	8217167	8214111.06	8218841.72	0.10	0.14	0.08
14	3p3d	$^3D_1$	8523303	8516747	8514797.93	8521718.88	0.08	0.10	0.02
15	3p3d	$^3P_2$	9276423	9237871	9235690.69	9239301.91	0.42	0.44	0.40
16	3p3d	$^3F_3$	9313664	9266005	9264352.53	9268160.41	0.51	0.53	0.49
17	$3p^2$	$^3P_2$	10524747	10505626	10514459.09	10516028.5	0.18	0.10	0.08
18	$3p^2$	$^1S_0$	10688467	10672224	10681784.45	10684558	0.15	0.06	0.04
19	3p3d	$^3D_2$	12166079	12155328	12158656.26	12161963.2	0.09	0.06	0.03
20	3p3d	$^3P_0$	12245423	12241460	12244988.02	12249071.1	0.03	0.00	0.03
21	3p3d	$^1F_3$	12252878	12241637	12245796.14	12249788.9	0.09	0.06	0.03
22	3p3d	$^3P_1$	12260695	12245435	12249013.68	12253015.1	0.12	0.10	0.06
23	3p3d	$^3F_4$	12962287	12913890	12917870.27	12918083.4	0.37	0.34	0.34
24	3p3d	$^1D_2$	13055335	13013743	13017773.21	13018717.2	0.32	0.29	0.28
25	3p3d	$^3D_3$	13220603	13170344	13175365.53	13177430.9	0.38	0.34	0.33
26	3p3d	$^1P_1$	13322750	13279799	13285634.92	13288267.5	0.32	0.28	0.26
27	$3d^2$	$^3F_2$	13916827	13913209	13911729.51	13921985.1	0.03	0.04	0.04
28	$3d^2$	$^3P_0$	14137651	14144256	14144095.48	14156950.4	0.05	0.05	0.14
29	$3d^2$	$^3F_3$	14773827	14734119	14733014	14739629.2	0.27	0.28	0.23
30	$3d^2$	$^3P_2$	14869267	14837565	14836947.5	14844932.9	0.21	0.22	0.16
31	$3d^2$	$^1G_4$	14911425	14857585	14857576.42	14864903.1	0.36	0.36	0.31
32	$3d^2$	$^3P_1$	14911979	14885502	14884787.64	14893382.6	0.18	0.18	0.12
33	$3d^2$	$^3F_4$	15710577	15631219	15631221.75	15635041.2	0.51	0.51	0.48
34	$3d^2$	$^1D_2$	15788150	15722082	15722410.12	15727520.7	0.42	0.42	0.39
35	$3d^2$	$^1S_0$	16028288	15966090	15968778.42	15976528.1	0.39	0.37	0.32

[a][6]. [b][4] [c][7]

In Table 2, the energy levels above the ionization level ($2p^53s^23p$ and $2p^53s^23d$ levels) are presented as new data. The core $1s^22s^22p^6$ or $1s^22s^2$ is omitted in the tables.

Table 2 Energy levels (cm^{-1}) for the levels of $2p^53s^23p$ and $2p^53s^23d$ for Pt LXVII

Levels	Energy Levels	Levels	Energy Levels
$2p^53s^23p$ $^3S_1$	75642112	$2p^53s^23d$ $^3P_1$	81203100
$2p^53s^23p$ $^3D_2$	75666263	$2p^53s^23d$ $^1F_3$	81277389
$2p^53s^23p$ $^3D_3$	79269022	$2p^53s^23d$ $^3D_2$	81318928
$2p^53s^23p$ $^1P_1$	79269634	$2p^53s^23d$ $^3F_4$	81952173
$2p^53s^23p$ $^3P_2$	79377445	$2p^53s^23d$ $^1D_2$	81993492
$2p^53s^23p$ $^1S_0$	79941286	$2p^53s^23d$ $^3D_3$	82080818
$2p^53s^23d$ $^3P_0$	80969439	$2p^53s^23d$ $^1P_1$	82379269

Here, electric dipole transitions parameters comparisons have been made graphically. Figure 3 presents the comparison of weighted oscillator strengths. As shown from Figure 3, there is a qualitative agreement with the results of MCDHF

[4] and FAC [7]. Linear correlation coefficient R^2 is 0.9992 for MCDHF.
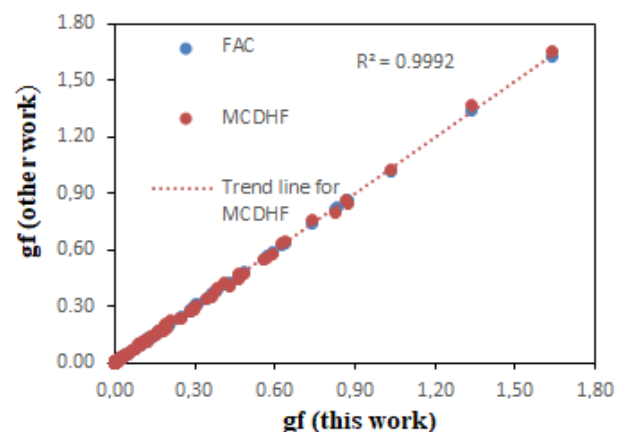
Figure 3 The comparison of weighted oscillator strengths between present AUTOSTRUCTURE results and other MCDHF [4] and FAC [7] results for E1 transitions

In figure 4 the transition probabilities have been presented and compared. Linear correlation

coefficient R^2 is 0.9994 for MCDHF. From this figure, one can see that our calculated transition probabilities match well with the theoretically calculated MCDHF [4] and FAC [7] results.
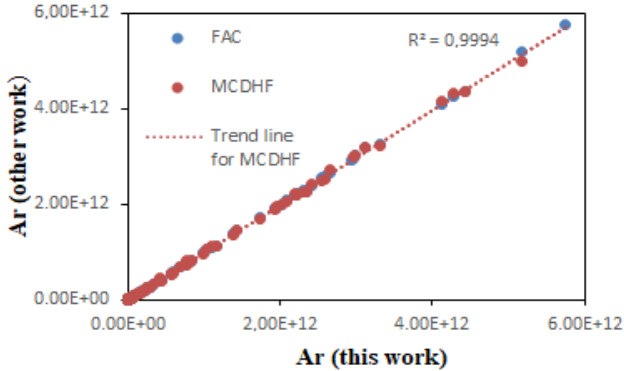
Figure 4 The comparison of transition probabilities between present AUTOSTRUCTURE results and other MCDHF [4] and FAC [7] results for E1 transitions

Table 3 shows the transition probabilities, weighted oscillator strengths, and wavelengths, for some electric dipole (E1) transitions between $2p^5 3s^2 3l$ ($l=1,2$) and $3l3l'$ ($l, l'=0,1,2$) levels in Mg-like Pt. In the table, the number in brackets represents the power of 10. These data on E1 transitions for this ion have been presented for the first time. In the table, the number in brackets represents the power of 10.

Table 3 Transition probabilities, A_r (s^{-1}), weighted oscillator strengths, (gf), and wavelengths, λ (Å), for some electric dipole (E1) transitions between $2p^5 3s^2 3l$ ($l=1,2$) and $3l3l'$ ($l, l'=0,1,2$) levels in Pt LXVII

Transitions	A_r(s^{-1})	gf	λ(Å)
$2p^5 3s^2 3p\ ^3S_1$- $3s3p\ ^3P_0$	1.10(14)	8.89(2)	1.34
$2p^5 3s^2 3p\ ^3S_1$-$3s3p\ ^3P_1$	5.09(13)	4.15(2)	1.34
$2p^5 3s^2 3p\ ^3S_1$-$3s3p\ ^3P_2$	2.64(10)	2.38(5)	1.41
$2p^5 3s^2 3p\ ^3S_1$-$3s3p\ ^1P_1$	4.70(08)	4.29(7)	1.42
$2p^5 3s^2 3p\ ^3S_1$-$3p3d\ ^3F_2$	7.57(08)	7.49(7)	1.48
$2p^5 3s^2 3p\ ^3S_1$-$3p3d\ ^3D_1$	5.37(09)	5.36(6)	1.48
$2p^5 3s^2 3p\ ^3S_1$-$3p3d\ ^3P_2$	8.45(10)	8.62(5)	1.50
$2p^5 3s^2 3p\ ^3D_2$-$3s3p\ ^3P_1$	1.69(14)	2.29(1)	1.34
$2p^5 3s^2 3p\ ^3D_2$-$3s3p\ ^3P_2$	1.15(10)	1.73(5)	1.41
$2p^5 3s^2 3p\ ^3D_2$-$3s3p\ ^1P_1$	5.18(11)	7.87(4)	1.42
$2p^5 3s^2 3p\ ^3D_2$-$3p3d\ ^3F_2$	3.93(09)	6.48(6)	1.48
$2p^5 3s^2 3p\ ^3D_2$-$3p3d\ ^3D_1$	1.18(09)	1.97(6)	1.48
$2p^5 3s^2 3p\ ^3D_2$-$3p3d\ ^3P_2$	5.53(09)	9.40(6)	1.50
$2p^5 3s^2 3d\ ^3P_0$-$3p^2\ ^3P_1$	1.11(14)	3.01(2)	1.34
$2p^5 3s^2 3d\ ^3P_0$-$3s3d\ ^3D_1$	9.40(13)	2.57(2)	1.35
$2p^5 3s^2 3d\ ^3P_1$-$3s^2\ ^1S_0$	7.94(12)	5.41(3)	1.23
$2p^5 3s^2 3d\ ^3P_1$-$3p^2\ ^3P_0$	4.77(11)	3.50(4)	1.27
$2p^5 3s^2 3d\ ^3P_1$-$3p^2\ ^1D_2$	2.27(13)	1.83(2)	1.34
$2p^5 3s^2 3d\ ^3P_1$-$3p^2\ ^3P_1$	2.75(13)	2.22(2)	1.34
$2p^5 3s^2 3d\ ^3P_1$-$3s3d^3D_1$	4.91(13)	4.00(2)	1.34
$2p^5 3s^2 3d\ ^3P_1$-$3s3d\ ^3D_2$	3.25(13)	2.66(2)	1.34
$2p^5 3s^2 3d\ ^3P_1$-$3s3d\ ^1D_2$	2.06(10)	1.73(5)	1.36

4. CONCLUSION

Employing the AUTOSTRUCTURE code, the excitation energies, wavelengths, transition probabilities, and oscillator strengths for the electric dipole transitions of Mg-like Pt have been calculated. Comparisons with three independent atomic structure codes, show that the present AUTOSTRUCTURE results are highly accurate: the differences (%) for the energy levels, oscillator strengths and transition probabilities are around 0.5, 6.2 and 6.0 respectively. We can say that, good agreement has been found with other available theoretical results. The new results reported in this work considerably increase the amount of data available in Mg-like ions. In the end, we believe that our detailed discussion of these data could serve as benchmarks in future experimental work. Further, they will be helpful in plasma physics.

Funding

The Declaration of Conflict of Interest/ Common Interest

No conflict of interest or common interest has been declared by the author.

The Declaration of Ethics Committee Approval

This study does not require ethics committee permission or any special permission.

The Declaration of Research and Publication Ethics

The authors of the paper declare that they comply with the scientific, ethical and quotation rules of SAUJS in all processes of the paper and that they

do not make any falsification on the data collected. In addition, they declare that Sakarya University Journal of Science and its editorial board have no responsibility for any ethical violations that may be encountered, and that this study has not been evaluated in any academic publication environment other than Sakarya University Journal of Science.

REFERENCES

[1] K. Ikeda, "ITER on the road to fusion energy," Nucl. Fusion, vol. 50, pp. 014002-10, 2010.

[2] E. Hinnov, "Highly ionized atoms in tokamak discharges," Phys. Rev. A, vol. 14, pp. 1533-1541, 1976.

[3] I. Martinson and A. Gaupp, "Atomic physics with ion accelerators - beam-foil spectroscopy," Phys. Rep., vol.15, pp. 113-180, 1974.

[4] F. Hu, M. Mei, C. Han, B. Han, G. Jiang, and J. Yang, "Accurate multiconfiguration Dirac–Hartree–Fock calculations of transition probabilities for magnesium-like ions" J. Quant. Spectrosc. Radiat.Transfer, vol.149, pp.158-167, 2014.

[5] J.A. Santana and E. Trabert. "Resonance and intercombination lines in Mg-like ions of atomic numbers $Z = 13$–92," Phys. Rev. A, vol. 91, pp. 022503-7, 2015.

[6] J.A. Santana, "Relativistic MR-MP energy levels: Low-lying states in the Mg isoelectronic sequence," At. Data Nucl. Data Tables, vol. 111-112, pp. 87-186, 2016.

[7] C. Iorga and V. Stancalie, "The study of the core–valence and core–core correlation effects on the radiative properties along the magnesium isoelectronic sequence,"Atomic Data and Nuclear Data Tables, vol. 123–124, pp.313-328, 2018.

[8] L. Özdemir, G. Günday Konan and S. Kabakçı, "Energies and Radiative Transition Parameters for Mg-Like Tungsten," Acta Phys. Pol. A, vol.124, no.4, pp. 649-657, 2013.

[9] G. G. Konan, S. Kabakçı and L. Özdemir, "E1, E2 and M1 transitions between n=3 levels in magnesium-like tungsten,"Iran. J. Sci. Technol., vol. 38A4, pp. 415-421, 2014.

[10] G. G. Konan, L. Özdemir and G. Ürer, "Energy levels and strong electric dipole transitions in magnesium-like gold," J. Quant. Spectrosc. Radiat. Transfer, vol. 145, pp. 110-120, 2014.

[11] G. G.Konan and L. Ozdemir, "Energies, wavelengths, transition probabilities, and oscillator strengths for electric dipole transitions of Na-like and Mg-like mercury," Can. J. Phys., vol. 96, pp. 1098–1103, 2018.

[12] G. G. Konan, "Calculation of energy levels and electric dipole (E1) transition parameters for magnesium-like bismuth, "Can. J. Phys., vol. 97, pp. 959–965, 2019.

[13] N. R. Badnell, "A Breit–Pauli distorted wave implementation for AUTOSTRUCTURE," Comput. Phys. Commun., vol. 182, pp.1528-1535, 2011.

[14] N. R. Badnell, "Dielectronic recombination of Fe $^{22+}$ and Fe^{21+}," J. Phys. B, vol. 19, pp. 3827-3835, 1986.

[15] https://www.adas.ac.uk/man/chap7-01.pdf

[16] N. R. Badnell, "On the effects of the two-body non-fine-structure operators of the Breit - Pauli Hamiltonian," J. Phys. B, vol. 30, pp. 1-11, 1997.

[17] L.W.Acton, M.E. Bruner and W.A. Brown, "Rocket spectrogram of a solar- flareinthe 10–100 Å region,"Astrophys. Journal, vol.291, pp. 865-78, 1985.

[18] F.P. Keenan, J.J.Drake, S.Chung, N.S.Brickhouse, K.M.Aggarwal ans A.Z.

Msezane, et al. , "Soft x-ray emission lines of Fe XV in solar flare observations and the chandra spectrum of capella, "Astrophys. Journal, vol. 645, pp. 597–604, 2006.

[19] S.O. Kastner, M.Swartz, A.K.Bhatia and J.Lapides, "Observations of n=3, n=4 transitions in the Mg I and Si I sequences for elements chromium through zinc," J Opt. Soc. Am., vol.68, pp. 1558–64, 1978.

Sakarya University Journal of Science
SAUJS

Title: Bipolar Fuzzy Supra Topological Spaces

Authors: Hami MALKOÇ, Banu PAZAR VAROL

Bipolar Fuzzy Supra Topological Spaces

Hami MALKOÇ[1], Banu PAZAR VAROL*[2]

Abstract

In the present work, we introduce bipolar fuzzy supra topological space as a generalization of fuzzy supra topological space, investigate the basic properties, give the concepts of interior and closure and encouraged them by examples and counterexamples. Moreover, we study the concepts of bipolar fuzzy supra continuity and S^* bipolar fuzzy supra continuity and see that composition of two S^* bipolar fuzzy supra continuous functions may not be a S^* bipolar fuzzy supra continuous function. Also, we attempt to define the concept of compactness on bipolar fuzzy supra topology.

Keywords: Bipolar fuzzy set, bipolar fuzzy supra topology, bipolar fuzzy supra continuity, bipolar fuzzy supra compactness.

1. INTRODUCTION

The fundamentals of theory of fuzzy sets were given by L. Zadeh [1] in 1965. Fuzzy generalizations of different mathematical concepts were introduced and studied such as interval valued fuzzy sets [2], intuitionistic fuzzy sets [3], fuzzy soft sets [4] etc. In 1994, Zhang [5] introduced the notion of a bipolar fuzzy set and in 2004, Lee [6] gave the definition of bipolar fuzzy sets as an extension of fuzzy sets. In bipolar fuzzy sets membership degree space is extended from the interval [0, 1] to [−1, 1]. In this set, the membership degree 0 produces that elements are irrelevant to the corresponding property, the membership degrees on (0, 1] assign that element somewhat supply the property and the membership degrees on [−1, 0) assign that elements somewhat supply the implicit counter

property. At present, studies on bipolar fuzzy theory are very popular and have been applied in various fields. In 2013, M. S. Anitha et. al. [7] defined the concept of bipolar fuzzy subgroup and worked some properties. S.P. Subbian et. al. [8] studied on bipolar valued fuzzy ideals of ring in 2018. B. Pazar Varol [9] gave the definition of bipolar fuzzy submodule of a given classical module and investigated some fundamental properties in 2021. The concept of bipolar fuzzy topology was introduced by M. Azhagappan and M. Kamaraj [10] in 2016. Then, J. H. Kim et. al. [11] introduced the bipolar fuzzy neighborhood structure, base and subbase in 2019.

In 1983, Mashhour et al. [12] defined the concept of supra topology, which is the weaker version of classical topology and they also studied supra closed (open) sets and supra continuous functions.

* Corresponding author: banupazar@kocaeli.edu.tr

[1] Kocaeli University, Institute of Natural Sciences
E-mail: hami.malkoc.4161@gmail.com
ORCID: https://orcid.org/0000-0002-0321-0316
Kocaeli University, Faculty of Science and Literature, Department of Mathematics
ORCID: https://orcid.org/0000-0002-8627-7910

They called a family $\tau \subset \wp(X)$ a supra topology on X if it contains X and $\emptyset$ and is closed under arbitrary union. In 1987, Abd El-Monsef et al. [13] defined fuzzy supra topological space as a generalization of the concept of supra topological space and studied fundamental concepts of fuzzy supra topological spaces. Then, many authors studied supra topology and its extensions such as supra soft topology and fuzzy supra (soft) topology ([14], [15], [16], [17], [18], [19]). In this paper, we have given the definition of bipolar fuzzy supra topology and have investigated some concepts on bipolar fuzzy supra topology such as interior, closure, continuity and compactness. In bipolar fuzzy supra topological spaces we have lost some of the properties in bipolar fuzzy topological spaces, for example, the concept of closure (interior) does not have distributive property on union (intersection). We have showed these by the examples. We have defined S^* bipolar fuzzy supra continuity and seen that composition of two S^* bipolar fuzzy supra continuous functions may not be a S^* bipolar fuzzy supra continuous function.

2. PRELIMINARIES

Definition 2.1: [6] Let U be a nonempty set. A bipolar fuzzy set X in U is defined as

$$X = \{< u, \mu_X^+(u), \mu_X^-(u) > \mid u \in U\}$$

where $\mu_X^+: U \longrightarrow [0,1]$ and $\mu_X^-: U \longrightarrow [-1,0]$ are two functions. $\mu_X^+(u)$ is called the positive membership degree of u and it denotes the satisfaction degree of u is to be the element of X. $\mu_X^-(u)$ is called the negative membership degree and it denotes the satisfaction degree of u to some implicit counter property of bipolar valued fuzzy set X.

The family of all bipolar fuzzy set in U is denoted by $BPF(U)$.

Example 2.2: $X = \{< a, 0.6, -0.4 >, < b, 0.8, -0.3 >, < c, 0.5, -0.5 >\}$ is a bipolar fuzzy set in $U = \{a, b, c\}$.

Definition 2.3: [10] 1. Universal bipolar fuzzy set is a bipolar fuzzy set on U and denoted by $\mathbf{1}_{BP} =$

$(\mathbf{1}_{BP}^+, \mathbf{1}_{BP}^-)$ where for each $u \in U$, $\mathbf{1}_{BP}^+(u) = 1$ and $\mathbf{1}_{BP}^-(u) = -1$.

2. Bipolar fuzzy empty set is a bipolar fuzzy set on U and denoted by $\mathbf{0}_{BP} = (\mathbf{0}_{BP}^+, \mathbf{0}_{BP}^-)$ where for each $u \in U$, $\mathbf{0}_{BP}^+(u) = \mathbf{0}_{BP} = \mathbf{0}_{BP}^-(u)$.

Definition 2.4: [6] Let $X, Y \in BPF(U)$. Then,

1. $X \subseteq Y \Longleftrightarrow \mu_X^+(u) \leq \mu_Y^+(u)$ and

$$\mu_X^-(u) \geq \mu_Y^-(u), \text{ for each } u \in U.$$

2. $X = Y \Longleftrightarrow \mu_X^+(u) = \mu_Y^+(u)$ and $\mu_X^-(u) = \mu_Y^-(u)$, for each $u \in U$.

3. $X \cap Y = \{< x, \mu_{X \cap Y}^+(u), \mu_{X \cap Y}^-(u) > \mid u \in U\}$, where

$$\mu_{X \cap Y}^+(u) = \min\{\mu_X^+(u), \mu_Y^+(u)\}$$

and

$$\mu_{X \cap Y}^-(u) = \max\{\mu_X^-(u), \mu_Y^-(u)\}.$$

4. $X \cup Y = \{< x, \mu_{X \cup Y}^+(u), \mu_{X \cup Y}^-(u) > \mid u \in U\}$, where

$$\mu_{X \cup Y}^+(u) = \max\{\mu_X^+(u), \mu_Y^+(u)\}$$

and

$$\mu_{X \cup Y}^-(u) = \min\{\mu_X^-(u), \mu_Y^-(u)\}.$$

5. The complement of a bipolar fuzzy set X is defined as,

$$X^c = \{< u, 1 - \mu_X^+(u), -1 - \mu_X^-(u) > \mid u \in U\}.$$

Proposition 2.5: [11] Let X, Y and W be bipolar fuzzy sets in common universal set U. Then followings are satisfied.

1. $X \cup X = X$ and $X \cap X = X$.

2. $X \cup Y = X \cup Y$ and $X \cap Y = Y \cap X$.

2. $X \cup (Y \cup Z) = (X \cup Y) \cup Z$ and

$\quad X \cap (Y \cap Z) = (X \cap Y) \cap Z.$

3. $X \cup (Y \cap Z) = (X \cup Y) \cap (X \cup Z)$ and

$X \cap (Y \cup Z) = (X \cap Y) \cup (X \cap Z)$.

4. $X \cup (X \cap Y) = X$ and $X \cap (X \cup Y) = X$.

5. $X \cap Y \subset X$ and $X \cap Y \subset Y$.

6. $X \subset X \cup Y$ and $Y \subset X \cup Y$.

7. $(X^c)^c = X$.

8. $(X \cup Y)^c = X^c \cap Y^c$ and $(X \cap Y)^c = X^c \cup Y^c$.

9. If $X \subset Y$ and $Y \subset Z$ then $X \subset Z$.

10. If $X \subset Y$, then

$X \cap Z \subset Y \cap Z$ and $X \cup Z \subset Y \cup Z$.

Definition 2.6: [6] Let U be a nonempty set and $\left(X_j\right)_{j \in J}$ be a family of some bipolar fuzzy sets in U.

1. The intersection of $\left(X_j\right)_{j \in J}$ is a bipolar fuzzy set in U, denoted by $\bigcap_{j \in J} X_j$ and defined by

$\left(\bigcap_{j \in J} X_j\right)(u) = \left(\bigwedge_{j \in J} \mu_X^+(u), \bigvee_{j \in J} \mu_X^-(u)\right)$

for each $u \in U$.

2. The union of $\left(X_j\right)_{j \in J}$ is a bipolar fuzzy set in U, is denoted by $\bigcup_{j \in J} X_j$ and defined by

$\left(\bigcup_{j \in J} X_j\right)(u) = \left(\bigvee_{j \in J} \mu_X^+(u), \bigwedge_{j \in J} \mu_X^-(u)\right)$

for each $u \in U$.

Corollary 2.7: [11] Let U be a nonemty set, $X \in BPF(U)$ and $\left(X_j\right)_{j \in J} \subset BPF(U)$. Then followings are satisfied:

1. (Generalized distributive laws):

$X \cup \left(\bigcap_{j \in J} X_j\right) = \bigcap_{j \in J}(X_j \cup X)$,

$X \cap \left(\bigcup_{j \in J} X_j\right) = \bigcup_{j \in J}(X_j \cap X)$.

2. (Generalized De Morgan's laws):

$\left(\bigcup_{j \in J} X_j\right)^c = \bigcap_{j \in J} X_j^c$,

$\left(\bigcap_{j \in J} X_j\right)^c = \bigcup_{j \in J} X_j^c$.

Definition 2.8: [11] Let $g: U \longrightarrow V$ be a mapping and $X \in BPF(U)$, $Y \in BPF(V)$.

1. The image of X under g, denoted by $g(X)(v) = \left(\mu_{g(X)}^+(v), \mu_{g(X)}^-(v)\right) = \left(g(\mu_X^+)(v), g(\mu_X^-)(v)\right)$, is a bipolar fuzzy set in V defined as follows.

$$g(\mu_X^+)(v) = \begin{cases} \bigvee \mu_X^+(u), & u \in g^{-1}(v), \\ 0, & other \end{cases}$$

$$g(\mu_X^-)(v) = \begin{cases} \bigwedge \mu_X^-(u), & u \in g^{-1}(v), \\ 0, & other \end{cases}, \forall v \in V.$$

2. The preimage of Y under g, denoted by $g^{-1}(Y) = \left(g^{-1}(\mu_Y^+), g^{-1}(\mu_Y^-)\right)$, is a bipolar fuzzy set in U defined as follows.

$[g^{-1}(\mu_Y^+)](u) = \mu_Y^+ \circ g(u)$

and

$[g^{-1}(\mu_Y^-)](u) = \mu_Y^- \circ g(u), \forall u \in U.$

Corollary 2.9: [11] Let $f: U \longrightarrow V$ be a mapping and $X, X_1, X_2 \in BPF(U)$, $\left(X_j\right)_{j \in J} \subset BPF(U)$, Y, $Y_1, Y_2 \in BPF(V)$ and $\left(Y_j\right)_{j \in J} \subset BPF(V)$. Then the followings are satisfied.

1. If $X_1 \subset X_2$ then $f(X_1) \subset f(X_2)$.

2. $f(X_1 \cup X_2) = f(X_1) \cup f(X_2)$,

$f\left(\bigcup_{j \in J} X_j\right) = \bigcup_{j \in J} f(X_j)$.

3. $f(X_1 \cap X_2) \subset f(X_1) \cap f(X_2)$,

$f\left(\bigcap_{j \in J} X_j\right) \subset \bigcap_{j \in J} f(X_j)$.

4. If f is one to one, then

$f(X_1 \cap X_2) = f(X_1) \cap f(X_2)$,

$f\left(\bigcap_{j \in J} X_j\right) = \bigcap_{j \in J} f(X_j)$.

5. If $Y_1 \subset Y_2$, then $f^{-1}(Y_1) \subset f^{-1}(Y_2)$.

6. $f(X) = \mathbf{0}_{BP} \Leftrightarrow X = \mathbf{0}_{BP}$.

7. $f^{-1}(Y_1 \cup Y_2) = f^{-1}(Y_1) \cup f^{-1}(Y_2)$,

   $f^{-1}(\cup_{j \in J} Y_j) = \cup_{j \in J} f^{-1}(Y_j)$.

8. $f^{-1}(Y_1 \cap Y_2) = f^{-1}(Y_1) \cap f^{-1}(Y_2)$,

   $f^{-1}(\cap_{j \in J} Y_j) = \cap_{j \in J} f^{-1}(Y_j)$.

9. $f^{-1}(Y) = \mathbf{0}_{BP} \Leftrightarrow Y \cap f(\mathbf{1}_{BP}) = \mathbf{0}_{BP}$.

10. $X \subset (f^{-1} of)(X)$, the equality holds if

    f is injective.

11. $(f of^{-1})(Y) \subset Y$, the equality holds if

    f is surjective.

12. $f^{-1}(Y^c) = (f^{-1}(Y))^c$.

13. If $f \colon U \longrightarrow V$ and $g \colon V \longrightarrow W$ are two functions, then $(g of)(X) = (g(f(X))$ for every $X \in BPF(U)$.

14. If $f \colon U \longrightarrow V$ and $g \colon V \longrightarrow W$ are two functions, then $(g of)^{-1}(Y) = f^{-1}(g^{-1}(Y))$ for every $Y \in BPF(W)$.

Definition 2.10: [10] Let U be a nonempty set and $\tau \subset BPF(U)$. Then τ is called a bipolar fuzzy topology on U if it satisfies the following conditions.

1. $\mathbf{0}_{BP}, \mathbf{1}_{BP} \in \tau$.

2. $X \cap Y \in \tau$, for $X, Y \in \tau$.

3. $(\cup_{j \in J} X_j) \in \tau$, for every $(X_j)_{j \in J} \subset \tau$.

3. BIPOLAR FUZZY SUPRA TOPOLOGICAL SPACES

Definition 3.1: Let U be a nonempty set and $\tau \subset BPF(U)$. Then τ is called a bipolar fuzzy supra topology on U if it satisfies the following conditions.

1. $\mathbf{0}_{BP}, \mathbf{1}_{BP} \in \tau$.

2. τ is closed under arbitrary union.

In this case the pair of (U, τ) is called bipolar fuzzy supra topological space. Members of τ are named bipolar fuzzy supra open sets and members whose complements are belong to τ are called bipolar fuzzy supra closed sets. We will denote the family of all bipolar fuzzy supra topologies on U as $BPFST(U)$.

Let τ be a bipolar fuzzy supra topology on U. Then τ^* is called associated bipolar fuzzy topology with the $\tau :\Leftrightarrow \tau^* \subset \tau$.

From definition of bipolar fuzzy supra topological spaces it is clear that every bipolar fuzzy topological space is a bipolar fuzzy supra topological space.

Remark 3.2: There is no need to satisfy the arbitrary intersection property in bipolar fuzzy supra topological spaces. For example, let $U = \{a, b\}$, $X, Y \in BPF(U)$ and $\tau = \{\mathbf{0}_{BP}, \mathbf{1}_{BP}, X, Y\}$. Here,

$X(a) = (1; -0,1)$, $X(b) = (0,5; -1)$ and

$Y(a) = (0,6; -1)$, $Y(b) = (1; -0,5)$.

Therefore

$(X \cup Y)(a) = (1; -1) \in \tau$ and

$(X \cup Y)(b) = (1; -1) \in \tau$

but since

$(X \cap Y)(a) = (0,6; -0,1) \notin \tau$ and

$(X \cap Y)(b) = (0,5; -0,5) \notin \tau$

then we have what we desire.

Definition 3.3: Let τ and σ be two bipolar fuzzy supra topological spaces on U. If $\tau \subset \sigma$, then we say that τ is coarser than σ or σ is finer than τ and it's denoted by $\tau \leqslant \sigma$.

Example 3.4:

1. Let U be a nonempty set and $\tau^0 = \{\mathbf{0}_{BP}, \mathbf{1}_{BP}\}$. In this case, τ^0 is a bipolar fuzzy supra topology on U. τ^0 is called indiscrete bipolar fuzzy supra topology and (U, τ^0) is called indiscrete bipolar fuzzy supra topological space.

2. Let U be a nonempty set and $\tau^1 = BPF(U)$. In this case, τ^1 is a bipolar fuzzy supra topology on X. τ^1 is called discrete bipolar fuzzy supra topology and (U, τ^1) is called discrete bipolar fuzzy supra topological space.

3. Let (U, τ) be a bipolar fuzzy supra topological space. The families

$\tau^+ = \{\mu_X^+ \in I^U | X \in \tau\}$ and

$\tau^- = \{-\mu_X^- \in I^U | X \in \tau\}$

are two fuzzy supra topologies in the sense of Abd El Monsef and Ramadan [13].

Proposition 3.5: Let (U, τ) be a bipolar fuzzy supra topological space and $X \in BPF(U)$. Then the set $\tau_X = \{X \cap O | O \in \tau\}$ is a bipolar fuzzy supra topology on X.

Proof: Since $\mathbf{0}_{BP}, \mathbf{1}_{BP} \in \tau$ then we have

$X \cap \mathbf{0}_{BP} = \mathbf{0}_{BP}$ and $X \cap \mathbf{1}_{BP} = X$.

2. Let J be an index set and $Y_j \in \tau_X$ for each $j \in J$. Then by the definition of τ_X there exists a $Z_j \in \tau$ such that $Y_j = X \cap Z_j$ for each $j \in J$. Since τ is a bipolar fuzzy supra topology, we have $\bigcup_{j \in J} Z_j \in \tau$. Thus

$\left(\bigcup_{j \in J} Z_j\right) \cap X = \bigcup_{j \in J}(Z_j \cap X) = \bigcup_{j \in J} Y_j.$

By the definition of τ_X, $\bigcup_{j \in J} Y_j \in \tau_X$.

The set of τ_X is called bipolar fuzzy supra topology induced by X and the pair of (X, τ_X) is called bipolar fuzzy supra subspace.

Theorem 3.6: Let (U, τ) be a bipolar fuzzy supra topological space and $X \in BPF(U)$. Then, the family

$\eta_\tau = \{X \in BPF(U) | X \cap Y \in \tau, \ for \ \forall Y \in \tau\}$

is a bipolar fuzzy topology on U and $\eta_\tau \subseteq \tau$.

Proof:

(T1) For $X \in \tau$ we have $X \cap \mathbf{1}_{BP} = X \in \tau$ and $X \cap \mathbf{0}_{BP} = \mathbf{0}_{BP} \in \tau$. Therefore $\mathbf{0}_{BP}, \mathbf{1}_{BP} \in \eta_\tau$.

(T2) Let $X_1, X_2 \in \eta_\tau$ and $Y \in \tau$. We have $(X_1 \cap X_2) \cap X = X_1 \cap (X_2 \cap Y)$. Since $X_1 \in \eta_\tau$ and $Y \in \tau$, $X_1 \cap Y \in \tau$ and since $X_2 \in \eta_\tau$ and $Y \in \tau$, $X_2 \cap Y \in \tau$. So, $X_1 \cap (X_2 \cap Y) \in \tau$. Hence, $X_1 \cap X_2 \in \eta_\tau$.

(T3) Let $\{X_i | i \in J\} \subset \eta_\tau$ and $Y \in \tau$. Then for each $i \in J$, we have $(\bigcup_{i \in J} X_i) \cap Y = \bigcup_{i \in J}(X_i \cap Y)$.

Since $\{X_i | i \in J\} \subset \eta_\tau$ and $Y \in \tau$, we get $X_i \cap Y \in \tau$. τ is bipolar fuzzy supra topology, so

$\bigcup_{i \in J}(X_i \cap Y) = (\bigcup_{i \in J} X_i) \cap Y \in \tau.$

Hence $\bigcup_{i \in J} X_i \in \eta_\tau$.

Let $K \in \eta_\tau$. Since $\mathbf{1}_{BP} \in \tau$, $K \cap \mathbf{1}_{BP} = K \in \tau$ then $K \in \tau$. Therefore $\eta_\tau \subseteq \tau$.

Theorem 3.7: Let $\mathscr{F}$ be the family of all bipolar fuzzy supra closed sets in the bipolar fuzzy supra topological space (U, τ). Then the followings are true.

i. $\mathbf{0}_{BP}, \mathbf{1}_{BP} \in \mathscr{F}$.

ii. Let $X_i \in \mathscr{F}$ for each $i \in I$. Then $\bigcap_{i \in I} X_i \in \mathscr{F}$.

Proof: Straightforward.

Theorem 3.8: Let (U, τ_1) and (U, τ_2) be two bipolar fuzzy topological spaces. Then $(U, \tau_1 \cap \tau_2)$ is a bipolar fuzzy supra topological space.

Proof: Straightforward.

Definition 3.9: Let (U, τ) be a bipolar fuzzy supra topological space and $X \in BPF(U)$.

i. The union of all bipolar fuzzy supra open sets that contained in X is called the bipolar fuzzy

supra interior of X and denoted by $int_\tau(X)$. Then, $int_\tau(X) = \cup\{O \subseteq X | O \in \tau\}$.

ii. The intersection of all bipolar fuzzy supra closed sets that contains X is called the bipolar fuzzy supra closure of X and denoted by $cl_\tau(X)$. Then, $cl_\tau(X) = \cap\{X \subseteq K | K^c \in \tau\}$.

Theorem 3.10: Let $X, Y \in BPF(U)$ and (U, τ) be a bipolar fuzzy supra topological space. Then followings are satisfied.

1. X is a bipolar fuzzy supra open (closed) set $\Leftrightarrow$ $X = int_\tau(X)$ $(X = cl_\tau(X))$.

2. If $X \subseteq Y$, then $int_\tau(X) \subseteq int_\tau(Y)$ and $cl_\tau(X) \subseteq cl_\tau(Y)$.

3. $cl_\tau(X) \cup cl_\tau(Y) \subseteq cl_\tau(X \cup Y)$.

4. $int_\tau(X) \cup int_\tau(Y) \subseteq int_\tau(X \cup Y)$.

5. $int_\tau(X \cap Y) \subseteq int_\tau(X) \cap int_\tau(Y)$.

6. $cl_\tau(X \cap Y) \subseteq cl_\tau(X) \cap cl_\tau(Y)$.

7. $int_\tau(\mathbf{1}_{BP} - X) = \mathbf{1}_{BP} - cl_\tau(X)$.

8. $cl_\tau(\mathbf{1}_{BP}) = \mathbf{1}_{BP} = int_\tau(\mathbf{1}_{BP})$ and $cl_\tau(\mathbf{0}_{BP}) = \mathbf{0}_{BP} = int_\tau(\mathbf{0}_{BP})$.

9. $int_\tau(int_\tau(X)) = int_\tau(X)$, $cl_\tau(cl_\tau(X)) = cl_\tau(X)$.

Proof: We only give here proofs of (3.), (5.) and (7.). The others can be proved in the same way.

3. Since $X \subseteq X \cup Y$ and $Y \subseteq X \cup Y$ and from (2.) we have $cl_\tau(X) \subseteq cl_\tau(X) \cup cl_\tau(Y)$ and $cl_\tau(Y) \subseteq cl_\tau(X) \cup cl_\tau(Y)$. Therefore $cl_\tau(X) \cup cl_\tau(Y) \subseteq cl_\tau(X \cup Y)$.

5. Since $X \cap Y \subseteq X$ and $X \cap Y \subseteq Y$ and from (2.) we have $int_\tau(X \cap Y) \subseteq int_\tau(X)$ and $int_\tau(X \cap Y) \subseteq int_\tau(Y)$. Therefore, we have $int_\tau(X \cap Y) \subseteq int_\tau(X) \cap int_\tau(Y)$.

7. $int_\tau(\mathbf{1}_{BP} - X)$

$= \cup\{K^c | K^c \text{ is closed in } U \text{ and } K^c \subseteq X^c \}$

$= \mathbf{1}_{BP} - cl_\tau(X)$.

Remark 3.11: In bipolar fuzzy topological spaces the followings are true.

$int_\tau(A \cap B) = int_\tau(A) \cap int_\tau(B)$ and

$cl_\tau(A) \cup cl_\tau(B) = cl_\tau(A \cup B)$.

But in bipolar fuzzy supra topological spaces there is no need to be true these two properties.

Example 3.12:

Let $U = \{a, b\}$ and $\tau = \{\mathbf{0}_{BP}, \mathbf{1}_{BP}, X, Y\}$. Here X and Y are two bipolar fuzzy sets on U such that;

$X = \{\langle a, 1, -0.4\rangle, \langle b, 0.3, -1\rangle\}$,

$Y = \{\langle a, 0.7, -1\rangle, \langle b, 1, -0.7\rangle\}$.

Therefore, the complements of these two bipolar fuzzy sets are;

$X^c = \{\langle a, 0, -0.6\rangle, \langle b, 0.7, 0\rangle\}$,

$Y^c = \{\langle a, 0.3, 0\rangle, \langle b, 0, -0.3\rangle\}$.

The family of all bipolar fuzzy supra closed sets is; $\tau^c = \{\mathbf{0}_{BP}, \mathbf{1}_{BP}, X^c, Y^c\}$.

Let us define two bipolar fuzzy sets such that;

$Z = \{\langle a, 0, -0.5\rangle, \langle b, 0.1, 0\rangle\}$,

$T = \{\langle a, 0.2, 0\rangle, \langle b, 0, -0.2\rangle\}$.

Therefore

$Z \cup T = \{\langle a, 0.2, -0.5\rangle, \langle b, 0.1, -0.2\rangle\}$.

Since $Z \subseteq \mathbf{1}_{BP}, X^c$ and $T \subseteq \mathbf{1}_{BP}, Y^c$ then

$cl_\tau(Z) = \mathbf{1}_{BP} \cap X^c = \{\langle a, 0, -0.6\rangle, \langle b, 0.7, 0\rangle\}$,
$cl_\tau(T) = \mathbf{1}_{BP} \cap Y^c = \{\langle a, 0.3, 0\rangle, \langle b, 0, -0.3\rangle\}$.

and

$cl_\tau(Z) \cup cl_\tau(T) = \{\langle a, 0.3, -0.6\rangle, \langle b, 0.7, -0.3\rangle\}$.

Since $Z \cup T \subseteq \mathbf{1}_{BP}$ then $cl_\tau(Z \cup T) = \mathbf{1}_{BP} = \{\langle a, 1, -1\rangle, \langle b, 1, -1\rangle\}$.

Thus we clearly have $cl_\tau(Z \cup T) \neq cl_\tau(Z) \cup cl_\tau(T)$.

Example 3.13: Let us consider the same topology and the same set U in the previous example and define two bipolar fuzzy sets as follows:

$G = \{\langle a, 1, -0.5 \rangle, \langle b, 0.4, -1 \rangle\}$,

$H = \{\langle a, 0.8, -1 \rangle, \langle b, 1, -0.9 \rangle\}$.

Then the intersection of these two sets is;

$G \cap H = \{\langle a, 0.8, -1 \rangle, \langle b, 0.4, -0.9 \rangle\}$.

Since $\mathbf{0}_{BP}$, $A \subseteq G$ and $\mathbf{0}_{BP}$, $B \subseteq H$ then

$int_\tau(G) = \{\langle a, 1, -0.4 \rangle, \langle b, 0.3, -1 \rangle\}$,

$int_\tau(H) = \{\langle a, 0.7, -1 \rangle, \langle b, 1, -0.7 \rangle\}$

and since $\mathbf{0}_{BP} \subseteq G \cap H$ then $int_\tau(G) \cap int_\tau(H)$
$= \{\langle a, 0.7, -0.4 \rangle, \langle b, 0.3, -0.7 \rangle\}$.

Thus we clearly have

$int_\tau(G \cap H) \neq int_\tau(G) \cap int_\tau(H)$.

4. CONTINUOUS MAPPINGS ON BIPOLAR FUZZY SUPRA TOPOLOGICAL SPACES

Definition 4.1: Let (U, τ) and (V, σ) be two bipolar fuzzy supra topological spaces and

$f : (U, \tau) \longrightarrow (V, \sigma)$ be a mapping.

1. For every $X \in \tau$ if $f(X) \in \sigma$, then f is called a bipolar fuzzy supra open mapping.

2. For every $Y^c \in \tau$ if $[f(X)]^c \in \sigma$, then f is called a bipolar fuzzy supra closed mapping.

3. For every $X \in \sigma$ if $f^{-1}(X) \in \tau$, then f is called a bipolar fuzzy supra continuous function. Moreover, $f : (U, \tau) \longrightarrow (V, \sigma)$ is a bipolar fuzzy supra continuous: $\Leftrightarrow f^{-1}(\sigma) \subset \tau$.

Definition 4.2: Let (U, τ) and (V, σ) be two bipolar fuzzy supra topological spaces, τ^* and σ^* be two associated bipolar fuzzy topologies with τ and σ, respectively. Let $f : (U, \tau^*) \longrightarrow (V, \sigma^*)$ be a mapping.

1. For every $X \in \tau^*$ if $f(X) \in \sigma$, then f is called a S^* bipolar fuzzy supra open mapping.

2. For every $Y^c \in \tau^*$ if $(f(Y))^c \in \sigma$, then f is called a S^* bipolar fuzzy supra closed mapping.

3. For every $X \in \sigma^*$ if $f^{-1}(X) \in \tau$, then f is called a S^* bipolar fuzzy supra continuous mapping. Moreover, $f : (U, \tau) \longrightarrow (V, \sigma)$ is a S^* bipolar fuzzy supra continuous: $\Leftrightarrow f^{-1}(\sigma^*) \subset \tau$.

Remark 4.3: From the Definition.4.2 it is clear that every S^* bipolar fuzzy supra continuous function is a bipolar fuzzy supra continuous mapping.

Theorem 4.4: Let (U, τ) and (V, σ) be two bipolar fuzzy supra topological spaces, τ^* and σ^* be two associated with bipolar fuzzy topologies with τ and σ, respectively.

Let $f : (U, \tau^* \subseteq \tau) \longrightarrow (V, \sigma^* \subseteq \sigma)$ be a mapping. Then the followings are equivalent.

1. The mapping f is S^* bipolar fuzzy supra continuous.

2. For every bipolar fuzzy supra closed set Y in (V, σ^*), $(f^{-1}(Y))^c \in \tau$.

3. For every bipolar fuzzy supra Y in (V, σ^*), $cl_\tau(f^{-1}(Y)) \subseteq f^{-1}(cl_{\sigma^*}(Y))$.

4. For every bipolar fuzzy set X in (U, τ^*), $f(cl_\tau(X)) \subseteq cl_{\sigma^*}(f(X))$.

5. For every bipolar fuzzy set Y in (V, σ^*), $f^{-1}(int_{\sigma^*}(Y)) \subseteq int_\tau(f^{-1}(Y))$.

Proof: (1$\Longrightarrow$2) Let $f : (U, \tau^* \subseteq \tau) \longrightarrow (V, \sigma^* \subseteq \sigma)$ be a S^* bipolar fuzzy supra continuous mapping and $Y^c \in \sigma$. Hence $f^{-1}(Y^c) = f^{-1}(\mathbf{1}_{BP} - Y) = \mathbf{1}_{BP} - f^{-1}(Y) \in \tau$. This means that $f^{-1}(Y)$ is bipolar fuzzy supra closed in U.

(2$\Longrightarrow$3) Since $cl_{\sigma^*}(Y)$ is a bipolar fuzzy closed set for any $Y \in \sigma^*$, then $f^{-1}(cl_{\sigma^*}(Y))$ is a bipolar fuzzy supra closed in τ. Hence

$$f^{-1}(cl_{\sigma^*}(Y)) = cl_\tau\left(f^{-1}(cl_{\sigma^*}(Y))\right)$$
$$\underset{B \subseteq cl_{\sigma^*}(B)}{\supseteq} \quad cl_\tau(f^{-1}(Y))$$

and we get $cl_\tau\big(f^{-1}(Y)\big) \subseteq f^{-1}\big(cl_{\sigma^*}(Y)\big)$.

$(3 \Rightarrow 4)$ Let $f(X) = Y$. Then $cl_\tau\big(f^{-1}(Y)\big) \subseteq f^{-1}\big(cl_{\sigma^*}(Y)\big)$, therefore

$$f^{-1}\big(cl_{\sigma^*}(f(X))\big) \supseteq cl_\tau\big(f^{-1}(f(X))\big) \supseteq cl_\sigma(Y)$$

and $cl_{\sigma^*}(f(X)) \supseteq f\big(f^{-1}\big(cl_{\sigma^*}(f(X))\big)\big) \supseteq f\big(cl_\tau(X)\big)$. Hence, we have the inclusion $f\big(cl_\tau(X)\big) \subseteq cl_{\sigma^*}(f(X))$.

$(4 \Rightarrow 2)$ Let Y be a bipolar fuzzy closed in (Y, σ^*) and $X = f^{-1}(Y)$. Then,

$$f\big(cl_\tau(X)\big) \subseteq cl_{\sigma^*}(f(X)) \subseteq$$
$$cl_{\sigma^*}\big(f(f^{-1}(Y))\big) \subseteq cl_{\sigma^*}(Y) = Y$$

and

$$cl_\tau(X) \subseteq f^{-1}\big(f(cl_\tau(X))\big) \subseteq f^{-1}(Y) = X.$$

Since the closure of a bipolar fuzzy supra set always includes the set itself and we have

$cl_\tau(X) = X$ and then X is a bipolar fuzzy supra closed set. Therefore $f^{-1}(Y)$ is a bipolar fuzzy supra closed set in U.

$(5 \Rightarrow 1)$ Let Y be a bipolar fuzzy open set in V. Then the complement set $\mathbf{1}_{BP} - Y$ is a bipolar fuzzy closed set and $f^{-1}(\mathbf{1}_{BP} - Y) = \mathbf{1}_{BP} - f^{-1}(Y)$ is a bipolar fuzzy supra closed set in X. Therefore $f^{-1}(Y)$ is a bipolar fuzzy supra open set in U. Hence f is a S^* bipolar fuzzy supra continuous mapping.

$(1 \Rightarrow 5)$ Let $Y \in \sigma^*$, since f is a S^* bipolar fuzzy supra continuous mapping then $f^{-1}\big(int_{\sigma^*}(Y)\big) \in \tau$. But since $f^{-1}\big(int_{\sigma^*}(Y)\big)$ is bipolar fuzzy open it is the same set as bipolar fuzzy supra interior of itself so $f^{-1}\big(int_{\sigma^*}(Y)\big) = int_\tau\big(f^{-1}\big(int_{\sigma^*}(Y)\big)\big)$. Since $int_{\sigma^*}(Y) \subseteq Y$, $f^{-1}\big(int_{\sigma^*}(Y)\big) = int_\tau\big(f^{-1}\big(int_{\sigma^*}(Y)\big)\big) \subseteq int_\tau\big(f^{-1}(Y)\big)$ and then

$$f^{-1}\big(int_{\sigma^*}(Y)\big) \subseteq int_\tau\big(f^{-1}(Y)\big).$$

Theorem 4.5: Let (U, τ^*) and (V, σ^*) be two bipolar fuzzy topological spaces, τ^* and σ^* be two associated bipolar fuzzy topologies with τ and σ, respectively. Let $f \colon (U, \tau^*) \longrightarrow (V, \sigma^*)$ be a mapping. Then the followings are equivalent.

1. The mapping f is bipolar fuzzy supra continuous.

2. The inverse image of every bipolar fuzzy supra closed set in (V, σ), is bipolar fuzzy supra closed in (U, τ).

3. For every bipolar fuzzy set Y in V,

$$cl_\tau\big(f^{-1}(Y)\big) \subseteq f^{-1}\big(cl_\sigma(Y)\big) \subseteq f^{-1}\big(cl_{\sigma^*}(Y)\big).$$

4. For every bipolar fuzzy set X in U,

$$f\big(cl_\tau(X)\big) \subseteq cl_\sigma\big(f(X)\big) \subseteq cl_{\sigma^*}\big(f(X)\big).$$

5. For every bipolar fuzzy set Y in V,

$$int_\tau\big(f^{-1}(Y)\big) \supseteq f^{-1}\big(int_\sigma(Y)\big) \supseteq f^{-1}\big(int_{\sigma^*}(Y)\big).$$

Proof: It can easily be shown by the previous theorem.

Theorem 4.6: If $f \colon (U, \tau) \longrightarrow (V, \sigma)$ is a bipolar fuzzy supra continuous and $g \colon (V, \sigma) \longrightarrow (W, \delta)$ is a S^* bipolar fuzzy supra continuous, then the function $g \circ f \colon (U, \tau) \longrightarrow (W, \delta)$ is a S^* bipolar fuzzy supra continuous.

Proof: Let $Z \in \delta^* \subset \delta$. Since g is S^* bipolar fuzzy supra continuous then $g^{-1}(Z) \in \sigma$. From the bipolar fuzzy supra continuity of f we have $f^{-1}\big(g^{-1}(Z)\big) = (g \circ f)^{-1}(Z) \in \tau$ and therefore, $g \circ f \colon (U, \tau) \longrightarrow (W, \delta)$ is bipolar fuzzy supra continuous mapping.

Theorem 4.7: If $f \colon (U, \tau) \longrightarrow (V, \sigma)$ and $g \colon (V, \sigma) \longrightarrow (W, \delta)$ are two bipolar fuzzy supra continuous functions, then the function $g \circ f \colon (U, \tau) \longrightarrow (W, \delta)$ is bipolar fuzzy supra continuous.

Proof: Straightforward.

Theorem 4.8: If $f \colon (U, \tau) \longrightarrow (V, \sigma)$ and $g \colon (V, \sigma) \longrightarrow (W, \delta)$ are two S^* bipolar fuzzy supra

continuous functions, then the function $g \circ f$: $(U, \tau) \longrightarrow (W, \delta)$ is bipolar fuzzy supra continuous.

Proof: Since f and g are two S^* bipolar fuzzy supra continuous mapping from Remark 4.3 they are bipolar fuzzy supra continuous mappings and by Theorem 4.7 we get the result.

Remark 4.9:

i. Let $f: (U, \tau) \longrightarrow (V, \sigma)$ and $g: (V, \sigma) \longrightarrow (W, \delta)$ be two S^* bipolar fuzzy supra continuous mapping. Thus, the mapping $g \circ f : (U, \tau) \longrightarrow (W, \delta)$ is no need to be S^* bipolar fuzzy supra continuous. Consider the given topologies in the following tables and the diagram:
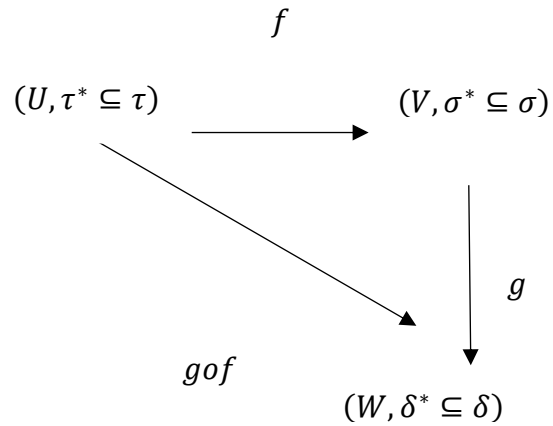
$U = \{a, b\}$
$\tau^* = \{\mathbf{0}_{BP}, \mathbf{1}_{BP}, A^*\}$
$A^* = \{\langle a, 0.5, -0.4 \rangle, \langle b, 0.6, -0.7 \rangle\}$
$\tau = \{\mathbf{0}_{BP}, \mathbf{1}_{BP}, A, B\}$
$A = \{\langle a, 1, -0.5 \rangle, \langle b, 0.7, -1 \rangle\}$
$B = \{\langle a, 0.5, -0.4 \rangle, \langle b, 0.6, -0.7 \rangle\}$

$V = \{c, d\}$
$\sigma^* = \{\mathbf{0}_{BP}, \mathbf{1}_{BP}, C^*\}$
$C^* = \{\langle c, 0.2, -0.3 \rangle, \langle d, 0.3, -0.6 \rangle\}$
$\sigma = \{\mathbf{0}_{BP}, \mathbf{1}_{BP}, C, D\}$
$C = \{\langle c, 0.2, -0.3 \rangle, \langle d, 0.3, -0.6 \rangle\}$
$D = \{\langle c, 1, -0.4 \rangle, \langle d, 0.5, -1 \rangle\}$

$W = \{e, k\}$
$\delta^* = \{\mathbf{0}_{BP}, \mathbf{1}_{BP}, E^*\}$
$E^* = \{\langle e, 0.4, -0.5 \rangle, \langle k, 0.2, -0.8 \rangle\}$
$\delta = \{\mathbf{0}_{BP}, \mathbf{1}_{BP}, E, F\}$
$E = \{\langle e, 0.5, -1 \rangle, \langle k, 1, -0.9 \rangle\}$
$F = \{\langle e, 1, -0.6 \rangle, \langle k, 0.3, -1 \rangle\}$

If we define $f(a) = c, f(b) = d, g(c) = e, g(d) = k$ then we clearly have

$$(g \circ f)^{-1}(E^*) = \begin{cases} \left(\mu_{E^*}^+(g \circ f)(a), \mu_{E^*}^-(g \circ f)(a) \right), \\ \left(\mu_{E^*}^+(g \circ f)(b), \mu_{E^*}^-(g \circ f)(b) \right) \end{cases}$$

$$= \left\{ \left(\mu_{E^*}^+(e), \mu_{E^*}^-(e) \right), \left(\mu_{E^*}^+(k), \mu_{E^*}^-(k) \right) \right\}$$

$$= \{(0.4, -0.5), (0.2, -0.8)\} \notin \tau.$$

ii. If we take g as a bipolar fuzzy supra continuous mapping in the same remark, then the mapping $g \circ f$ may not be a bipolar fuzzy supra continuous.

5. COMPACTNESS IN BIPOLAR FUZZY SUPRA TOPOLOGICAL SPACES

Definition 5.1: 1. Let (U, τ) be a bipolar fuzzy supra topological space and

$$\{X_i | i \in I\} = \left\{ \langle u, \mu_{X_i}^+(u), \mu_{X_i}^-(u) \rangle \big| i \in I, u \in U \right\}$$

be a family of bipolar fuzzy supra open sets on U.

If $\bigcup_{i \in I} X_i = 1_{BP}$ then $\{X_i | i \in I\}$ is called bipolar fuzzy supra open cover of U. This means that $\bigvee_{i \in I} \mu_{X_i}^+(u) = 1$ and $\bigwedge_{i \in I} \mu_{X_i}^-(u) = -1$.

2. A finite subfamily of a bipolar fuzzy supra open cover $\{X_i | i \in I\}$ of U, is called finite subcover of U.

3. A family

$$\{K_i | i \in I\} = \left\{ \langle u, \mu_{K_i}^+(u), \mu_{K_i}^-(u) \rangle \big| i \in I \right\}$$

of bipolar fuzzy supra closed sets in U satisfies the finite interseciton property if finite subfamily $\left\{\langle u, \mu_{K_{i_\alpha}}^+(u), \mu_{K_{i_\alpha}}^-(u)\rangle \,\middle|\, \alpha = 1,2,\dots,n\right\}$

satisfies the condition

$$\bigcap_{\alpha=1}^n \left\{\langle u, \mu_{K_{i_\alpha}}^+(u), \mu_{K_{i_\alpha}}^-(u)\rangle\right\} \neq 0_{BP}.$$

Definition 5.2: Let (U, τ) be a bipolar fuzzy supra topological space. (U, τ) is called bipolar fuzzy supra compact topological spaces if every bipolar fuzzy supra open cover of X has a finite subcover.

Theorem 5.3: (U, τ) is a bipolar fuzzy supra compact topological space if and only if every family of bipolar fuzzy closed sets with finite intersection property has a nonempty intersection.

Proof: ($\Longrightarrow$) Let (U, τ) be a bipolar fuzzy supra compact topological space and let $\mathcal{A} := \{X_\alpha | \alpha \in \Lambda\}$ be a family of bipolar fuzzy supra closed sets with finite intersection property of U. Let us consider $\bigcap_{\alpha \in \Lambda} X_\alpha = 0_{BP}$. Then

$$1_{BP} = (0_{BP})^c = \left(\bigcap_{\alpha \in \Lambda} X_\alpha\right)^c = \bigcup_{\alpha \in \Lambda} (X_\alpha)^c$$

Therefore, the family $\{(X_\alpha)^c\}_{\alpha \in \Lambda}$ is a bipolar fuzzy supra open cover of U. Since U is bipolar fuzzy supra compact, then this cover has a bipolar fuzzy supra finite subcover, so for $\exists\, \alpha_1, \alpha_2, \dots \alpha_n$, $1_{BP} = \bigcup_{i=1}^n \left((X_{\alpha_i})^c\right)$.

Hence

$$0_{BP} = (1_{BP})^c = \left(\bigcup_{i=1}^n \left((X_{\alpha_i})^c\right)\right)^c = \bigcap_{i=1}^n X_{\alpha_i}$$

This contradicts the fact that $\mathcal{A}$ has the finite intersection property. So $\bigcap_{\alpha \in \Lambda} X_\alpha \neq 0_{BP}$.

($\Longleftarrow$) Let us consider U is not compact. Therefore U has a finite open subcover $\mathcal{A} := \{X_\alpha | \alpha \in \Lambda\}$ such that none of any finite subfamily of $\mathcal{A}$ covers U. So, for any $\alpha_1, \alpha_2, \dots \alpha_n \in \Lambda$

$$1_{BP} \neq \bigcup_{i=1}^n X_{\alpha_i}.$$

Since $0_{BP} = (1_{BP})^c \neq \left(\bigcup_{i=1}^n X_{\alpha_i}\right)^c$ then we have $\bigcap_{i=1}^n \left((X_{\alpha_i})^c\right) \neq 0_{BP}$.

Hence the family of $\left\{(X_{\alpha_i})^c \,\middle|\, \alpha \in \Lambda\right\}$ is a family of bipolar fuzzy supra closed sets with finite intersection property. Since $1_{BP} = \bigcup_{\alpha \in \Lambda} X_\alpha$ then $\bigcap_{\alpha \in \Lambda}((X_\alpha)^c) = (\bigcup_{\alpha \in \Lambda} X_\alpha)^c = 0_{BP}$.

So intersection of the members of $\left\{(X_{\alpha_i})^c \,\middle|\, \alpha \in \Lambda\right\}$ is empty. This contradicts the hypothesis, so U is compact.

Theorem 5.4: Let (U, τ) and (V, σ) be two bipolar fuzzy supra topological spaces and

$f: (U, \tau) \longrightarrow (V, \sigma)$ be continuous and onto bipolar fuzzy supra mapping. If (U, τ) is a bipolar fuzzy supra compact topological space, then (V, σ) is so.

Proof: Let $\mathcal{A}$ be a bipolar fuzzy supra open cover of V. Then since f is bipolar fuzzy supra continuous, $\mathcal{B} = \{f^{-1}(Y) | Y \in \mathcal{A}\}$ is a bipolar fuzzy supra open cover of U. Since (U, τ) is bipolar fuzzy supra compact, then there exists a finite subcover such that

$$\{f^{-1}(Y_1), f^{-1}(Y_2), \dots, f^{-1}(Y_n)\}$$

of $\mathcal{B}$. Since f is a surjection then $\{Y_1, Y_2, \dots, Y_n\}$ is a bipolar fuzzy supra finite subcover of $\mathcal{A}$.

Definition 5.5: Let (U, τ) be a bipolar fuzzy supra topological space and (X, τ_X) be a bipolar fuzzy supra subspace where $X \in BPF(U)$. A family of $\mathfrak{B}$ subsets of U called the covering of X if the union of its elements contains X.

Theorem 5.6: Let (U, τ) and (V, σ) be two bipolar fuzzy supra topological spaces and $f: (U, \tau) \longrightarrow (V, \sigma)$ be continuous and onto bipolar fuzzy supra mapping. If X is bipolar fuzzy supra compact set in (U, τ) then $f(X)$ is bipolar fuzzy supra compact in (V, σ).

Proof: Straightforward.

Theorem 5.7: Let (U, τ) be a bipolar fuzzy supra compact topological space and X be a bipolar fuzzy supra closed set on U. Then (X, τ_X) is a bipolar fuzzy supra compact topological space.

Proof: Let X be a bipolar fuzzy supra closed subspace of the bipolar fuzzy supra compact space U. Let $\mathcal{A}$ be a bipolar fuzzy supra open covering of X by sets bipolar fuzzy supra open in U. Since X is bipolar fuzzy supra closed, then X^c is bipolar fuzzy supra open. If we add the bipolar fuzzy supra open set X^c to $\mathcal{A}$, we get a bipolar fuzzy supra open cover of U such

$\mathfrak{B} = \mathcal{A} \cup \{X^c\}$. Some finite subcollection of $\mathfrak{B}$ covers A. If subcollection $\mathfrak{B}$ contains $\{X^c\}$ discard $\{X^c\}$, otherwise take the subcollection as it is. The resulting collection is a finite subfamily of $\mathcal{A}$ that covers X.

Definition 5.8: Let (U, τ) and (V, σ) be two bipolar fuzzy supra topological spaces and

$X \in BPF(U), Y \in BPF(V)$. The product of X and Y is a bipolar fuzzy set on $U \times V$ defined by

$X \mathrm{x} Y = \{\langle (u, v), (\mu_A^+(u) \wedge \mu_B^+(v)), (\mu_A^-(u) \vee \mu_B^-(v)) \rangle : (u, v) \in U \mathrm{x} V\}$.

We can define a bipolar fuzzy supra topology on $U \times V$. The bipolar fuzzy supra topology on the product set $U \times V$ is given by the coarsest bipolar fuzzy supra topology makes following projections

$p_1 : U \times V \longrightarrow V, p_1(u, v) = u$ and

$p_2 : U \times V \longrightarrow V, p_2(u, v) = v$

are bipolar fuzzy supra continuous.

We have

$p_1^{-1}(\mu_G^+)(u, v) = \mu_G^+(p_1(u, v)) = \mu_G^+(u)$ and

$p_1^{-1}(\mu_G^-)(u, v) = \mu_G^-(p_1(u, v)) = \mu_G^-(u)$

for $G \in \tau$. So

$p_1^{-1}(G) = \{\langle (u, v), \mu_G^+(u), \mu_G^-(u) \rangle\} = G \times \mathbf{1}_{BP_V}$.

By the same procedure

$p_2^{-1}(H) = \{\langle (u, v), \mu_H^+(u), \mu_H^-(v) \rangle\} = \mathbf{1}_{BP_U} \times H$
for $H \in \sigma$.

Hence $\{G \times \mathbf{1}_{BP_V} | G \in \tau\} \cup \{\mathbf{1}_{BP_U} \times H | H \in \sigma\}$ is a base (A family $\mathscr{B} \subset BPF(U)$ is called a base for a bipolar fuzzy supra topology if $\mathscr{B} \subset \tau$ and every member of τ is a union of a number of members of $\mathscr{B}$.) for the product bipolar fuzzy supra topology δ on $U \times V$. Since τ and σ are bipolar fuzzy supra topologies, the families $\{G \times \mathbf{1}_{BP_V} | G \in \tau\}$ and $\{\mathbf{1}_{BP_U} \times H | H \in \sigma\}$ are closed under arbitrary unions and so we have

$\delta = \{(G \times \mathbf{1}_{BP_V}) \cup (\mathbf{1}_{BP_U} \times H) | G \in \tau, H \in \sigma\}$.

Theorem 5.9: Let (U, τ) and (V, σ) be two bipolar fuzzy supra topological spaces and $(U \times V, \delta)$ be their product. Then $(U \times V, \delta)$ is a compact bipolar fuzzy supra topological space if and only if (U, τ) and (V, σ) are bipolar fuzzy supra compact.

Proof: ($\Rightarrow$:) Since projections p_1 and p_2 are bipolar fuzzy supra continuous, we have the result.

($\Leftarrow$:) Let U and V be two bipolar fuzzy supra compact spaces.

$\mathcal{A} = \{(G_i \times \mathbf{1}_{BP_V}) \cup (\mathbf{1}_{BP_U} \times H_i) : i \in J\}$ is a bipolar fuzzy supra open cover of $U \times V$, where $G_i = \{\langle u, \mu_{G_i}^+(u), \mu_{G_i}^-(u) \rangle : u \in U\} \in \tau$ and

$H_i = \{\langle v, \mu_{H_i}^+(v), \mu_{H_i}^-(v) \rangle : v \in V\} \in \sigma$.

We suggest that $\{G_i : i \in J\}$ is cover of U and $\{H_i : i \in J\}$ is a cover of V. We need to show that

$\bigvee_{i \in J} \mu_{G_i}^+(u) = 1, \bigwedge_{j \in J} \mu_{G_i}^-(u) = -1$

and

$\bigvee_{i \in J} \mu_{H_i}^+(v) = 1, \bigwedge_{j \in J} \mu_{H_i}^-(v) = -1$.

We have $(G_i \times \mathbf{1}_{BP_V}) \cup (\mathbf{1}_{BP_U} \times H_i) = \{\langle (u, v), \mu_{G_i}^+(u) \vee \mu_{H_i}^+(v), \mu_{G_i}^-(u) \wedge \mu_{H_i}^-(v) \rangle\}$. Hence,

$\bigvee \{\mu_{G_i}^+(u) : i \in J\} \vee \bigvee \{\mu_{H_i}^+(v) : i \in J\} = \bigvee_{i \in J} \{\mu_{G_i}^+(u) \vee \mu_{H_i}^+(v)\} = 1$

and

$\wedge\{\mu_{G_i}^-(u) : i \in J\} \wedge \wedge\{\mu_{H_i}^-(v) \, i \in J\} =$
$\wedge_{i \in J}\{\mu_{G_i}^-(u) \wedge \mu_{H_i}^-(v)\} = -1.$

Then we have a finite subset J^* of J for which

$$\vee_{i \in J^*} \mu_{G_i}^+(u) = 1, \wedge_{j \in J^*} \mu_{G_i}^-(u) = -1$$

and

$$\vee_{i \in J^*} \mu_{H_i}^+(v) = 1, \wedge_{j \in J^*} \mu_{H_i}^-(v) = -1.$$

Hereby, $\{(G_i \times \mathbf{1}_{BP_V}) \cup (\mathbf{1}_{BP_U} \times H_i) : i \in J^*\}$ is a finite subcover of $\mathcal{A}$. Then $(U \times V, \delta)$ is bipolar fuzzy supra compact topological space.

6. CONCLUSION

We have introduced bipolar fuzzy supra topological spaces and investigated some of their important properties. In future, we plan to study on neighborhood structures of bipolar fuzzy point [11] and other topological structures such as separation axioms and connectedness in bipolar fuzzy supra topological space.

The Declaration of Conflict of Interest/ Common Interest

No conflict of interest or common interest has been declared by the authors.

Authors' Contribution

The authors contributed equally to the study.

The Declaration of Ethics Committee Approval

This study does not require ethics committee permission or any special permission.

The Declaration of Research and Publication Ethics

The authors of the paper declare that they comply with the scientific, ethical and quotation rules of SAUJS in all processes of the paper and that they do not make any falsification on the data collected. In addition, they declare that Sakarya University Journal of Science and its editorial board have no responsibility for any ethical violations that may be encountered, and that this study has not been evaluated in any academic publication environment other than Sakarya University Journal of Science.

REFERENCES

[1] L. Zadeh, "Fuzzy sets," Information and Control, vol. 8, pp. 338–353, 1965.

[2] L. Zadeh, "The concept of a linguistic variable and its application to approximate reasoning-I," Inform. Sci., vol. 8, pp. 199–249, 1975.

[3] K. T. Atanassov, "Intuitionistic fuzzy sets," Fuzzy sets and Systems, vol. 20, pp. 87-96, 1986.

[4] P.K Maji., R. Biswas and A. R. Roy, "Fuzzy soft sets," J. Fuzzy Math., vol. 9, no. 3, pp. 589–602, 2001.

[5] W-R. Zhang, "Bipolar fuzzy sets and relations: a computational framework for cognitive modeling and multiagent decision analysis," NAFIPS/IFIS/NASA'94, pp. 305-309, 1994.

[6] K. M. Lee, "Comparison of interval-valued fuzzy sets, intuitionistic fuzzy sets, and bipolarvalued fuzzy sets," J. Fuzzy Logic Intelligent Systems, vol. 14, pp. 125-129, 2004.

[7] M. S. Anitha, K. L. Muruganantha and K. Arjunan, "Notes on bipolar valued fuzzy subgroups of a group," The Bulletin of Society for Mathematical Services and Standards, vol. 7, pp. 40-45, 2013.

[8] S. P. Subbian and M. Kamaraj, "Bipolar-valued fuzzy ideals of ring and bipolar-valued fuzzy ideal extensions in subrings," International Journal of Mathematics Trends and Technology, vol. 61, no. 3, pp. 155-163, 2018.

[9] B. Pazar Varol, An approach to bipolar fuzzy submodules, TWMS J. App. and Eng. Math., 11 (1), 168-175, 2021.

[10] M. Azhagappan and M. Kamaraj, "Notes on bipolar valued fuzzy RW-closaed and bipolar valued fuzzy RW-open sets in bipolar valued fuzzy topological spaces," International Journal of Mathematical Archive, vol. 7, no. 3, pp. 30-36, 2016.

[11] J. Kim, S. K. Samanta, P. K. Lim, J. G. Lee, K. Hur, "Bipolar fuzzy topological spaces," Annals of Fuzzy Mathematics and Informatics, vol. 17, no. 3, pp. 205-229, 2019.

[12] A. S. Mashhour, A. A. Allam, F. S. Mahmoud and F. H. Khedr, "On supratopological spaces," Indian J. Pure Appl. Math., vol. 14, no 4, pp. 502-510, 1983.

[13] M. E. Abd El-Monsef and A. E. Ramadan, "On Fuzzy Supra Topological Spaces," Indian J. Pure Appl. Math., vol. 18, no. 4, pp. 322-329, 1987.

[14] M. E. Abd El-Latif, "Some properties of fuzzy supra soft topological spaces," Europen Journal of Pure and Applied Mathematics, vol. 12, no. 3, pp. 999-1017, 2019.

[15] T. M. Al-Shami and M. E. Shafei, "On supra topological ordered spaces," Arab Journal of Basic and Applied Science, vol. 26, no. 1, pp. 433-445, 2019.

[16] T. M. Al-Shami and M. E. Shafei, "Two types of separation axioms on supra soft topological spaces," Demonstratio Mathematica, vol. 52, pp. 147-165, 2019.

[17] T. M. Al-Shami, "Paracompactness on supra topological spaces," Journal of Linear and Topological Algebra, vol. 9, no. 2, pp. 121-127, 2020.

[18] T. M. Al-Shami, M. Al Shumrani and C. Özel, "Another form of supra ordered separation axioms," Journla of Mathematical Extension, vol. 15, no 1, pp. 105-125, 2021.

[19] N. Turanlı, "An overview of intuitionistic fuzzy supratopological spaces," Hacettepe Journal of Mathematics and Statistics, vol. 32, pp. 17-26, 2003.

Title: A Clustering-based Simulated Annealing Algorithm with Taguchi Method for the Discrete Ordered Median Problem

Authors: Mustafa Serdar TOKSOY

A Clustering-based Simulated Annealing Algorithm with Taguchi Method for the Discrete Ordered Median Problem

Mustafa Serdar TOKSOY*[1]

Abstract

Researchers have studied discrete location problems for a long time because of their importance in practice. The Discrete Ordered Median Problem (DOMP) generalizes discrete facility location problems. The DOMP generalizes the main facility location problems' objective functions such as the p-median, p-center and p-centdian location problems. As these problems, also known as the problems of location-allocation, have NP-hard structure, it is inevitable to use heuristic methods for solution. In this study, a metaheuristic algorithmic suggestion will be put forward by examining the DOMP to find optimal solutions. For that purpose, we proposed a Simulated Annealing (SA) metaheuristic with K-means Clustering Algorithm in initialization for the DOMP. Novel approaches for initial solution and K-exchange algorithm-based neighborhoods for local search were analysed. In addition, best level of selected parameters were determined by Taguchi method. Forty common p-median instances derived from OR-LIB were used to test the SA performance, and the results were compared with three state-of-art algorithms in the literature. According to the computational results, 21 best solutions were obtained on instances despite gap values and CPU times increasing proportionally to the scale of the instances. In a conclusion, the proposed clustering-based SA algorithm is competitive and can be a robust alternative for the DOMP.

Keywords: Discrete ordered median problem, Simulated Annealing, Taguchi, K-means clustering.

1. INTRODUCTION

There is no doubt that people have been thinking about location decisions since cave life. The term of the facility is used intensively. It has a broad meaning, including many locations such as air and seaports, manufacturing centers, warehouses, retail outlets, schools, hospitals, childcare centers, bus stops, metro stations, electronic power stations, computer terminals, pluviometers, emergency warning sirens, and satellites.

However, few of these items have been investigated in researches [1].

Location decision problems have a direct relationship with supply chain management and logistics. Therefore, location analysis and models have a great interest from many disciplines such as operations research and administrative science. The solution approaches of location models for optimality are generally crucial. The simplest models for large-scale problem examples are not easily obtained numerically. Formulation and

---

* Corresponding author: mstoksoy@erzincan.edu.tr
[1] Erzincan Binali Yıldırım University
ORCID: https://orcid.org/0000-0002-7333-9676

solution of location models with numerical complexity were complicated until developing high-speed working computers.

Accordingly, the Discrete location theory (DLT) that processing in discrete optimization space covers a development period about the next thirty years with an expeditiously growing and developing literature [2]. Uncapacitated facility location problem, p-median problem, p-center problem, set covering problem, p-dispersion problem, maximal covering problem, hub location problem can be given fundamental facility location problems in DLT [1]. Especially, 4 location models considering the p-median problem, p-center problem, uncapacitated facility location problem, and quadratic assignment problem are considered more than other location problems in literature. These four fundamental problems are used for facility location selection and allocation of demand points to single or multiple facilities. Hence, these kinds of problems are primarily described as location-allocation problems. The demand points supplied from the candidate facilities are given in a network among these models. The general problem is the establishment of new facilities that will optimize different objectives. It is essential for such problems that distance or some measurements (trip time or cost, demand satisfaction) are less functional than others in terms of distance.

The p-median problem is one of the best-known location-allocation problems in the literature described initially by Hakimi [3]. The problem focuses on selecting the number of p facilities in a network covering a minimized weighted/unweighted distance to meet all demand. Several studies considering the total distance between demand points and facilities have been published since 1995. Following ten years, studies have increased on solution methods [4].

Another location problem called the p-center problem involves a number of p facilities in a network covering a weighted/unweighted maximum distance that must be minimized to meet all demand. As can be understood from the statement, p-median problem objectives minisum considers minimization of the total distance between demand points and facilities while p-center problem objectives minimax considers minimizing the maximum distance between demand points and facilities.

The discrete ordered median problem (DOMP) observed in this study is a general form of classic location facility problems. The solution of the DOMP contains possible facility points and a finite set of customers whose demands are met by these facilities, as in the case of other location problems.

The DOMP is firstly defined by Nickel [5] and then Boland et al. [6]. The objective function of the DOMP generalizes these well-known facility location problems such as median, center, and centdian (convex combination) problem functions. However, this generalization is not limited to these problems. It is possible to obtain solutions for different objective functions with a coefficient Λ and an ordering factor embedded in the DOMP formulation. Therefore, the DOMP is a beneficial method for solving many location problems and having a simple condition in applying mentioned factors for problems [6].

As in many location problems, the DOMP is NP-hard and cannot obtain optimal solutions in an acceptable time for large-scale problems. Hence, heuristic algorithms have to be used in general. In recent years, it has been observed that metaheuristics that combine basic heuristics methods search solution space more effectively and have high-quality solutions commonly.

In this study, the solution of p-median, p-center, and p-centdian problems were observed in the DOMP simultaneously, and for that purpose, the Simulated Annealing (SA) metaheuristic was proposed for the DOMP. The SA is a local optimization method that solves complex combinatorial optimization problems. Studies about this topic point out that simulating of solids annealing process can be presented as a model [7]-[8] and can be proposed for optimization problems [9]. Since then, the model has been utilized in a large field, from scheduling problems to locational analysis, from molecular physics and chemistry to image processing.

Forty p-median instances between 100-900 nodes derived from OR-LIB [10] were used for the application. In the 2nd section of the study, a definition of the DOMP is available. The 3rd section presents the basic steps of the proposed SA approach. Computational evaluation in the 4th section contains parameter optimization by Taguchi experimental design method, application of the algorithm to test problems, and compared results with other benchmark solutions in the literature. The 5th section is composed of the conclusion and proposals.

2. DOMP DEFINITION

2.1. Literature Review

P-median, p-center, and p-centdian problems have been studied in detail because of their importance in practical applications by Daskin [11]; Drezner and Hamacher [1]; Mirchandani and Francis [2]. These studies include a finite set for potential location areas and another set for customers whose demand is supplied by these facilities. The focus point of these problems that have a significant number of alternative solution approaches proposed in the literature is the existence of fixed number locations have to be diversified areas in a specific set of candidates in which any customer can be supplied by only one facility. For each customer-facility pair, a substantial cost for customer demand must be met by a facility settled down in the determined area.

A remarkable attribute of DLP is the diversity of considered objective functions. The primary aim of the p-median problem is to minimize total service cost for all customers supplied by facilities located in all chosen areas. The p-center problem is a minimization of the maximum service cost of a customer from among chosen areas that covers all customers. As for the p-centdian problem, the primary aim is to obtain a convex combination of median and center problems. Like this, the minimization of both total cost and the highest cost is ensured. There are three standard objective functions observed in the literature, and there are specific solution methods and algorithm approaches for these problems [11].

Kalcsics et al. [12] defined necessity discrete location models for strategic supply chain management and submitted novel and flexible location models. For that purpose, Nickel [5] introduced a discrete ordered Weber problem that generalizes objective functions frequently in discrete location theory. The objective function of this problem includes a sanction implementation for the service cost of a customer related to a cost situation associated with other customers' service costs. For example, a different sanction could be applied in the presence of 5. highest customer service cost rather than 2. highest customer service cost. An "ordering" function affects the solution and makes formulation more interesting.

The generalized model that includes the "ordering" factor has been studied for large-scale planar and network type location problems [14]-[15]. Due to these various studies, the DOMP entered the literature, a specific formulation of discrete conditions [5]. Studies about the solution of the DOMP were proposed by Nickel [5] and Boland et al. [6]. Exact methods can be used in instances away from large-scale real-life problems.

The ordered median location problem with continuous, discrete, and networks was presented by Puerto and Rodriguez [15], which is based on a hierarchy of semidefinite programs that can approximate up to any degree of solution accuracy of any ordered median problem infinite-dimensional spaces. Another exact solution method was the column generation approach to solve the continuous relaxation of the model. Then, a Branch-Cut and Price algorithm was studied to moderate the size of the DOMP in competitive computational time [16].

A Lagrangean Relaxation was carried out on this formulation to produce lower and upper bounds on the optimal value of the DOMP, which contains p-median, p-center, and k-centrum problems through a parallelized algorithm [17]. Various Mixed Integer Linear Programming (MILP) formulations for the DOMP have been investigated in the literature [18] - [20]. Labbé [21] carried out a comprehensive study that presents several new formulations for the DOMP. A polyhedral study of assignment polytope of the

Mustafa Serdar TOKSOY

A Clustering-based Simulated Annealing Algorithm with Taguchi Method for the Discrete Ordered Median ...

formulation was used that showed its proximity to the convex hull of the integer solutions.

Although there have been significant improvements in computational processes, none of the exact methods are sufficient for solving large-scale DOMP samples. Although some heuristic methods have been developed to solve medium or large scaled samples, their number is quite limited.

For that purpose, a robust tool called Evolution Program based on Genetic Algorithms (GA) within an acceptable time was submitted firstly by Holland [22], Davis [23], Goldberg et al. [24]. Variable Neighbourhood Search (VNS) is another metaheuristic method for combinatorial problems proposed by firstly Mladenovic [25] then Hansen and Mladenovic [26], which is a well-known technique used for discrete facility location problems and generally provides high-quality solutions. Domínguez-Marín et al. [27] developed two approximate heuristic solution methods, comprised of a GA, and an Evolution Program. Two GA with different coding schemes (binary coded HGA1 and integer coded HGA2) was proposed Stanimirovi'c et al. [28]. Later, Puerto et al. [29] proposed a modified VNS metaheuristic algorithm based on new neighborhood structures avoiding sorting in the evaluation of the objective function at each considered solution.

Recently, Olender and Ogryczak [30] developed a revised VNS called as REV-VNS outperforms the other methods, both in computing time and in solution quality. In the study, researchers introduced a regularization concept that intensifies the searching process for problems with a not strictly monotonic objective function.

However, all these algorithms still yield poor quality solutions for the p-center problem. There are also significant differences in the quality of solutions for other types of problems.

2.2. Mathematical Model

The mathematical model presented by Domínguez-Marín for the DOMP is as follows [31]: Let A denote a given set of M locations which $\{A = 1\ defines, ..., M\}$ with i,...,M

variables. Let c_{kj} denote a $M\ x\ M$ non-negative and symmetric matrix in which total demand of customer k is supplied by facility j for $(c_{kj})_{k,j=1,...M}$. $P \leq M$ indicates a number of facilities must be located among candidate facilities. Let a solution for facility location problem be given by a set $X \subseteq A$ of candidates N under the condition that $|X| = P$. It is assumed that each facility is uncapacitated in the study. So, supplying the fixed demand of customer k with the least cost by a facility j that is located in solution set X, can be formulated in Equation (1) as follows:

$$c_{kj} = c_k(x) = \min_{i \in X} c_{kj} \tag{1}$$

The objective function ensures the difference of the problem from the classic uncapacitated p-median problem. To get this function, customer servicing cost $(c_1(X), ..., c_M(X))$ is ordered in a non-decreasing array. σ_x is defined as a permutation on $\{1,...,M\}$ for the following inequalities in Equation (2).

$$c_{\sigma_x(1)}(X) \leq c_{\sigma_x(2)}(X) \leq \cdots \leq c_{\sigma_x(M)}(X) \tag{2}$$

So, a valid permutation for X is searched for any permutation mentioned above. Cost vector associated with a given set of X and related ordered cost vector is presented in following as Equation (3) and (4):

$$c(X) = \left(c_1(X), ..., c_M(X)\right) \tag{3}$$

$$c_\leq(X) = c_{\sigma_x(1)}(X) \leq \cdots \leq c_{\sigma_x(M)}(X) \tag{4}$$

Then, the objective function utilizes a linear cost function for i. least service cost of customer $c_{\sigma_x(i)}(X)$ for each $i=1,...,M$ with the help of $\lambda_1 \geq 0$. Supposing that $\Lambda = (\lambda_1, ..., \lambda_M)$ is a given vector will be required for different discrete facility location problems with $\lambda_i \geq 0$, $i=1,...,$ M. Inclusive of all this information, the general formulation (Equation (5)) of the DOMP can be defined as follows.

$$\min_{X \subseteq A, |X| = P} F_\Lambda(X) = (\Lambda, c_\leq(X)) = \sum_{i=1}^{M} \lambda_i c_{\sigma_x(i)}(X) \tag{5}$$

Mustafa Serdar TOKSOY

A Clustering-based Simulated Annealing Algorithm with Taguchi Method for the Discrete Ordered Median ...

The structure of the DOMP taking into consideration formulation elements above is as follows in Equation (6).

$$P/D/\bullet/\bullet/\sum ord \qquad (6)$$

P represents the number of candidate facilities; D represents a distance between facilities, and "ord" state represents the ordering factor. Different discrete problem solutions derived from the DOMP for (0-1) values of λ variable are noted in the classification schema of location problems proposed by Hamacher and Nickel [32] below.

Table 1 Classification of the DOMP problems

No	Formulation	Solution
1	$P/D/\Lambda = (1,1,,,,1,1)/\bullet/\sum ord$	p-median
2	$P/D/\Lambda = (0,0,,,,0,1)/\bullet/\sum ord$	p-center
3	$P/D/\Lambda = (\lambda,\lambda,,,,\lambda,1)/\bullet/\sum ord$	p-centdian

Definition of the DOMP enables to model for classic facility location problems. Classic facility location problems, which are specific cases of the DOMP, can be seen according to Λ vector ensures different varieties for objective functions below. Also, novel facility location problems can be solved. So that, by exploring this problem, varied objective function types can be obtained through a unique theoretical point of view (combining classic facility location problems) and the existence of real-life problems for different vector options.

$P / D / \Lambda = (1,1, \dots 1,1)/\bullet \sum_{ord} 1$ resulted in the p-median problem. $P/D/\bullet/\bullet/\sum ord$ points out the problem, which minimizes the sum of costs for supplying the total demand of each customer.

$P / D / \Lambda = (0,0, \dots 0,1)/\bullet \sum ord$ resulted in the p-center problem. $P/D/\bullet/\bullet/max$ points out the problem, which minimizes the maximal cost for supplying total demand among customers.

$P / D / \Lambda = (\mu,\mu, \dots, \mu, 1)/\bullet \sum ord$ resulted in the μ-centdian problem for $0 < \mu < 1$. $P/D/\bullet/\bullet /CD_\mu$ points out the convex combination of median ve center objective functions.

2.3. Illustrative Example

In 2010, Daskin published a simple p-median example with a topological graph to illustrate the method of solving a simple p-median problem by utilizing spreadsheets (Figure 1).
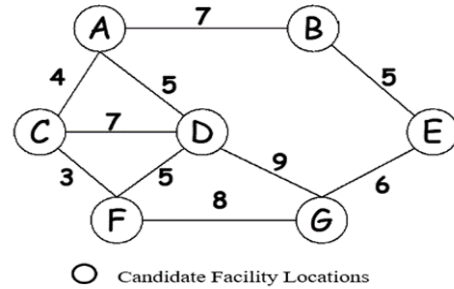
Figure 1 A graph of candidate facility locations

Let $M= \{A,...,G\}$ be a set of candidate facilities in an example (Figure 1). Suppose that a decision will be made about which p=2 facilities have to be selected among them. A cost matrix is below associated with facilities and customers supplied/serviced by these facilities. Table 2 represents a distance matrix occurred by the closest distances of customers.

Table 2 Distance matrix of example for the DOMP

	A	B	C	D	E	F	G
A	0	8	5	6	13	8	15
B	8	0	12	13	6	15	12
C	5	12	0	8	17	4	12
D	6	13	8	0	16	6	10
E	13	6	17	16	0	15	7
F	8	15	4	6	15	0	8
G	15	12	12	10	7	8	0

Complete enumeration method can be used to analyse all alternative solutions by virtue of small-scale structure of the problem. For $M=7$, p=2 and C (M, p) =21, total, 21 number of different solutions are obtained. These solutions are ordered as $x_1 = (A,B)$, $x_2 = (A,C)$, $x_3 = (A,D)$, $x_4 = (A,E)$, $x_5 = (A,F)$, $x_6 = (A,G)$, $x_7 = (B,C)$, $x_8 = (B,D)$, $x_9 = (B,E)$, $x_{10} = (B,F)$, $x_{11} = (B,G)$, $x_{12} = (C,D)$, $x_{13} = (C,E)$, $x_{14} = (C,F)$, $x_{15} = (C,G)$, $x_{16} = (D,E)$, $x_{17} = (D,F)$, $x_{18} = (D,G)$, $x_{19} = (E,F)$, $x_{20} = (E,G)$, $x_{21} = (F,G)$.

Mustafa Serdar TOKSOY

A Clustering-based Simulated Annealing Algorithm with Taguchi Method for the Discrete Ordered Median ...

Then, all c_{kj} variables are determined according to Equation (1) as $c_1(x_1) = 0$, $c_2(x_1) = 0$, $c_3(x_1) = 5$, $c_4(x_1) = 6$, $c_5(x_1) = 6$, $c_6(x_1) = 8$ and $c_7(x_1) = 12$ for c_{1j}. Afterwards, $c_{\leq}(A,B) = c_{\sigma_{(A,B)}(1)}(A,B) \leq .. \leq c_{\sigma_{(A,G)}(7)}(A,B)$ and $c_{\leq}(A,B) = (0,0,5,6,6,8,12)$ is obtained for $X(A,B)$ according to Equation (3) ve (4), respectively. In the p-median (2-median) solution, the vector $\Lambda = (1,1,1,1,1)$ is taken and when applied to the Equation (5), $\underset{X \subseteq A, |X| = P}{min} F_\Lambda(A,B) = \Lambda, c_{\leq}(A,B)) = (1,1,1,1,1) * (0,0,5,6,6,8,12) = 37$ is calculated for $X(A,B)$.

Finally, facility C and facility E $(X(C,E)$ is determined for a 2-median optimal solution when all solutions (21) are calculated (Figure 2). The objective function value is easily obtained as 25. Facility C and facility E are supplied by themselves; facility A, facility D, and facility F are supplied by the closest selected facility C, while facility B and facility G are supplied by the facility closest selected 4.
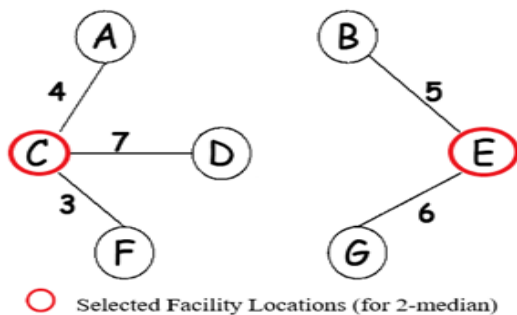
Figure 2 Solution graph of 2-median

While the same problem is analysed for the 2-center problem with $\Lambda = (0,0,0,0,1)$, an optimal solution of the problem is obtained X (1,4), and objective function value is found 12 when the solution is analysed. According to the graph, facilities 2 and 4 are supplied by themselves, facilities 3 and 5 are supplied by closest facility 1, and facility 2 is supplied by closest facility 4. If we pay attention to the solutions obtained here, it can be seen that the same solution value is obtained for p-median and p-center problems randomly, but due to the structure of $\Lambda = (\lambda_1, ..., \lambda_M)$ objective function values are different.

3. PROPOSED SIMULATED ANNEALING ALGORITHM

3.1. Simulated Annealing Algorithm

The Simulated Annealing (SA) is a stochastic search metaheuristic method capable of getting good solutions for combinatorial optimization problems, which is similar to the physical annealing process of the solids. SA algorithm, independent of each other, was described by Kirkpatrick et al. [7] and Cerny [8]. SA has been used to solve many combinatorial optimization problems such as traveling salesman problem, scheduling, assignment problem, network design [33] - [34].

In the SA algorithm, the control parameter is the temperature and assesses the probability of achieving a better solution for minimization problems. the SA is one of the neighborhood-based search algorithms. The descent algorithm, a simple form of neighborhood search, begins to search with an arbitrarily chosen initial solution. This solution produces a neighborhood solution through a suitable iteration mechanism, and the change in cost is calculated. If there is a cost reduction, the neighborhood solution is accepted as the new solution; otherwise, the current solution is not changed. This process continues until neighbours cannot improve the current solutions with cost improvements, and the descent algorithm ends with a local optimum.

The quality of the resolution obtained by the descent algorithm is based on the initial solution. The performance of a heuristic should not depend on only the initial solution. The initial solution should accept the bad solutions in a controlled way to reduce this dependency. To avoid the disadvantage of the descent algorithm, sometimes the neighborhood iterations leading to the raise at cost are accepted in the SA algorithm to escape the local optima traps. The acceptance or rejection of an iteration leads to an increase at cost is randomly determined in a controlled manner. The function that gives the probability of accepting the iteration leading to arise as a near as Δ in the cost function is called the accept function (Equation 7). In the following accept function, T is a control

Mustafa Serdar TOKSOY

A Clustering-based Simulated Annealing Algorithm with Taguchi Method for the Discrete Ordered Median ...

parameter corresponding to the temperature at the physical annealing.

$$P(accept) = e^{-\left(\frac{\Delta}{T}\right)} \qquad (7)$$

According to the accept function, the probability of accepting small increments in the objective function is greater than the probability of accepting large increments. Moreover, most iterations will be accepted when T is high, and if T is near zero, iterations leading to an increase in the objective function will be rejected. That is why the SA algorithm starts with a relatively high T value to prevent the solution from falling into the local optima trap. The SA algorithm continues to search by attempting a definite number of iterations at each temperature value while gradually decreases the temperature on the other hand. The parameters mentioned above are as follows:

x_{best}: The best solution for the problem.

M_{tb}: Neighbourhood solution number for each temperature level.

$T(t)$: Temperature value at t. iteration

The choice of the cooling plan has a very significant effect on the algorithm's performance. When probing specific decisions are taken, the CPU time must be used effectively, and the best solution in the SA must be closed to global optima.

The initial solution, neighborhood structure, solution space, and cost function are key factors affecting these decisions. These parameters determine the convergence speed of the SA to global optima.

Neighborhood structure must be small enough to be researched in a few of the number of iterations. Each solution in the neighborhood cluster must be reached by simple movements from each solution in the same cluster. The neighborhood solution must be produced randomly to use the run time effectively and must be chosen in which the difference between the solution and the objective function can be easily calculated.

3.2. Initialization

In this kind of classical solution technics, selecting a suitable initial population accelerates the algorithm's convergence. In the study, we used two novel initialization techniques, which are described as "sorting min to max", "the number of minimal selections" and a well-known "clustering-based solution", respectively to reach optimal/near-optimal solutions.

X₀ (I) Sorting min to max: Performs by selecting a number of *p* facilities in which the total distance of each facility to other facilities is sorted from minimum to maximum in the *M* x *M* distance matrix (see Table 3).

In Table 3, there is a list comprised of p=5 candidate facilities (②-⑦-⑨-⑬-⑳) listed according to the sum of their minimum distances (minisum) 525-642-824-953 to other all facilities (customers) (M=100).

Table 3 Sorting min to max initial solution

M	②	⑦	⑨	⑬	⑳
1	15	47	89	66	87
-	-	-	-	-	-
100	32	73	58	25	48
Total distance	525	642	724	824	953

X₀ (II) Number of minimal selections: Performs by the selection of *p* facilities that ordered minimum to maximum according to the selecting number of minimum distances of each facility to all other facilities depending on p-median values derived from *X₀(1)* initial solution (Table 4).

Table 4 Number of the minimal selecting initial solution

M	⑳	⑬	⑨	⑦	②
1	87	66	89	47	<u>15</u>
-	-	-	-	-	-
100	48	<u>25</u>	58	73	32
nms	5	13	22	29	31

In Table 5, the minimal distance to the first customer of the candidate facility ② is underlined as <u>15</u>, while the same measure for the candidate facility ⑬ to the hundredth customer is <u>25.</u> In this context, the total number of selection is

13 for the candidate facility ⑬ while 31 for the candidate facility ②. Ordered rows from minimal to maximum size can be seen in nms line (number of selection).

X₀(III) Clustering-based solution: Initial solution in which a number of p facility is selected by K-means clustering algorithm (KMCA).

KMCA is one of the best-known and widely used clustering algorithms in various applications, such as data mining, image processing, and machine learning. KMCA is the simplest and un tutorial clustering algorithm ever developed used to participate the given data into K number of clusters according to their characteristics or properties [35]. As a result of the clustering, although the similarity between the elements within the cluster is high, the similarity between the inter clusters is very low.

The algorithm's basic working principle is based on randomly determining K initial center points of the cluster $C_i (i = 1, …, K)$. For this purpose, firstly, distances of each node to cluster centers are calculated. Then, each element is assigned to the cluster at the closest distance. At the second step, the centers of the clusters are recalculated. These steps are repeated iteratively until the centers are no longer changed. Thus, conversion stability is provided. This study uses the Euclidean distance to calculate the distance between nodes and clusters. The clustering is provided by the optimization of Equation (8) given below [36].

$$minimize\ f = \sum_{i=1}^{K} \sum_{j=1, j\epsilon G_i}^{N} \lVert x_j - C_i \rVert^2 \qquad (8)$$

In Equation (8), K symbolizes the number of clusters, N symbolizes the number of nodes (vertices), x_j symbolizes the coordinate of vertex j, C_i symbolizes the coordinate of the cluster i, and G_i symbolizes the group of nodes belonging to cluster i.

The closest squared distance is determined by moving the cluster centers in space. The algorithm continuously updates the cluster center considering the assignment of all the nodes to it.

Equation (9) is used for the calculation of centers as follows:

$$C_i = \frac{1}{|G_i|} \sum_{j=1, j\epsilon G_i}^{N} x_j \qquad (9)$$

The number of vertices contained in cluster i is symbolized as $|G_i|$ in Equation (9).

In this study, KMCA was adopted for the DOMP. First, the K number of clusters was assumed to equal to p facilities $(K = p)$. Then, all distances between the cluster centers and their nodes were calculated considering the Euclidean distance. The closed node to each cluster center was determined and accepted the facility that services other nodes (customers). Figure 3 represents the pseudo-code of KMA adopted for the DOMP.

```
Set the K (p) number of clusters center randomly;
repeat
        for each vertex do
            Calculate distance measure to each cluster;
            Assign it to the closest cluster;
        end
        Recalculate the positions of cluster centers;
until stop condition is reached;
calculate closed node for each cluster center;
accept the selected node as p-facility;
```

Figure 3 The proposed KMA pseudo code

There can be found studies in which the SA and the KMCA were used as hybrid or combined structures for different problem types in literature [37] - [43].

3.3. Local Search

After the initializing process, we developed four novel solution approaches based on K-exchange neighborhoods, one of the most widely used types of neighborhood relations, to improve the performance of the proposed SA. The algorithm improves the current solution by removing a node or nodes in the solution and replacing it with a node, not in the solution. It is implemented if an exchange of this sort can be found and improves the solution. The algorithm terminates when there is no such exchange that improves the solution.

Mustafa Serdar TOKSOY

A Clustering-based Simulated Annealing Algorithm with Taguchi Method for the Discrete Ordered Median ...

The steps of the K-exchange algorithm is described below.

In the first step, a solution is initialized by any set of p facilities. Sites in the current solution and candidate sites not in the solution are removed in the following steps. Then, it is investigated that removing one site from the current solution and replacing it with a site that is not in the current solution will improve the objective function. If so, substitution is actualized, and the algorithm terminates. The proposed model adopted four different novel neighborhood functions for the DOMP. These functions are presented as a chromosome structure for p=5 facilities, sorted according to their total distance values.

N(I) Random exchange: A non-solution random facility enters the solution in place of a random candidate in the current solution.

N(II) Max2-exchange: 2 non-solution random facilities enter the current solution in place of 2 facilities leading to the maximum total distance (Figure 4).

Figure 4 Max2-exchange neighborhood

In Figure 4, a solution set X comprised of ②, ⑨, ⑦, ⑬ and ⑳ nodes and their total distance to the other whole facilities are sorted from minimum to maximum (see Table 4). Then, nodes related to max two values (⑬ and ⑳) are exchanged with two random nodes ⑰ and ⑪ derived from other facilities in the M set.

Similar exchanges are performed according to other neighborhood conditions below.

N(III) Max-exchange: A non-solution random candidate facility enters the solution in place of a facility leading to the maximum total distance.

N(IV) Min-exchange: A non-solution random facility enters the solution in place of a facility leading to the minimum total distance.

N(V) Min2-exchange: 2 non-solution random facilities enter the solution in place of 2 facilities leading to the minimum total distance.

The main steps of the proposed SA algorithm are as follows in Figure 5:

```
1   x_0 ← Generate an initial solution by the KMCA
2   bestSolution  ←  x_0
3   T ← maxTemperature
4   while  T_0 > minTemperature do
5      iter ← 0
6      while iter < maxIterations do
7         x' ←
8         Δ ← f(x') − f(x_o)
9         if  Δ < 0 then
10            x_0 ← x
11            if f(x') < f(bestSolution)  then
12               bestSolution ← x'
13            else if  rand(0,1) < e^{−Δ/T}  then
14               x_0 ← x'
15         iter ← iter + 1
16      T ← T * u
17  return bestSolution
```

Figure 5 Pseudo-code of the proposed SA

4. COMPUTATIONAL STUDY

In the study, 40 p-median test instances [10] consisting of 100-900 nodes and 5-90 candidate solutions were used. Fundamental decisions in adopting DOMP to the SA metaheuristic were determined as; T_0= 1000-10000, M_{tb}=1-4, u = 0.999, and T=0.100 (stopping condition of the algorithm). On the condition that M defines the total number of facility M and the number of candidate facility p, two different adopted novel initial solutions x_0 and four different novel neighborhood structures (N) were proposed for the DOMP as probing specific decisions.

4.1. Data Set

The performance of the proposed SA algorithm with the Taguchi method for the DOMP was coded in MATLAB software and evaluated by the test problems [10] derived from OR-LIB literature. Hence, optimal parameter levels were observed using pmed1 data instance comprised of M=100 customers and p=5 candidate facilities. The experimental procedure was performed on

Mustafa Serdar TOKSOY

A Clustering-based Simulated Annealing Algorithm with Taguchi Method for the Discrete Ordered Median ...

Intel(R) Core (TM) i7-6500U at 2.59 GHz with 4 gigabytes of RAM.

4.2. Parameter Tuning

Taguchi method was utilized for parameter optimization to obtain the best levels of parameters of the proposed SA in this study. Genichi Taguchi has introduced a solution called his name that will enhance realizing and evaluating experiments with his approach [44]. In this regard, it is possible to significantly reduce the number of experiments required for detailed analysis and evaluation before the experimental process. The Taguchi method is an advantageous technique for system design at high quality beyond being an experimental design technique.

The experimental design has been used to reduce variation, and Taguchi defined some criteria called signal/noise ratio as a performance criterion (Table 5) [45].

Table 5 Signal/noise ratio criterions

Target	Signal/noise criterion
Maximum Best	$-10log\,(\frac{\sum_{i=1}^{n}\frac{1}{y_i^2}}{n})$
Minimum Best	$-10log\,(\frac{\sum_{i}^{n}y_i^2}{n})$
Nominal Best	$-10log\,(\frac{y^{-2}}{S^2})$

The optimal parameter combination can be determined by an experimental study with the help of the various parameters and levels changing according to the structure of the problem. Several studies are available in which the Taguchi method is used for the parameter optimization for the SA algorithm [46] - [50].

In this study, four parameters with only three levels were used (neighborhood structure, initial temperature, number of solutions executed at each temperature and initial solution) as input data for Taguchi method to design an appropriate experimental pattern. Orthogonal array L9 was chosen for Taguchi method by the help of MINITAB software. Levels of parameters were determined by the help of pre-experimental studies; in other words, some of the levels were

ignored which have a low significant effect on the solution quality.

To analyse the effectiveness of neighborhood structures by pre-experimental studies, five neighborhoods were investigated in preliminary studies with %100 and %20 (equal) probability, respectively. Then, the current solution was converted to the hill-climbing heuristic by dividing the P(accept) value with a big number, to reduce the probability of accepting a temporary bad solution.

According to the results of all these pre-experimental studies, obtained parameter set for the developed algorithm set is shown in Table 6 below; efficiency percentages of neighborhood structures changed as %41 N(III), %21 N(I), %19 N(II), %11 N(IV) and % 8 N(V).

Table 6 Efficiency rates of neighborhood structures

N(I)	N(II)	N(III)	N(IV)	N(V)
0 - 0.21	0.21 - 0.40	0.40 - 0.81	0.81 - 0.92	0.92 -1

In this respect, two neighborhood structures were ignored. N (4) Min-exchange and N (5) Min2-exchange with %19 and %11 efficiency percentages, respectively, were evaluated as low efficient according to other neighborhoods. All parameters and levels chosen for the proposed SA were presented in Table 7.

Table 7 Parameters and levels of the proposed SA

Symbol	Parameter	Level I	Level II	Level III
A	Neighborhood	*N(I)*	*N(II)*	*N(III)*
B	Initial temperature	*900°*	*600°*	*300°*
C	Repetition	*1*	*2*	*3*
D	Initial solution	$x_0(I)$	$x_0(II)$	$x_0(III)$

In this way, orthogonal array L9 (3^4) was utilized as the experimental pattern, and four trials were carried out for each case. Orthogonal array of parameter levels, S/N ratios and mean values obtained by MINITAB is given in Table 8.

Table 8 Orthogonal array and obtained data

Standard Array	A	B	C	D	S/N ratio	Mean
1	1	1	1	1	-75.8922	6231.25
2	1	2	2	2	-75.7373	6121.50
3	1	3	3	3	-75.5081	5961.79
4	2	1	2	3	-75.6856	6084.92
5	2	2	3	1	-75.6733	6076.50
6	2	3	1	2	-75.7708	6145.25
7	3	1	3	2	-75.7204	6109.50
8	3	2	1	3	-75.6415	6054.33
9	3	3	2	1	-75.6597	6067.00

The obtained mean S/N ratio plot for each level of the parameters was given in Figure 6. Note that the pmed-1 instance was used to determine the optimal parameter combination.
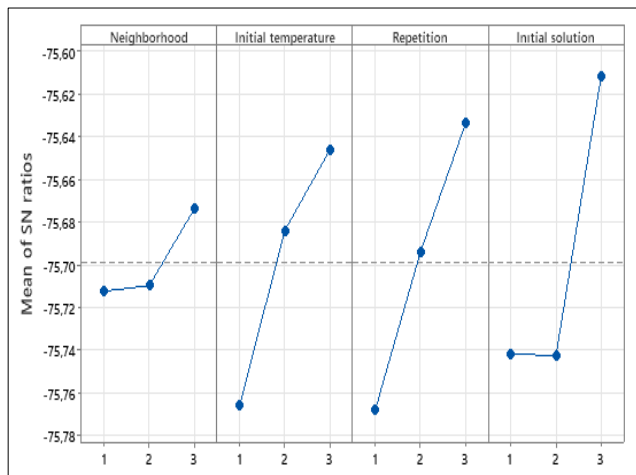

Figure 6 The mean S/N ratio plot for each level of the parameters (Alpha = 0.5)

According to Figure 6; the best level for the local search was obtained as N (3) Max-exchange, the best level for initial solutions was obtained as $x_0(III)$ clustering-based solution, the best level for neighborhood solution number for each temperature (M_{tb}) was obtained as 3, and initial temperature (T_0) was obtained as 300º.

It does not mean that N (I) Max2-exchange and N(II) Random-exchange does not affect the solution quality as much as N (III). Similar to the parameter set by pre-experimental studies, the max-exchange heuristic has the highest percentage value for neighborhood functions. Table 9 shows the best levels of parameters obtained with the help of the Taguchi method.

Table 9 The best levels of the parameters

N	x_0	M_{tb}	T_0
N(III)	$x_0(III)$	3	300^0

4.3. Computational Results

In this study, the proposed clustering-based SA algorithm was implemented in MATLAB software, and the performance of the algorithm was tested on the p-median test problems (Beasley) derived from OR-LIB [10]. For this purpose, 20 trials were run for each problem. The results of test problems were given in Table 10, with the benchmark results of the DOMP.

Table 10 includes the instance name, name of the problem, the number of facilities (M), number of facilities to supply others (p), best-known solutions (BKS), gap value (objective function value - BKS)/BKS × 100, processing times in seconds, respectively. The proposed clustering-based SA algorithm is compared with the results three state-of-the-art algorithms: Evolution Program (EP) [27] based on a GA to solve optimization problems, hybrid of a GA and a generalization of the well-known Fast Interchange heuristic (HGA1) [28] and Revised Variable Neighbourhood Search (REV-VNS) [30] in which a regularization concept that intensifies the searching process for problems with a not strictly monotonic objective function was introduced.

Table 10 The benchmarking results of algorithms for the DOMP

Instance	M	p	BKS	EP			HGA1			REV-VNS			Proposed SA		
				Best	Gap (%)	CPU	Best	Gap (%)	CPU	Best	Gap (%)	CPU	Best	Gap (%)	CPU
Pmed1		5	5819	5819	0.00	25.42	5819	0.00	0.93	5819	0.00	0.07	5819	0.00	11.85
Pmed2		10	4093	4093	0.00	37.55	4093	0.00	1.17	4093	0.00	0.19	4093	0.00	17.47
Pmed3	100	10	4250	4250	0.00	37.88	4250	0.00	1.08	4250	0.00	0.17	4250	0.00	17.60
Pmed4		20	3034	3046	0.40	61.48	3034	0.00	1.62	3034	0.00	0.54	3034	0.00	28.59
Pmed5		33	1355	1361	0.44	93.22	1355	0.00	1.91	1355	0.00	0.65	1355	0.00	43.17

Mustafa Serdar TOKSOY

A Clustering-based Simulated Annealing Algorithm with Taguchi Method for the Discrete Ordered Median ...

Instance	Group	p	Opt	Best	Gap	CPU	Best	Gap	CPU	Best	Gap	CPU	Best	Gap	CPU
Pmed6	200	5	7824	**7824**	0.00	36.25	**7824**	0.00	2.38	**7824**	0.00	0.23	**7824**	0.00	17.20
Pmed7		10	5631	5645	0.25	55.39	**5631**	0.00	3.33	**5631**	0.00	0.59	**5631**	0.00	26.26
Pmed8		20	4445	4465	0.45	91.81	**4445**	0.00	4.29	**4445**	0.00	1.79	**4445**	0.00	43.42
Pmed9		40	2734	2762	1.02	170.25	**2734**	0.00	4.64	**2734**	0.00	3.16	2745	0.40	79.65
Pmed10		67	1255	1277	1.75	290.53	1259	0.32	6.29	**1255**	0.00	3.05	1265	0.79	81.04
Pmed11	300	5	7696	**7696**	0.00	47.98	**7696**	0.00	4.16	**7696**	0.00	0.57	**7696**	0.00	22.18
Pmed12		10	6634	**6634**	0.00	75.63	**6634**	0.00	7.36	**6634**	0.00	1.33	**6634**	0.00	36.69
Pmed13		30	4374	4432	1.33	193.22	**4374**	0.00	7.55	**4374**	0.00	7.07	4386	0.26	91.84
Pmed14		60	2968	2997	0.98	359.58	2969	0.03	11.89	**2968**	0.00	11.59	2979	0.37	169.97
Pmed15		100	1729	1749	1.16	580.98	1736	0.40	15.29	1730	0.06	10.01	1739	0.56	271.46
Pmed16	400	5	8162	8183	0.26	56.89	**8162**	0.00	7.77	**8162**	0.00	1.10	**8162**	0.00	28.18
Pmed17		10	6999	**6999**	0.00	95.08	**6999**	0.00	14.13	**6999**	0.00	2.10	**6999**	0.00	47.42
Pmed18		40	4804	4880	1.48	320.38	**4809**	0.00	13.04	**4809**	0.00	15.21	4826	0.45	153.17
Pmed19		80	2845	2891	1.62	604.36	2851	0.21	26.59	2846	0.04	20.66	2862	0.59	287.42
Pmed20		133	1789	1832	2.40	963.44	1794	0.28	32.03	**1789**	0.00	29.98	1809	1.10	454.78
Pmed21	500	5	9138	**9138**	0.00	70.14	**9138**	0.00	8.72	**9138**	0.00	1.32	**9138**	0.00	34.49
Pmed22		10	8579	8669	1.05	116.59	**8579**	0.00	20.5	**8579**	0.00	3.67	**8579**	0.00	59.20
Pmed23		50	4619	4651	0.69	486.08	4624	0.11	23.55	**4619**	0.00	25.45	4631	0.26	233.86
Pmed24		100	2961	3009	1.62	924.66	2966	0.17	50.86	**2961**	0.00	43.25	2983	0.72	445.09
Pmed25		167	1828	1890	3.39	1484.13	1838	0.55	71.56	**1828**	0.00	56.14	1857	1.54	708.71
Pmed26	600	5	9917	9919	0.02	84.34	**9917**	0.00	14.25	**9917**	0.00	2.15	**9917**	0.00	42.56
Pmed27		10	8307	8330	0.28	136.53	**8307**	0.00	22.73	**8307**	0.00	5.42	**8307**	0.00	69.30
Pmed28		60	4498	4573	1.67	673.30	4500	0.04	42.87	**4498**	0.00	46.26	4530	0.71	329.32
Pmed29		120	3033	3099	2.18	1268.89	3036	0.10	85.06	3034	0.03	72.89	3050	0.56	618.06
Pmed30		200	1989	2036	2.36	2043.33	2008	0.96	110.94	1992	0.15	73.35	2015	1.31	925.05
Pmed31	700	5	10086	**10086**	0.00	92.67	**10086**	0.00	14.73	**10086**	0.00	2.55	**10086**	0.00	44.41
Pmed32		10	9297	9319	0.24	156.50	**9297**	0.00	34.05	**9297**	0.00	6.19	**9297**	0.00	77.77
Pmed33		70	4700	4781	1.72	894.19	4719	0.40	60.09	**4700**	0.00	65.46	4734	0.72	418.23
Pmed34		140	3013	3100	2.89	1762.69	3027	0.46	135.27	3016	0.10	131.11	3051	1.24	824.26
Pmed35	800	5	10400	**10400**	0.00	109.86	**10400**	0.00	19.44	1040	0.00	3.62	**10400**	0.00	53.00
Pmed36		10	9934	9947	0.13	182.06	9951	0.17	36.2	**9934**	0.00	9.15	9945	0.11	89.61
Pmed37		80	5057	5126	1.36	1190.25	5063	0.12	70.77	5058	0.02	110.56	5099	0.83	557.03
Pmed38	900	5	11060	**11060**	0.00	120.14	**11060**	0.00	27.13	**11060**	0.00	4.88	**11060**	0.00	59.65
Pmed39		10	9423	**9423**	0.00	207.75	**9423**	0.00	38.73	**9423**	0.00	9.40	**9423**	0.00	101.35
Pmed40		90	5128	5188	1.17	1492.59	5133	0.10	213.39	5131	0.06	158.68	5167	0.75	734.58
Average				564.5	0.86	442.35	5538.50	0.11	31.71	5301.63	0.01	23.54	5545.55	0.33	208.87
Number of best solutions				12			24			33			21		

When the best results are examined on 40 Beasley test instances in Table 10; it can be seen that the proposed clustering-based SA algorithm achieves the best result in a total of 21 instances (Pmed1, Pmed2, Pmed3, Pmed4, Pmed5, Pmed6, Pmed7, Pmed8, Pmed11, Pmed12, Pmed16, Pmed17, Pmed21, Pmed22, Pmed26, Pmed27, Pmed31, Pmed32, Pmed35, Pmed38, and Pmed39) while the other results are closed optimal solutions. Moreover, the average gap value was obtained as 0.33, and the average CPU was obtained as 208.87 seconds.

While considering average gap values of the comparison algorithms; it is observed that the proposed clustering-based SA (0.33) gives a better result than the EA (0.86) with 12 best solutions, relatively close to HGGA1 (0.11) with 24 best solutions and falls behind the REV-VNS (0.01) with 33 best solution and ranks as third. According to CPU times, the proposed clustering-based SA (208.87) ranks third again among EP (442.35), HGA1 (31.71), and REV-VNS (23.54).

5. CONCLUSION

It is seen that the location theory, which constitutes the basis of this study and especially the discrete location problems which have been studied extensively by the researchers as day-to-day and different studies will continue to increase. Therefore, the researchers have received much attention to developing a standard solution for these kinds of problems. The DOMP, which has an NP-hard structure, ensures effective and quick solutions for such problems in a single formulation. Already the studies focus on the DOMP are recent and insufficient.

Mustafa Serdar TOKSOY

A Clustering-based Simulated Annealing Algorithm with Taguchi Method for the Discrete Ordered Median ...

This paper proposed a clustering-based SA metaheuristic, which has not been tried to solve the DOMP. The performance of the SA was compared with the p-median solutions of three state-of-the-art algorithms developed for the DOMP. Although the SA is a relatively simple and easy-to-apply metaheuristic compared to other algorithms, it is observed that it can achieve effective results for the DOMP. In order to improve the performance of the algorithm, novel initial solution methods and neighborhood structures were analysed. The KMCA was adapted to strengthen the initial solution. Moreover, The Taguchi method is utilised as a parameter tuning tool to determine the best levels of parameters used in the SA.

As a result, we developed a clustering-based SA algorithm was developed in this study. The algorithm is capable to be used in combination with other methods. According to the results, although the relatively high processing times are remarkable, the proposed algorithm is competitive and can be a robust alternative for the DOMP. Furthermore, it can be used to solve different location problems (not only p-median, p-center, and p-centdian) that are combined on a single model, simultaneously. Future work can be summarized as below:

The performance of the algorithm can be improved with other heuristic/metaheuristic algorithms in hybrid or combined structure. Neighborhood structures can be developed to take into account the processing times. Problems can be combined into a multi-objective decision-making problem. Besides, the proposed algorithm can be adapted to new models for different applications of location analysis.

Funding

The Declaration of Conflict of Interest/ Common Interest

No conflict of interest or common interest has been declared by the authors.

Authors' Contribution

The author confirms sole responsibility for all sections of the manuscript.

The Declaration of Ethics Committee Approval

This study does not require ethics committee permission or any special permission.

The Declaration of Research and Publication Ethics

The author of the paper declare that they comply with the scientific, ethical and quotation rules of SAUJS in all processes of the paper and that they do not make any falsification on the data collected. In addition, they declare that Sakarya University Journal of Science and its editorial board have no responsibility for any ethical violations that may be encountered, and that this study has not been evaluated in any academic publication environment other than Sakarya University Journal of Science.

REFERENCES

[1] Z. Drezner and H. W. Hamacher, "Facility location: applications and theory," Springer Science & Business, pp. 81-107, 2004.

[2] P. B. Mirchandani and R. L. Francis, "Discrete location theory," Wiley Periodicals, 1990.

[3] S. L. Hakimi, "Optimum distribution of switching centers in a communication network and some related graph theoretic problems," Operations Research, vol. 13, no. 3, pp. 462–475, 1965.

[4] J. Reese, "Solution methods for the p-median problem: an annotated

Mustafa Serdar TOKSOY

A Clustering-based Simulated Annealing Algorithm with Taguchi Method for the Discrete Ordered Median ...

bibliography," Networks: An International Journal, vol. 48, no. 3, pp. 125-142, 2006.

[5] S. Nickel, "Discrete ordered weber problems," Operations Research Proceedings, Springer, pp. 71-76, 2001.

[6] N. Boland, P. Domínguez-Marín, S. Nickel, and J. Puerto, "Exact procedures for solving the discrete ordered median problem," Computers Operations Research, vol. 33, no. 11, pp. 3270-3300, 2006.

[7] S. Kirkpatrick, C. D. Gelatt, and M. P. Vecchi, "Optimization by simulated annealing," Science, vol. 220, no. 67, pp. 671-680, 1983.

[8] V. A. Cerny, "Thermodynamical approach to the traveling salesman problem: an efficient simulated algorithm," Journal of Optimization Theory and Applications, vol. 45, no. 1, pp. 41-51, 1985.

[9] N. Metropolis, A. W. Rosenbluth, A. H. Teller, and E. Teller, "Equation of state calculation by fast computing methods," Journal of Chemical Physics, vol. 21, no. 6, pp. 1087-1093, 1953.

[10] J. E. Beasley, "A note on solving large p-median problems," In European Journal of Operational Research, vol. 21, no. 2, pp. 270-273, 1985.

[11] M. S. Daskin, "Network and discrete location: models, algorithms and applications," John Wiley & Sons, 1995.

[12] J. Kalcsics, T. Melo, S. Nickel, and V. Schmid-Lutz, "Facility location decisions in supply chain management," Operations Research Proceedings 1999, pp. 467-472, 1999.

[13] S. Nickel and J. Puerto, "A unified approach to network location problems," Networks, vol. 34, pp. 283–290, 1999.

[14] J. Kalcsics, S. Nickel, and J. Puerto, "Multifacility ordered median problems on networks: a further analysis," Networks, vol. 41, no. 1, pp. 1-12, 2003.

[15] J. Puerto and A. M. Rodríguez-Chía, "Ordered Median Location Problems," Springer, pp. 249-288, 2015.

[16] P. L. Diego, "The Discrete Ordered Median Problem Revisited: New Formulations, Properties and Algorithms," Doctoral Dissertation, Université Libre de Bruxelles, 2016.

[17] J. L. Redondo, A. Marín, and P. M. Ortigosa, "A parallelized lagrangean relaxation approach for the discrete ordered median problem," Annals of Operations Research, vol. 246, no. 1, pp. 253-272, 2016.

[18] W. Ogryczak and P. Olender, "Ordered median problem with demand distribution weights," Optimization Letters, vol. 10, no. 5, pp. 1071-1086, 2016.

[19] W. Ogryczak and T. Śliwiński, "On solving linear programs with the ordered weighted averaging objective," European Journal of Operational Research, vol. 148, no. 1, pp. 80-91, 2003.

[20] P. Olender, "Hybrid models for the OWA optimization," Journal of Telecommunications and Information Technology, vol. 4, pp. 22-30, 2016.

[21] M. Labbé, D. Ponce, and J. Puerto, "A comparative study of formulations and solution methods for the discrete ordered p-median problem," In Computers & Operations Research, vol. 78, pp. 230-242, 2017.

[22] J. H. Holland, "Adaptation in Natural and Artificial Systems," MIT Press, 1975.

[23] L. Davis, "Genetic Algorithms and Simulated Annealing," Morgan Kaufmann Publishers, 1987.

[24] D. E. Goldberg and J. H. Holland, "Genetic Algorithms in Search, Optimization and

Mustafa Serdar TOKSOY

A Clustering-based Simulated Annealing Algorithm with Taguchi Method for the Discrete Ordered Median ...

Machine Learning," Addison Wesley, 1989.

[25] N. Mladenovic, "A variable neighborhood algorithm - a new metaheuristic for combinatorial optimization," Abstracts of papers presented at Optimization Days, pp. 234, 1995.

[26] P. Hansen and N. Mladenovic, "Variable neighborhood search for the p-median," Location Science, vol. 5, no. 4, pp. 207-226, 1997.

[27] P. Dominguez-Marin, S. Nickel, P. Hansen, and N. Mladenović, "Heuristic procedures for solving the discrete ordered median problem," Annals of Operations Research, vol. 136, no. 1, pp. 145-173, 2005.

[28] Z. Stanimirović, J. Kratica, and D. Dugošija, "Genetic algorithms for solving the discrete ordered median problem," European Journal of Operational Research, vol. 182, no. 3, pp. 983-1001, 2007.

[29] J. Puerto, D. G. Pérez-Brito, and C. García-González, "A modified variable neighborhood search for the discrete ordered median problem," In European Journal of Operational Research, vol. 234, no. 1, pp. 61-76, 2014.

[30] P. Olender and W. Ogryczak, "A revised variable neighborhood search for the discrete ordered median problem," European Journal of Operational Research, vol. 274, no. 2, pp. 445-465, 2019.

[31] P. Domínguez-Marín, "The Discrete Ordered Median Problem: Models and Solution Methods: Models and Solution Methods," Springer Science & Business Media, 2013.

[32] H. W. Hamacher and S. Nickel, "Combinatorial algorithms for some 1-facility median problems in the plane," European Journal of Operational Research, vol. 79, pp. 340–351, 1994.

[33] H. I. Demir, R. K. Phanden, A. Kökçam, B. Erkayman and C. Erden, "Hybrid evolutionary strategy and simulated annealing algorithms for integrated process planning, scheduling and due-date assignment problem," Academic Platform Journal of Engineering and Science, vol. 9, no. 1, pp. 86-91, 2021.

[34] E. Erdem, T. Aydın, and B. Erkayman, "Flight scheduling incorporating bad weather conditions through big data analytics: A comparison of metaheuristics," Expert Systems, vol. 38, no. 8, pp. 1-19, 2021.

[35] K. Wagstaff, C. Cardie, S. Rogers, and S. Schrödl, "Constrained k-means clustering with background knowledge," In LCML. vol. 1. pp. 577-584, 2001.

[36] L. Tan, Y. Tan, G. Yun, and Y. Wu, "Genetic Algorithms Based on Clustering for Traveling Salesman Problems," 12th International Conference on Natural Computation, Fuzzy Systems and Knowledge Discovery, pp. 103-108, 2016.

[37] S. Z. Selim and K. Alsultan, "A simulated annealing algorithm for the clustering problem," Pattern Recognition, vol. 24, no. 10, pp. 1003-1008, 1991.

[38] G. P. Babu and M. N. Murty, "Simulated annealing for selecting optimal initial seeds in the k-means algorithm," Indian Journal of Pure and Applied Mathematics, vol. 25, no. 1-2, pp. 85-94, 1994.

[39] G. T. Perim, E. D. Wandekokem, and F. M. Varejão, "K-means initialization methods for improving clustering by simulated annealing," In Ibero-American Conference on Artificial Intelligence, Springer, pp. 133-142, 2008.

[40] Z. H. Che, "A two-phase hybrid approach to supplier selection through cluster analysis with multiple dimensions," International Journal of Innovative Computing

Mustafa Serdar TOKSOY

A Clustering-based Simulated Annealing Algorithm with Taguchi Method for the Discrete Ordered Median ...

Information and Control, vol. 6, no. 9, pp. 4093-4111, 2010.

[41] R. Kittaneh, S. Abdullah, and A. Abuhamdah, "Iterative simulated annealing for medical clustering problems," Trends in Applied Sciences Research, vol. 7, no. 2, pp. 103-117, 2012.

[42] T. Lu, J. Fu, and X. Hu, "A Dynamic Path Planning Model Based on K-means Algorithm and Simulated Annealing Algorithm," 2019 IEEE 3rd Information Technology, Networking, Electronic and Automation Control Conference, pp. 2390-2394, 2019.

[43] P. Rani, J. Shokeen, A. Agarwal, A. Bhatghare, A. Majithia, and J. Malhotra, "Credit Card Fraud Detection Using Blockchain and Simulated Annealing K-means Algorithm," International Conference on Innovative Computing and Communications, pp. 51-59, 2022.

[44] G. T. Clausing and G. Taguchi, "Robust quality," Harvard Business Review, vol. 13, pp. 27-42, 1990.

[45] D. C. Montgomery, "Design and Analysis of Experiments," John Wiley & Sons, 2001.

[46] J. L. Liu, "Novel Taguchi-simulated annealing method applied to airfoil and wing planform optimization," Journal of Aircraft, vol. 43, no. 1, pp. 102-109, 2006.

[47] S. A. Seyed-Alagheband, S. F. Ghomi, and M. Zandieh, "A simulated annealing algorithm for balancing the assembly line type II problem with sequence-dependent setup times between tasks," International Journal of Production Research, vol. 49, no. 3, pp. 805-825, 2011.

[48] N. Zoraghi, A. A. Najafi, and N. S. T. Akhavan, "An integrated model of project scheduling and material ordering: a hybrid simulated annealing and genetic algorithm," Journal of Optimization in Industrial Engineering, vol. 8, no. 1, pp. 19-27, 2012.

[49] S. Ghalme, A. Mankar, and Y. Bhalerao, "Integrated Taguchi-simulated annealing (SA) approach for analyzing wear behaviour of silicon nitride," Journal of Applied Research and Technology, vol. 15, no. 6, pp. 624-632, 2017.

[50] I. Mahdavi, S. Firouzian, M. M. Paydar, and M. Saadat, "Simulated annealing and artificial immune system algorithms for cell formation with part family clustering," Journal of Industrial Engineering and Management Studies, vol. 7, no. 1, pp. 191-219, 2020.

Title: Investigation of Ricochet Angles for 5 mm Various Metal Plates with AP 7.62
Bullets

Authors: Ümit YILMAZ, Oktay KAYA, Mutlu Tarık ÇAKIR

Investigation of Ricochet Angles for 5 mm Various Metal Plates with AP 7.62 Bullets

Ümit YILMAZ*[1], Oktay KAYA[1], Mutlu Tarık ÇAKIR[1]

Abstract

In this study, the effect of a high-speed AP 7.62 bullet on Ti6Al4V, AISI 4340, Inconel-718, AlSi10Mg and Al 6061 - T6 materials at different impact angles were investigated by using the finite element package software LS-DYNA 971. AISI 4340 was taken as the bullet material and 850 m/s as a speed for high-speed ballistic investigation. Angle of the obliquity of the bullet against the plates has been taken in the range of 0-80º. Simulations were carried out at 5 degrees increments. It has been investigated that at what angle the bullet touches the materials, the bullet will ricochet. Also, deformations on plates have been examined. The results showed a good correlation with the literature. The lowest ricochet angle has been obtained in Inconel-718 as 20 º followed by AISI 4340 as 25º, Ti6Al4V as 55º, Al 6061 - T6 as 75º and lastly AlSi10Mg as 80 º.

Keywords: Ricochet, penetration angle, residual velocities, ballistic limit, oblique impact

1. INTRODUCTION

Aluminum alloys are frequently used in light armor applications in the defense industry due to their physical and mechanical characteristics, low density, high strength, and high energy absorption capacity [1]. Although the strength of aluminum is lower than steel, more strength can be obtained with dimensional changes in thickness or diameter compared to steel. Despite the growth in dimensions, the low density of aluminum, the total weight of these materials is lower than that of steel materials.

Aluminum and its alloys extensively have been investigated in the past studies for ballistic purposes. Bullet geometry, penetration angle, ballistic limit, and residual velocities are some of the research topics of armor applications. Bullet penetration angle is one of the most important parameters for the perforation of the armor. When the bullet reaches the critical obliquity angle, the bullet doesn't perforate the target, and it ricochets.

Özer et al. investigated the effects of thicknesses of Titanium, Ti6Al4V, and AISI 4340 materials against different bullet geometries. It was seen that the least deformation encountered in AISI 4340 [2].

Iqbal et al. [3] studied the effect of Blunt-nosed, Ogive-nosed, Hemispherical-nosed projectile on

* Corresponding author: uyilmaz@sivas.edu.tr
[1] Sivas University of Science and Technology, Faculty of Engineering and Natural Sciences, Department of Mechanical Enginerring
E-mail: okaya@sivas.edu.tr, tcakir@sivas.edu.tr
ORCID: https://orcid.org/0000-0001-8922-2387, https://orcid.org/0000-0003-4199-3128, https://orcid.org/0000-0002-0107-594X

the single and layered aluminum plate. They have found that aluminum plates for all different thicknesses have the highest ballistic resistance for Hemispherical-nosed projectile. In another study of Iqbal et al. [4], they have used ogive nosed projectile and 1100-H12 aluminum targets to examine the effect of penetration angle. They demonstrated that the ballistic limit of aluminum target increased with the increasing obliquity.

Piekutowski et al. [5] have used 6061-T651 aluminum plates and 4340 ogive-nose steel rods to perform perforation experiments. They have carried out normal and oblique impacts on plates to evaluate residual velocities and perforation. Finally, they came up with a perforation equation, which precisely estimates the ballistic limit and residual velocities. Gupta et al. [6] have examined the effects of the nose shape and velocity of the bullet and target thickness, blunt and hemispherical nose on bullet impact on aluminum plate. In addition, they demonstrated that hemispherical nose-shaped bullets had more ballistic limits than blunt. Zaid Mohammad et al. [7] presented the effect of the angle of obliquity on single layer and double layered 2 mm-thick 1100-H12 aluminum material, in both set-up, hemispheric nose have showed higher ballistic resistance. Corbett et al. [8] conducted experimental studies and revealed that low obliquity below 30° didn't affect the ballistic limits and behavior of the target. But obliquity greater than this value increased the ballistic limits, so the resistance of the target significantly increased.

Bhuarya et al. [9] studied the ballistic effect of bullet hitting on aluminum alloy with different angles and thicknesses. They have examined critical thickness and angle values for perforation, ricochet and embedment.

Børvik et al. [10] used different types of bullets to examine the effect of penetration to a 20 mm thick AA6082-T4 aluminum plate with different penetration angles. Hardcore bullets velocity drop doesn't affect penetration angle up to 30°. But soft-core bullets have a decreasing trend in velocity with increasing angle. Above 30° and below the 60° velocity drops were considerable. At 60° penetration, none of the bullets was able to penetrate the target plate. In literature, single-layer aluminum plates were found to be more resistant to bullet impact than layered aluminum plates. While thin plates (0,5 mm - 1.5 mm) are more resistant to the impact of blunt-nosed projectile, thick plates (2 mm - 3 mm) leaded to better resistance to the effect of ogive-nosed projectile [3, 11]. Similar studies have been conducted by Gupta et al. [12]. These studies demonstrated that for thin plates (0.5 mm - 1.5 mm), the most efficient penetrator was ogive nosed projectile. For thick plates (2 mm - 3 mm) blunt-nosed projectiles required the least energy to perforate the target plates.

Zhou et al. [13] studied the effects of obliquity and projectile shape on the ballistic limit of a single layer, double-layered, and sandwiched steel plates. Flat nosed projectile causes a higher ballistic limit on layered plates, however, when it comes to hemispherical nosed projectile no significant differences are observed on the ballistic limit. With increasing obliquity, firstly ballistic limit demonstrated a decrease and subsequently increasing tendency. For both projectile shapes and layer numbers, the lowest

Table 1

Johnson Cook Parameters of used materials in FEM analyze

JC parameters	Yield stress, A (MPa)	Strain hardening parameter, B (MPa)	Strain hardening exponent, n	Strain rate sensitivity parameter, C	Temperature exponent, m	D1	D2	D3	D4	D5
Al6061 T6	324	113.8	0.42	0.002	1,34	-0.77	1,5	-0.47	0	1,6
AlSi10Mg	167	396	0,551	0,001	0,859	0,047	1,155	-0,841	-0,042	0
Ti6Al4V	1000	331	0.34	0.012	0,8	-0.09	0.25	-0.5	0.014	3,9
4340 Steel	793	510	0.25	0.14	1,3	0,05	3,4	-2.12	0.002	0.61
Inconel-718	985	949	0.4	0.01	1,61	0.04	0.75	-1.45	0.04	0.89

ballistic limit was seen at penetration angles between 30º and 45º.

AlSi10Mg is manufacturable material in SLM. Its properties of lightweight and high energy absorbability per mass makes it researched. Kristoffersen et al. [14] investigated the ballistic limit of 5mm SLM manufactured AlSi10Mg plates. They use both experimental tests and numerical analyses. Nirmal at. Al.[15] found Johnson-Cook strength ad damage parameters via Split-Hopkinson pressure bar setup. Then, they use these parameters to investigate ballistic parameter of AlSi10Mg plates.

Israr ul Haq et al.[16] and Marcos Rodríguez-Millán et al. [17] investigated effects of the nose tip angle (geometry) of bullet which penetrate to Inconel-718 plate. They showed geometry affected the deformation mode of the Inconel-718 plate and ballistic limit significantly.

Borja Erice et al. [18]have researched effects of the temperature of Inconel-718 plate on ballistic performance when impacted by spherical projectiles. J. Michael Pereira [19] have researched the effects of the annealing and aging processes on the ballistic performance of the materials. Annealing and aging have yielded difference in strength and toughness which greatly influenced the ballistic performance.

In literature several research can be found related to ballistic research on Inconel-718. But there aren't enough researches to evaluate the ricochet angle for Inconel-718. In this research, we have aimed to investigate the ricochet angle of bullet penetrates to Inconel-718 plate with different angle and test result compared with common armor materials.

In this study, we aimed to investigate ricochet angle occurred in high-speed bullet penetration to different material in the oblique impact of AP 7.62 bullets. Additionally, additively manufactured AlSi10Mg and novel Inconel-718 nickel alloy's ballistic performance have been investigated and compared with the traditional ballistic materials, AISI 4340 as 25º, Ti6Al4V as 55º, Al 6061. We employed the finite element package software LS-DYNA 971. Plate thickness

and bullet velocity were kept as 5 mm and 850 m/s respectively in all test samples. The angle of obliquity was increased gradually with 5 degrees increments up to ricochet.

2. METHODOLOGY

Ballistic performance effect on bullet pitch angle, target plate thickness and target plate material were investigated. AP 7.62 bullet was chosen as a projectile and the initial velocity was 850 m/s. This velocity was chosen because it was the average velocity for AP 7.62 bullets [20]. The size of the target was 10cmx10cm in size, 5mm in thickness in Figure 1. Angle of obliquity was taken in the range 0-80 º.
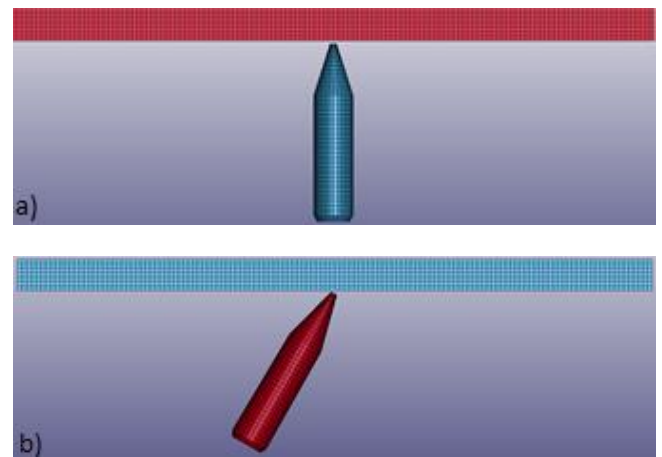

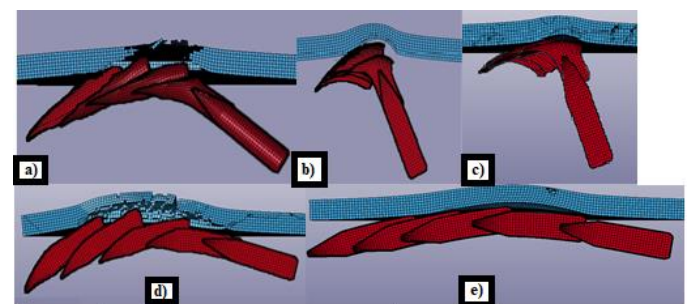Figure 1 Mesh of the bullet and target at different obliquity angles.

Figure 2 Ricochets of bullets for Ti6Al4V (a), AISI-4340 (b), and Inconel 718(c), Al 6061 - T6 (d), and AlSi10Mg (e) plates.

In this paper, ballistic numerical simulations were made in LS-DYNA 971 which is an explicit solver of the non-linear finite element method. Previous studies have shown that this program simulates ballistic performance very well [21,

22]. Johnson Cook Model (MAT_15) was used for strength and damage evolution for ductile materials. The eqs. (1)-(3) shows the fracture criteria, damage parameters and failure damage[15, 23, 24]. Johnson Cook (JC) model simulates a von Mises plasticity, initial yielding, linear elasticity, strain hardening, strain-rate hardening, damage evolution and fracture. This model predicts equivalent stress with using of temperature, strain rate and strain parameters:

$$\sigma(\varepsilon,\dot{\varepsilon},T) = [A + B\varepsilon^n]\left[1 + C\,ln\frac{\dot{\varepsilon}}{\varepsilon_{ref}}\right]\left[1 - \left(\frac{T-T_0}{T_m-T_0}\right)^m\right] \quad (1)$$

A, B, n, C and m are yield stress, strain hardening parameter, strain hardening exponent, strain rate sensitivity parameter and temperature exponent respectively. T_0, T_m are a reference and melting temperature. ε_ref is reference strain rate.

Fracture strain for Johnson-Cook Model depends on the stress triaxiality, strain rate and temperature:

$$\varepsilon_f(\sigma^*,\dot{\varepsilon},T) = [D_1 + D_2 e^{D_3\sigma^*}][1 + D_4 ln\dot{\varepsilon}]\left[1 + D_5\frac{T-T_0}{T_m-T_0}\right] \quad (2)$$

where D1 - D5 are fracture model constants of the Johnson-Cook model, σ^* is the stress triaxiality ratio.

Damage evolution keeps zero during elastic region. After some certain threshold of the accumulated plastic strain, damage evolves. The equation of Johnson Cook damage evolution is:

$$\dot{D} = \begin{cases} 0, & \varepsilon < p_d \\ \frac{D_c}{\varepsilon_f - p_d}\dot{\varepsilon}, & \varepsilon \geq p_d \end{cases} \quad (3)$$

Pd is the damage threshold, ε_f is fracture strain and Dc is the critical damage. When D reaches to 1 then the element is deleted and removed from calculation.

Johnson Cook parameters of AISI 4340-H steel alloy, Al6061-T6, Ti6Al4V, AlSi10Mg and Inconel-718 are Table 1. JC material parameters and Equation of State parameters are taken from these studies [25-32]. Materials assumed anisotropic. 3D cad model used for solid with full of hexagonal mesh.

Hourglass IHQ=5 and QH=0.1 is used for energy control. The plates are fixed from bottom edges. ERODING_SURFACE_TO_SURFACE eroding algorithm is used with 0.3 static friction and 0.2 dynamic friction and pinball segment-based contact (SOFT=2). Maximum mesh size 0.75mm is used and total number of elements is 180000.

3. RESULT AND DISCUSSION

When evaluating simulation results in Figure 3, bullet deformations were lowest for aluminum targets at each angle and bullet penetrates until ricochet angle. Also, the Von-Misses stresses on the plates were shown in the same figure. For steel and Inconel plates, they showed bulletproof at each angle. Steel and Inconel plates had better ballistic performance at the same volume in these material options. The ricochet angle of steel was found to be 25º and that of Inconel was 20º. Impact results and residual velocity were presented at Figure 3 and at Figure 4 respectively. With increasing bullet angle, deformation on target were decreased. Bullets deformation was the highest at steel plates followed by Inconel, titanium and aluminum alloys. For comparison, the normal impact, 15˚ and 30˚ were investigated for all materials, but the result of 15˚ for aluminum alloys weren't added to the figure; because aluminum alloys didn't show much difference in deformation between 0˚ and 30˚.

Titanium has higher yield strength than steel but steel has better ballistic performance because the first thing to check for ballistic performance is hardness[33] and density. Hardness is needed to deform the bullet; the kinetic energy of the bullet should be absorbed in deformation mechanisms and one of the deformation mechanisms is the deformation of the bullet that absorbs kinetic energy. Also, density has significant effect on deformation of bullets. Titanium has lower density and hardness value than Inconel and steel. Therefore, Inconel and steel are better bullet-proof materials in same volumes. Material strength affects ballistic performance after density and hardness.

For titanium plates, it has a higher ballistic limit and better ballistic performance against aluminum

alloys, however steel bullet still penetrates until the ricochet angle. In Figure 3, it is seen that some erosions on steel bullet. The bullet is stacked at 50º, but it has a residual velocity at 55º. Therefore, 55º is chosen for ricochet angle in this situation. When the residual velocities are examined, there is a continual decrease until 50º, residual velocity increases after that angle.

To compare residual velocities for different materials, Figure 4 (a) was presented below. In the figure, the highest residual velocities emerged in AlSi10Mg at ricochet angle. Kinetic energy greatly was absorbed by AISI 4340 and Inconel. This can be concluded that AlSi10Mg has lowest density and hardness values in this research.

According to G. Tiwari et al. 's study [34], ricochet angle is changing with the target thickness, target span, bullet nose geometry and bullet velocity. Because of the influence of so many parameters to ricochet angle, it is difficult to compare the results of different studies. In G. Tiwari's study, the ricochet angle is found around 60 degrees for 1mm 1100-H12 aluminum plates and at low velocities (less than 200 m/s) with ogive nosed bullet, which shows that our aluminum ricochet angle result is in accordance with the literature.
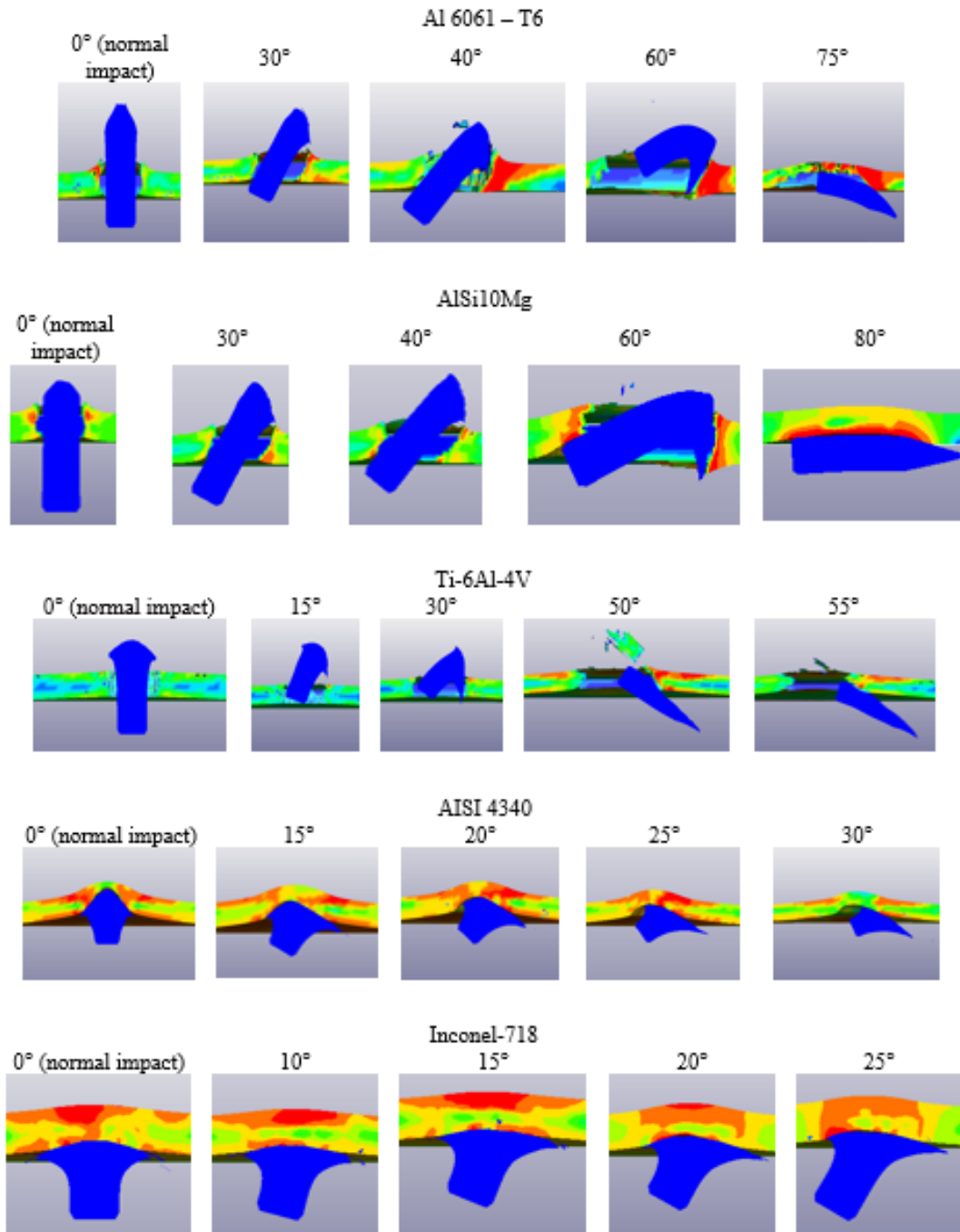
Figure 3 Impact results at different angles for different materials

Residual velocities of the bullets at different angles are presented in Figure 4 from (b) to (f). Looking at the test of aluminum alloy plates at different angles, there is a continuous decrease at residual velocity with increasing pitch angle until ricochet angles. At 75º for Al6061 and 80º for AlSi10Mg, it is seen that residual velocity is higher than 70º and 75º impacts, so 75º for Al6061 and 80º for AlSi10Mg are the ricochet angle for a 5 mm aluminum alloy plates. This high angle is reasonable because it sorts together with experimental ricochet tests. Aluminum is a soft material when compared to steel, therefore aluminum gets eroded easily. The density and hardness difference between AlSi10Mg and Al6061 are considerably low, the material strength and damage parameters taken literature; therefore, it is unclear whether the cause of the allistic difference is the alloy itself or the heat treatment difference. Aluminum also has the

lowest yield and tensile properties than steel and titanium have. In Figure 2, the bullet has ricocheted in steel without too much damage while aluminum deforms easily. Also, Al6061 has some cracks inside after impact.

It is concluded that the ricochet angle was increased with material hardness or density decreased with looking aluminum alloys, steel, Inconel and titanium plates. FEM JC material model was managed to catch the relations. Also, time interval 80 µs for simulation was sufficient converge to equilibrium.
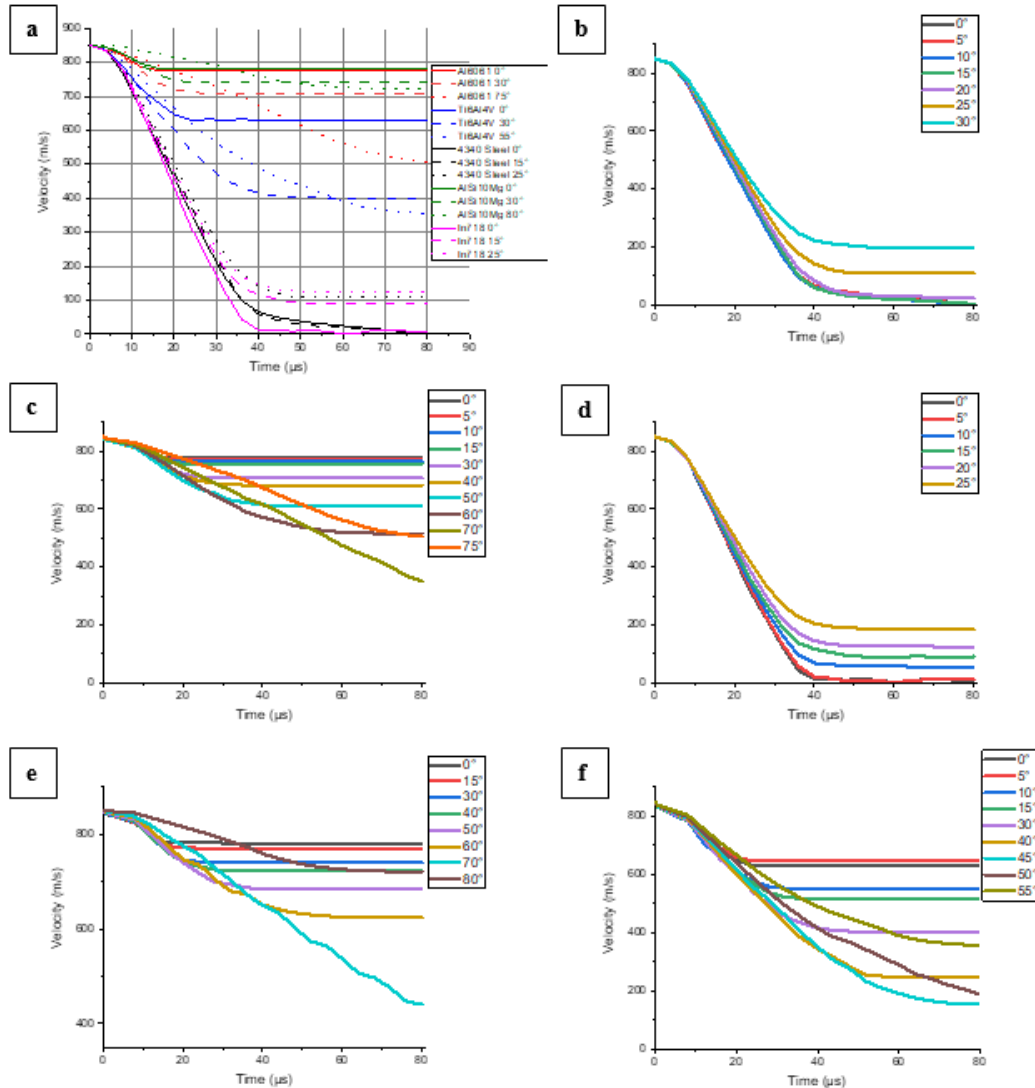

Figure 4 a) Comparision of the residual velocities with respect to time and materials and b), c), d), e), and f) residual velocities at different angles for AISI4340, Al6061, Inconel718 and AlSi10Mg and Ti6Al4V plates, respectively.

4. SUMMARY

In this article, during the bullet penetration to different materials, titanium, steel, Inconel, Al6061 and AlSi10Mg ricochet angles were investigated by using finite element package software LS-DYNA 971. Ricochet angles were found 20º for Inconel-718, 25º for AISI4340, 55º for Ti6Al4V, 75º for Al6061 and 80 º for AlSi10Mg. The ballistic performance of these materials is discussed. The results showed a good correlation with the literature.

The Declaration of Conflict of Interest/ Common Interest

No conflict of interest or common interest has been declared by the authors.

Authors' Contribution

The authors contributed equally to the study.

The Declaration of Ethics Committee Approval

This study does not require ethics committee permission or any special permission.

The Declaration of Research and Publication Ethics

The authors of the paper declare that they comply with the scientific, ethical and quotation rules of SAUJS in all processes of the paper and that they do not make any falsification on the data collected. In addition, they declare that Sakarya University Journal of Science and its editorial board have no responsibility for any ethical violations that may be encountered and that this study has not been evaluated in any academic publication environment other than Sakarya University Journal of Science.

REFERENCES

[1] M. Hakan, R. Güneş and M.K. Apalak, "Alüminyum Plakaların Balistik Performansının Araştırılması,", XIX. Ulusal Mekanik Kongresi, Trabzon, pp. 525-535, 2015.

[2] İ. Özer, M.G. Atahan and A. Yapıcı, "Balistik Çarpma Etkisinin Sonlu Elemanlar Yöntemiyle İncelenmesi," Selçuk Üniversitesi Mühendislik, Bilim ve Teknoloji Dergisi, vol. 1, no. 3, pp. 21-30, 2013.

[3] M. Iqbal and N. Gupta, "Ballistic limit of single and layered aluminium plates," Strain, vol. 47, pp. e205-e219, 2011.

[4] M. Iqbal, G. Gupta and N. Gupta, "3D numerical simulations of ductile targets subjected to oblique impact by sharp nosed projectiles," International Journal of Solids and Structures, vol. 47, no. 2, pp. 224-237, 2010.

[5] A. Piekutowski, et al., "Perforation of aluminum plates with ogive-nose steel rods at normal and oblique impacts," International Journal of Impact Engineering, vol. 18, no. 7-8, pp. 877-887, 1996.

[6] N. Gupta, M. Iqbal and G. Sekhon, "Experimental and numerical studies on the behavior of thin aluminum plates subjected to impact by blunt-and hemispherical-nosed projectiles," International Journal of Impact Engineering, vol. 32, no. 12, pp. 1921-1944, 2006.

[7] Z. Mohammad, P.K. Gupta, and A. Baqi, "Experimental and numerical investigations on the behavior of thin metallic plate targets subjected to ballistic impact," International Journal of Impact Engineering, vol. 146, p. 103717, 2020.

[8] G. Corbett, S. Reid and W. Johnson, "Impact loading of plates and shells by free-flying projectiles: a review," International Journal of Impact Engineering, vol. 18, no. 2, pp. 141-230, 1996.

[9] M.K. Bhuarya, M.S. Rajput and A. Gupta, "Finite element simulation of impact on metal plate," Procedia Eng, vol. 173, pp. 259-263, 2017.

[10] T. Børvik, et al., "Normal and oblique impact of small arms bullets on AA6082-T4 aluminium protective plates," International

Journal of Impact Engineering, vol. 38, no. 7, pp. 577-589, 2011.

[11] J. Radin and W. Goldsmith, "Normal projectile penetration and perforation of layered targets," International Journal of Impact Engineering, vol. 7, no. 2, pp. 229-259, 1988.

[12] N. Gupta, M. Iqbal and G. Sekhon, "Effect of projectile nose shape, impact velocity and target thickness on deformation behavior of aluminum plates," International Journal of Solids and Structures, vol. 44, no. 10, pp. 3411-3439, 2007.

[13] D. Zhou and W. Stronge, "Ballistic limit for oblique impact of thin sandwich panels and spaced plates," International journal of impact engineering, vol. 35, no. 11, pp. 1339-1354, 2008.

[14] M. Kristoffersen, et al., "On the ballistic perforation resistance of additive manufactured AlSi10Mg aluminium plates," International Journal of Impact Engineering, vol. 137, p. 103476, 2020.

[15] R. Nirmal, B. Patnaik and R. Jayaganthan, "FEM Simulation of High Speed Impact Behaviour of Additively Manufactured AlSi10Mg Alloy," Journal of Dynamic Behavior of Materials, vol. 7, pp. 469-489, 2021.

[16] I. ul Haq, et al., "Study of Various Conical Projectiles Penetration into Inconel-718 Target," Procedia Structural Integrity, vol. 13, pp. 1955-1960, 2018.

[17] M. Rodríguez-Millán, et al., "Experimental and numerical analysis of conical projectile impact on inconel 718 plates," Metals, vol. 9, no. 6, p. 638, 2019.

[18] B. Erice, M.J. Pérez-Martín and F. Gálvez, "An experimental and numerical study of ductile failure under quasi-static and impact loadings of Inconel 718 nickel-base superalloy," International Journal of Impact Engineering, vol. 69, pp. 11-24, 2014.

[19] J.M. Pereira and B.A. Lerch, "Effects of heat treatment on the ballistic impact properties of Inconel 718 for jet engine fan containment applications," International Journal of Impact Engineering, vol. 25, no. 8, pp. 715-733, 2001.

[20] M. Iqbal, et al., "Oblique impact on single, layered and spaced mild steel targets by 7.62 AP projectiles," International Journal of Impact Engineering, vol. 110, pp. 26-38, 2017.

[21] T. Børvik, O.S. Hopperstad and K.O. Pedersen, "Quasi-brittle fracture during structural impact of AA7075-T651 aluminium plates," International Journal of Impact Engineering, vol. 37, no. 5, pp. 537-551, 2020.

[22] H. Hafizoglu, N. Durlu and H.E. Konokman, "Effects of sintering temperature and Ni/Fe ratio on ballistic performance of tungsten heavy alloy fragments," International Journal of Refractory Metals and Hard Materials, vol. 81, pp. 155-166, 2019.

[23] LSTC, LS-DYNA, "Keyword User's Manual," vol. I, 2007.

[24] R. Scazzosi, M. Giglio and A. Manes, "Experimental and numerical investigation on the perforation resistance of double-layered metal shields under high-velocity impact of soft-core projectiles," Engineering Structures, vol. 228, p. 111467, 2021.

[25] L.E.Schwer and C. Windsor, "Aluminum plate perforation: a comparative case study using Lagrange with erosion, multi-material ALE, and smooth particle hydrodynamics," in 7th European LS-DYNA conference, 2009.

[26] A. Rashed, et al., "Investigation on high-velocity impact performance of multi-layered alumina ceramic armors with polymeric interlayers," Journal of

Composite Materials, vol. 50, no. 25, pp. 3561-3576, 2016.

[27] S. Akram, et al., "Numerical and experimental investigation of Johnson–Cook material models for aluminum (Al 6061-T6) alloy using orthogonal machining approach," Advances in Mechanical Engineering, vol. 10, no. 9, pp. 1-14, 2018.

[28] K. Gregory, "Failure modeling of titanium 6Al-4V and aluminum 2024-T3 with the Johnson-cook material model," US William J. Hughes Technical Center, Washington, 9, 2003.

[29] S. Shasthri and V. Kausalyah, "Effect of ballistic impact on Ti6Al-4V titanium alloy and 1070 carbon steel bi-layer armour panel," International Journal of Structural Integrity, vol. 11, no. 4, pp. 557-565, 2020.

[30] Y. Zhang, J. Outeiro and T. Mabrouki, "On the selection of Johnson-Cook constitutive model parameters for Ti-6Al-4 V using three types of numerical models of orthogonal cutting," Procedia Cirp, vol. 31, pp. 112-117, 2015.

[31] E. Segebade, et al., "Influence of anisotropy of additively manufactured AlSi10Mg parts on chip formation during orthogonal cutting," Procedia CIRP, vol. 82, pp. 113-118, 2019.

[32] Z. Hao, et al., "Study on constitutive model and deformation mechanism in high speed cutting Inconel718," Archives of Civil and Mechanical Engineering, vol. 19, no. 2, pp. 439-452, 2019.

[33] P.J. Hazell, "Armour: materials, theory, and design," CRC press., 2015.

[34] G. Tiwari, M.A. Iqbal and P.K. Gupta, "Impact Response of Thin Aluminium Plate with Varying Projectile Obliquity and Span Diameter," Iranian Journal of Science and Technology, Transactions of Mechanical Engineering, vol. 44, no. 1, pp. 93-102, 2020.

Title: Pd/BP2000 Nanocomposites: Efficient Catalyst for Hydrolytic Dehydrogenation of Ammonia-borane

Authors: Melike SEVİM

Pd/BP2000 Nanocomposites: Efficient Catalyst for Hydrolytic Dehydrogenation of Ammonia-borane

Melike SEVİM*[1]

Abstract

In current work, the activity of BP2000 supported Pd nanoparticles (NPs) were researched based on hydrolysis of ammonia borane (AB) reaction. Borane-tert-butylamine used for reduction of palladium (II) acetylacetonate for synthesize procedure of Pd NPs under mild conditions. As prepared Pd NPs were assembled on the BP2000, by liquid-phase self-assembly method. X-ray diffraction (XRD), transmission electron microscopy (TEM) and inductively coupled plasma-mass spectroscopy (ICP-MS) -advanced analytical techniques- were performed for detailed characterization. BP2000-supported Pd NPs were exhibited excellent activity and stability for the hydrolysis of AB. Pd/BP2000 nanocatalyst were showed the enhance catalytic activity that calculated turnover frequency (TOF) of 20.4 min^{-1}. The detailed report clarified the kinetics of Pd/BP2000 nanocatalyst parameters on catalyst amount, AB concentration, temperature and reusability. After the hydrolysis of AB with Pd/BP2000 nanocatalyst, activation energy of reaction was calculated to be 41.5 kJ mol^{-1}.

Keywords: Palladium, nanoparticles, BP2000, hydrogen, ammonia-borane.

1. INTRODUCTION

Energy consumption has been really high in these days because of ındustrial companies and human habits. Scientists focus on the new energy sources which contains less harmful poisoning-gas products. Hydrogen is still clean and safe energy source but transferring of hydrogen is still problem in an economic way. At this point, researchers ınterested in some compounds which has high hydrogen capacity. Formic acid [1], dimethlyamine borane [2-5], methlyamine borane [6] and ammonia-borane [7-10] are high hydrogen containing compounds. Ammonia-borane is well-known hydrogen carrier with the capacity of 19.6% hydrogen. When ıt is catalyzed by the convenient catalyst, ıt gives 3 moles of hydrogen [11]. (Eq1) It has unique specialties that non-poisining, high solubility, eco-friendly and good stability at room temperature [12].

$$NH_3BH_3(aq)+2H_2O(1)\rightarrow$$
$$NH_4BO_2(aq)+3H_2(g) \qquad (1)$$
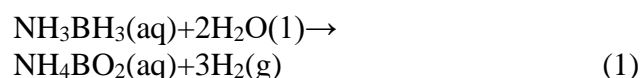
Up to now, many noble-metal catalysts, RuPd [13], Ru [14], Rh [15,16], Pt [17,18], RuRh [19] and Pd [20] nanoparticles were studied for hydrolysis of AB and showed high catalytic activity. Chen et al. [21] synthesized chitosan supported Pd nanocomposites with the range of 4-8 nm and showed good stability of chitosan structure onto the Pd nanoparticles for hydrolysis of AB with TOF value of 24.76 min^{-1}. Deka et al. [22] studied on carboxylic acid functionalized

* Corresponding author: melike.sevim@atauni.edu.tr
[1] Atatürk University, Faculty of Science, Department of Chemistry
ORCID: https://orcid.org/0000-0002-9410-0234

mesoporous organosilicas supported Pd nanoparticles or hydrolysis of AB and investigated the effect of carbocyclic acid groups. Pd nanoparticles are also catalyzed many important organic coupling reactions [23-25]. Sun et al. [26] synthesized Pd nanoparticles and supported on graphene oxide nanosheets and they worked on hydrogen generation from p-nitrophenol. The other support material is graphene hydrogel also active for hydrolysis of ammonia-borane. [27] Jia et al. also synthesized magnetic-graphene oxide Pd nanoparticles reusable and active catalyst for this reaction [28].

Inspired by these studies, this work focused on the cheaper and high surface area carbon materials which is called BP2000 commercial carbon. Firstly, Pd nanoparticles were synthesized under mild- conditions and supported onto the BP2000 surface by liquid-phase self-assembly method. Advanced analytical techniques were used for characterization for 3.5nm Pd/BP2000 nanocomposites.

2. EXPERIMENTAL

2.1. Materials and Methods

Oleylamine (OAm) (>70%), 1-octadecene (ODE, 90%), palladium (II) acetylacetonate (Pd(acac)$_2$, 99%), borane-tert-butylamine (BTB, 97%), hexane (99%), ethanol (99%), acetone (97%), were purchased from Sigma-Aldrich® and used as received. BP2000 carbon was received from Cabot.

2.2. Instrumentation

All transmission electron microscope (TEM) images were recorded by transmission electron microscope (TEM, Hitachi HT7700 with EXALENS, 120 kV) working at high-resolution (HR) mode with the magnification range of 10-800k. X-ray diffraction (XRD) patterns were recorded on a PANalytical Empyrean diffractometer with Cu-Kα radiation (40 kV, 15 mA, 1.54051 Å) over a 2θ range from 10º-90º at room temperature. Elemental analysis measurements were carried out by inductively coupled plasma-mass spectroscopy (ICP-MS,

Agilent Technologies 7700) after each sample was completely dissolved in aqua-regia (HCl/HNO$_3$: 3/1 vol. ratio).

2.3. Synthesis of Pd nanoparticles and supported onto the BP2000

Pd nanoparticles were synthesized under mild conditions with minör modifications [29]. In four-neckled reactor, Pd metal salt (100 mg) were disssolved in oleylamine (5 mL) and 1-octadecen (8 mL) in argon atmosphere and the second solution was prepered for the reduction of metal. Borane-tert-butylamine (173 mg) was dissolved in oleylamine (2 mL) and added to the first solution at 80˚C. Reaction mixture was raised up to 100˚C and mixed at this temperature for 1 hour. After reaction to get nanoparticles, reaction mixture was centrifuged with acetone and ethanol at 8500 rpm, 10 min, respectively. The colloidal nanoparticles was dispersed in hexane. 52 mg colloidal nanoparticles were founded after the centrifuge procedure. To support BP2000; 104 mg BP2000 was dissolved in an ethanol and sonicated half an hour. After that Pd nanoparticles was added by dropwise and sonicated 2 hours and then centrifuged at 7500 rpm, 10 min to remove the unsupported nanoparticles.

2.4. Hydrolytic dehydrogenation of Ammonia-borane catalyzed by Pd/BP2000 nanocomposites

For measuring of released hydrogen, there is set-up with water filled buret system for hydrogen production. In a typical set-up 10 mg catalyst is sonicated in 7 mL of water for 10 min. and 1mmol of AB is dissolved in 3 mL of water. The mechanism temperature is set up 25 ± 1˚C. Two necked-jacketed reaction tube set up and stirrer is arranged to 1000 rpm. After that AB solution is injected to the catalyst solution and the reaction is start-up. Hydrogen production is measured. The detailed reaction kinetics are research with the same hydrogen production set-up. Different temperature (293, 298, 303, 308 K), different AB amount (50, 100, 150, 200 mM) and different catalyst amount (2.5, 5, 7.5, 10mg) kinetics are studied keeping to stabile all of other parameters. For the last one, Durability of catalyst was tested.

20 mg catalyst was used for this experiment. After first cycle, the catalyst is centrifuged and washed then ıt is used for the second cycle. This procedure is done for five cycles.

3. RESULTS AND DISCUSSIONS

Monodisperse Pd nanoparticles were synthesized under mild conditions. OAm was used as surfactant, ODE was used as solvent and BTB was used as reducing agent ın this recipe. TEM images of colloidal nanoparticles were showed ın the Fig. 1. The homogenous dispersion and spherical shape of 3.5 nm of Pd nanoparticles can be seen ın the Fig. 1, Pd nanoparticles were also dispersed onto the BP2000 surface with sonication. (Fig 1. b)
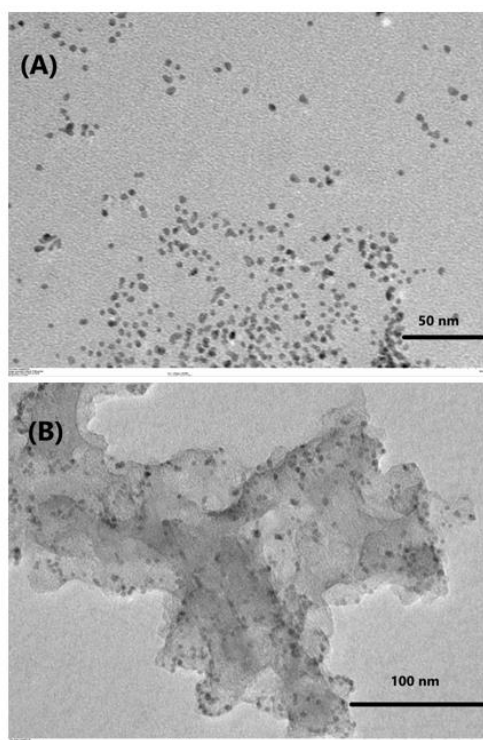

Figure 1 TEM images of a) colloidal Pd nanoparticles b) Pd/BP2000 nanocomposites.

XRD analyses of Pd/BP2000, (Fig. 2) ıt can be seen fcc-Pd(111) peak at 39.2º, the other characteristic peak of Pd 44.8º (200); 66.5 º (220); 80.04 º (311) (JCPDS card no 05-0681) [30] and observed peak at 21.5º corresponds to the BP2000. To find the metal ratio of composite, ICP-MS was performed for the nanocomposite and ıt was found 17.3% Pd.
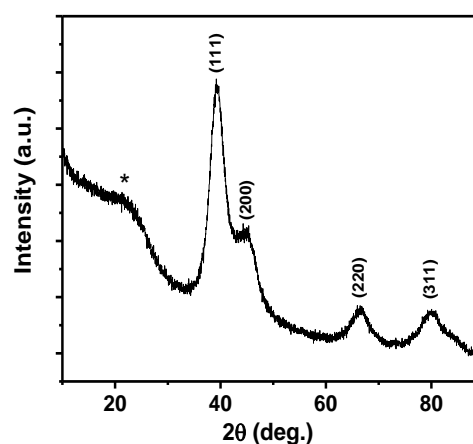
Figure 2 XRD patterns of Pd/BP2000 nanocomposites.

After detailed characterization of Pd/BP2000, the kinetics of hydrolytic dehydrogenation of AB was performed. The detailed report showed the kinetics of Pd/BP2000 nanocatalyst parameters on AB concentration, catalyst amount, temperature and reusability. Figure 3 shows the production of hydrogen versus to time plots during the hydrolysis of AB (100 mM) at different Pd/BP2000 nanocomposite amounts (2.5–10 mg,) at $25 \pm 1 ˚C$, 1mmol AB. According to the results, when amount of catalyst was increase, hydrogen production rate was also increased. In Fig. 3, linear curves were used as reference for calculating of reaction rate for each nanocatalyst concentrations. The linear increase is can be seen from Fig. 4 between the reaction rate and Pd/BP2000 concentration. $\ln[rate] = 0.66634\ln[Pd] + 3.52148$ equation was calculated. From the linear graph (slope of this line 0.66) the hydrogen releases to the first rate law according to the catalyst concentration.

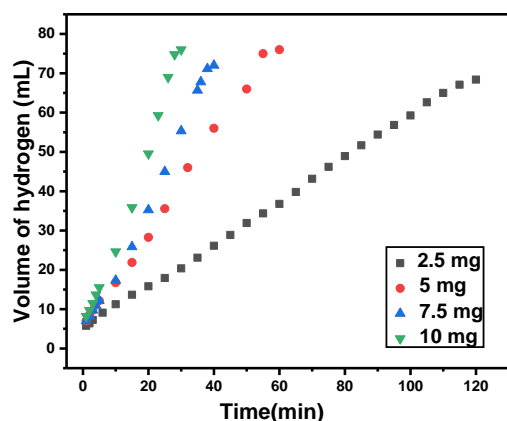Figure 3 Hydrogen gas generation versus time throughout the hydrolysis of AB by Pd/BP2000 nanocomposites at different amount.

Figure 5 Hydrogen gas generation versus time throughout the hydrolysis of AB by Pd/BP2000 nanocomposites at different amount of AB.
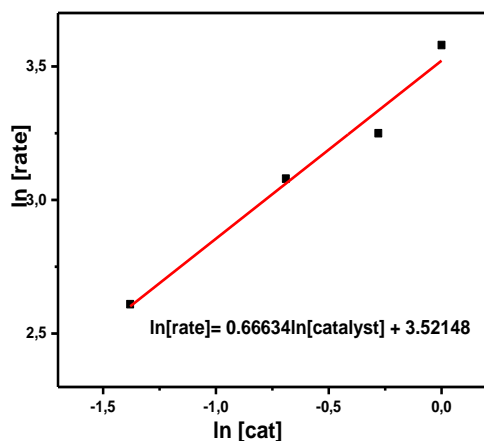
Figure 4 Logarithmic plots of H_2 generation rate versus catalyst concentrations

Figure 6 Logarithmic plots of H_2 generation rate versus AB concentrations.

In the Fig. 5, 10 mg catalyst was performed versus AB concentration was changed between 50-200 mM and hydrogen released at room temperature. The amount of produced hydrogen gas versus to time for each concentration was plotted. The reaction equation was found as ln[rate] = -0.00431ln[AB] + 2.63528. According to this equation, hydrogen was produced zeroth order kinetic rule versus to the concentration of AB in assisting of Pd/BP2000 catalyst.

The other kinetic study was performed for different temperature (293-308 K), 1 mmol AB and 10 mg of catalyst. According to the Fig 7, When the temperature is increased, hydrogen releasing rate is increased and ıt is compatible with molecular kinetic energy laws. The resulted values were plotted against 1/T, and the Arrhenius plot y = −5066.87x + 19.8648 given in Figure 8 was plotted. Activation energy of reaction was calculated to be 41.5 kJ mol^{-1}. Arrhenius equation is given below.

$$k = Ae-\frac{Ea}{RT} \qquad (1)$$
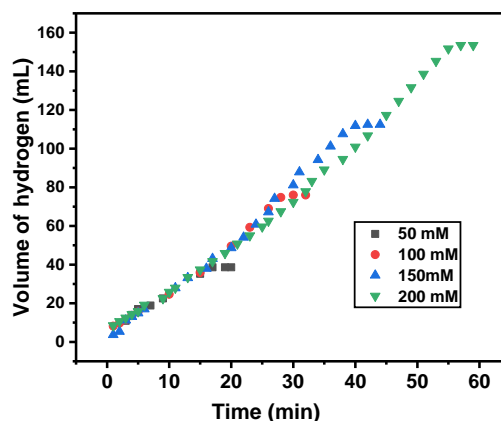
$$lnk = -\frac{Ea}{RT} + ln\ A \qquad (2)$$
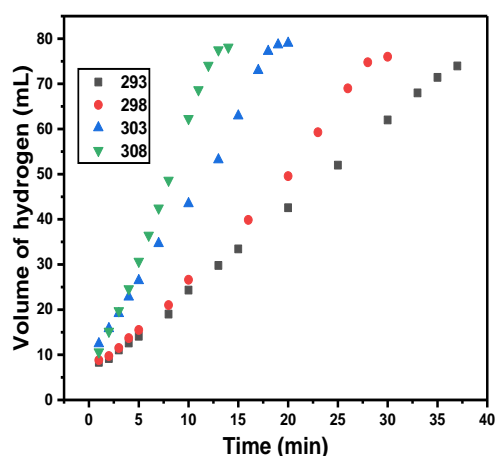
Figure 7 Hydrogen gas generation versus time throughout the hydrolysis of AB by Pd/BP2000 nanocomposites at different temperutares.
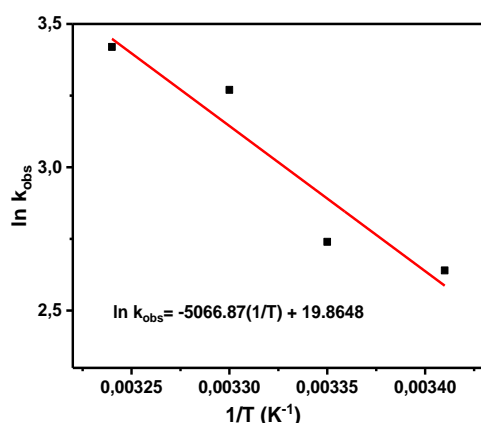
Figure 8 Arrhenius plot of ln k_{obs} versus 1/T.

After the detailed kinetic reactions of catalyst, the stability of catalyst was performed during the five hydrolysis cycle. In the Fig. 9, ıt can be seen that activity of catalyst was not decreased too much with the advantage of using commercial BP2000 carbon. It is still an efficient catalyst for hydrolysis of AB. The morphology and homogeneous dispersion of the catalyst are still the same (Fig 9, inset). It is stable and excellent catalyst for the hydrolysis of AB.
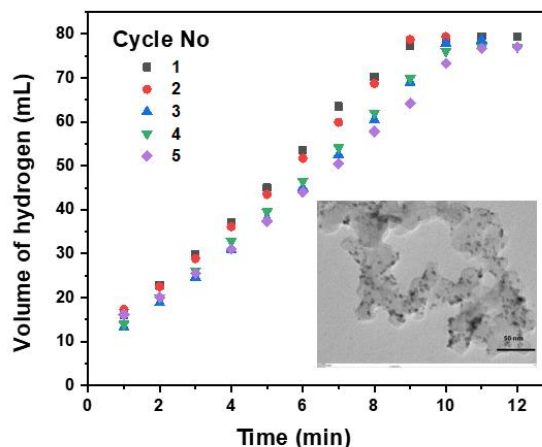
Figure 9 The five cycle hydrolysis of Pd/BP2000 nanocatalyst. inset: TEM image of the catalyst after five cycle.

4.CONCLUSIONS

In summary, monodisperse Pd nanoparticles were synthesized with stabilizers and reducing agent under mild conditions and they were assembled on BP2000 surface. After detailed characterization of Pd/BP2000 nanocatalyst was performed for hydrolytic dehydrogenation of AB. It shows high performance, 20.4 min^{-1} high TOF value and recyclability for the hydrolysis of AB.

The Declaration of Conflict of Interest/ Common Interest

No conflict of interest or common interest has been declared by the authors.

The Declaration of Ethics Committee Approval

The author declares that this document does not

require an ethics committee approval or any special permission

The Declaration of Research and Publication Ethics

The authors of the paper declare that they comply with the scientific, ethical and quotation rules of SAUJS in all processes of the paper and that they do not make any falsification on the data collected. In addition, they declare that Sakarya University Journal of Science and its editorial board have no responsibility for any ethical violations that may be encountered, and that this study has not been evaluated in any academic publication environment other than Sakarya University Journal of Science.

REFERENCES

[1]   M. Grasemann and G. Laurenczy, "Formic acid as a hydrogen source–recent developments and future trends," Energy & Environmental Science, vol. 5, no. 8, pp. 8171-8181, 2012.

[2]   Y. Chen, J. L. Fulton, J. C. Linehan, and T. Autrey, "In situ XAFS and NMR study of rhodium-catalyzed dehydrogenation of dimethylamine borane," Journal of the American Chemical Society, vol.127, no.10 pp. 3254-3255, 2005.

[3]   Z. Wen, Q. Fu, J. Wu, G. Fan, "Ultrafine Pd Nanoparticles Supported on Soft Nitriding Porous Carbon for Hydrogen Production from Hydrolytic Dehydrogenation of Dimethyl Amine-Borane," Nanomaterials, vol.10, no.8 pp.1612, 2020.

[4]   S. Karaboga, S. Özkar, "Ceria supported ruthenium nanoparticles: Remarkable catalyst for H_2 evolution from dimethylamine borane," International Journal of Hydrogen Energy, vol.44, no.48 pp.26296-26307, 2020.

[5]   L. L. Al-mahamad, "Gold nanoparticles as a catalyst for dehydrogenation reaction of dimethylamine borane at room temperature, "International Journal of Hydrogen Energy, vol.45, no.21, pp.11916-11922, 2020.

[6]   N. Cao, J. Su, W. Luo, and G. Cheng, "Hydrolytic dehydrogenation of ammonia borane and methylamine borane catalyzed by graphene supported Ru@ Ni core–shell nanoparticles," International journal of hydrogen energy, vol. 39, no.1, pp. 426-435, 2014.

[7]   M. C. Denney, V. Pons, T. J. Hebden, D. M. Heinekey, and K. I. Goldberg, "Efficient catalysis of ammonia borane dehydrogenation," Journal of the American Chemical Society, vol. 128, no. 37, pp. 12048-12049, 2006.

[8]   A. Al-Kukhun, H. T. Hwang, and A. Varma, "Mechanistic studies of ammonia borane dehydrogenation," International journal of hydrogen energy, vol. 38, no. 1, pp. 169-179, 2013.

[9]   O. Metin, V. Mazumder, S. Ozkar, and S. Sun, "Monodisperse nickel nanoparticles and their catalysis in hydrolytic dehydrogenation of ammonia borane, "Journal of the American Chemical Society, vol. 132, no. 5, pp. 1468-1469, 2010.

[10]   W. W. Zhan, Q. L. Zhu, and Q. Xu, "Dehydrogenation of ammonia borane by metal nanoparticle catalysts," Acs Catalysis, vol. 6, no. 10, pp. 6892-6905, 2016.

[11]   M. Chandra, and Q. Xu, "A high-performance hydrogen generation system: Transition metal-catalyzed dissociation and hydrolysis of ammonia–borane," Journal of Power Sources, vol. 156, no. 2, pp. 190-194, 2006.

[12]   M. Chandra, and Q. Xu, "Room temperature hydrogen generation from aqueous ammonia-borane using noble metal nano-clusters as highly active catalysts," Journal of Power Sources, vol. 168, no. 1, pp.135-142, 2007.

[13]   Y. T. Li, X. L. Zhang, Z. K. Peng, P. Liu, and X. C. Zheng, "Highly efficient hydrolysis of ammonia borane using ultrafine bimetallic RuPd nanoalloys

encapsulated in porous g-C$_3$N$_4$, '' Fuel, vol. 277, no.1 pp. 118243, 2020.

[14] C. Du, Q. Ao, N. Cao, L. Yang, W. Luo, and G. Cheng, "Facile synthesis of monodisperse ruthenium nanoparticles supported on graphene for hydrogen generation from hydrolysis of ammonia borane,'' International Journal of Hydrogen Energy, vol. 40, no. 18, pp. 6180-6187, 2015.

[15] S. Akbayrak, Y. Tonbul, and S. Özkar, "Ceria supported rhodium nanoparticles: superb catalytic activity in hydrogen generation from the hydrolysis of ammonia borane,''Applied Catalysis B: Environmental, vol. 198, pp. 162-170, 2016.

[16] F. Zhong, Q. Wang, C. Xu, Y. Wang, B. Xu, Y. Zhang, and G. Fan, "Catalytically active rhodium nanoparticles stabilized by nitrogen doped carbon for the hydrolysis of ammonia borane,'' International Journal of Hydrogen Energy, vol. 43, no. 49, pp. 22273-22280, 2018.

[17] M. Yuan, Z. Cui, J. Yang, X. Cui, M. Tian, D. Xu, Z. Dong, "Ultrafine platinum nanoparticles modified on cotton derived carbon fibers as a highly efficient catalyst for hydrogen evolution from ammonia borane,'' International Journal of Hydrogen Energy, vol. 42, no.49, pp.29244-29253, 2017.

[18] S. Akbayrak, and S. Özkar, "Cobalt ferrite supported platinum nanoparticles: Superb catalytic activity and outstanding reusability in hydrogen generation from the hydrolysis of ammonia borane,'' Journal of Colloid and Interface Science, vol. 596, pp.100-107, 2021.

[19] M. Rakap, "PVP-stabilized Ru–Rh nanoparticles as highly efficient catalysts for hydrogen generation from hydrolysis of ammonia borane,'' Journal of Alloys and Compounds, vol. 649, pp. 1025-1030, 2015.

[20] N. Tunç, B. Abay, and Rakap, M. "Hydrogen generation from hydrolytic dehydrogenation of hydrazine borane by poly (N-vinyl-2-pyrrolidone)-stabilized palladium nanoparticles,'' Journal of Power Sources, vol. 299, pp. 403-407, 2015.

[21] X. Chen, X. J. Xu, X. C. Zheng, X. X. Guan, and P. Liu, "Chitosan supported palladium nanoparticles: The novel catalysts for hydrogen generation from hydrolysis of ammonia borane,'' Materials Research Bulletin, vol.103, pp. 89-95, 2018.

[22] J. R. Deka, D. Saikia, P. H. Chen, K. T. Chen H. M. Kao, and Y. C. Yang, "Palladium nanoparticles encapsulated in carboxylic acid functionalized periodic mesoporous organosilicas as efficient and reusable heterogeneous catalysts for hydrogen generation from ammonia borane,'' Materials Research Bulletin, vol. 125, pp. 110786, 2020.

[23] A. Balanta, C. Godard, C. Claver, "Pd nanoparticles for C–C coupling reactions,'' Chemical Society Reviews, vol. 40, no.10, pp.4973-4985, 2011.

[24] M. T. Reetz, E. Westermann, "Phosphane-free palladium-catalyzed coupling reactions: the decisive role of Pd nanoparticles,'' Angewandte Chemie International Edition, vol.39, no.1, pp.165-168, 2000.

[25] Z. Zhang, Z. Wang, "Diatomite-supported Pd nanoparticles: an efficient catalyst for Heck and Suzuki reactions,'' The Journal of organic chemistry, vol. 71, no.19, pp.7485-7487, 2006.

[26] W. Sun, X. Lu, Y. Tong, Z. Zhang, J. Lei, G. Nie, and C. Wang, "Fabrication of highly dispersed palladium/graphene oxide nanocomposites and their catalytic properties for efficient hydrogenation of p-nitrophenol and hydrogen generation,'' International journal of hydrogen energy, vol. 39, no. 17, pp. 9080-9086, 2014.

[27] X. K. Tian, C. Yang, Z. X. Zhou, X. W. Liu, and Y. Li, "Active 3D Pd/graphene aerogel catalyst for hydrogen generation from the hydrolysis of ammonia-borane,'' International Journal of Hydrogen Energy, vol. 41, no. 34, pp. 15225-15235, 2016.

[28] H. Jia, Y. Zhu, X. Song, X. Zheng, and P. Liu, "Magnetic graphene oxide-ionic liquid grafted chitosan composites anchored Pd (0) nanoparticles: A robust heterogeneous catalyst with enhanced activity and superior reusability for hydrogen generation from ammonia borane,'' International Journal of Hydrogen Energy, vol. 43, no. 43, pp. 19939-19946, 2018.

[29] V. Mazumder, and S. Sun, "Oleylamine-mediated synthesis of Pd nanoparticles for catalytic formic acid oxidation,'' Journal of the American Chemical Society, vol. 131, no. 13, pp. 4588-4589, 2009.

[30] M. Celebi, K. Karakas, I. E. Ertas, M. Kaya, and M. Zahmakiran, "Palladium nanoparticles decorated graphene oxide: active and reusable nanocatalyst for the catalytic reduction of hexavalent chromium (VI),'' ChemistrySelect, vol. 2, no. 27, pp. 8312-8319, 2017.

Title: Investigation of the Efficiency of Ultra High Range Water Reducing Admixture in Roller Compacted Concrete Production

Authors: İsmail KILIÇ, Saadet Gökçe GÖK

Investigation of the Efficiency of Ultra High Range Water Reducing Admixture in Roller Compacted Concrete Production

İsmail KILIÇ*[1], Saadet Gökçe GÖK[1]

Abstract

In this study, roller compacted concretes were produced by using polycarboxylate-based third generation high-performance mortar and concrete admixture, which provides ultra-high range water reduction and long workability time. In roller compacted concrete production, the chemical admixture dosage was 1%, which was the maximum dosage recommended by the manufacturer, and the amount of water used was reduced by 10, 20, 30 and 40% compared to the concrete produced without the use of concrete admixture. The physical and mechanical properties of the roller compacted concrete specimens were investigated. When the ultra-high range water reducer was used as 1% of the cement weight in the production of roller compacted concrete, optimum values in terms of unit weight, compressive strength, water absorption, ultrasonic pulse velocity and dynamic modulus of elasticity were obtained by reducing the mixing water by 10%. Although the water/cement ratio decreased, further reduction in water amount resulted in a decrease in compressive strength and affected the concrete quality negatively.

Keywords: Compactibility, chemical admixture, compressive strength, roller compacted concrete, water reducer.

1. INTRODUCTION

Mechanical properties of roller compacted concrete (RCC) are affected by water/binder ratio, cement content, mineral admixture and aggregate composition, as in conventional concretes [1, 2]. Roller compacted concretes are dry mixtures compared to ordinary Portland cement concretes and need to be compacted in order to reach their final shape, a proper consistency must be provided in these concretes so that the vibrating compaction hammer is not damaged and the compression energy can be reduced [3]. Although chemical admixtures used in conventional concrete production can also be used in roller compacted concretes, working with a much drier consistency in RCCs creates differences in the properties of fresh concrete and the admixture dosage may need to be changed to achieve the desired concrete properties. Workability of concrete is considered to consist of cohesion, compactibility, resistance to segregation, workability retention, water reduction and consistency; the improvement in workability for a particular mixture varies depending on the internal friction angle, the amount of air in the concrete, the type of admixture and its dosage, as well as these components [4, 5]. Roller compacted

* Corresponding author: ismail.kilic@klu.edu.tr
[1] Kırklareli University, Faculty of Engineering, Department of Civil Engineering
E-mail: saadet.gokce.gok@hotmail.com
ORCID: https://orcid.org/0000-0001-5556-512X, https://orcid.org/0000-0002-7879-1610

concretes exhibit abnormal behavior in terms of mechanical strength, as indicated by deviations from Abrams' law, and it is argued that the water/binder ratio is not a comprehensive parameter to explain the overall concrete behavior and trends [5].

Various mineral admixtures such as fly ash, silica fume, rice husk ash can be used in roller compacted concrete, as well as chemical admixtures such as plasticizers, set accelerators and retarders [6-12]. According to the Concrete Roads Technical Specification [13], air-entraining, water-reducing, high-range water-reducing, set retarding chemical admixtures and concrete admixtures that provide long workability time are used in production of concrete pavements, these chemical admixtures used to improve concrete properties must comply with TS EN 934-1 [14] and TS EN 934-2 [15] standards. Although production with admixtures is not required in roller compacted concrete applications, the use of admixtures is preferred to improve the properties of fresh and/or hardened concrete [16].

Hazaree [5] aimed to explain the roles of different chemical admixtures in affecting the workability and strength performances of RCC, and found that the amount of air in the concrete played a decisive role in affecting the concrete performance. In his experimental study, it was also stated that the compactibility was effective on the concrete strengths and higher dosages of admixtures were needed in roller compacted concrete production [5].

In roller compacted concretes, water-reducing admixtures are used to increase the consistency, decrease the water/cement ratio and increase the concrete strength by easing the dispersion of the cement paste [17]. The increases in compressive strength seen in these concretes with the addition of superplasticizers are due to the uniform distribution of the cement paste, it provides better compaction and reduces the voids in hardened concrete [18]. On the other hand, excessive use of superplasticizers causes the presence of excess water, this water fills the pore volume, and then leaves voids in the hardened RCC matrix by drying, so microcracks develop in the concrete

during loading, premature fracture occurs and bending strength reduces [18]. Generally, the use of plasticizers in roller compacted concrete creates a denser concrete structure, decreases the concrete porosity, and increases the thermal conductivity [12].

An important body of knowledge has been added about the use of chemical admixtures in roller compacted concretes, and atypical behaviors in influencing fresh and hardened concrete properties have been explained by presenting plausible mechanisms for binder-admixture interactions [5]. However, more research is needed on this subject, as roller compacted concrete is a newer building material than conventional concrete. Hazaree et al. [4] tested the ten most commonly used chemical admixtures in a typical roller compacted concrete mixture, and observed that each individual mixture provides different benefits and improves different properties of fresh RCC, including changing the setting and finishing properties. They presented a series of recommendations as well as some precautions to be taken in separate use [4].

Nero [19] investigated the effects of the use of superplasticizer and air-entraining admixtures in roller compacted concrete. The use of several different chemical admixtures without evaluating the dosage and quality of chemical admixtures can cause various problems in concrete, some admixtures may not be suitable for use in RCC production, so the components to be used in concrete should be carefully designed and investigated [20]. On the other hand, it should be taken into account that differences between field conditions and laboratory conditions may affect the properties of roller compacted concrete.

In this study, roller compacted concrete with a cement content of 300 kg/m^3 was produced. In production of roller compacted concrete, a third generation high performance mortar and concrete admixture, which provides ultra-high water reduction and long workability in conventional concrete, was used. The chemical admixture was used at the maximum dosage recommended by the manufacturer, as 1% of the cement weight, and the amount of water used in the production of roller compacted concrete was reduced by 10, 20,

30 and 40% compared to the concrete produced without the use of admixtures. With the use of chemical additives, it was aimed to reduce the porosity of RCC and to increase the unit weight and compressive strength values. Unit weight, ultrasonic pulse velocity, dynamic modulus of elasticity, water absorption and compressive strength of the roller compacted concretes were determined.

2. MATERIALS AND METHODS

In roller compacted concrete production, Kırklareli tap water, crushed stone II, crushed stone I, stone dust, natural sand and as the binder CEM I 42.5 R Portland cement were used. The TS EN 1097-6 [21] standard was used to determine the specific gravity of aggregates. The specific gravity of dolomite origin crushed stone II, crushed stone I and stone dust was 2.80, the specific gravity of sand was 2.75 and the specific gravity of cement used was 3.12. Sieve analysis of aggregates was made in accordance with TS EN 933-1 [22] and was given in Table 1. Polycarboxylate-based high range water-reducing chemical admixture was used as 1% of the cement weight and different mixtures were prepared by reducing the amount of water by 10, 20, 30, 40%. The produced mixtures were designed to have a dry consistency as shown in the Figure 1 and a zero slump value.

Figure 1 Consistency of RCC mixture

Table 1 Sieve analysis

Percentage Passing					
Sieve Size (mm)	Crushed Stone II (20%)	Crushed Stone I (35%)	Stone Dust (15%)	Natural Sand (30%)	Mixture (100%)
22.5	100.00	100.00	100.00	100.00	100.00
16.0	47.12	100.00	100.00	100.00	86.78
12.5	0.00	94.32	100.00	100.00	73.58
9.5	0.00	79.29	100.00	100.00	69.82
4.0	0.00	9.16	91.73	97.20	49.52
2.0	0.00	0.00	87.45	93.62	45.27
1.0	0.00	0.00	54.44	83.95	34.60
0.5	0.00	0.00	28.21	52.68	20.22
0.25	0.00	0.00	16.06	30.19	11.56
0.125	0.00	0.00	8.03	3.68	2.93
0.075	0.00	0.00	4.32	1.24	1.39

The properties of the ultra-high range water-reducing chemical admixture were given in Table 2.

Table 2 The properties of the chemical admixture [23]

	Property
Appearance/colour	Light brown liquid
Chemical base	Modified polycarboxylate based polymer
Density	1.10±0.02 kg/l at 20°C
pH	3–7
Freezing point	-10°C
Soluble Cl content	Max 0.1%, does not contain Cl (TS EN 934-2)

The material amounts in one cubic meter of roller compacted concrete mixes were given in Table 3. The concrete mix design was made considering the surface dry water-saturated state of the aggregates. The total aggregate mixture consists of 20% crushed stone II, 35% crushed stone I, 15% stone dust and 30% natural sand by weight.

The production of roller compacted concrete specimens was carried out in accordance with the ASTM C1435 [24] standard as shown in the Figure 3. The compaction process was done by using specially produced heads that are compatible with the mold shape. Standard cube specimens were compacted in a monolayer for 15 seconds. Since cold joint formation was encountered in the compaction operations that was performed in more than one layers, compaction in a single layer has been preferred.

İsmail KILIÇ, Saadet Gökçe GÖK

Investigation of the Efficiency of Ultra High Range Water Reducing Admixture in Roller Compacted Conc...

Table 3 The material amounts in one cubic meter of roller compacted concrete mixes

Concrete Code	Water Reduction (%)	Water/Cement	Water (kg)	Cement (kg)	Natural Sand (kg)	Stone Dust (kg)	Crushed Stone I (kg)	Crushed Stone II (kg)	Chemical Admixture (kg)
K0	0	0,34	102	300	661	337	785	449	-
K10	10	0,30	88,8	300	670	341	795	454	3
K20	20	0,26	78,6	300	678	345	805	460	3
K30	30	0,23	68,4	300	686	349	815	466	3
K40	40	0,19	58,2	300	695	354	825	472	3

When calculating the percentage of compactibility in the specimens, firstly, cube molds of 15 cm×15 cm×15 cm were filled with RCC mixture up to the upper level, compacted for 15 seconds after leveling, and the gap depth formed at the end of compaction was measured from the middle points of the four edges of the mold. After measuring from four points, the arithmetic averages of these values were taken, and the percentage of compactibility of the RCC specimen was determined by proportioning the determined average value to the inner edge length of the cube mold. The percentage of compactibility has been calculated by considering the Figure 2 and Equation (1) given below, assuming that it can give information about the consistency of the RCC mixtures produced using a vibratory hammer.
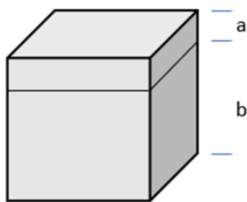
Figure 2 Measured lengths

$$S = \frac{a \times 100}{(a+b)} \qquad (1)$$

S= Percentage of compactibility (%)

a= Compaction (mm)

b= Height of the compracted specimen after the mold is filled and leveled (mm)

Figure 3 RCC production

RCC specimens shown in Figure 4 were demolded one day after the production and kept in the curing pool in lime-saturated water until the testing time.

Figure 4 RCC specimens

In determining the compressive strength of roller compacted concretes, 3 and 28-day specimens were tested according to the TS EN 12390-3 [25] standard. Three specimens were tested for each experimental group and average values were

İsmail KILIÇ, Saadet Gökçe GÖK

Investigation of the Efficiency of Ultra High Range Water Reducing Admixture in Roller Compacted Conc...

determined. The loading rate was taken as 0.602 MPa/s.

Total water absorption percentages of roller compacted concrete specimens at the age of 28 days were determined according to EN 772-11 [26] standard. The weights of the roller compacted concrete specimens, which were dried in a drying-oven for 48 hours and reached a constant weight, were recorded, then these specimens were kept in water for 24 hours and water absorption percentages were calculated.

Ultrasonic pulse velocity of specimens at the age of 28 days were measured in accordance with ASTM C597 [27] standard and dynamic modulus of elasticity of RCC were determined. Proceq brand Pundit PL-200 ultrasonic test device was used to obtain ultrasonic pulse velocity and dynamic modulus of elasticity. For these experiments, 28-d cube RCC specimens with a size of 15 cm×15 cm×15 cm were used. While presenting the experimental findings, three specimens from each series were tested and average values were given.

3. RESULTS AND DISCUSSION

Average compactibility percentages of roller compacted concrete specimens were given in Table 4. As the amount of water was reduced up to 30%, the compactibility percentage decreased in roller compacted concrete, while the compactibility percentage increased slightly when the reduction of water was changed from 30% to 40%. The compactibility percentage decreased by 8.21%, 29.67%, 50.54% and 46.19% in the K10, K20, K30 and K40 specimens, respectively, compared to the reference specimen.

Table 4 Compactibility percentages

Concrete Code	Compactibility Percentage (%)
K0	10.11
K10	9.28
K20	7.11
K30	5.00
K40	5.44

The 3 and 28-day compressive strengths of standard cube RCC specimens were given in Table 5.

Table 5 Compressive strengths (MPa)

Concrete Code	3-d	28-d
K0	26.8	29.9
K10	33.3	39.8
K20	25.5	31.6
K30	13.6	21.6
K40	11.3	12.6

When the 3-d concrete compressive strengths were examined, it was seen that the optimum design was K10 mixture. It can be expected that the compressive strength of concrete will increase as the water/cement ratio decreases, but roller compacted concretes are mixtures with a rather dry consistency compared to normal concrete, and the slump value of the produced concretes was zero. Reducing the mixing water too much makes dissolution of chemical admixture difficult and prevents the distribution of plasticizer properly in concrete, and the chemical admixture cannot show the expected performance when the amount of mixing water reduced more than a certain value.

While the admixture used can provide water reduction of up to 30% in conventional concrete, it has been observed that water reduction of more than 10% in roller compacted concrete causes a decrease in compressive strength due to problems in workability and compaction. A 10% reduction in water content, which makes a decrease in water/binder ratio, provided a 24% increase in compressive strength compared to the reference concrete in 3-d specimens. Reducing the mixing water by 20% caused a 5% decrease in the 3-d compressive strength, while reducing the water amount by 30% decreased the compressive strength by 49%. Reducing the mixing water by 40% in the roller compacted concrete mixture caused the 3-d concrete compressive strength to be 58% lower than the reference concrete.

When the 28-day concrete compressive strengths were examined, it was seen that the highest values were obtained with the K10 specimen. By reducing the mixing water by 10%, the 28-d compressive strength has increased by 33%

İsmail KILIÇ, Saadet Gökçe GÖK

Investigation of the Efficiency of Ultra High Range Water Reducing Admixture in Roller Compacted Conc...

compared to the reference concrete. When the amount of water was reduced by 20%, this increase was limited to 6%, while further reduction of the amount of water caused a decrement in the compressive strength of concrete. When the water amount was reduced by 30%, the 28-d compressive strength of the concrete decreased by 28%, and when the water amount was reduced by 40%, the strength decreased by 58%. Here, the hyper plasticizer admixture, which was suitable for conventional concrete production, did not work effectively in RCC mixtures where the amount of water was very low, compressive strengths decreased in contrast to the expected outcome related to the decrease in water/binder ratio. Even if the ultra-high range water reducer was used, reducing the amount of water by more than 10% adversely affected the mechanical properties. After compaction process, the amount of voids in concrete and the porosity of RCC can also be effective in obtaining this result.

Adamu et al. stated that the use of 1% chemical additives in RCC production increased the compressive strength value [18]. Nero and Haldenbilen determined that the compressive strength values of the specimens they produced using 1% chemical additives increased by 4% [20]. In addition, Alnusair et al. determined that the use of 0.75% chemical additives increased the compressive strength value by 24% [28].

The water absorption percentages of the roller compacted concrete specimens were given in Table 6. Among the RCC specimens, the K10 specimen had the lowest water absorption percentage.

Table 6 Water absorption percentages

Concrete Code	Water Absorption (%)
K0	7.58
K10	6.22
K20	7.79
K30	8.54
K40	7.76

The unit weights of roller compacted concretes were given in Table 7. When the dry unit weights were compared, it was seen that the densest structure was obtained with the K10 specimen,

and the porosity was the lowest in this specimen. Dry unit weights were consistent with compressive strengths. It was observed that the compressive strengths increased as the compactness of the material increased. The saturated unit weight was affected by the water absorption percentage of the material.

Table 7 Unit weights

Concrete Code	Dry Unit Weight (g/cm^3)	Saturated Unit Weight (g/cm^3)
K0	2.39	2.57
K10	2.45	2.60
K20	2.42	2.61
K30	2.38	2.58
K40	2.34	2.52

Ultrasonic pulse velocity and dynamic modulus of elasticity of roller compacted concretes at the age of 28 days were given in Table 8. As the ultrasonic pulse velocity increased, the dynamic modulus of elasticity and compressive strength increased, the highest values were obtained with the K10 specimen.

Table 8 Ultrasonic pulse velocity and dynamic modulus of elasticity

Concrete Code	Ultrasonic Pulse Velocity (km/s)	Dynamic Modulus of Elasticity (GPa)
K0	4.44	30.34
K10	4.60	32.05
K20	4.02	24.30
K30	3.95	23.30
K40	3.41	19.68

When the ultrasonic pulse velocities were examined, there was a 3.60% increase in the K10 specimen, a 9.46% decrease in the K20 specimen, an 11.04% decrease in the K30 specimen, and a 23.20% decrease in the K40 specimen, compared to the reference.

According to the ASTM C 597 [27] standard, if the ultrasonic pulse velocity is between 3.5 and 4.5 km/s, the concrete quality is considered as good. Since K0, K20 and K30 specimens met this condition, it can be said that these concretes' quality was good. While the K10 specimen was in very good condition in terms of concrete quality, it was observed that the concrete quality in the K40 specimen was insufficient compared to other

İsmail KILIÇ, Saadet Gökçe GÖK

Investigation of the Efficiency of Ultra High Range Water Reducing Admixture in Roller Compacted Conc...

concretes. In K40 specimen, excessive reduction in water/binder ratio and the uneven distribution of the cement paste resulted in workability problems, weakening of the aggregate-matrix interface, and consequently affecting the physical and mechanical properties adversely.

When the dynamic modulus of elasticity values were examined, it was seen that there is a 5.64% increase in the K10 specimen, a 19.91% decrease in the K20 specimen, a 23.20% decrease in the K30 specimen, and a 35.14% decrease in the K40 specimen compared to the reference.

The relationships between ultrasonic pulse velocity (UPV)-concrete compressive strength and UPV-dynamic modulus of elasticity were shown in Figure 5. The results obtained were affected by the void structure of concrete. As the amount of voids in the RCC increased, the ultrasonic pulse velocity decreased, and the

compressive strength and dynamic modulus of elasticity decreased.

Measurement of ultrasonic pulse velocity is a non-destructive test method and can be affected by parameters such as the measurement point and direction of compaction in RCCs. Ultrasonic pulse velocity is directly related to the amount of voids in the concrete, since the compressive strength is also affected by the porosity, it is useful to determine the UPV in order to have an idea about the compressive strength without damaging the concrete. A close linear relationship was obtained between the ultrasonic pulse velocity and the concrete compressive strength, as expected. In addition, there was a strong linear correlation between ultrasonic pulse velocity and dynamic modulus of elasticity.
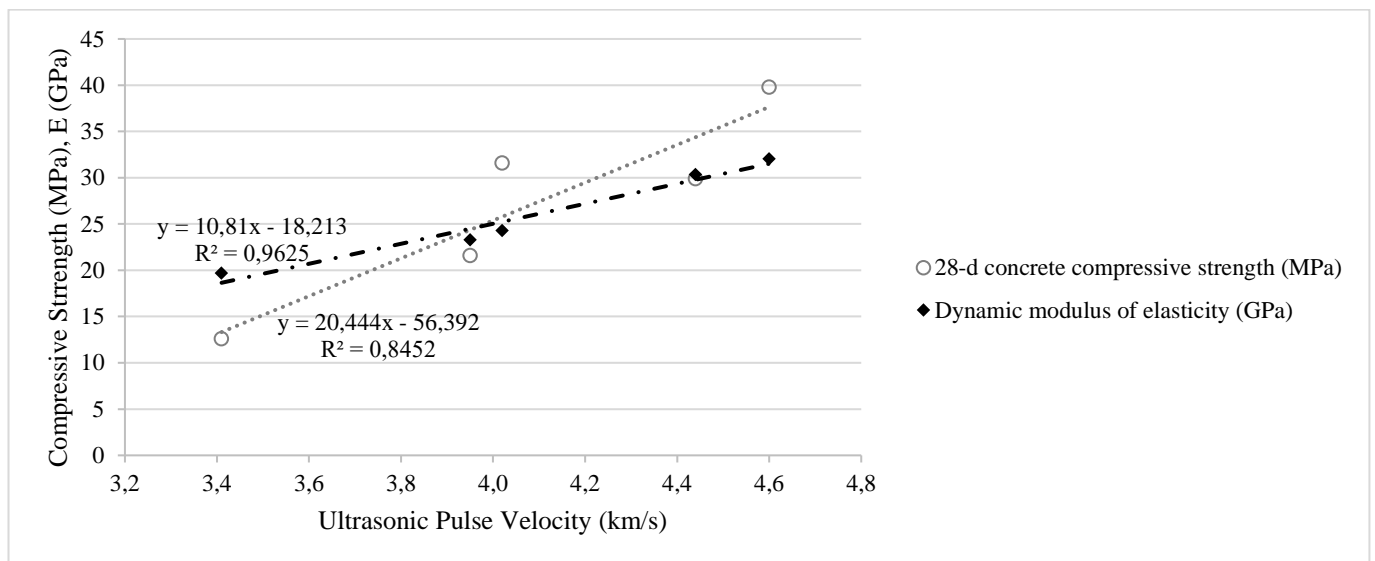
Figure 5 Ultrasonic pulse velocity (UPV), concrete compressive strength and dynamic modulus of elasticity

4. CONCLUSION

Based on the data from the experimental study, the following conclusions were drawn:

When the ultra-high range water reducing admixture was used in RCC as 1% of the weight of cement, the best results were obtained in terms of concrete compressive strength at the ages of 3

and 28 days by reducing the amount of water by 10%.

When the water/cement ratio was reduced below a certain value in roller compacted concrete, the expected increase in compressive strength does not occur due to problems in compactibility and workability.

İsmail KILIÇ, Saadet Gökçe GÖK

Investigation of the Efficiency of Ultra High Range Water Reducing Admixture in Roller Compacted Conc...

At earlier ages, with the reduction of the amount of mixing water in the concrete by more than 10%, the compressive strength of the concrete produced by using chemical admixtures was lower than the reference specimen. Based on this result, it was thought that chemical admixtures should dissolve in water and disperse homogeneously in the concrete in order to work effectively. In roller compacted concrete, a much drier mixture is obtained than conventional concrete. When the amount of water in the RCC mixture is reduced too much, the admixture used cannot have a positive effect on the workability due to the inability to disperse in the concrete, negatively affecting the mechanical properties.

In RCC production, by using a modified polycarboxylate-based plasticizer at the rate of 1% of the cement weight, optimum values were obtained in terms of unit weight, compressive strength, water absorption, ultrasonic pulse velocity and dynamic modulus of elasticity by reducing the amount of mixing water by 10%. In this mixture, the porosity was the lowest, the concrete quality was at the best level and higher compressive strength values were obtained compared to the other series.

Funding

The authors have no received any financial support for the research, authorship or publication of this study.

The Declaration of Conflict of Interest/ Common Interest

No conflict of interest or common interest has been declared by the authors.

Authors' Contribution

The authors contributed equally to the study.

The Declaration of Ethics Committee Approval

This study does not require ethics committee permission or any special permission.

The Declaration of Research and Publication Ethics

The authors of the paper declare that they comply with the scientific, ethical and quotation rules of SAUJS in all processes of the paper and that they do not make any falsification on the data collected. In addition, they declare that Sakarya University Journal of Science and its editorial board have no responsibility for any ethical violations that may be encountered, and that this study has not been evaluated in any academic publication environment other than Sakarya University Journal of Science.

REFERENCES

[1] Ş. Yazıcı, "Silindirle Sıkıştırılmış Beton (SSB)", 2008. Retrieved from https://www.imo.org.tr/resimler/ekutuphane/pdf/14954.pdf Access Date: 30.06.2021.

[2] İ. Kılıç and S. G. Gök, "Silindirle Sıkıştırılmış Betonlarda Su/Çimento Oranının Etkileri", Dicle Üniversitesi Fen Bilimleri Enstitüsü Dergisi, vol. 10, no. 1, pp. 73–84, Jun. 2021.

[3] C. Chhorn and S. W. Lee, "Consistency control of roller-compacted concrete for pavement", KSCE J Civ Eng, vol. 21, pp. 1757–1763, 2017.

[4] C. V. Hazaree, H., Ceylan, P. Taylor, K. Gopalakrishnan, K. Wang and F. Bektas, "Use of Chemical Admixtures in Roller-Compacted Concrete for Pavements", InTrans Project Reports. 57, 2013. Retrieved from https://lib.dr.iastate.edu/intrans_reports/57 Access Date: 27.06.2021

[5] C. V. Hazaree, "Workability and strength attributes of RCC: Effects of different chemical admixtures and resulting paste", Graduate Theses and Dissertations, 11250, 2010. Retrieved from https://lib.dr.iastate.edu/etd/11250 Access Date: 01.06.2021

[6] D. Harrington, F. Abdo, W. Adaska, C. V.

İsmail KILIÇ, Saadet Gökçe GÖK

Investigation of the Efficiency of Ultra High Range Water Reducing Admixture in Roller Compacted Conc...

Hazaree, H. Ceylan and F. Bektas, "Guide for roller-compacted concrete pavements", 2010.

[7] A. Modarres and Z. Hosseini, "Mechanical properties of roller compacted concrete containing rice husk ash with original and recycled asphalt pavement material", Materials and Design, vol. 64, pp. 227–236, 2014.

[8] E. Şengün, M. A. Aykutlu and İ. Ö. Yaman, "Silindirle Sıkıştırılmış Beton Yollar Üzerine Güncel Bir Tarama - Bölüm 1: Özellikleri ve Karışım Tasarımı", Çimento ve Beton Dünyası, vol. 120, no. Kasım-Aralık 2017, pp. 93–114, 2017.

[9] TÇMB, "Silindirle Sıkıştırılmış Beton Yollar Teknik Şartnamesi", Ankara, 2018.

[10] E. Yetim and D. Yılmaz, "Beton Yollar ve Silindirle Sıkıştırılmış Betonun Türkiye'deki Yeni Uygulama Alanı", 2019. Retrieved from https://webdosya.csb.gov.tr/db/yfk/icerikler/makale---beton-yollar-9-eylul-2019-20191220130448.pdf Access Date: 03.06.2021.

[11] L. Shen, Q. Li, W. Ge and S. Xu, "The mechanical property and frost resistance of roller compacted concrete by mixing silica fume and limestone powder: Experimental study", Construction and Building Materials, vol. 239, 117882, 2020.

[12] M. Hashemi, P. Shafigh, I. Asadi, A. Mahpour and A. Samadian, "The effect of superplasticizer admixture on the engineering characteristics of roller-compacted concrete pavement", International Journal of Pavement Engineering, pp. 1–16, 2020.

[13] KGM, "Beton Yollar Teknik Şartnamesi", Karayolları Genel Müdürlüğü, Ankara, 2016.

[14] TS EN 934-1, "Kimyasal katkılar - Beton, harç ve şerbet için - Bölüm 1: Katkılara ait ortak gerekler", TSE, Ankara, 2010.

[15] TS EN 934-2+A1, "Kimyasal katkılar - Beton, harç ve şerbet için - Bölüm 2: Beton kimyasal katkıları - Tarifler, gerekler, uygunluk, işaretleme ve etiketleme", TSE, Ankara, 2013.

[16] Y. Engin, İ. Gökalp, E. Önkol, H. Ağaç and H. Ekim, "Türkiye'de Silindirle Sıkıştırılmış Beton Yol Uygulamaları", Hazır Beton, Eylül-Ekim 2019, pp. 69–75, 2019.

[17] M. Adamu, B. S. Mohammed and N. Shafiq, "Effect of Polycarboxylate Superplasticizer Dosage on the Mechanical Performance of Roller Compacted Rubbercrete for Pavement Applications", Journal of Engineering and Applied Sciences, 12(20), pp. 5253–5260, 2017. DOI: 10.36478/jeasci.2017.5253.5260.

[18] M. Adamu, B. S. Mohammed and N. Shafiq, "Evaluating the effect of superplasticizer on the properties of roller compacted concrete using response surface methodology", ARPN Journal of Engineering and Applied Sciences, vol. 12, no. 21, pp. 6206–6215, 2017.

[19] M. A. Nero, "Silindirle Sıkıştırılmış Betonlar İçin Kimyasal Katkıların Etkilerinin Belirlenmesi", Yüksek Lisans Tezi, Pamukkale Üniversitesi, Denizli, Türkiye, 2019.

[20] M. A. Nero and S. Haldenbilen, "Determining the Effects of Chemical Admixtures on Roller Compacted Concrete (RCC)", American Journal of Engineering and Technology Management, vol. 5, no. 1, pp. 27–34, 2020.

[21] TS EN 1097-6, "Agregaların mekanik ve fiziksel özellikleri için deneyler - Bölüm 6: Tane yoğunluğu ve su emme oranının tayini", Türk Standartları Enstitüsü, Ankara, 2013.

İsmail KILIÇ, Saadet Gökçe GÖK

Investigation of the Efficiency of Ultra High Range Water Reducing Admixture in Roller Compacted Conc...

[22] TS EN 933-1, "Agregaların geometrik özellikleri için deneyler-bölüm 1: tane büyüklüğü dağılımının tayini-eleme yöntemi", Türk Standartları Enstitüsü, Ankara, 2012.

[23] Url-1 <https://heris.com.tr/Resimler/2d9557f65cSika%20Viscocrete%20SF%2018%2020%20072201%20TR.pdf> Retrieved on 03.07.2021.

[24] ASTM C1435/1435M-20, "Standard Practice for Molding Roller-Compacted Concrete in Cylinder Molds Using a Vibrating Hammer", American Society for Testing and Materials, ASTM International, USA, 2020.

[25] TS EN 12390-3, "Beton - Sertleşmiş beton deneyleri-bölüm 3: sertleşmiş beton deney numunelerinde basınç dayanımının tayini", Türk Standartları Enstitüsü, 2019.

[26] EN 772-11, "Methods of Test for Masonry Units Part 11: Determination of water absorption of aggregate concrete, autoclaved aerated concrete, manufactured stone and natural stone masonry units due to capillary action and the initial rate of water absorption of clay masonry units", BSI Stand. Publ., London, UK, 2011.

[27] ASTM C597-16, "Standard Test Method for Pulse Velocity Through Concrete", ASTM International, West Conshohocken, PA, 2016.

[28] A. H. Alnusair, H. Y. Katman, M. R. Ibrahim, N. A. Rahman, "The Effect of Superplasticizer on Performance of Roller Compacted Concrete Pavement Containing High Volume Fly Ash", International Journal of Recent Technology and Engineering (IJRTE), vol. 8, no. 4, ISSN: 2277-3878, November 2019.

Title: Observation of Marine Areas (Çandarlı and Gökova Bays) and Their Biodiversity

Authors: Oğuz KURT, Sevilay ÖZTÜRK

Observation of Marine Areas (Çandarlı and Gökova Bays) and Their Biodiversity

Oğuz KURT*[1], Sevilay ÖZTÜRK[1]

Abstract

This study aimed to investigate to determine the number and biodiversity of species (especially seaweed populations) in the Çandarlı and Gökova Bays. Çandarlı and Gökova Bays are defined as "Special Environmental Protection Area (SEPA)" by the Ministry of Environment and Forestry of the Republic of Turkey, Special Environmental Protection Agency Presidency. For this purpose, in the study, i) description of habitats and facies in the studied areas, ii) determination of the number and diversity of species, iii) retrieval of underwater photo recordings, operations were carried out. The approach of collecting these data in such a way as to make comparisons and comments, especially for the future, has been followed. The literature shows that the existing ecological conditions and habitat characteristics of the areas restricted to SEPA and fisheries are studied. Thus, a comprehensive database is developed that will be extremely useful in terms of future works. On the other hand, the studies carried out are particularly inadequate for marine algae (macroalgae) in the related areas. As a result of the study, a total of 316 taxa were identified and observed, including 192 marine algae (20 Cyanobacteria, 54 Phaeophyceae, 93 Rhodophyta, 25 Chlorophyta), 3 seagrasses, 70 invertebrates (9 Porifera, 13 Cnidaria, 2 Annelida, 19 Mollusca, 16 Arthropoda, 10 Echinodermata, 2 Tunicata) and 51 fish (2 Chondrichthyes, 49 Osteichthyes).

Keywords: Çandarlı Bay, Gökova Bay, marine algae, marine organisms, monitoring

1. INTRODUCTION

Although the seas of Turkey differ in terms of ecological, geographical, geomorphological, meteorological, and similar features, they form a part of the Mediterranean water system. Among these seas, the Aegean Sea is richer in species diversity than the Mediterranean, Marmara, and Black Seas. Located between 41°-35° north latitude and 23°-27°/28° east longitude, the Aegean Sea has a length of approximately 660 km from north to south. It covers an area of approximately 214,000 km² within these borders. In terms of its morphological features, the Aegean Sea, which is divided into three different regions as North Aegean, Middle Aegean, and South Aegean, in terms of its morphological features, is a semi-enclosed sea with about 3,000 large and small islands/islets. At the same time, it forms a complementary front road of the straits connecting the Black Sea and the Mediterranean and a transition area between the Black Sea and

---

* Corresponding author: fokurt@yahoo.com
[1] Manisa Celal Bayar University, Faculty of Sciences and Letters, Department of Biology, 45140, Manisa, Turkey
E-mail: seviozturk@yahoo.com
ORCID: https://orcid.org/0000-0002-3721-6855, https://orcid.org/0000-0002-3436-0472

the Mediterranean in terms of its biological and hydrological characteristics.

There are sub-activities carried out within the scope of the "Strengthening the System of Marine and Coastal Protected Areas of Turkey" Project in different coastal areas of our country by the Republic of Turkey Ministry of Environment and Forestry, Special Environmental Protection Agency Presidency. One of these; is a study titled "The Current Situation of Fishing in the Marine and Coastal Protected Areas in Five Special Environmental Protection Areas and Ayvalık Islands Nature Park and the Monitoring of Fishing Restricted Areas Determined in Gökova SEPA". Güçlüsoy [1] stated that a total of 8 MCPAs comprising 5 SEPAs, 2 NPs, and 1 NAP are located on the Turkish Aegean coasts. It also explains in detail all the features of the areas.

It is known that in this and similar monitoring studies, qualified scientific studies have been carried out, mostly evaluating the fish stocks and the status of fish populations in Fisheries Restricted Areas in SEPAs. In these studies, the bio-ecology of fish populations was studied, virtual population analyzes (length-based VPA) were made, and data were collected to make future comparisons and interpretations between restricted and free areas for fishing [2-6]. There are also a large number of similar studies on fish diversity and sea creatures on the coasts of Turkey [1, 7-15]. In addition to fish populations, natural habitats and facies of the studied areas and detailed habitat characteristics of fishery-restricted areas should be determined. For the realization of these determinations, SCUBA dives, photos, and video recordings should be taken underwater. In this context, there are few studies in detail on marine algae and seagrasses [16].

As it can be seen, although there are similar studies in the literature, there is no study in which all groups constituting the biodiversity of Çandarlı and Gökova SEPA areas are observed, and the macroalgae of these two ecosystems are determined in detail. The main objective of this study is to observe the Çandarlı and Gökova Bays, identify the habitats and facies in the studied areas

in detail, determine the number/variety of species, and obtain underwater imaging records.

For this purpose, the approach followed in the study was as follows; a) compilation of qualified scientific studies on marine algae, seagrasses, invertebrates, and fishes up to now in Çandarlı and Gökova Bays, b) detection of the living group's populations in Çandarlı and Gökova Bays, c) observing and recording the marine life in the study areas.

2. MATERIALS AND METHODS

2.1. Sampling, Observing, and Recording

Sampling and observing were carried out monthly in 2017-2018 from stations determined on the shores of Çandarlı (38°55'39" N - 26°59'04" E) and Gökova (37°02'00" N - 28°17'01" E) Bays. Circalittoral, mediolittoral, and infralittoral zones were sampled, observed, and recorded in the sampling studies. Snorkeling was used from the shore to the deep, and scuba diving was also made with SCUBA dive equipment. The GoPro Hero 4 underwater action camera with special equipment was used for taking digital recordings and photographing species groups. Species that could be identified underwater were photographed in their natural habitats during dives and recorded digitally.

Algae and seagrasses species collected for identification were fixed by the species group. Collected algae and seagrasses samples were fixed in jars containing 2-4% formaldehyde-water, and the labels with the necessary information were affixed on them.

Also, macro biological diversity was tried to be determined by applying the Underwater Visual Observation/Counting (UVOC) technique, which is one of the different sampling techniques used to evaluate the macrofauna and flora diversity in the marine ecosystem, especially for invertebrates and fishes species [17]. These studies were carried out with direct observation and sampling methods during snorkeling and SCUBA dives. Dead individuals (Mollusca, Arthropoda, etc. shells) were also collected in the observed line, and those

whose identifiable characters were not lost were taken into consideration. During this period, imaging techniques (photo-video) were also applied.

2.2. Identification

Collected algae and seagrasses species were determined using stereo, light, and fluorescence microscopy, following procedures appropriate to species groups (taxonomic and systematic positions, and morphological structures of the samples, etc.), respectively. Most of the invertebrates and all fish species were identified in situ or from digital records. The methods determined suitable and valid for each species group by evaluating the necessary visual (internet, determination keys, CDs, etc.) and written (book, article, monograph) literature were used in performing these processes. Digital records were kept of the species photographed in their natural environment or the laboratory (for the algae and the seagrasses) during species identification.

Taxonomy and nomenclature follow Guiry and Guiry [18] for the marine algae and seagrasses, WoRMS Editorial Board [19] for the invertebrates and fishes.

3. RESULTS

This study was carried out for the main purpose of observing the Çandarlı and Gökova Bays, determining the number and diversity of species in the studied areas, and taking underwater photograph recordings. In particular, it is aimed to determine the marine algae populations. As a result of the study, a total of 316 species were identified and taken underwater photo records. The identified species as follows; 192 marine seaweeds (20 Cyanobacteria, 54 Phaeophyceae, 93 Rhodophyta, and 25 Chlorophyta), 3 seagrasses, 70 invertebrates (9 Porifera, 13 Cnidaria, 2 Annelida, 18 Mollusca, 16 Arthropoda, 10 Echinodermata, and 2 Tunicata), and 51 fishes (including 2 Chondrichthyes and 49 Osteichthyes). In this context, taxa determined from the marine algae groups are given in Table 1.

The main purpose of this study is to determine seaweed populations. However, as an observational study, seagrasses, invertebrates, and fish species observed in the Çandarlı and Gökova Bays were also tried to be determined and their underwater photographs were taken. The seagrasses, invertebrates, and fish species identified and observed in this context are given in Table 2.

Table 1 Distribution of the identified algae according to taxonomic categories

Classis	Taxa
Cyanophyceae	*Aphanocapsa litoralis* Hansgirg 1892
	A. marina Hansgirg in Foslie 1890
	Merismopedia mediterranea Nägeli 1849
	Gloeocapsa atrata Kützing 1843
	G. cf. *salina* Hansgirg 1893
	Chroococcus minutus (Kützing) Nägeli 1849
	C. varius A.Braun in Rabenhorst 1876
	Entophysalis deusta (Meneghini) F.E.Drouet & W.A.Daily 1948
	Xenococcus schousboei Thuret in Bornet & Thuret 1880
	Dermocarpa acervata (Setchell & Gardner) Pham-Hoàng Hô 1969
	Spirulina subsalsa Oersted ex Gomont 1892
	Leibleinia epiphytica (Hieronymus) Compère 1985
	Leptolyngbya fragilis (Gomont) Anagnostidis & Komárek 1988
	Phormidium litorale Golubic 1960
	Lyngbya confervoides C.Agardh ex Gomont 1892
	L. majuscula Harvey ex Gomont 1892
	L. salina Kützing ex Gomont 1892
	Calothrix aeruginea Thuret ex Bornet & Flahault 1886
	Dichothrix compacta Bornet & Flahault 1886
	Rivularia nitida C.Agardh ex Bornet & Flahault 1886
Phaeophyceae	*Ectocarpus fasciculatus* Harvey 1841

E. siliculosus (Dillwyn) Lyngbye 1819
Feldmannia irregularis (Kützing) Hamel 1939
F. mitchelliae (Harvey) H.-S.Kim 2010
F. padinae (Buffham) Hamel 1939
Cladosiphon mediterraneus Kützing 1843
Corynophlaea umbellata (C.Agardh) Kützing 1843
Myriactula rivulariae (Suhr ex Areschoug) Feldmann 1937
Myriotrichia clavaeformis Harvey 1834
Hecatonema terminale (Kützing) Kylin 1937
Punctaria latifolia Greville 1830
Colpomenia sinuosa (Mertens ex Roth) Derbès & Solier in Castagne 1851
Hydroclathrus clathratus (C.Agardh) M.Howe in N.L.Britton & C.F.Millspaugh 1920
Petalonia fascia (O.F.Müller) Kuntze 1898
Scytosiphon lomentaria (Lyngbye) Link 1833
Nemacystus flexuosus var. *giraudyi* (J.Agardh) De Jong 1997
Spermatochnus paradoxus (Roth) Kützing 1843
Stilophora tenella (Esper) P.C.Silva in P.C.Silva, Basson & Moe 1996
Pseudolithoderma adriaticum (Hauck) Verlaque 1988
Hapalospongidion macrocarpum (Feldmann) León-Álvarez&González-González 1993
Pseudoralfsia verrucosa (Areschoug) Parente, Fletcher & G.W.Saunders 2020
Cutleria multifida (Turner) Greville 1830
Zanardinia typus (Nardo) P.C.Silva in Greuter 2000
Dictyopteris polypodioides (A.P.De Candolle) J.V.Lamouroux 1809
Dictyota dichotoma (Hudson) J.V.Lamouroux 1809
D. dichotoma var. *intricata* (C.Agardh) Greville 1830
D. fasciola (Roth) J.V.Lamouroux 1809
D. implexa (Desfontaines) J.V.Lamouroux 1809
D. spiralis Montagne 1846
Padina pavonica (Linnaeus) Thivy in W.R.Taylor 1960
Stypopodium schimperi (Kützing) Verlaque & Boudouresque 1991
Taonia atomaria (Woodward) J.Agardh 1848
Cladostephus hirsutus (Linnaeus) Boudouresque & M.Perret-Boudouresque ex Heesch & al. 2020
Sphacelaria cirrosa (Roth) C.Agardh 1824
S. fusca (Hudson) S.F.Gray 1821
S. rigidula Kützing 1843
S. tribuloides Meneghini 1840
Halopteris filicina (Grateloup) Kützing 1843
H. scoparia (Linnaeus) Sauvageau 1904
Cystoseira compressa (Esper) Gerloff & Nizamuddin 1975
C. compressa f. *plana* (Ercegovic) Cormaci, G.Furnari, Giaccone, Scammanca & D.Serio 1992
C. corniculata (Turner) Zanardini 1841
C. foeniculacea (Linnaeus) Greville 1830
C. foeniculacea f. *tenuiramosa* (Ercegovic) A.Gómez Garreta, M.C.Barceló, M.A.Ribera & J.Rull Lluch 2001
C. humilis Schousboe ex Kützing 1860
C. humilis var. *myriophylloides* (Sauvageau) J.H.Price & D.M.John in J.H.Price, D.M.John & G.W.Lawson 1978
Ericaria crinita (Duby) Molinari & Guiry 2020
E. mediterranea (Sauvageau) Molinari & Guiry 2020
E. zosteroides (C.Agardh) Molinari & Guiry 2020
Gongolaria barbata (Stackhouse) Kuntze 1891
G. montagnei (J.Agardh) Kuntze 1891
Sargassum acinarium (Linnaeus) Setchell 1933
S. hornschuchii C.Agardh 1820
S. vulgare C.Agardh 1820

Bangiophyceae	*Chroodactylon ornatum* (C.Agardh) Basson 1979
	Stylonema alsidii (Zanardini) K.M.Drew 1956
	Erythrotrichia carnea (Dillwyn) J.Agardh 1883
	Sahlingia subintegra (Rosenvinge) Kornmann 1989
	Bangia atropurpurea (Mertens ex Roth) C.Agardh 1824
	Neopyropia leucosticta (Thuret) L.-E.Yang & J.Brodie 2020
	Porphyra umbilicalis Kützing 1843

	Acrochaetium secundatum (Lyngbye) Nägeli in Nägeli & Cramer 1858
	Colaconema daviesii (Dillwyn) Stegenga 1985
	C. savianum (Meneghini) R.Nielsen 1994
	Ganonema farinosum (J.V.Lamouroux) K.C.Fan & Yung C.Wang 1974
	Gelidium serra (S.G.Gmelin) E.Taskin & M.J.Wynne, nom. rejic. 2013
	G. spathulatum (Kützing) Bornet 1892
	Huismaniella nigrescens (Feldmann) G.Furnari, Cormaci, Alongi & Perrone 2018
	Millerella pannosa (Feldmann) G.H.Boo & L.Le Gall 2016
	Asparagopsis armata Harvey 1855
	Corallina officinalis Linnaeus 1758
	Ellisolandia elongata (J.Ellis & Solander) K.R.Hind & G.W.Saunders 2013
	Jania longifurca Zanardini 1844
	J. rubens (Linnaeus) J.V.Lamouroux 1816
	J. virgata (Zanardini) Montagne 1846
	J. virgata var. *attenuata* (Kützing) Taşkin 2019
	Amphiroa beauvoisii J.V.Lamouroux 1816
	A. rigida J.V.Lamouroux 1816
	A. cryptarthrodia Zanardini 1843
	Lithophyllum stictiforme (Areschoug) Hauck 1877
	L. corallinae (P.Crouan & H.Crouan) Heydrich 1897
	L. cystoseirae (Hauck) Heydrich 1897
	Titanoderma trochanter (Bory) Benhissoune, Boudouresque, Perret-Boudouresque & Verlaque 2002
	Hydrolithon cruciatum (Bressan) Y.M.Chamberlain 1994
	H. farinosum (J.V.Lamouroux) Penrose & Y.M.Chamberlain 1993
	Neogoniolithon brassica-florida (Harvey) Setchell & L.R.Mason 1943
	N. hauckii (Rothpletz) R.A.Townsend & Huisman 2018
	Pneophyllum fragile Kützing 1843
	Choreonema thuretii (Bornet) F.Schmitz 1889
	Melobesia membranacea (Esper) J.V.Lamouroux 1812
	Mesophyllum lichenoides (J.Ellis) Me.Lemoine 1928
Florideophyceae	*M. philippii* (Foslie) Adey 1970
	Caulacanthus ustulatus (Mertens ex Turner) Kützing 1843
	Chondracanthus acicularis (Roth) Fredericq in Hommersand, Guiry, Fredericq & Leister 1993
	Hypnea musciformis (Wulfen) J.V.Lamouroux 1813
	Peyssonnelia rubra (Greville) J.Agardh 1851
	P. squamaria (S.G.Gmelin) Decaisne ex J.Agardh 1842
	Gymnogongrus griffithsiae (Turner) C.Martius 1833
	Botryocladia botryoides (Wulfen) Feldmann 1941
	B. skottsbergii (Børgesen) Levring 1941
	Callithamnion corymbosum (Smith) Lyngbye 1819
	Centroceras clavulatum (C.Agardh) Montagne 1846
	Ceramium brevizonatum H.E.Petersen 1918
	C. cupulatum Womersley 1978
	C. ciliatum var. *robustum* (J.Agardh) Mazoyer 1938
	C. circinatum (Kützing) J.Agardh 1851
	C. diaphanum (Lightfoot) Roth 1806
	C. gaditanum var. *mediterraneum* (Debray) Cremades in Cremades & Pérez-Cirera 1990
	C. siliquosum var. *lophophorum* (Feldman-Mazoyer) Serio 1994
	Gayliella flaccida (Harvey ex Kützing) T.O.Cho & L.J.McIvor 2008
	Corallophila cinnabarina (Grateloup ex Bory) R.E.Norris 1993
	Crouania attenuata (C.Agardh) J.Agardh 1842
	Griffithsia schousboei Montagne in P.B.Webb 1840
	Ptilothamnion pluma (Dillwyn) Thuret in Le Jolis 1863
	Spermothamnion repens (Dillwyn) Magnus 1873
	Spyridia filamentosa (Wulfen) Harvey in W.J.Hooker 1833
	Wrangelia penicillata (C.Agardh) C.Agardh 1828
	Dasya rigidula (Kützing) Ardissone 1878
	Heterosiphonia crispella (C.Agardh) M.J.Wynne 1985
	Hypoglossum hypoglossoides (Stackhouse) Collins & Hervey 1917
	Nitophyllum punctatum (Stackhouse) Greville 1830
	Taenioma nanum (Kützing) Papenfuss 1952
	Chondria capillaris (Hudson) M.J.Wynne 1991

	C. dasyphylla (Woodward) C.Agardh 1817
	C. mairei G.Feldmann 1949
	Palisada patentiramea (Montagne) Cassano, Sentíes, Gil-Rodríguez & M.T.Fujii in Cassano *et al.* 2009
	P. perforata (Bory) K.W.Nam 2007
	P. thuyoides (Kützing) Cassano, Sentíes, Gil-Rodríguez & M.T.Fujii in Cassano *et al.*2009
	Digenea simplex (Wulfen) C.Agardh 1822
	Dipterosiphonia rigens (C.Agardh) Falkenberg 1901
	Halopithys incurva (Hudson) Batters 1902
	Herposiphonia secunda (C.Agardh) Ambronn 1880
	H. tenella (C.Agardh) Ambronn 1880
	Laurencia microcladia Kützing 1865
	L. obtusa (Hudson) J.V.Lamouroux 1813
	L. pyramidalis Bory ex Kützing 1849
	Osmundea pinnatifida (Hudson) Stackhouse 1809
	Lophosiphonia cristata Falkenberg 1901
	L. obscura (C.Agardh) Falkenberg in F.Schmitz & Falkenberg 1897
	Chondrophycus glandulifer (Kützing) Lipkin & P.C.Silva 2002
	Polysiphonia atra Zanardini 1847
	Carradoriella denudata (Dillwyn) Savoie & G.W.Saunders 2019
	C. elongata (Hudson) Savoie & G.W.Saunders 2019
	Vertebrata fruticulosa (Wulfen) Kuntze 1891
	V. fucoides (Hudson) Kuntze 1891
	Rytiphlaea tinctoria (Clemente) C.Agardh 1824
	Womersleyella setacea (Hollenberg) R.E.Norris 1992
Ulvophyceae	*Ulothrix implexa* (Kützing) Kützing 1849
	Ulva compressa Linnaeus 1753
	U. intestinalis Linnaeus 1753
	U. intestinalis f. *attenuata* (Ahlner) M.J.Wynne 2014
	U. lactuca Linnaeus 1753
	U. linza Linnaeus 1753
	Umbraulva dangeardii M.J.Wynne & G.Furnari 2014
	Anadyomene stellata (Wulfen) C.Agardh 1823
	Chaetomorpha aerea (Dillwyn) Kützing 1849
	Cladophora dalmatica Kützing 1843
	C. glomerata (Linnaeus) Kützing 1843
	C. prolifera (Roth) Kützing 1843
	Lychaete pellucida (Hudson) M.J.Wynne 2017
	Dasycladus vermicularis (Scopoli) Krasser in Beck & Zahlbruckner 1898
	Acetabularia acetabulum (Linnaeus) P.C.Silva 1952
Bryopsidophyceae	*Bryopsis corymbosa* J.Agardh 1842
	B. hypnoides J.V.Lamouroux 1809
	Pseudobryopsis myura (J.Agardh) Berthold in Oltmanns 1904
	Caulerpa prolifera (Forsskål) J.V.Lamouroux 1809
	C. racemosa (Forsskål) J.Agardh 1873
	C. cylindracea Sonder 1845
	Codium bursa (Linnaeus) C.Agardh 1817
	Derbesia tenuissima (Moris & De Notaris) P.Crouan & H.Crouan 1867
	Halimeda tuna (J.Ellis & Solander) J.V.Lamouroux 1816
	Flabellia petiolata (Turra) Nizamuddin 1987

Table 2 Distribution of the identified and observed seagrasses, invertebrates, and fish species according to taxonomic categories

Taxonomic group	*Taxa*
Tracheophyta	*Posidonia oceanica* (Linnaeus) Delile 1813
	Cymodocea nodosa (Ucria) Ascherson 1870
	Halophila stipulacea (Forsskål) Ascherson in Anon. 1867
Porifera	*Chondrosia reniformis* Nardo, 1847
	Axinella cannabina Esper, 1794
	A. verrucosa Esper, 1794
	Crambe crambe Schmidt, 1862

	Agelas oroides Schmidt, 1864
	Petrosia ficiformis Poiret, 1789
	Spongia agaricina Pallas, 1766
	Sarcotragus foetidus Schmidt, 1862
	Verongia aerophoba Nardo, 1833
Cnidaria	*Aurelia aurita* Linnaeus, 1758
	Nausithoae punctata Kölliker, 1853
	Penneria disticha Goldfuss, 1820
	Cladocora caespitosa Linnaeus, 1767
	Alcyonium acaule Marion, 1878
	Eunicella singularis Esper, 1791
	Actinia equina Linnaeus, 1758
	Anemonia viridis Forsskål, 1775
	Condylactis aurantiaca Delle Chiaje, 1825
	Cerianthus lloydii Gosse, 1859
	Parazoanthus axinella Schmidt, 1862
	Madracis pharensis Heller, 1868
	Balanophyllia europaea Risso, 1826
Annelida	*Hermodice carunculata* Pallas, 1766
	Sabella spallanzanii Gmelin, 1791
Mollusca	*Mytilus galloprovincialis* Lamarck, 1819
	Pinna nobilis Linnaeus, 1758
	P. rudis Linnaeus, 1758
	Venus verrucosa Linnaeus, 1758
	Tonna galea Linnaeus, 1758
	Bolinus brandaris Linnaeus, 1758
	Hexaplex trunculus Linnaeus, 1758
	Semicassis granulata Born, 1778
	Conomurex persicus Swainson, 1821
	Dendostrea frons Linnaeus, 1758
	Pinctada imbricata radiata Leach, 1814
	Cerithium vulgatum Bruguière, 1792
	Acanthocardia sp.
	Peltodoris atromaculata Bergh, 1880
	Flabellina affinis Gmelin, 1791
	Octopus vulgaris Cuvier, 1797
	O. macropus Risso, 1826
	Loligo vulgaris Lamarck, 1798
	Sepia officinalis Linnaeus, 1758
Arthropoda	*Melicertus hathor* Burkenroad, 1959
	Alpheus rapacida de Man, 1908
	Scyonia carinata Brünnich, 1768
	Penaeus japonicus Spence Bate, 1888
	Palaemon elegans Rathke, 1837
	Stenopus spinosus Risso, 1827
	Homarus gammarus Linnaeus, 1758
	Pagurus prideaux Leach, 1815
	Palinurus elaphas Fabricius, 1787
	Scyllarides latus Latreille, 1803
	Scyllarus arctus Linnaeus, 1758
	Calcinus tubularis Linnaeus, 1767
	Pachygrapsus marmoratus Fabricius, 1787
	Ilia nucleus Linnaeus, 1758
	Eriphia verrucosa Forsskål, 1775
	Callinectes sapidus Rathbun, 1896
Echinodermata	*Antedon mediterranea* Lamarck, 1816
	Ophiomyxa pentagona Lamarck, 1816
	Marthasterias glacialis Linnaeus, 1758
	Astropecten platyacanthus Philippi, 1837
	Echinaster sepositus Retzius, 1783
	Paracentrotus lividus Lamarck, 1816
	Arbacia lixula Linnaeus, 1758
	Sphaerechinus granularis Lamarck, 1816
	Holothuria forskali Delle Chiaje, 1823

	H. tubulosa Gmelin, 1791
Tunicata	*Clavelina lepadiformis* Müller, 1776
	Halocynthia papillosa Linnaeus, 1767
Chondrichthyes	*Dasyatis pastinaca* Linnaeus, 1758
	Raja sp.
Osteichythyes	*Muraena helena* Linnaeus, 1758
	Apogon imberbis Linnaeus, 1758
	Merluccius merluccius Linnaeus, 1758
	Zeus faber Linnaeus, 1758
	Scopaena parcus Linnaeus, 1758
	S. scrofa Linnaeus, 1758
	Trigla lucerna Linnaeus, 1758
	Epinephelus aeneus Geoffroy Saint-Hilaire, 1817
	E. guaza Anonymous
	Serranus cabrilla Linnaeus, 1758
	S. scriba Linnaeus, 1758
	Gobius niger Linnaeus, 1758
	Echeneis naucrates Linnaeus, 1758
	Seriola dumerili Risso, 1810
	Trachinotus ovatus Linnaeus, 1758
	Trachurus mediterraneus Steindachner, 1868
	T. trachurus Linnaeus, 1758
	Xyrichtys novacula Linnaeus, 1758
	Coryphaena hippurus Linnaeus, 1758
	Boops boops Linnaeus, 1758
	Dentex dentex Linnaeus, 1758
	Diplodus annularis Linnaeus, 1758
	D. puntazzo Walbaum, 1792
	D. sargus sargus Linnaeus, 1758
	D. vulgaris Geoffroy Saint-Hilaire, 1817
	Lithognathus mormyrus Linnaeus, 1758
	Oblada melanura Linnaeus, 1758
	Pagellus erythrinus Linnaeus, 1758
	Pagrus pagrus Linnaeus, 1758
	Sarpa salpa Linnaeus, 1758
	Sparus aurata Linnaeus, 1758
	Umbrina cirrosa Linnaeus, 1758
	Sciaena umbra Linnaeus, 1758
	Mullus barbatus Linnaeus, 1758
	M. surmuletus Linnaeus, 1758
	Liza aurata Risso, 1810
	Mugil cephalus Linnaeus, 1758
	Sparisoma cretense Linnaeus, 1758
	Uranoscopus scaber Linnaeus, 1758
	Trachinus araneus Cuvier, 1829
	Sphyraena sphyraena Linnaeus, 1758
	Trichiurus lepturus Linnaeus, 1758
	Euthynnus alletteratus Rafinesque, 1810
	Scomber japonicas Houttuyn, 1782
	S. scombrus Linnaeus, 1758
	Spicara maena Linnaeus, 1758
	Solea solea Linnaeus, 1758
	Bothus podas Delaroche, 1809
	Balistes carolinensis Gmelin, 1789

4. DISCUSSION AND CONCLUSIONS

Considering that such diversity has not been determined in previous studies in research areas in the literature, the number and variety of species identified, observed, and recorded in this study are pretty remarkable. For example, Zeki [20] reported 75 taxa belonging to the south of the Gökova SEPA. While Rhodophyta took first place with 38 species, 20 Heterokontophyta, 15

Chlorophyta, and 2 Cyanophyta were determined. Canbolat et al. [6] reported 30 marine algae, 10 secondary aquatic plants (6 of which are freshwater forms distributed in Azmak Stream), 9 Invertebrates, and 58 Fish species in their study in Gökova Bay.

Güçlüsoy [1] reported that Gökova Bay is one of the most studied Marine and Coastal Protected Area in Turkey, and eleven marine and coastal projects on such as marine species inventory, ICM, fisheries, and management plan preparation were carried out between 2000 and 2012. Also, Okuş et al. [4] inventoried 723 macroscopic species comprising 79 flora and 644 fauna taxa. Since macroalgae are the primary goal in this study, a large surplus was determined in macroalgae diversity. As a natural consequence of this, fauna diversity remains lower.

Özaydın et al. [21] were determined a total of 60 fish species (including 11 Chondrichthyes and 49 Osteichthyes) in the Çandarlı Bay. Again, 54 Gastropod species distributed in Çandarlı Bay were identified by Aksoy [22]. Compared to these two studies, the diversity of fauna and flora observed in this study is greater.

In the literature, there are some checklists (as Review Articles) on the coasts of Turkey that represent a lot of species belonging to the related taxonomic categories; the marine fishes [14], Cnidaria and Ctenophora [15], the marine arthropods [23], Echinodermata [24], Tunicata [25].

Due to the open system of the study areas, fish and other invertebrates can be found in monthly or seasonal migration behaviors for both breeding and feeding purposes. In short-term studies, information can be obtained only about fish and invertebrate species belonging to the relevant period. Therefore, it was concluded that it is necessary to establish a long-term monitoring project.

When evaluated in terms of habitats, the relevant protection strategies should be determined by evaluating the relationship between the habitats determined in the regions and the ecological system in the region should be applied considering this differentiation.

On the other hand, not only marine environments but also terrestrial environments, which are in contact with the nature of the coastal area, should be carefully protected. Conservation activities in the region should continue not only in the marine but also in the coastal area.

The Declaration of Conflict of Interest/ Common Interest

No conflict of interest or common interest has been declared by the authors.

Authors' Contribution

The first author contributed 60%, the second author 40%.

The Declaration of Ethics Committee Approval

This study does not require ethics committee permission or any special permission.

The Declaration of Research and Publication Ethics

The authors of the paper declare that they comply with the scientific, ethical and quotation rules of SAUJS in all processes of the paper and that they do not make any falsification on the data collected. In addition, they declare that Sakarya

University Journal of Science and its editorial board have no responsibility for any ethical violations that may be encountered and that this study has not been evaluated in any academic publication environment other than Sakarya University Journal of Science.

REFERENCES

[1] T. Katağan, A. Tokaç, Ş. Beşiktepe, B. Öztürk, (Eds.), "The Aegean Sea Marine Biodiversity, Fisheries, Conservation and Governance," Turkish Marine Research Foundation (TUDAV), Publication No: 41, Istanbul, Turkey, 2015.

[2] F. Öğretmen, "Gökova Körfezi (Muğla) Balık Faunasının Araştırılması," MSc Thesis, Muğla University, Muğla, Turkey, 2002.

[3] UNEP-WCMC (United Nations Environmental Programme-World Conservation and Monitoring Centre), 2005. http://www.unep-wcmc.org

[4] E. Okuş and A. Yüksek, "Determination of Biological Diversity of Coastal and Marine Areas of Gökova Special Environmental Protection Area, Final Report," Republic of Turkey Ministry of Environment and Forestry Special Environmental Protection Agency Presidency, 2006.

[5] V. Ünal and M. Erdem, "Annex-4 Traditional Fishing in Gökova Inner Bay," SMAP III European Union Gökova Project. Muğla University Printing House, Muğla, Turkey, 2009.

[6] A. F. Canbolat, B. A. Çiçek, A. Akbulut, O. Kurt, A. C. Hoş, A. Türkmen, H. Metin, M. Öztürk, E. Taşkın, T. Ceyhan, A. Küsbeci, D. K. Közer, T. Ceylan and U. Uyan, "Current Situation of Fishing in the Marine and Coastal Protected Areas in Five Special Environmental Protection Areas and Ayvalık Islands Nature Park and Monitoring of Fisheries Restricted Areas Determined in Gökova SEPA," Republic of Turkey Ministry of Environment and Forestry Special Environmental Protection Agency, Ankara, Turkey, 2010.

[7] T. Katağan, A. Kocataş, N. Bilecik and H. Yılmaz, "Süngerler ve Süngercilik," Turkish Republic Ministry of Agriculture and Rural Affairs, Fisheries Research Institute, Publication No: 5, Bodrum, Turkey, 60p, 1991.

[8] A. Kocataş and N. Bilecik, "Ege Denizi ve Canlı Kaynakları," Turkish Republic Ministry of Agriculture and Rural Affairs, Fisheries Research Institute, Publication No: 7, Bodrum, Turkey, 88p, 1992.

[9] N. Demir, "İhtiyoloji," Istanbul University Press, Istanbul, Turkey, Issue: 3903, XI+393p, 1996.

[10] B. Gözcelioğlu and Ö. F. Aydıncılar, "Derin Mavi Atlas," Tubitak Publications, Ankara, Turkey, 182p, 2001.

[11] B. Öztürk, B. Topaloğlu and A. Dede, "Deniz Canlıları Rehberi," Turkish Marine Research Foundation (TUDAV), Education Series No: 6, Istanbul, Turkey, 181p., 2003.

[12] L. Bat, Y. Erdem, S. Ustaoğlu Tırıl and Ö. Yardım, "Balık Sistematiği," Nobel Publication No: 1330, 1st Edition, XVIII+272p., 2008.

[13] M. Yokeş, M. Bilecenoğlu, M. Cınar, E. Okudan, V. Demir, E. Kalkan, et al., "Determination Work on Marine Biodiversity at Ayvalık Adaları Nature Park," PIMS 3697: Strengthening the System of the Marine and Coastal Protected Areas of Turkey. Ankara: UNDP Turkey, 2013.

[14] M. Bilecenoğlu, M. Kaya, B. Cihangir and E. Çiçek, "An updated checklist of the marine fishes of Turkey," Turkish Journal of Zoology, vol. 38, pp. 901–929, 2014.

[15] M. E. Çınar, M. B. Yokeş, A. Şermin and A. K. Bakir, "Checklist of Cnidaria and Ctenophora from the coasts of Turkey,"

Turkish Journal of Zoology, vol. 38, no. 6, pp. 677–97, 2014.

[16] Ş. Cirik, B. Akçalı and N. Bilecik, "Gökova Körfezi (Ege Denizi) Deniz Bitkileri," Dokuz Eylul University Institute of Marine Sciences and Technology, Izmir, Turkey, 96p., 2001.

[17] M. De Girolamo and C. Mazzoldi, "The application of visual census on Mediterranean rocky habitats," Marine Environmental Research, vol. 51, pp. 1–16, 2001.

[18] M.D. Guiry and M.D. Guiry, AlgaeBase. World-wide electronic publication, National University of Ireland, Galway. https://www.algaebase.org; searched on February 1, 2022.

[19] WoRMS Editorial Board, World Register of Marine Species. Available from https://www.marinespecies.org at VLIZ. Accessed 2022-02-02. doi:10.14284/170.

[20] S. Zeki, "Gökova Özel Çevre Koruma Bölgesi Güneyi Üst İnfralittoral Makroalgleri Üzerine Araştırmalar," Istanbul University Institute of Marine Sciences and Management, MSc Thesis, Istanbul, Turkey, 2006.

[21] O. Özaydın, S. Akalın and D. İlhan, "Bottom trawl fish composition of Çandarlı Bay (Aegean Sea)," Ege Journal of Fisheries and Aquatic Sciences, vol. 31, no. 4, pp. 181–185, 2014.

[22] Ö. Aksoy, "Çandarlı Körfezi (Aliağa, Yenişakran kıyıları) kıyısal ekosisteminde dağılım gösteren prosobranchia (gastropoda, mollusca) türleri," İzmir Katip Çelebi University, MSc Thesis, Izmir, Turkey, 2016.

[23] A. K. Bakir, T. Katağan, H. V. Aker, T. Özcan, M. Sezgin, A. S. Ateş, et al., "The marine arthropods of Turkey," Turkish Journal of Zoology, vol. 38, no. 6, pp. 765–831, 2014.

[24] B. Öztoprak, A. Doğan and E. Dağli, "Checklist of Echinodermata from the coasts of Turkey," Turkish Journal of Zoology, vol. 38, no. 6, pp. 892–900, 2014.

[25] M. E. Çınar, "Checklist of the phyla Platyhelminthes, Xenacoelomorpha, Nematoda, Acanthocephala, Myxozoa, Tardigrada, Cephalorhyncha, Nemertea, Echiura, Brachiopoda, Phoronida, Chaetognatha, and Chordata (Tunicata, Cephalochordata, and Hemichordata) from the coasts of Turkey," Turkish Journal of Zoology, vol. 38, no. 6, pp. 698–722, 2014.

Title: Indoor Radon Levels in Dwellings of Kirklareli, Turkey

Authors: Selin ÖZDEN, Serpil AKÖZCAN

Indoor Radon Levels in Dwellings of Kirklareli, Turkey

Selin ÖZDEN*[1], Serpil AKÖZCAN[1]

Abstract

The indoor radon concentrations in Kirklareli, Turkey were measured in living rooms of 19 houses during winter in 2019 using Airthings 222 Corentium Home Radon Gas Detector. The short-term and long-term measurements were performed in 1 and 7 days for each house to investigate radioactive radon gas exposure in Kirklareli buildings. The indoor radon concentrations were varied from 23 to 156 Bq m^{-3} for 1 day period and were varied from 16 to 77 Bq m^{-3} for 7 days period. The average radon gas concentration was found as 43.5 Bq m^{-3} and this result is higher than the average of Turkey and the world average. The annual effective doses due to radon gas exposure were also estimated. The annual effective dose rate ranged from 0.61 to 2.94 mSv y^{-1} with a mean value of 1.09 mSv y^{-1}.

Keywords: Radon, indoor radon concentration, radioactivity, effective dose

1. INTRODUCTION

Radon is a natural radioactive gas and is a member of natural decay of the uranium-238 (^{238}U), thorium-232 (^{232}Th) and uranium-235 (^{235}U). Three essential radioactive isotopes of radon are radon (^{222}Rn) in the ^{238}U chain, thoron (^{220}Rn) in the ^{232}Th chain and actinon (^{219}Rn) in the ^{235}U chain with a half-life of 3.82 days, 55.6 s and 4 s, respectively [1]. Among these isotopes, ^{222}Rn is the main cause of radiation exposure indoors due to high concentrations of ^{238}U in the ground. However, ^{220}Rn and ^{219}Rn have a short half-life and can transfer short distances before decay [2].

Radon is a significant source of ionizing radiation and responsible for more than % 50 of radiation from natural radioactivity sources [3]. Radon is a colorless, tasteless and odorless heavy noble gas which is produced by alpha decay of radium (^{226}Ra) and it exists in different levels in soil, water and air [4-6]. As a result of uranium decay in soil and rock, radon migrates through the ground, diffuses into the air and dissolves into the groundwater. Radon gas penetrates into dwellings through the cracks and pores. Although the outdoor radon gas concentration levels are generally very low, indoor radon gas concentrations depend on the type of building material, soil permeability, water usage, floor level and meteorological conditions such as air temperature and pressure [6-8]. Radon mostly accumulates in closest levels of the dwellings to the soil and rocks such as ground floors and cellars. Studies have shown that indoor radon concentrations tend to increase in winter due to lack of ventilation [9, 10]. In addition, radon concentration levels highly depend on soil

* Corresponding author: selinnozden@gmail.com
[1] Kırklareli University
E-mail: sakozcan35@yahoo.com
ORCID: https://orcid.org/0000-0003-3860-8444, https://orcid.org/0000-0001-6661-5540

permeability and high soil permeability increases penetration of radon from soil into dwellings [11].

Indoor radon exposure and inhalation of radon and its progenies are significantly hazardous for human health. Radon progenies stick to dust and particles in the air and human breathes these radioactive dust and particles when radon progenies accumulate in the indoor air. As a result of breathing radon and its progenies, human tissues are affected by alpha particles and tissues are damaged especially in lungs [12]. Inhalation of radon and its progenies is a major reason of lung cancer after smoking and between %3 and %14 of lung cancers is associated to radon [12, 13]. Human exposure to radon and recommended limits of radon gas differ from country to country and change between a few Bq m^{-3} to several thousand Bq m^{-3}. According to The Turkey Atomic Energy Agency, upper limit of inhaled radon in the homes is 400 Bq m^{-3} and in work areas is 1000 Bq m^{-3} [14].

The objective of this research is to carry out radon concentrations in the dwellings of Kirklareli Province. The radon concentration measurements were performed for 19 different dwellings in winter. The effect of floor level on radon concentration was investigated and the average indoor radon concentrations in different floors were calculated. The annual effective dose rates were estimated from measured radon activities. In addition; measured indoor radon concentrations and estimated annual effective dose rates in dwellings were compared with the results of various studies performed around the world and Turkey.

2. MATERIAL AND METHODS

Indoor radon activity levels were measured in 19 dwellings in Kirklareli, Turkey during winter in 2019. The measurements were performed in 1 and 7 days for each house to investigate radioactive radon gas exposure in Kirklareli buildings. In Figure 1, the locations of the dwellings under study are shown.

The ^{222}Rn activity concentrations were measured using the Airthings 222 Corentium Home Radon Gas Detector. The system is a digital radon gas detector and gives results in a maximum accuracy and speed. The detector measures the energy of alpha particles coming out of the decay products of ^{238}U chain. The detector has an accuracy of < 5% ± 5 Bq m^3. The measurement range of the detector is 0 to 9999 Bq m^3.

Figure 1 Study area and dwelling locations

3. RESULTS AND DISCUSSION

The measured radon concentrations in 19 dwellings at the study area are given in Table 1. Indoor radon concentration change graphs with houses for one day and seven days measurement periods are shown in Figure 2. The concentrations of radon in the dwellings ranged from 23 to 156 Bq m^{-3} for short-term 1 day measurements. The arithmetic mean of indoor ^{222}Rn concentration was calculated as 46.2 Bq m^3 and the geometric

mean of indoor ^{222}Rn concentration was estimated as 40.4 Bq m^{-3} for 1 day measurement period. In addition, for 7 days period, the level of radon concentration in the dwellings ranged from 16 to 77 Bq m^{-3}. The arithmetic and the geometric mean of indoor ^{222}Rn acticity were found to be 40.8 and 37.5 Bq m^{-3} for 7 days measurement period, respectively.

Indoor radon concentration levels measured in this study are below the concentration levels of 200 Bq m^{-3} recommended by International Commission on Radiological Protection (ICRP) and below the concentration levels of 400 Bq m^{-3} recommended by Turkey Atomic Energy Agency (TAEK) [14, 15]. The average indoor radon concentrations in this study are higher than the Turkey average (35 Bq m^{-3}) and slightly above the world average (40 Bq m^{-3}) [16, 17].

Table 1 Indoor radon concentrations for one day and seven days periods

Houses	^{222}Rn (Bq m^{-3})	
	1 Day	7 Days
1	36	43
2	25	23
3	55	29
4	156	77
5	29	57
6	58	54
7	80	31
8	33	34
9	24	30
10	42	27
11	55	37
12	38	26
13	24	40
14	60	65
15	33	77
16	23	34
17	24	27
18	45	16
19	38	49
Arithmetic Mean	46.2	40.8
Geometric Mean	40.4	37.5

The highest indoor radon levels (77 and 156 Bq m^3) were measured in Kayali region (House 15) and Taşağıl Village (House 4). House 4 was an old building and because of old construction materials had a higher radon concentration level [18]. In addition, Kayali region is covered by various rock types especially metamorphic rocks

which are rich in uranium and thorium [19]. The studies have shown that the rock type affecting the concentration of indoor radon activity [20, 21].
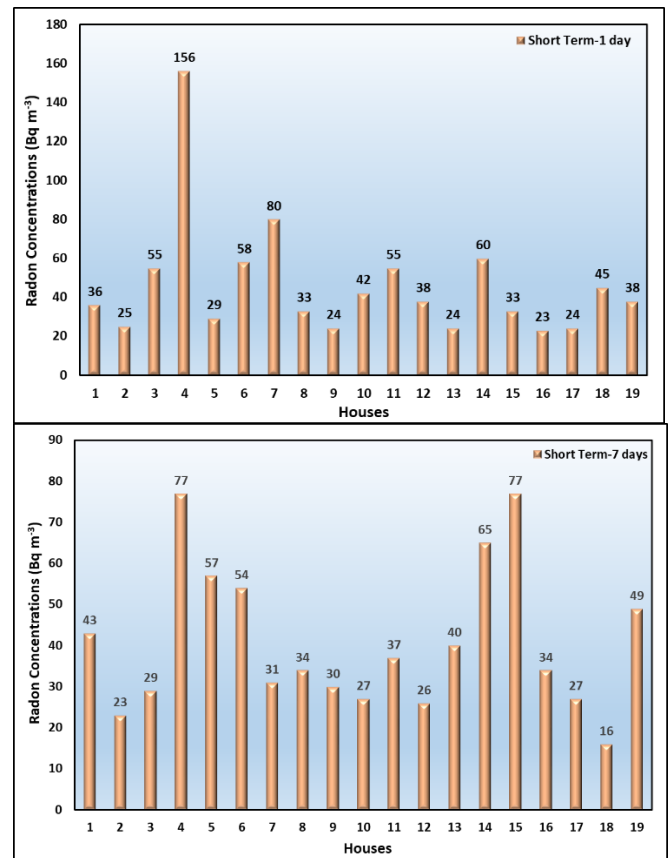

Figure 2 Indoor radon concentration change graphs with houses for one day and seven days measurement periods

Floor level of the house is also important for indoor radon activity concentration results. The effect of floor level on radon activity was investigated and the average indoor radon concentrations in different floors were shown in Figure 3. The average radon concentrations at floor levels were computed as the arithmetic mean of the results. As seen in Figure 3, the average radon concentration value in the first floor was higher compared to those in the 2 nd, 3 rd and 4 th floor. The average radon concentrations were calculated as 62.4, 44.8, 32.6 and 35.0 Bq m^{-3} for 1 st, 2nd, 3rd and 4th floors, respectively. It can be said that the floor level plays a significant role in estimating the indoor radon concentration levels and people in the first floors would have a higher risk of radon gas exposure.
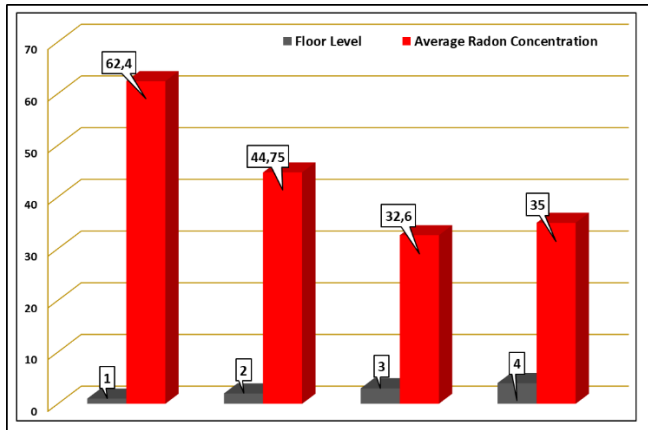
Figure 3 The change of average indoor radon concentrations in Bq m^{-3} with floor level

Epidemiological studies points that indoor radon exposure is responsible for an important number of lung cancers in the general population. For radon gas, the annual effective dose can be predicted from measured radon activity concentrations based on conversion factors given by United Nations Scientific Committee on the Effects of Atomic Radiation (UNSCEAR) report [3].

The annual effective radiation dose (AED) in units of mSv y^{-1} is calculated by the following equation [3]:

$$AED = A_{Rn} \times D_f \times O_f \times E_f \times 24h \times 365 \times 10^{-6}$$
(1)

where A_{Rn} is the measured ^{222}Rn activity in indoor (Bq m^{-3}), D_f is the dose conversion factor (9.0 nSv h^{-1} per Bq m^{-3}), O_f is the indoor occupancy (0.8) and E_f is the radon equilibrium factor between radon and its decay products (0.4 for buildings).

The calculated AED values are given in Table 2 and the graph of the change of calculated AED values with dwellings is shown in Figure 4. As seen in Table 1 and Figure 4, the range of annual effective radiation dose ranged from 0.61 (house 2) to 2.94 (house 4) mSv y^{-1}. The average annual radon effective dose rate was found as 1.09 mSv y^{-1}. It has been observed that the all values of the AED are below the recommended action level of 3–10 mSv y^{-1} by ICRP [22, 23].

In Figure 5, the plot of AED values against the average indoor radon gas concentration is shown.

It is found that the correlation between average indoor radon concentration and the calculated AED values is high (R^2=1).

Table 2 The calculated AED values in dwellings at the study area

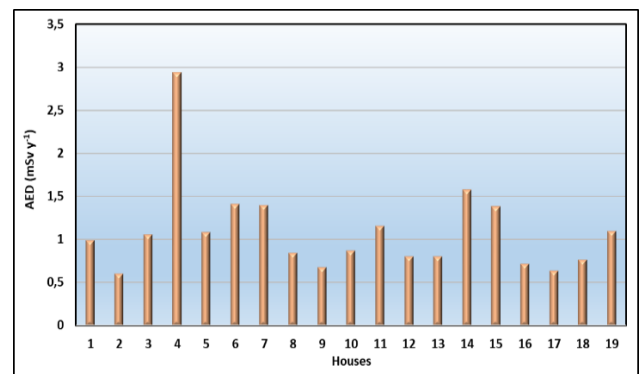| Houses	AED (mSv y^{-1})
1	1.00
2	0.61
3	1.06
4	2.94
5	1.08
6	1.41
7	1.40
8	0.85
9	0.68
10	0.87
11	1.16
12	0.81
13	0.81
14	1.58
15	1.39
16	0.72
17	0.64
18	0.77
19	1.10
Average	1.09

Figure 4 The change of calculated AED (mSv y^{-1}) values with dwellings

Many studies have been reported in the literature to measure radon concentrations in indoor. A comparison of measured indoor radon activity levels in dwellings with the results of various studies performed around the world and Turkey was given in Table 3.

Some of the ^{222}Rn activities for dwellings were found to be lower than İstanbul, Turkey (10-260 Bq m^{-3}); Kastamonu, Turkey (29-177 Bq m^{-3}); Çanakkale, Turkey (9-300 Bq m^{-3}); Ireland (21-

338 Bq m^{-3}); Italy (6.5-388 Bq m^{-3}); Mexico (15-295 Bq m^{-3}); Kosovo (35-814 Bq m^{-3}); Bulgaria (20-1117 Bq m^{-3}) and Portugal (36-1324 Bq m^{-3}). The highest value of the annual effective dose rate of ^{222}Rn in this study were lower than İzmir, Turkey (4.3 mSv y^{-1}); Manisa, Turkey (7.3 mSv y^{-1}); Kastamonu, Turkey (4.46 mSv y^{-1}); Çanakkale, Turkey (5.2 mSv y^{-1}); Ireland (13.3 mSv y^{-1}) and Kosovo (6.47 mSv y^{-1}).
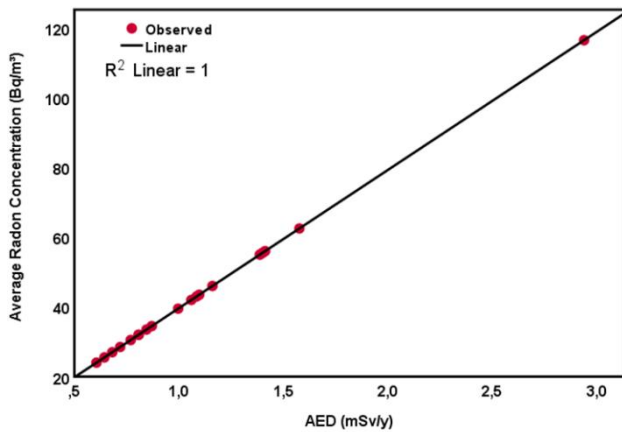

Figure 5 The plot of the calculated AED values against the average indoor radon concentration

Table 3 The comparison of ^{222}Rn activities and annual effective dose rates for indoor air with other studies around the world and Turkey

Location	^{222}Rn (Bq m^{-3})	AED (mSv y^{-1})	Reference
İzmir, Turkey	53-86	2.69-4.3	[24]
İstanbul, Turkey	10-260	-	[25]
Manisa, Turkey	47-146	2.35-7.3	[26]
Kastamonu, Turkey	29-177	0.73-4.46	[27]
Çanakkale, Turkey	9-300	0.4-5.2	[22]
Ireland	21-338	0.8-13.3	[28]
Italy	6.5-388	-	[29]
Mexico	15-295	-	[30]
Kosovo	35-814	0.28-6.47	[31]
Bulgaria	20-1117	-	[32]
Lebanon	3-79.3	-	[33]
Portugal	36-1324	-	[34]
Kirklareli, Turkey	16-156	0.61-2.94	Present Study

The results have shown that measured radon activity levels and the annual effective dose rates for Kirklareli in this study are lower than other studies around the world and Turkey.

Statistical data for average indoor radon concentrations was evaluated using the SPSS software, version 25.0 (SPSS Inc., USA). Mean, median, range, standard deviation, variance, geometric mean, kurtosis and skewness are summarized for average indoor radon concentrations in Table 4. The positive value of the skewness obtained in the statistical data shows that indoor radon concentration distribution is asymmetric with the right tail longer than the left tail. In addition, the positive kurtosis suggests that the indoor radon concentration distribution is higher and narrower than the normal.

Table 4 Statistical data for average indoor radon concentrations in dwellings at the study area

Parameter	Indoor Radon (Bq m^{-3})
Mean	43.53
Median	39.50
Standard Deviation	21.03
Range	24-117
Variance	442.40
Geometric Mean	40.20
Kurtosis	7.93
Skewness	2.48

4. CONCLUSIONS

In present study, indoor radon activity levels were investigated for Kirklareli province, Turkey. Indoor radon concentration measurements were performed in a total of 19 houses during winter in 2019. The arithmetic mean and the geometric mean of indoor ^{222}Rn concentration were calculated as 46.2 Bq m^{-3} and 40.4 Bq m^{-3} for 1 day measurement period, respectively. The arithmetic and the geometric mean of indoor ^{222}Rn activity were found to be 40.8 and 37.5 Bq m^{-3} for 7 days measurement period, respectively.

Indoor radon concentration levels found in this study are below the concentration levels recommended by International Commission on Radiological Protection (ICRP) and Turkey Atomic Energy Agency (TAEK). The mean of indoor ^{222}Rn concentrations is higher than the Turkey average (35 Bq m^{-3}) and slightly above the world average (40 Bq m^{-3}). It is found that the higher indoor radon concentrations are associated with floor level, old construction materials and rock type. In addition; the annual effective

radiation dose rates were estimated and it has been found that all AED values are below the recommended action level by ICRP.

Funding

The author (s) has no received any financial support for the research, authorship or publication of this study.

The Declaration of Conflict of Interest/ Common Interest

No conflict of interest or common interest has been declared by the authors.

Authors' Contribution

The first author contributed 60%, the second author 40%.

The Declaration of Ethics Committee Approval

This study does not require ethics committee permission or any special permission.

The Declaration of Research and Publication Ethics

The authors of the paper declare that they comply with the scientific, ethical and quotation rules of SAUJS in all processes of the paper and that they do not make any falsification on the data collected. In addition, they declare that Sakarya University Journal of Science and its editorial board have no responsibility for any ethical violations that may be encountered, and that this study has not been evaluated in any academic publication environment other than Sakarya University Journal of Science.

REFERENCES

[1] G. Milic, L. Gulan, P. Bossew, B. Vuckovic, and Z.S. Zunic, "Indoor radon mapping: a survey of residential houses of Kosovo and Metohija," Rom. Journ. Phys., 58 (Supplement), 180–188, 2015.

[2] H. V. Le, S. S. Dong, S. N. An, and D. T. Huu, "Measurement of Indoor Radon Concentration in Dalat area," Science and Technology Development Journal, vol. 21, no. 2, pp. 71-77, 2018.

[3] United Nations Scientific Committee on the Effects of Atomic Radiation, "Sources and effects of ionizing radiation," UNSCEAR Report to the General Assembly, with Scientific Annexes. United Nations, 2000.

[4] S. Narang, D. Kumar, D. K. Sharma, and A. Kumar, "A study of indoor radon, thoron and their exhalation rates in the environment of Fazilka district, Punjab, India," Acta Geophysica, vol. 66, no. 5, pp. 1233-1241, 2018.

[5] S. Sharma, V. Duggal, A. K. Srivastava, R. Mehra, and A. Rani, "Radon concentration in groundwater and associated effective dose assessment in Western Haryana, India," Internat. Jour. Inn. Res. Sci. Engg, vol. 3, pp. 69-78, 2017.

[6] H. A. Yalım, A. Gümüş, C. Başaran, M. Bağcı, A. Yıldız, D. Açil, and R. Ünal, "Comparison of radon concentrations in soil gas and indoor environment of Afyonkarahisar Province," Arabian Journal of Geosciences, vol. 11, no. 11, p. 246, 2018.

[7] R. P. Chauhan, M. Nain, and K. Kant "Radon diffusion studies through some building materials: Effect of grain size," Radiation Measurements, vol. 43, pp. S445-S448, 2008.

[8] O. Günay, S. Aközcan, and F. Kulalı, "Measurement of indoor radon concentration and annual effective dose estimation for a university campus in Istanbul," Arabian Journal of Geosciences, vol. 12, no. 5, pp. 171, 2019.

[9] M. Abd El-Zaher, "Seasonal variation of indoor radon concentration in dwellings of Alexandria city, Egypt," Radiation protection dosimetry, vol. 143, no. 1, pp. 56-62, 2010.

[10] E. Algin, C. Asici, H. Sogukpinar, and N. Akkurt, "A Case Study on the Use of Seasonal Correction Factors for Indoor Radon Measurements," Radiation protection dosimetry, vol. 183, no. 4, pp. 423-431, 2019.

[11] K. Y. Lee, S. Y. Park, and C. G. Kim, "Effects of radon on soil microbial community and their growth," Environmental Engineering Research, vol. 25, no. 1, pp. 29-35, 2020.

[12] N. Mohammed, "Indoor radon concentration levels and annual effective doses for residence of houses near uranium deposit in Bahi district, Dodoma, Tanzania," Tanzania Journal of Science, vol. 44, no. 1, pp. 159-168, 2018.

[13] J. Milner, C. Shrubsole, P. Das, B. Jones, I. Ridley, Z. Chalabi, and P. Wilkinson, "Home energy efficiency and radon related risk of lung cancer: modelling study," Bmj, 348, f7493, 2014.

[14] TAEK. Regulations for the radiation safety, No. 23999, TAEK Official Journal, 2000.

[15] International Commission on Radiological Protection (ICRP), "Protection Against 222Rn at Home and at Work," Publication 65, Pergamon Press, 1993.

[16] E. M. Köksal, N. Çelebi, and B. Özçınar, "Indoor 222Rn concentrations in Istanbul houses," Health Phys., vol. 65, no. 1, pp. 87–88, 1993.

[17] B. Kucukomeroglu, Y. O. Yesilbag, A. Kurnaz, N. Çelik, U. Çevik, and N. Celebi, "Radiological characterisation of Artvin and Ardahan provinces of Turkey," Radiation Protection Dosimetry, vol. 145, no. 4, pp. 389-394, 2011.

[18] K. Hadad and J. Mokhtari, J. "Indoor radon variations in central Iran and its geostatistical map," Atmospheric Environment, vol. 102, pp. 220-227, 2015.

[19] H. H. Selim, "Tectonics of the buried Kırklareli Fault, Thrace Region," NW Turkey. Quaternary international, vol. 312, pp. 120-131, 2013.

[20] J. A. Gunby, S. C. Darby, J. C. Miles, B. M. Green, and D. R. Cox, "Factors affecting indoor radon concentrations in the United Kingdom," Health Physics, vol. 64, no. 1, pp. 2-12, 1993.

[21] A. Popit and J. Vaupotič, "Indoor radon concentrations in relation to geology in Slovenia," Environmental Geology, vol. 42, no. 4, pp. 330-337, 2002.

[22] Y. Örgün, N. Altınsoy, S. Y. Şahin, B. Ataksor, and N. Çelebi, "A study of indoor radon levels in rural dwellings of Ezine (Çanakkale, Turkey) using solid-state nuclear track detectors," Radiation Protection Dosimetry, vol. 131, no. 3, pp. 379-384, 2008.

[23] International Commission on Radiological Protection (ICRP) Publication 65, "Protection Against Radon 222 at Home and at Work," Ann. ICRP, 23, 1993.

[24] F. S. Erees and G. Yener, "Radon levels in new and old buildings," Fundamentals for the assessment of risks from environmental radiation, Springer, Dordrecht, pp. 65-68, 1999.

[25] E. M. Köksal, N. Celebi and B. Ozcinar, "Indoor 222Rn concentrations in Istanbul houses," Health physics, vol. 65, no. 1, pp. 87-88, 1993.

[26] F. S. Ereeş, S. Aközcan, Y. Parlak, and S. Cam, "Assessment of dose rates around Manisa (Turkey)," Radiation Measurements, vol. 41, no. 5, pp. 598-601, 2006.

[27] E. Kam and A. Bozkurt, "Environmental radioactivity measurements in Kastamonu region of northern Turkey," Applied Radiation and Isotopes, vol. 65 no. 4, pp. 440-444, 2007.

[28] J. Elío, Q. Crowley, R. Scanlon, J. Hodgson, and L. Zgaga, "Estimation of residential radon exposure and definition of Radon Priority Areas based on expected lung cancer incidence," Environment international, vol. 114, pp. 69-76, 2018.

[29] L. Vimercati, F. Fucilli, D. Cavone, L. De Maria, F. Birtolo, G. M. Ferri, and P. Lovreglio, "Radon Levels in Indoor Environments of the University Hospital in Bari-Apulia Region Southern Italy," International journal of environmental research and public health, vol. 15, no. 4, pp. 694, 2018.

[30] G. Espinosa, J. I. Golzarri, J. Rickards, and R. B. Gammage, "Distribution of indoor radon levels in Mexico," Radiation measurements, vol. 31, no. 1-6, pp. 355-358, 1999.

[31] G. Nafezı, M. Bahtıjarı, B. Xhafa, G. Hodollı, S. Kadırı, S. Makollı, and Z. Mulaj, "Monitoring of indoor radon concentration in some elementary and secondary schools of Kosovo," Yüzüncü Yıl Üniversitesi Fen Bilimleri Enstitüsü Dergisi, vol. 19, no. 1-2, pp. 43-47, 2014.

[32] K. Ivanova, Z. Stojanovska, M. Tsenova, and B. Kunovska, "Building-specific factors affecting indoor radon concentration variations in different regions in Bulgaria," Air Quality, Atmosphere & Health, vol. 10, no. 9, pp. 1151-1161, 2017.

[33] R. R. Habib, R. Y. Nuwayhid, Z. Hamdan, I. Alameddine, and G. Katul, "Indoor and outdoor radon concentration levels in Lebanon," Health physics, vol. 115, no. 3, pp. 344-353, 2018.

[34] A. Curado, J. Silva, L. Carvalho, and S. I. Lopes, "Indoor Radon concentration assessment in a set of single family houses: case study held in Barcelos, North of Portugal," Energy Procedia, vol. 136, pp. 109-114, 2017.